



Ministero dell' Istruzione
dell' Università e della Ricerca



Università
degli Studi di Palermo

PhD in "Ingegneria Chimica e dei Materiali"
***Polymeric and bio-hybrid nanovectors
for drug-delivery and imaging devices***

Grimaldi Natascia

SSD Chim-07

Supervisors

Dr. C. Dispenza

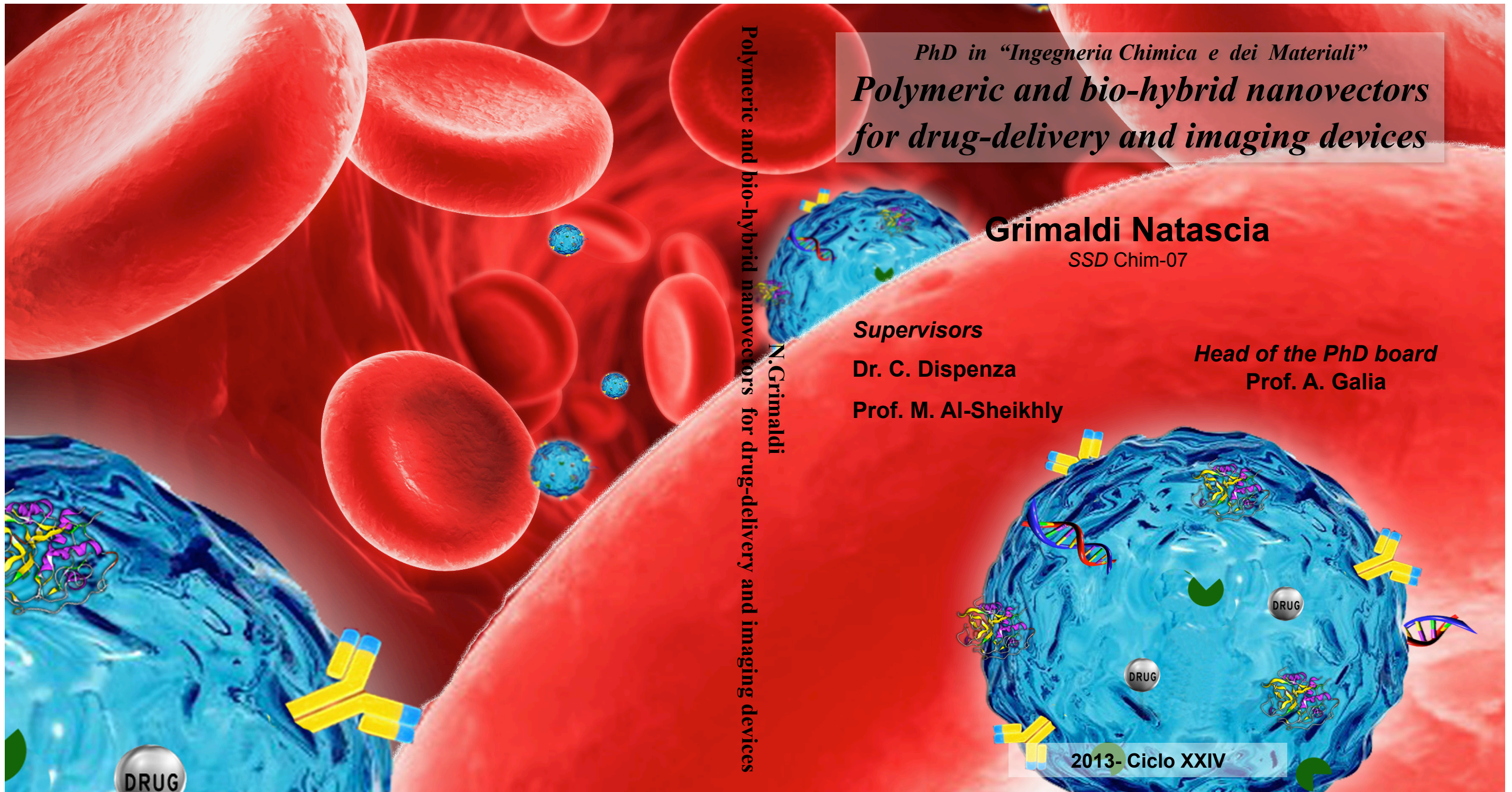
Prof. M. Al-Sheikhly

Head of the PhD board

Prof. A. Galia

Polymeric and bio-hybrid nanovectors for drug-delivery and imaging devices
N. Grimaldi

2013- Ciclo XXIV





Ministero dell' Istruzione
dell' Università e della Ricerca



Università
degli Studi di Palermo

*Polymeric and bio-hybrid nanovectors
for drug-delivery and imaging devices*

Natascia Grimaldi

Supervisors

Dr. Clelia Dispenza
Università di Palermo

Prof. M. Al-Sheikhly
University of Maryland

PhD in “Ingegneria Chimica e dei Materiali”,
2012/13-Ciclo XXIV

List of Papers

Some of the results of this thesis are included in the following papers:

- I *Studies of network organization and dynamics of e-beam crosslinked PVPs: From macro to nano.* 2012. Rad. Phys. Chem. 81(9), 1349–1353.
C. Dispenza, N. Grimaldi*, M.A. Sabatino, S. Todaro, D. Bulone, D. Giacomazza, G. Przybytniak, S. Alessi, G. Spadaro.
- II *Minimalism in Radiation Synthesis of Biomedical Functional Nanogels.* 2012. Biomacromolecules.13(6), 1805–1817.
C. Dispenza*, M.A. Sabatino, N. Grimaldi, D. Bulone, M. L. Bondi, M. P. Casaletto, S. Rigogliuso, G. Adamo, G. Gherzi.
- III *Large Scale Radiation Manufacturing of Hierarchically Assembled Nanogels.* 2012. Chem. Eng. Trans. 27, 229-232.
C. Dispenza*, M.A. Sabatino, N. Grimaldi, G. Spadaro, D. Bulone, M. L. Bondi, G. Adamo, S. Rigogliuso.
- IV *Polymeric Nanogels: nanocarriers for Drug Delivery Application.* 2012. Chem. Eng. Trans. 27, 247-250.
S. Rigogliuso*, M.A. Sabatino, G. Adamo, N. Grimaldi, C. Dispenza, G. Gherzi.
- V *High-energy radiation processing, a smart approach to obtain PVP-graft-AA nanogels.* 2014. Radiat. Phys. Chem. 94, 76-79.
N. Grimaldi*, M.A. Sabatino, G. Przybytniak, I. Kaluska, M.L. Bondi, D. Bulone, S. Alessi, G. Spadaro, C. Dispenza.
- VI *Structure and biological evaluation of amino-functionalized PVP nanogels for fast cellular internalization.* 2014. React. Funct. Polymer, 73, 1103- 1113.
C. Dispenza*, S. Rigogliuso, N. Grimaldi, M.A. Sabatino, D. Bulone; M. L. Bondi, G. Gherzi.

- VII Oligonucleotides-decorated-poly (N-vinylpyrrolidone) nanogels for gene therapy. 2014. J Appl. Polym. Sci. 131(2), 39774-39782.
C. Dispenza*, G. Adamo, M.A. Sabatino, N. Grimaldi, S. Rigogliuso, G. Gherzi.
- VIII *Water-borne Polymeric Nanoparticles for Glutathione-Mediated Intracellular Delivery of Anticancer Drugs*. 2013. NSTI-Nanotech 2013, www.nsti.org, ISBN 978-1-4822-0586-2. 3, 155-158.
N. Grimaldi*, M.A. Sabatino, D. Bulone, G. Adamo, S. Rigogliuso, G. Gherzi, C. Dispenza.
- IX *Large-scale manufacturing of radiation sculptured therapeutic nanogels*. 2013. NSTI-Nanotech 2013, www.nsti.org, ISBN 978-1-4822-0586-2. 3, 202-205.
C. Dispenza*, N. Grimaldi, M.A. Sabatino, G. Adamo, S. Rigogliuso, G. Gherzi.
- X *Glutathione-sensitive nanogels for drug release*. Submitted.
G. Adamo*, N. Grimaldi, S. Campora, M.A. Sabatino, C. Dispenza, G. Gherzi.
- XI *Radiation-engineered carboxyl-functionalized nanogels as building blocks for the generation of new therapeutic devices*. In preparation.
N. Grimaldi*, M.A. Sabatino, D. Bulone, M. Mangione, C. Dispenza.

* corresponding author

My contribution to the papers:

Papers I: Part of the characterizations. Contributes to manuscript's write up.

Paper II: NGs synthesis and characterizations (NMR and Raman spectroscopies excluded). Design of the conjugation protocols. Conjugation reactions and characterization of conjugated systems. Contributes to manuscript's write up.

Paper III, IV: NGs synthesis and characterizations. Design of the conjugation protocols. Conjugation reactions and characterization of conjugated systems.

Paper V: NGs design, synthesis and characterizations. Manuscript's write up.

Paper VI: NGs design, synthesis and characterizations (NMR and XPS spectroscopies excluded). Design of the conjugation protocols. Conjugation reactions and characterization of conjugated systems. Contributes to manuscript's write up.

Paper VII: NGs design, synthesis and characterizations. Contributes to manuscript's write up.

Paper VIII: NGs design, synthesis and characterizations. Design of the protocols. Conjugation reactions and characterization of conjugated systems. Design and experimental work on the in vitro release experiments. Manuscript's write up.

Paper IX: NGs design, synthesis and characterizations. Design of the protocols. Conjugation reactions and characterization of conjugated systems. Write up of the first draft.

Paper X: NGs design, synthesis and characterizations. Design of the protocols. Conjugation reactions and characterization of conjugated systems. Design and experimental work on the in vitro release experiments. Contributes to manuscript's write up.

Paper XI: NGs design, synthesis and characterizations. Design of the conjugation protocols. Conjugation reactions and characterization of conjugated systems. Design and experimental work on the in vitro release experiments. Write up of the first draft.

Abstract

Nanotechnology applied to the Medicine is providing new tools to the current therapeutic and diagnostic approaches to fight cancer and other diseases. However, many of the proposed nanodevices show some deficits related to both their inherent properties and performance, and the synthetic strategies proposed for their production.

In the present work, a new promising approach based on e-beam radiation-induced radical crosslinking of a water soluble, biocompatible synthetic polymer has been developed. In particular, the possibility of generating Poly-N-(Vinyl-Pyrrolidone)(PVP)-based nanocarriers, i.e. nanogels with a base PVP structure, tailored physico-chemical properties (particles size distribution, surface charge density) and multifunctionality has been explored. A thorough product analysis on the generated nanoparticles through different characterization techniques, such as dynamic and static light scattering, photo-correlation spectroscopy, FT-IR, Raman, solid state NMR and XPS spectroscopies, SEM and AFM, has been carried. PVP-based nanogels have been then used as building blocks for the assembly of tumor-target “composite” nanodevices. “Model” ligands with various biological functions and drugs have been conjugated to the nanogels. Moreover, the biocompatibility and localization pattern of the nanocarriers in cell cultures have been evaluated.

It has been demonstrated that all the NGs produced are biocompatible and able to be internalized by cells. Furthermore, the many functional groups grafted on the NGs are available for coupling reactions with bioactive molecules, such as targeting moieties, drugs and metal-ions chelating agents. This collective evidence validates the generated nanostructures for the intent they have been designed for, i.e. as nanocarriers in the biomedical field.

E-beam irradiation using industrial type accelerators has demonstrated to be a viable manufacturing process since it grants high yields in terms of recovered product and high throughputs. Moreover, through a proper selection of the experimental parameters, this approach has allowed to obtain NGs with the desired properties, in terms of size, surface charge density, degree of crosslinking and

functionality.

All the evidences collected in this study, in terms of favorable properties-by-process of the nanostructures generated and inherent advantages in the manufacturing process developed, can represent the fundamentals for a further development and evaluation of this versatile “nanomaterial platform” for the treatment and diagnosis of various diseases, and cancer in particular.

Acknowledgements

I would like to thank several people that have contributed to my personal and professional growth in the last 3 years.

First, I would like to express my gratitude to my advisor, Dr. Clelia Dispenza, for her encouragement, inspiration, caring and patience throughout my work.

I want to deeply acknowledge my co-advisor Prof. Mohamad Al-Sheikhly, Department of Materials Science and Engineering, University of Maryland, for offering me the opportunity of joining his group and for his support and guidance.

I am also grateful to Dr. Maria Antonietta Sabatino, Dipartimento di Ingegneria Chimica e dei Materiali, Università di Palermo, for her invaluable technical advice, support and friendship.

I also would like to thank Professor Giuseppe Spadaro, Dipartimento di Ingegneria Chimica e dei Materiali, Università di Palermo, for his advice, thoughtful suggestions and encouragement.

I would like to acknowledge Prof. A.G. Chimielewski and Dr. G. Przybytniak for letting me carry my e-beam irradiation experiments at the Centre for Radiation Research and Technology, Institute of Nuclear Chemistry and Technology, Warsaw, Poland.

I extend my thanks to Dr. Donatella Bulone, Istituto di Biofisica-CNR-Palermo, and Dr Wyatt N. Vreeland, Biochemical Science Division, National Institute of Standards and Technology, for their valuable discussions and training in light scattering analysis.

Dr. M.L. Bondi is gratefully thanked for her help with ζ -potential measurements.

My appreciation extends to Dr. Ghersi, Dipartimento di Scienze e Tecnologie Biologiche, Chimiche e Farmaceutiche (STEBICEF) Università di Palermo, and his group for their collaborations on the biological evaluations.

I also owe thanks to Dr P.L. San Biagio, Istituto di Biofisica-CNR-Palermo, Dr. Dianne Poster, Chemical Science and Technology Laboratory, National Institute of Standard and Technology, and to Dr. James Wishart, Chemistry Department,

Brookhaven National Laboratory, for offering me the opportunity of working at their Institutes.

The Italian Ministry of University and Scientific Research PRIN 2010-2011 (D.M. 1152/ric del 27/12/2011) *Nanotecnologie molecolari per il rilascio controllato di farmaci / NANO Molecular technologies for Drug delivery NANOMED* (prot. 2010FPTBSH) and the International Agency for Atomic Energy (IAEA), IAEA-CRP 2009-2012: IAEA *Coordinated Research Project* on "Nanoscale Radiation Engineering for Biomedical Applications" (Research Agreement N°15443) are acknowledged.

I want to thank all the colleagues in my research group at the University of Palermo and at the University of Maryland for their friendship, humor and encouragement.

Finally, I want to thank my family for their strong support through these years.

Table of contents

Acknowledgments.....	i
Table of Contents.....	iii
List of Tables.....	vii
List of Figures.....	ix
1. Scope and strategy.....	1
2. Introduction.....	4
2.1 Nanomaterials as carriers for drug delivery and imaging.....	4
2.1.1 <i>Expectations, goals and challenges in bio-imaging and drug delivery: an overview.....</i>	4
2.1.2 <i>Advanced Functional Nanomaterials in Medicine.....</i>	6
2.1.3 <i>Nanoparticle-based platforms.....</i>	13
2.1.4 <i>Conclusions.....</i>	16
2.2 Nanogels.....	17
2.3 Chemical free-radical polymerization and crosslinking in microemulsion.....	18
2.4 High-energy radiation-induced crosslinking.....	21
2.4.1 <i>Interactions of high-energy radiation with matter.....</i>	21
2.4.2 <i>Radiation-induced crosslinking of Poly-N-(vinylpyrrolidone).....</i>	22
2.4.3 <i>Radiation-induced crosslinking of Poly-N-(vinylpyrrolidone) and simultaneous monomer grafting.....</i>	28
2.4.4 <i>Radiation-crosslinked PVP-based hydrogels: from macro to nano. Overview of the state of the art.....</i>	29
2.5 Poly-N-(Vinyl-Pyrrolidone)-based composite nanodevices for tumor-targeted delivery and imaging.....	35
2.5.1 <i>Fluorescent probes.....</i>	35
2.5.2 <i>Folic Acid as a model targeting moiety.....</i>	35
2.5.3 <i>Biomolecules for the generation of biohybrid nanogels.....</i>	36
2.5.4 <i>Doxorubicin as a model drug.....</i>	37
2.5.5 <i>Gadolinium for imaging purposes.....</i>	38
3. Experimental.....	40

3.1 Materials.....	40
3.2 Samples preparation.....	40
3.2.1 PVP-based nanogels obtained via chemical radical polymerization in inverse microemulsion.....	40
3.2.2 PVP-based nanogels obtained via high-energy radiation induced radical crosslinking.....	42
3.2.3 Preparation of PVP-based NGs composite nanodevices.....	44
3.2.4 Amino Fluorescein in vitro release studies.....	46
3.2.5 Doxorubicin in vitro release studies.....	47
3.3 Characterizations.....	47
3.3.1 Yield.....	47
3.3.2 Gel fraction.....	47
3.3.3 Hydrogels Morphology from SEM and liquid-phase AFM.....	48
3.3.4 Swelling.....	48
3.3.5 Rheology determination.....	48
3.3.6 Hydrodynamic size from DLS.....	49
3.3.7 Weight average molecular weight from SLS.....	49
3.3.8 Weight average molecular weight from GFC.....	50
3.3.9 Surface charge density from Photo Correlation Spectroscopy.....	50
3.3.10 Chemical structure from FT-IR.....	50
3.3.11 Chemical structure from NMR.....	51
3.3.12 Chemical structure from Raman Spectroscopy.....	52
3.3.13 Surface chemical composition from XPS analysis.....	53
3.3.14 Estimation of the conjugation degree via UV-vis absorption and emission.....	53
4. Nanogels obtained via chemical radical polymerization in inverse microemulsion.....	54
4.1 Physico-chemical properties of PVP-based nanostructures.....	54
4.2 Colloidal stability and redispersability of PVP-based nanostructures.....	58
4.3 Internal structure of PVP-based nanostructures.....	60
4.4 Biological evaluations on PVP-based nanogels.....	63

4.5 BSA conjugation to PVP-based nanogels.....	64
4.6 Conclusions.....	65
5. Base PVP nanogels obtained via high-energy radiation induced radical crosslinking.....	66
5.1 Effect of PVP concentration on dimensional control and properties of base NGs.....	66
5.1.1 Physico-chemical and rheological properties.....	69
5.1.2 Base PVP hydrogels morphology.....	74
5.1.3 Structural modification of PVP networks from macro to nano.....	76
5.1.4 Solid state ¹³ C NMR relaxation spectroscopy.....	85
5.2 Effect of the dose-rate on base PVP NGs properties.....	87
5.3 Effect of the dose-rate on base PVP NGs properties.....	93
5.4 Conclusions.....	100
6. Amino-functionalized e-beam crosslinked nanogels.....	102
6.1 Amino-functionalized NGs physico-chemical properties.....	102
6.1.1 Influence of APMAM concentration.....	103
6.1.2 Influence of dose and dose-rate.....	103
6.2 Surface charge density of base and amino grafted PVP micro/nanogels.....	106
6.3 Structural characterization of amino-functionalized PVP micro/nanogels.....	107
6.4 Biological evaluations on amino-functionalized PVP micro/nanogels.....	111
6.5 Conclusions.....	112
7. Carboxyl-functionalized e-beam crosslinked nanogels.....	113
7.1 Physico-chemical properties of carboxyl-functionalized PVP-based nanogels.....	113
7.1.1. Influence of PVP concentration on carboxyl-functionalized NGs size.....	113
7.1.2. Influence of PVP concentration on carboxyl-functionalized NGs molecular weight.....	114
7.1.3. Influence of PVP concentration on carboxyl-functionalized NGs surface charge density.....	117
7.2 Morphology of carboxyl-functionalized PVP-based nanogels.....	118
7.3 Structural properties of the bare carboxyl-functionalized PVP NGs.....	119

7.4 Colloidal stability of NGs upon storage and as function of pH.....	121
7.5 Biological evaluations on carboxyl-functionalized NGs.....	123
7.6 Conclusions.....	123
8. PVP-based composite nanodevices for tumor-targeted delivery	
and imaging	124
8.1 Conjugation of fluorescent probes to functionalized PVP micro/nanogels.....	124
8.1.1 <i>P*-g-A fluorescent variants' properties</i>	126
8.1.2 <i>P*-g-AA fluorescent variants properties</i>	130
8.1.3 <i>Estimation of the conjugation degree</i>	133
8.2 Folic Acid as model targeting moiety.....	135
8.2.1 <i>Estimation of the conjugation degree for NGs folate-variants</i>	136
8.2.2 <i>Localization of NGs folate variants in cell cultures</i>	138
8.3 Conjugation of “model” biomolecules for the generation of biohybrid	
nanogels	142
8.3.1 <i>BSA as a model protein</i>	143
8.3.2 <i>C37 as a model antibody</i>	144
8.3.3 <i>FAM-FW-N as a model oligonucleotide</i>	149
8.4 Conjugation of Doxorubicin to carboxyl-functionalized PVP nanogels.....	149
8.4.1 <i>Drug loading experiments</i>	149
8.4.2 <i>In vitro drug release experiments</i>	151
8.4.3 <i>Intracellular drug release experiments</i>	153
8.5 Gadolinium as model imaging agent.....	154
8.6 Conclusions.....	156
9. Final Remarks	158
10. References	159

List of Tables

3. Experimental

Table 3.1: Summary of the irradiation conditions and sample codes.....44

Table 3.2: Attribution of main carbon chemical shifts of non-irradiated (linear) PVP and APMAM.....51

4. Nanogels obtained via chemical radical polymerization in inverse microemulsion

Table 4.1: Feed composition of base, fluorescent and amino functionalized PVP nanogels.....55

Table 4.2: Average hydrodynamic radius, PDI and ζ -potential of nanogel systems in water.....55

Table 4.3: Average hydrodynamic radius and ζ -potential for an amino-graft crosslinked VP nanogels redispersed in PBS, as function of pH and temperature.....60

Table 4.4: ^1H -NMR proton chemical shifts (ppm).....61

Table 4.5: ^{13}C $\{^1\text{H}\}$ CP-MAS NMR- Proton spin-lattice relaxation time in the rotating frame ($T_{1\rho}\text{H}$).....62

5. Base PVP nanogels obtained via high-energy radiation induced radical crosslinking

Table 5.1: Gel fraction (GF), shear storage modulus (G'), shear loss modulus (G'') at 1 rad/s, molecular weight of the polymer chain between two neighboring crosslinking points (M_c), and network mesh size (ξ), rehydration ratio at plateau (RR_{plateau}).....70

Table 5.2: The average number of radicals per chain per pulse ($N_{\text{rad}} : N_{\text{chains}}$ per pulse), hydrodynamic radius (Rh) and corresponding weight average molecular weight (Mw) of nanogels.....73

Table 5.3: Instantaneous average number of radicals formed per each polymer chain for LAE 100 kGy/h and Elektronika 13000 kGy/h.....90

6. Amino-functionalized e-beam crosslinked nanogels

Table 6.1: Attribution of main ^{13}C NMR chemical shifts of P*-g-A(50) L80MG..109

Table 6.2: XPS surface quantitative analysis of the investigated samples.

Elemental concentration is expressed as atomic percentage (at. %). 111

Table 6.3: XPS surface distribution of carbon species resulting from the curve-fitting of C 1s photoelectron peak. Carbon species are expressed as peak area percentage. 111

7. Carboxyl-functionalized e-beam crosslinked nanogels

Table 7.1. dn/dc, weight average molecular weight of the polymer (MW) from SLS, mean hydrodynamic diameter (D_h) from DLS and their relative distribution widths for linear PVP and NGs. 115

Table 7.2: Surface charge density and relative standard deviation for linear PVP, base and carboxyl-functionalizedNGs. 117

8. PVP-based composite nanodevices for tumor-targeted delivery and imaging

Table 8.1: Emission intensity at λ_{peak} for the FITC conjugated systems. 128

Table 8.2: Degree of conjugation for folic acid expressed as number of ligand molecules per NG (left) and weight ratio between ligand and NGs (right). 138

List of Figures

1. Scope and Strategy

Figure 1.1: Bioactive composite nanodevices assembly.....2

2. Introduction

Figure 1.2: Schematic representation of an ideal “composite” nanodevice.....6

Figure 2.2: The basic anatomy of nanocarriers design.....7

Figure 2.3: Target-specific drug delivery EPR (Enhanced Permeability and Retention) effect.....10

Figure 2.4: Nanomaterial platforms available in literature.....13

Figure 2.5: Candau, Leong and Fitch model for microemulsion polymerization. I: Micelles form and monomer and initiator move from the continuous phase to the dispersed phase; II: Polymerization starts inside some micelles. Visited micelles grow up at the expenses of non-visited micelles; III: Nanoparticles form inside the micelles.....20

Figure 2.6: PVP-carbon-centered radicals formed upon the reaction of hydroxyl radicals with PVP.....24

Figure 2.7: PVP-carbon-centered radicals evolution through various reaction pathways. Dots represent the radicals, blue segments represent the repetitive unit in the polymer chains; red segments represent new bonds formed upon radiation...24

Figure 2.8: Pulse radiolysis of PAA (17.5%) in Ar saturated aqueous solution at pH=2.0. Exemplary second order kinetic plot of the decay of PAA radicals. Absorbance recorded at $\lambda=280$ nm after a pulse of 1.1 kGy. Inset: the same data plotted in coordinates resulting from the non-homogenous kinetics model (Eq. (2.7)), $\alpha=0.73$ (best fit).⁸⁷26

Figure 2.9. Disproportionation reaction mechanism of PVP carbon-centered free radicals..... 27

Figure 2.10. Properties of PVP in aqueous solution as a function of the average absorbed dose; M_w of PVP = 1.3×10^6 g mol⁻¹, dose/pulse = 320 Gy, pulse frequency = 0.5 Hz, pulse duration (width) = 2 μ s33

4. Nanogels obtained via chemical radical polymerization in inverse microemulsion

Figure 4.1: SEM micrographs of an air-dried deposit of (a) VP-MBA (formulation #1 - purification method 1); (b) VP-MBA-APMAM(200) (formulation #3- purification method 1); (c) VP-MBA-APMAM(50) (formulation #5- purification method 2); (d) detail of (c) at higher magnification. Both in (c) and (d) dry nanogels particles cover only part of the stub to evidence the difference in morphology with the gold sputtered substrate.....57

Figure 4.2: ζ -potential curves for PVP in water.58

Figure 4.3a-b: ^{13}C $\{^1\text{H}\}$ CPMAS NMR overlaid spectra of (a) linear PVP (red) and VP-MBA-APMAM(50) nanogels (blu) with expansion of carbonyl region in the inset; (b) VP-MBA-APMAM(50) nanogels (blu) and VP-MBA APMAM(10) macrogel (red).....61

Figure 4.4: UV-vis spectra for VP-MBA-APMAM(50) and VP-MBA-APMAM(50)BSA..... 63

5. Base PVP nanogels obtained via high-energy radiation induced radical crosslinking

Figure 5.1a-c: Hydrodynamic radii of nanogels obtained for three PVP concentration, 0.1, 0.25 and 0.5 wt%, at the variance of dose, for the dose-rates of a) 100 kGy/h; b) 500 kGy/h and c) 13000 kGy/h. Error bars represent the width of the size distribution.....67

Figure 5.2a-b: Storage modulus, G' , (a) and loss modulus, G'' , (b), as function of the frequency for macrogels obtained at the variance of polymer concentration in water.....72

Figure 5.3a-d: SEM images of dried residues of hydrogels obtained at the variance of polymer concentration in water: (a) 0.25 wt%; (b) 2 wt%; (c) 4 wt% (d) 8 wt%.....75

Figure 5.4a-e. Schematic representation of network organisation for the different polymer solutions: (a) densely networked micro/macro gel particles loosely tied

together (10-8 wt%); (b) long-range interconnected networks (6-4 wt%); (c) macro/microgel islands (2-0.5(gel) wt%); (d) mainly inter-molecularly crosslinked nanogels (0.5(sol)-0.25 wt%); (e) predominantly intra-molecular crosslinking nanogels (0.1-0.05 wt%). Representation is not in scale.....76

Figure 5.5: FT-IR spectra of nonirradiated PVP and macrogels at different concentrations. All spectra were normalized with respect to the peak at 2956 cm^{-1}79

Figure 5.6: FT-IR spectra of nonirradiated PVP and nanogels at different concentrations. All spectra were normalized with respect to the peak at 2956 cm^{-1} . Vertical dashed lines correspond to the following peaks: 1769, 1698, 1662, 1397, 1384, 1058 and 986 cm^{-1}80

Figure 5.7: Raman spectra of irradiated PVP at different concentrations. All spectra were normalized with respect to the peak at 1432 cm^{-1}81

Figure 5.8a-f. Modification of Raman spectra of irradiated aqueous PVP at different concentrations: peak intensity and band width for the pyrrolidone breathing mode (a-b); peak position and band width for pyrrolidone amide I band (c-d); peak position and intensity for formed succinimide at low concentration (e-f).82

Figure 5.9A-D. $^{13}\text{C} \{^1\text{H}\}$ CP-MAS NMR spectra of irradiated systems: enlargement of the spectral zone from 160 to 190 ppm, (A); carbonyl peak chemical shift, (B); enlargement of the spectral zone from 0 to 70 ppm, (C); C3 and C4 peaks integrals, (D).84

Figure 5.10: $^{13}\text{C} \{^1\text{H}\}$ CP-MAS NMR spectra of nanogels and non-irradiated PVP for comparison. The arrow points the chemical shift of C bonded to hydroxyl group..... 85

Figure 5.11a-d. Proton spin-lattice relaxation times in the rotating frame, $T_{1\rho}\text{H}$, and cross-polarization times, T_{CH} , for PVP networks spanning across different scales, from macro (2, 4, 6 and 8 wt%) to nano (0.1 wt%): $T_{1\rho}\text{H}$ and T_{CH} for the pyrrolidone ring carbonyl carbon (C1), (a) and (c), and for the methylene carbon (C3), (b) and (d), respectively.....86

Figure 5.12 a-b: a. Hydrodynamic diameter and b. molecular weight, at the variance of the polymer concentration for two dose-rates. Error bars represent the width of the size distribution.....89

Figure 5.13: FT-IR spectra of P*0.1L40-100 and P*0.1E40. All spectra have been normalized with respect to the peak at 2956 cm⁻¹..... 91

Figure 5.14a-b: FT-IR spectra of P*0.1L40-100 and P*0.1E40. All spectra have been normalized with respect to the peak at 2956 cm⁻¹. Vertical dashed lines correspond to the following peaks: 1769, 1698, 1662 and 1400 cm⁻¹.....92

Figure 5.15a-b: a) Hydrodynamic size and b) molecular weight for P*0.1 and P*0.25 systems obtained at the highest dose-rate (13000 kGy/h) for the three integrated doses of 20, 40 and 80 kGy. Error bars represent the width of the distributions.....94

Figure 5.16: ζ-potential distribution curves for linear PVP and P*0.1 systems. The mean value of each peak is reported in the figure as a tag.95

Figure 5.17: Average hydrodynamic size and ζ-potential values with their relative standard deviations for P*(0.1) system obtained at the highest dose-rate for the three integrated doses of 20, 40 and 80 kGy.....95

Figure 5.18: FT-IR spectra of P*0.1 E20, E40 and E80. All spectra have been normalized with respect to the peak at 2956 cm⁻¹.....96

Figure 5.19a-b: FT-IR spectra of P*0.1 E20, E40 and E80. All spectra have been normalized with respect to the peak at 2956 cm⁻¹. Vertical dashed lines correspond to the following peaks: 1769, 1698, 1662 and 1400 cm⁻¹.....97

Figure 5.20: FT-IR spectra of P*0.25 E20, E40 and E80. All spectra have been normalized with respect to the peak at 2956 cm⁻¹.....98

Figure 5.21a-b: FT-IR spectra of P*0.25 E20, E40 and E80. All spectra have been normalized with respect to the peak at 2956 cm⁻¹. Vertical dashed lines correspond to the following peaks: 1769, 1698, 1662 and 1400 cm⁻¹.....99

6. Amino-functionalized e-beam crosslinked nanogels

Figure 6.1a-c. MGs and NGs hydrodynamic diameters from DLS analysis at 20°C in water. (a) Systems irradiated with low dose-rate and the lower dose

(E40). Non-irradiated aqueous PVP both in the presence and in the absence of APMAM are reported for comparison. (b) Influence of irradiation dose for the different formulations. (c) Influence of dose-rate for the different formulations. Error bars represent the variance of the particle size distribution.105

Figure 6.2: Schematics of a typical base PVP nanogels (PVP RU/APMAM=0) with its network and negative surface charges; of an amino-grafted PVP (P*-g-A) nanogel (PVP RU/APMAM=100) and of a microgel (PVP RU/APMAM=50). The curly blue lines represent grafted APMAM carrying a primary amino group. Bold red lines represent APMAM monomers or oligomers bridging crosslinked PVP coils.....104

Figure 6.3: Surface charge density for the micro and nanogels produced at the different PVP RU:APMAM molar ratios and at the two doses of 40 and 80 kGy. Error bars represent the width of the surface charge distribution..... 106

Figure 6.4: ζ -potential curves for functionalized nanogels (P*-g-A(50) E80) in water..... 107

Figure 6.5: Comparison of FT-IR spectra of the non-irradiated PVP, base PVP nanogels (P*) and amino-functionalised variants irradiated with LAE 13/9 at 80 kGy. All spectra, except for APMAM, have been normalized with respect to the peak at 2956 cm⁻¹. Vertical dashed lines correspond to the following peaks: 1661, 1695, 1765, 1600, 1537 and 1388 cm⁻¹. 108

Figure 6.6. Overlaid ¹³C {¹H} CP MAS NMR spectra of non-irradiated PVP (P), APMAM monomer (A) and amino-functionalized nanogels (P*-g-A (25)-L80) in expanded scale. Spectra are normalized with respect to the carbonyl peak..... 109

7. Carboxyl-functionalized e-beam crosslinked nanogels

Figure 7.1a-d: Chromatograms from gel filtration chromatography for (a). linear PVP and base NGs; (b). P*0.1 and P*0.1AA50 NGs; (c). P*0.25, P*0.25AA50 and P*0.25AA25 NGs; (d). P*0.5 and P*0.5AA50 NGs..... 116

Figure 7.2a-d: Liquid-AFM images collected in tapping mode for APTES-mica substrate, P*0.1, P*0.5 and P*0.5AA50 wt% systems..... 119

Figure 7.3a-c: Comparison of FT-IR spectra of the not irradiated PVP (P), base PVP nanogels and carboxyl-functionalized variants (a) P, P*0.1 and P*0.1AA50 NGs; (b) P, P*0.25, P*0.25 AA50 and P*0.1AA25 NGs; (c) P, P*0.5 and P*0.5AA50 NGs . All spectra have been normalized with respect to the peak at 2956 cm⁻¹.....120

Figure 7.4: DLS autocorrelation function curves for P*0.5AA50, acquired after storage at 4°C for different times..... 121

Figure 7.6 : Hydrodynamic diameter and relative standard deviation for P*0.1AA50 and P*0.25AA50 reported at the variance of pH and constant ionic strength (1mM).....122

Figure 7.7: ζ-potential and relative standard deviation for P*0.1AA50 and P*0.25AA50 reported at the variance of pH and constant ionic strength (1mM)..... 122

8. PVP-based composite nanodevices for tumor-targeted delivery and imaging

Figure 8.1: Scheme of a typical conjugation reaction between FITC and P*-g-A NGs via borax protocol..... 125

Figure 8.2: Scheme of a typical conjugation reaction between AmFluor and P*-g-AA NGs via EDC protocol..... 126

Figure 8.3 a-b: UV-Vis emission spectroscopy of: (a) Non-conjugated amino-functionalized nanogels, two FITC-conjugated variants and corresponding FITC-conjugated base PVP nanogel (irradiation condition: E80); (b) Normalized emissions of a typical FITC-conjugated amino-grafted nanogels/microgel (P*-g-A^{FITC}); FITC-conjugated base PVP nanogels (P*^{FITC}); free FITC aqueous solution (FITC).....127

Figure 8.4: Normalized absorption spectra for a typical conjugated NG system and the free FITC solution.....129

Figure 8.5: ζ-potential curves for functionalized nanogels (P*-g-A(50) E80) in water.....129

Figure 8.6: ζ-potential curves for conjugated nanogels (P*-g-A(50)^{FITC} E80)

in water.....	130
Figure 8.7: Normalized absorption spectra for a typical conjugated NG system, the free FITC solution and the bare P*-g-AA NGs.....	131
Figure 8.8: Absorption spectra of the free AmFluor (0.48 mM) in solution in the presence or not of carboxyl-functionalized NGs.....	132
Figure 8.9: UV-vis calibration curves ($\lambda=450$ nm) for free AmFluor in solution in the presence or not of carboxyl-functionalized NGs.....	132
Figure 8.10: Study of the diffusion kinetics of AmFluor in the presence or not of carboxyl-functionalized NGs in water at RT.....	133
Figure 8.11: DLS autocorrelation function curves for P*0.5AA50 NGs, P*0.5AA50 NGs negative control and P*0.5AA50 NGs+AmFluor.	135
Figure 8.12: Scheme of a typical conjugation reaction between AmFluor and P*-g-AA NGs via EDC/Sulfo-NHS protocol. R-NH ₂ represents folic acid.	136
Figure 8.13: Absorption spectra of P*0.2AA50+FolicAcid purified using MWCO 12 kDa and 100 kDa membranes, free folic acid and the bare NGs (P*-g-AA).	137
Figure 8.14: Full absorption spectra of P*0.5AA50+AmFluor and P*0.5AA50+AmFluor+Folic systems.....	139
Figure 8.15: Absorption spectra of P*0.5AA50+AmFluor+FolicAcid, P*0.5AA50+AmFluor, free AmFluor and the bare NGs (P*0.5AA50).....	140
Figure 8.16: Absorption spectra of P*0.5AA50+AmFluor+FolicAcid, free folic acid and the bare NGs (P*0.5AA50).....	141
Figure 8.17: Localization studies in a co-culture of HeLa and NIH 3T3 cells. The red color refers to the cells and the green color to P*0.5AA50+AmFluor+FolicAcid. The images have been taken at the confocal microscopy after different incubation times (30', 1h and 2 hr).....	142
Figure 8.18. UV-Vis absorption spectra of BSA-conjugated P*-g-A(100) system; not conjugated P*-g-A(100) system as control; free BSA, as reference.	143
Figure 8.19: Emission spectra of non-conjugated NGs (P*-g-A), NGs conjugated with C37TRITC (P*-g-AC37 ^{TRITC}) and the free antibody (C37 ^{TRITC}) in solution ($\lambda_{exc}=280$ nm).....	144

Figure 8.20: Emission spectra of NGs conjugated with C37TRITC (P*-g-AC37^{TRITC}), non-conjugated NGs (P*-g-A), and the free antibody (C37^{TRITC}) in solution (λ_{exc} =550 nm).....145

Figure 8.21: Emission spectra of free FITC and P*-g-A^{FITC}C37^{TRITC} in solution (λ_{exc} =490nm).146

Figure 8.22: Emission spectra of free C37^{TRITC} and P*-g-A^{FITC}C37^{TRITC} in solution (λ_{exc} =550nm)..... 147

Figure 8.23: Localization study in ECV304 cells. The blue colors refers to cells nuclei. The red color refers to C37^{TRITC} conjugated on NGs and the green refers to FITC conjugated on the same NGs.....148

Figure 8.24. UV-vis spectra of a carboxyl-functionalized NG in water before and after conjugation with DOX and of free DOX in water.....151

Figure 8.25 : In vitro release of DOX from P*0.5AA50-AEDP-DOX NGs in PBS (pH 7.4) at 37 °C with or without GSH.....152

Figure 8.26: Viability of MC3T3-E1 cells cultured with free-DOX or P*0.5AA50-AEDP-DOX for 48 and 72 hr. The cells have been pretreated or not with 10mM of GSH-OEt.....153

Figure 8.27: Reaction scheme for the formation of NGs-mod DTPA-Gd³⁺ complexes. Step 1. Formation of amino-mod NGs; Step 2. Deprotonation of amino groups; Step 3. Formation of NGs-mod DTPA tBut ester; Step 4. Deprotonation of carboxyl groups; Step 5. Formation of NGs-mod DTPA-Gd³⁺ complexes.....155

Figure 8.28. UV-vis spectra for “free” Gd³⁺ in the uptake solution before (red) and after (blue) mixing with NGs. The spectra refer to the UV-vis detectable complex formed with Arsenazo III and Gd³⁺. In the inset: Gd³⁺-Arsenazo III complexes at different concentration used for calibration.....156

1 Scope and strategy

The interest in nanotech applications for medicine is constantly growing as it holds the promise of radical improvements of current therapies and diagnostic modalities. Several nanocarriers have been proposed in the literature and some of them have demonstrated highly successful in the application and are now being evaluated in clinical trials. However, the road to the market is still long and difficult for several reasons. Indeed, despite of some success cases, a huge gap between the *in vitro* properties and the *in vivo* behavior of such nanocarriers has been observed. Newer promising approaches have been developed in more recent times, which include nanogels. These nanoparticles have demonstrated excellent potential for systemic drug delivery and for the design of multifunctional nanocarriers (e.g., theranostics) and triggered drug-release nanodevices.

Another limitation still present in the field of Nanotechnology applied to Medicine is the lack of “simple” and “clean” manufacturing processes, that are simultaneously viable at industrial level and able to grant high control over the product properties.

In this context, the first goal of my research project is the design and synthesis of biocompatible nanogels, with tailored particle size distribution, long-term colloidal stability and functional groups that are reactive in mild reaction conditions. These engineered nanogels will become the substrates for the assembly of bioactive “composite” nanodevices for multi-modal theragnostic purposes (a combination of therapy and diagnosis; see Figure 1.1).

The second goal is the design and development of a synthetic strategy, which can be easily scaled up at industrial level and it can be proposed as reliable manufacturing process for nanocarriers production. Furthermore, the ambition is to use this synthetic route for the generation of a wide family of nanocarriers that can constitute a “base material platform” for the treatment and diagnosis of various diseases and cancer, in particular.

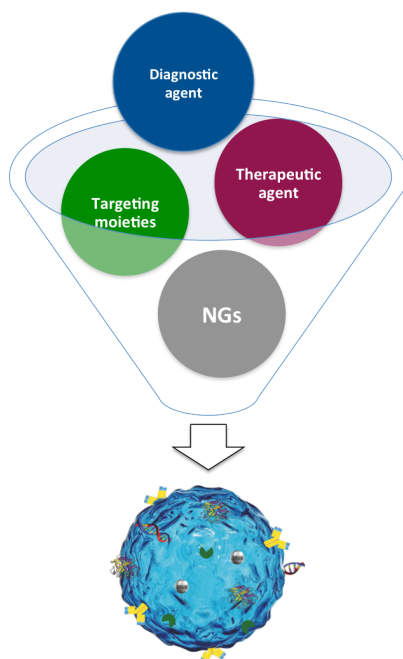


Figure 1.1: Bioactive composite nanodevices assembly.

In particular, Poly-N-(vinyl-Pyrrolidone) (PVP) has been chosen as base structural component. PVP-based nanostructures have been designed and synthesized using two different synthetic strategies: chemical radical polymerization in inverse microemulsion and high-energy radiation-induced radical crosslinking.

The first approach has been initially pursued with the intention of exploiting a conventional synthetic approach for assessing that *PVP-based nanogels* can be suitable nanocarriers; that is, the nanogels are colloidally stable, biocompatible, able to bypass the cell membrane and, by proper functionalization, to carry bioactive molecules, such as proteins.

Afterwards, all my efforts were spent in developing and evaluating an “alternative” synthetic approach that exploits the interaction of ionizing radiation with matter. Correlations between process and material properties are of utmost importance. To this goal two routes can be pursued: (i) a mechanistic study of the

2 Introduction

2.1 Nanomaterials as carriers for drug delivery and imaging

2.1.1 Expectations, goals and challenges in bio-imaging and drug delivery: an overview

A new frontier in Medicine is the design and development of advanced devices for imaging and therapy. Indeed, conventional approaches both in therapy and imaging suffer from limitations related to the low efficiency of therapeutic/imaging agents and the high impact of side-effects on the human body. In general, the critical stage in the delivery of therapeutics/imaging agents is the passage of the delivery system across numerous distinct physiological barriers, preserving the activity of the principle(s) and modulating the pharmacokinetics and tissue distribution profile.

Conventional drug administration may lead to poor bioavailability of the drug, with low and/or erratic absorption, and elevated toxic effects.¹⁻³ Two strategies have been proposed in order to improve the current limitations of therapeutics, either a change of the therapeutic agent itself or a change of the drug formulation. In particular, new therapeutic agents, such as DNA, siRNA, antibodies, proteins etc., have been widely proposed in alternative to conventional synthetic agents. These biomolecules would allow treating more efficiently many diseases, such as cancers, inflammatory and autoimmune diseases, hemophilia, cardiovascular disease, infectious diseases, and rare genetic diseases. However, the efficacy of these therapeutics is limited by three interrelated pharmaceutical issues: *in vitro* and *in vivo* instability, immunogenicity and short half-life in the body.⁴ For example, only “between 1 and 10 parts per 100,000 of intravenously administered monoclonal antibodies, which are widely used in cancer treatments, reach their targets”.⁵ Clearly, the development of new biotherapeutics poses challenges that are different from those set by the traditional small-molecule drugs. Therefore, the design of apt formulations for the delivery of biotherapeutics becomes also necessary.

The delivery of contrast agents for bioimaging share also some unmet challenges. About 35% of all clinical magnetic resonance (MR) scans utilize metal ions-based

contrast agents (CAs). Because of their low sensitivity, high concentration (0.1–0.6 mM) of CA is always required. At these high concentrations, potential toxicity, adverse side effects or even severe reactions to CAs may occur.⁶ Low molecular weight metal ions-chelates have enabled contrast-enhanced MRI for various applications, such as tumor detection and characterization, as well as vascular imaging. However, commercial low molecular weight metal ions-chelates have several shortcomings: (i) they rapidly extravasate from blood vessels to the interstitial space, making them inadequate for imaging of cardiovascular systems; (ii) they have a short circulation time, precluding accumulation in tumors; (iii) they show poor contrast at high magnetic fields.⁷

Finally, for the efficient treatment of some diseases, such as cancers, it is important to follow the fate of therapeutics and the evolution of the disease *on-line*, by “attaching” both the drug and the imaging agent on the same device. Image Guided Drug Delivery (IGDD) is a highly interdisciplinary technology that integrates the principles of therapy and imaging for a “personalized medicine” approach. The goal of IGDD is to devise patient-centered, efficacious and individualized therapeutic interventions. The process for developing such personalized therapies may incorporate patient information acquired from *ex vivo* or *in vivo* studies and follow responses to treatment. In this connection, real-time imaging offers tremendous advantages for developing personalized therapies, by providing feedback that allows active monitoring of drug delivery, release, and responses to therapy.^{8,9}

It can be concluded that common challenges and goals of advanced therapeutic and diagnostic approaches are:

- the enhancement of drug/imaging agent localization at the target site;
- the increase of drug/imaging agent residence time within the target site;
- the reduction of the drug/imaging agents concentration injected inside the body.

Nanotechnologies can offer the opportunity of overcome the issues described above.

2.1.2 Advanced Functional Nanomaterials in Medicine

Over the past three decades, nanomedicine has gained prominence in the treatment of diseases due to the possibility of achieving spatially and controlled drug release, localized therapy and minimally invasive treatments.

Bioactive “composite” nanosystems for diagnostic and therapeutic purposes have been developed. They consist of a nanocarrier, bioactive payloads for imaging, sensing and therapy, and optional targeting ligands. Each of these building blocks has a key role on the device performance and has to be properly designed. In Figure 1.2, a schematic representation of an *ideal* composite nanodevices is reported.

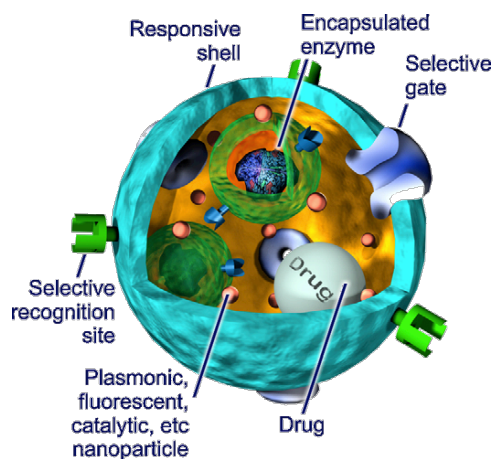


Figure 1.2: Schematic representation of an ideal “composite” nanodevice.¹⁰

The rationale behind the choice of using nanomaterials for biomedical applications is related to the observations that molecules, viruses, bacteria, and other biological relevant structures are in the nanometer-size range.¹¹ Although it is not fully elucidated how the physicochemical properties of naturally occurring nanosized complexes and structures influence their functions, it is clear that these biological structures follow precise design rules. It will be important to understand how the physicochemical properties of such nanostructures are related to their biological

interactions and functions in order to adequately materialize the potential of nanotechnology. Some basic principles have been identified, and while the research progresses, several nanocarriers have been engineered to show multiple functions.

Desirable features for the design of an *ideal* nanocarriers are (see Figure 2.2):

- Loading ability of drugs/imaging agents;
- Controlled size at the nanoscale, defined shape and surface properties;
- Controlled chemical structure and functionality;
- Chemical and colloidal stability;
- Clearance from the body and/or degradation ability;
- High biocompatibility and affinity with biological systems.

Some of these features will be discussed in more details in the following.



Figure 2.2: The basic anatomy of nanocarriers design.

Loading ability of drugs and imaging agents

Methods for incorporating payloads into engineered nanoparticles can be classified into two broad categories. In one category, the payload is physically entrapped in or absorbed onto the nanoparticle through non-covalent interactions. The second category includes examples in which the payload has been directly attached to the nanoparticle by cleavable or non-cleavable covalent bonds.¹²

In both cases, it is essential that the payloads are not prematurely released during circulation in order to insure maximal therapeutic efficacy with minimal side effects. Indeed, accidental leakages can result in the supply of payloads to healthy cells as well as the arrival of the empty nanocarrier at the disease site.¹²

In general, physical encapsulation is based on the distribution of the payload(s) between the interior of the nanocarrier and the bulk solvent. When the payloads are encapsulated within nanocarriers, release in response to a physical “stimulus” can be achieved. For example, the release can be governed by a change in the structure of the vehicle, such as swelling, which could be triggered by temperature, pH, etc.¹³ Furthermore, the delivery vehicle could be engineered to release the drug upon a chemical response.¹⁴

Physical encapsulation is the easiest approach for drug loading but it has some disadvantages. During circulation in turbulent flow conditions in the blood, the delivery vehicle encounters blood cells, serum, lipid-membranes and several potential hydrophobic components that can cause not-specific release of the payload(s). Indeed, the encapsulation stability in a complex environment like the blood is determined by the equilibrium rate of the payload(s) exchange with this environment and it is sensitive to environmental changes. For these reasons, predicting the stability of these systems with models is a difficult task.

When the payloads are chemically linked on nanoparticles a greater drug stability compared to conventional non-covalent encapsulation techniques can be achieved. Site-specific release mediated by a stimulus can be also achieved by exploiting several triggers, such as enzymes, biological chemicals, changes in pH or in the redox potential, or even external stimuli. The selection of the linkers is a delicate

step. Linkers that are sensitive to either the disease environment or to intracellular conditions very different from the conditions encountered during circulation should be selected; linkers that are easily hydrolysable or cleaved by ubiquitous enzymes, such as carbonates, anhydrides, esters, orthoesters and amides, should be avoided.¹⁵

Passive targeting

It is widely recognized that nanocarriers physico-chemical properties, such as shape, size and surface charge, may have a big impact on their *in vitro* and *in vivo* behavior.

In particular, an elevated number of studies have brought evidence that the cellular uptake and the toxicological profile of nanocarriers are strongly affected by their shape. Rods show the highest uptake, followed by spheres, cylinders, and cubes for particles with size around 100 nm, while in studies with sub-100-nm nanoparticles, spheres show an appreciable advantage over rods.^{11,16-20}

Within a given geometric shape, nanomaterial particles size distribution strongly determines nanoparticles distribution in the body compartments, escaping ability from the immunological system, ability to interact with cells and clearance by kidneys or liver.^{21,22} The hydrodynamic size of nanocarriers should not be too small, since particles with a hydrodynamic diameter of few nanometers undergo fast renal clearance and urinary excretion.^{23,24} They cannot be too big either, since particles of more than 200 nm typically exhibit a fast opsonization and uptake by the mononuclear phagocytic system (MPS) and show accumulation in the liver and spleen.²⁵⁻²⁸

Nanoparticles size can be tailored in order to induce a preferential accumulation of the drug in specific body compartments. Indeed, each disease shows specific biology and tissues morphology that can be used for targeting purposes. In particular, *passive* targeting, exploits the unique biology of the disease and the physico-chemical features of the nanocarriers, without involving any specific interactions between ligands and receptors. For example, in cancer therapy, an Enhanced Permeability and Retention (EPR) effect is described (see Figure 2.3). Solid tumors show hypervasculation of tissues with a defective anatomical structure of the blood

vessels characterized by leaks in the vessel walls and incomplete lymphatic drainage. Using these unique features of solid tumors, nanoscopic particles can accumulate preferentially near tumor sites.^{29,31}

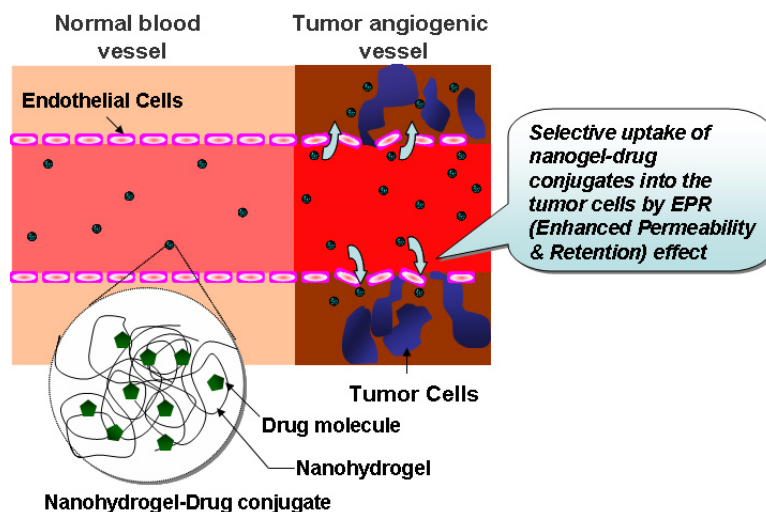


Figure 2.3. Target-specific drug delivery EPR (Enhanced Permeability and Retention) effect.

Particle size is also known to influence the mechanism of cellular internalization, i.e. phagocytosis, macropinocytosis, caveolar-mediated endocytosis or clathrin-mediated endocytosis. In particular, internalization of large particles ($> 1 \mu\text{m}$) can occur both through phago- and macropino-cytosis. Smaller nanoparticles can be internalized through several pathways, including caveolar-mediated endocytosis ($\sim 60 \text{ nm}$), clathrin-mediated endocytosis ($\sim 120 \text{ nm}$) and clathrin-independent and caveolin-independent endocytosis ($\sim 90 \text{ nm}$).³²⁻³⁴

As well as the hydrodynamic size, also the net charge on the surface is a relevant parameter with regards to nanoparticles colloidal stability and blood circulation time. The surface net charge has a great effect on aggregation, opsonization and clearance from the body. Usually a high net surface charge can prevent nanocolloids aggregation and increase their stability. In principle, a positive surface net charge is preferred for the application because physiological membranes show a negative net charge. However, it has been shown that positively charged particles attract negative charged plasma proteins and this leads to the onset of aggregation phenomena when

the charge is neutralized by a protein corona.³⁵ In conclusions, it must be acknowledged that withdraw general conclusions about the optimal hydrodynamic size and surface net charge is difficult; they have to be evaluated experimentally on a case-by-case basis.

Active targeting

Active targeting refers to the conjugation of moieties (ligands) that can enhance nanocarriers preferential accumulation at the target-site, exploiting the specific interaction between the ligand and cells receptors.

In order to achieve effective conjugation with (bio)molecules and to improve nanoparticles affinity toward the target biological system, e.g. an organ or a tissue or a cell type, a high degree of control on the nanoparticles chemistry is required. Specific chemical functionality must be present on nanoparticles, such as –COOH, –OH, –SH or –NH₂ groups.³⁶

The choice of the disease marker and the targeting moiety is a critical stage in the design of a composite nanodevice and it needs a full understanding of the disease molecular biology. In general, the targeting moiety should exhibit maximal binding affinity to the target while minimizing binding affinity to healthy tissue.³⁷ Typically, disease markers can be classified into three groups. The first group is the so called “clinically validated targets”, because of their proof-of-activity shown in humans. A validated approach has the highest probability of success. The second group is represented by “experimentally validated targets”, whose importance for disease mechanisms has been already demonstrated by a vast literature. Most cytokines and associated receptors for immunological disorders and tyrosine kinases receptors in oncology fall into this category, as the mechanisms driving these disorders are reasonably well known. The third group of targets consists of those new or less well studied target proteins that might be involved in pathogenic disorders, for which further extensive and careful validation is required.³⁸

A range of targeting bio-moieties has been proposed in the literature, including low molecular weight ligands (folic acid, thiamine, dimercaptosuccinic acid),

peptides (RGD, LHRD, antigenic peptides, internalization peptides), proteins (BSA, transferrin, antibodies, lectins, cytokines, fibrinogen, thrombin), polysaccharides (hyaluronic acid, chitosan, dextran, oligosaccharides, heparin), polyunsaturated fatty acids (palmitic acid, phospho- lipids), DNA, plasmids, siRNA, and so forth.³⁹

Clearance and Degradation

The final fate of nanocarriers is important likewise their therapeutic activity in the body. Indeed, the time that nanocarriers spend within our body needs to be optimized, since a prolonged retention in specific body compartments can increase toxicity. Nanoparticles properties, such as shape, size and surface properties, as already mentioned, can affect their clearance from the body.⁴⁰

Biodegradation represents one possible route for nanoparticles clearance. In order to exploit this route, nanoparticles have to be made using materials that can be degraded within the body. Some polymeric nanoparticles show this ability and their degradation often regulates release of payloads. In particular, by selecting the appropriate polymer type, molecular weight, and copolymer blend ratio, the degradation/erosion rate of the nanoparticles can be controlled to achieve the desired type and rate of release of the encapsulated drug. After the degradation of the nanocarriers, the degradation products should be easily removed from the organism.⁴¹

Toxicity

For practical applications of bioactive composite nanodevices, even if all of the above design criteria are met, the inherent toxicity of systems will ultimately decide their usefulness. Designing a non-toxic composite nanodevice is not easy since it combines the risks of specific payload(s) with the risks associated to the toxicity of nano-container. Some nanocarriers have shown a strong accumulation in specific tissues, such as macrophages, lung, liver, and kidney. The accumulation of nanocarriers in the wrong body compartments may also cause the deposit of a high amount of drug and/or degradation products. As a consequence, the risks associated

with the use of nanocarriers-based therapeutic devices (e.g. liver toxicity) are more complicated than the toxicity of a pure compound like a therapeutic agent.⁴²

2.1.3 Nanoparticle-based platforms

Several nanoparticles-based platforms such as liposomes, dendrimers, polymer nanoparticles (NPs), nanogels, carbon nanotubes, metallic NPs, virois and virois-like NPs, organic NPs, quantum dots and peptidic nanoparticles have been developed. Material platforms proposed in literature are schematically reported in Figure 2.4.

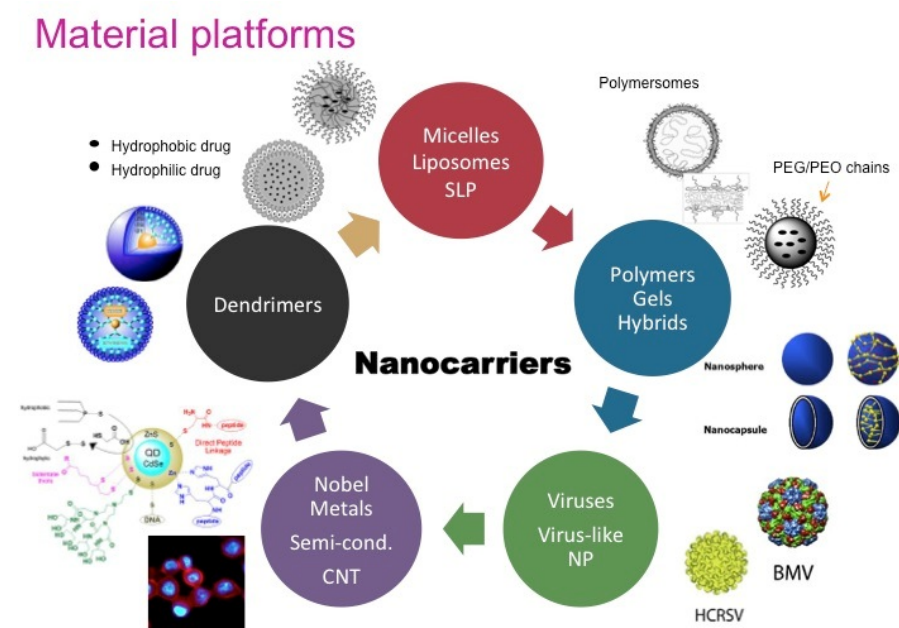


Figure 2.4: Nanomaterial platforms available in literature.

Liposomes

Liposomes are nano-sized drug delivery devices with the longest history in controlled drug-delivery. They have been first described in the 1960s by Alec Bangham.⁴³ These self-assembling structures with a spherical shape are composed of a lipid bilayer that entirely surrounds an aqueous core. Hydrophilic drug molecules can be incorporated in the internal aqueous core, while hydrophobic molecules can be integrated into the bilayer membrane. Different lipids can be used as starting material and the so generated liposomes show different physicochemical characteristics. There are several liposomes formulations already approved in the US and/or the European Union.⁴² Disadvantages of these systems are related to the manufacturing processes that are still expensive.

Polymeric Nanocarriers

Polymeric nanosystems have been also widely explored. Different type of polymers, biodegradable or not, synthetic or natural are being used for polymeric nanocarriers generation.^{25,44,45} All the systems proposed show tunable physicochemical properties, availability of multiple and complex functionality, high stability and ability to incorporate molecules with different properties. For example, cationic polymeric nanoparticles have been widely used for gene therapy, in particular siRNA delivery.⁴⁶ However, they show some limitations related to their low ability to mask the physicochemical and toxicological features of the active ingredients incorporated and the high manufacturing cost.⁴⁷

Dendrimers

Dendrimers are large and complexes molecules which have been pioneered in the early 80s.⁴⁸⁻⁵⁰ They are nearly perfect monodisperse macromolecules with a regular and highly branched tree-like architecture. Dendrimers are built up through a repeating sequence of chemical reactions, so their manufacturing process is rather

expensive.⁴² They have a good mechanical stability, but the payload/carrier ratio is low if compared to other platforms available.

Carbon Nanotubes

Carbon nanotubes are a distinct molecular form of carbon atoms, yielding a hexagonal structure. They have some suitable properties as nanocarriers such as their small inner core for the incorporation of payloads and their outer surface that can be easily modified to improve their biocompatibility and make them “smart”.^{51,52} Unfortunately, several *in vitro* and *in vivo* studies have shown that, dependent on size, length and surface topology, they can show high toxicity.⁵³ Their hydrophobicity and the consequent necessity to solubilize them in physiological liquids using surfactants are further limitations to their widespread use. These limitations can be overcome through tailor-made chemical modifications⁵⁴, but this route has a serious impact on costs.

Metallic Nanoparticles

Metallic nanoparticles, i.e. gold, silver and iron oxide, have also been widely explored as possible candidates for drug delivery and imaging applications. Each of the systems studied shows some favorable properties, such as controlled size, biocompatibility and magnetic properties, that can be used in magnetic resonance imaging.^{55,56,42} In particular, gold has been used in medicine since it is chemical inert, it shows suitable mechanical properties and it is biocompatible. Potential disadvantages are the absence of an inner cavity for payloads incorporation and lack of knowledge about the long-term behavior (bioaccumulation and elimination pathway).⁵⁷ Indeed, concern about metallic nanoparticles is also related to their build-up in the environment in a non-recyclable and non-degradable form.^{42,52}

Virus and Virus-like nanoparticles

Virus and virus-like nanoparticles have been proposed for gene therapy, since this kind of nanocarriers exhibits high efficiency for the delivery of both DNA and RNA to numerous cell lines.⁵⁸ However, some fundamental problems as toxicity, immunogenicity and difficult scale-up of the manufacturing process have been strongly hampered the diffusion of these systems.

Nanogels

Nanogels (NGs), or small particles formed by physically or chemically crosslinked polymer networks, represent a niche in the area of multifunctional nanoparticles for drug delivery and diagnostics. They are the subject of this work and their features will be described in the next paragraph.

2.1.4 Conclusions

For nanocarriers, the road to the market is still long and hard for several reasons.

They have shown to be able to protect the therapeutic/imaging agents incorporated, increase drug efficacy and CAs signal when many metal ions are coordinated to the same nanoparticle. Furthermore, it has been demonstrated that the adverse side effects induced by therapeutics and imaging agents can be minimized using nanocarriers.

However, despite of their success in the applications, the material-substrates proposed in literature often suffer from deficits coming from the high cost of the starting materials, the complexity or limitations imposed by the production processes and the poor knowledge of quality and safety of their final pharmaceutical preparations.⁵⁹ Indeed, the synthetic strategies available nowadays for the generation of most of the nanocarriers are not yet scaled at industrial level. They usually make recourse to organic solvents, toxic initiators or catalysts and surfactants, therefore expensive or time-consuming purification procedures are required. So, the availability of an easy, cost-viable and versatile synthetic methodology for the

development of effective nanocarriers-based theranostic device is essential. Moreover, the risks associated with the use of “composite” nanosystems are not well known yet.

Finally, the know-how on the interactions between nanoparticles and plasma proteins as well as the behavior of these nanoparticles into living organisms (*in-vivo* studies) is not yet fully understood and it is essential for translating these systems into clinical practices.

2.2 Nanogels

Hydrogels have been often proposed as matrices for incorporation and controlled release of drugs, owing to their benign toxicological profile, soft and rubbery consistency, tailored chemical and physical properties.

Further opportunities are offered by the control of size and shape of hydrogels down to the micro and the nanoscale. Differently from “gels”, that are macroscopic networks, their nanometric/micrometric analogues, “nanogels” (NGs) or “microgels” (MGs), may “dissolve” in solvents, just as linear macromolecules do, yet preserving an almost fixed molecular conformation. They offer unique advantages over nanosize delivery devices, including a large and flexible surface for multivalent bio-conjugation; an internal 3D aqueous environment for incorporation and protection of (bio)molecular drugs; the possibility to entrap molecules, metal or mineral nanoparticles for imaging or therapeutic purposes; stimuli-responsiveness to achieve temporal and/or site control of the release function and biocompatibility.^{23,60-62}

Major synthetic strategies for the preparation of nanogels belong to either micro-fabrication methodologies (photolithography, microfluidic, micromoulding) or to self-assembly approaches that exploit ionic, hydrophobic or covalent interactions.⁶³⁻

⁶⁵ For the latter, in particular, dimensional control has been often achieved by the recourse to surfactants. Therefore, while micro-fabrication methods are limited by the need of costly equipment, the recourse to surfactants as well as organic solvents,

initiators and catalysts may detrimentally affect the toxicological profile of the nanogels produced in colloidal systems.

The availability of inexpensive and robust preparation methodologies of such nanocarriers is at the basis of the development of effective NG-based theragnostic devices, and it has been one main limitation to their widespread use.

In the present work, Poly-N-(vinyl-Pyrrolidone) (PVP) nanogels have been designed and synthesized for controlled delivery of various diagnostic and therapeutic agents. In particular, two different synthetic strategies have been pursued and compared: chemical radical polymerization in inverse microemulsion and high-energy radiation-induced radical crosslinking. PVP has been chosen as building block since it is a biocompatible hydrophilic material able to complex ions, molecules and macromolecules.⁶⁶ Crosslinked PVP nanoparticles have already been proposed for gene delivery since they can to encapsulate and protect DNA from intracellular degradation, facilitating internalization into vesicular structures.⁶⁷ Moreover, it has been shown that PVP-based nanogels can be administered intravenously and remain in circulation for a considerable period of time evading the immune system.⁶⁸ Poly-N-(vinyl-Pyrrolidone)-based nanostructures here synthesized have been then used as building blocks for the assembly of tumor-target composite nanodevices. In particular, ligands with various bio-functions have been conjugated to the nanogels. In the following paragraphs, a detailed description of the synthetic strategies is reported. Furthermore, a brief description of the properties and functions of each ligand conjugated on nanogels is attempted.

2.3 Chemical free-radical polymerization and crosslinking in microemulsion

A conventional approach for the generation of chemically crosslinked polymer networks is the “free radical crosslinking copolymerization”(RCC) of monovinyllic monomers with di- or multifunctional co-monomers (crosslinkers). Using this approach both long-range networks, i.e. macroscopic networks, and nanometric or micrometric gels can be obtained. Several strategies have been developed in order to obtain networks with nanometric-tailored size. In heterogeneous polymerizations,

monomers polymerization and simultaneous crosslinking can be performed in a confined nanometric/micrometric space. They include (inverse) emulsion, miniemulsion, microemulsion, precipitation and dispersion polymerization processes.⁶⁹

In general, emulsions are heterophase systems in which droplets of one phase are dispersed in a second continuous phase. They are generated by mechanical agitation with the assistance of a surfactant, which stabilizes the droplets. Depending on surfactant concentration, emulsions can be “kinetically” or “thermodynamically” stable. In particular, when the concentration of the surfactant is below the critical micellar concentration (c'), the surface of the droplets is not completely covered by the surfactant molecules and the energy of the system is not minimized. Droplets are kinetically stable or metastable and they can undergo nucleation when the agitation is stopped. Otherwise, when the concentration of the surfactant is above the c' , the droplets are stable even if agitation is not provided and the emulsion is thermodynamically stable. In order to control the nanoparticles size, a high control over droplets diameter has to be granted. Droplets diameter is controlled by the type and amount of surfactant, and by the volume fraction of the dispersed phase. In particular, microemulsions are thermodynamically stable systems where the size of the initial monomer droplets can be lower than 20 nm.

Chemical radical polymerization in inverse microemulsion has been already proposed for the production of PVP nanogels.⁷⁰ However, the possibility of introducing reactive functional groups on PVP networks has not been widely explored.

Here, polymerization and simultaneous crosslinking of N-vinyl pyrrolidone (VP) and a water-soluble functional monomer, (3-aminopropyl)methacrylamide (APMAM), has been carried out inside the aqueous pods of a water-in-oil (w/o) microemulsion, using a crosslinker and an initiator. In detail, in w/o microemulsion polymerization, VP and the other monomers, as well as the water-soluble initiator, are favorably partitioned toward the water droplets (inverse micelles) that are dispersed in the continuous organic phase. Ideally, each monomer-swollen micelle (droplet) acts as a “nanoreactor” and is converted into a polymer particle of similar

size in the absence of mass transport phenomena and nucleation. A qualitative model, that schematically describes the scenario of polymerization and crosslinking in microemulsion, has been proposed by Candau, Leong and Fitch (CLF model) and it is shown in Figure 2.5.⁷¹ Radicals form upon thermal activation of the initiator. Since the initiator concentration is kept low, radicals will enter only in some micelles and the polymerization will start inside the radicals-visited micelles. The micelles not-visited by the radicals will act as monomer and surfactant reservoirs. Particles growth will take place by the diffusion of the monomer molecules through the continuous phase (primary growth) and by particles collisions as a result of their center mass Brownian motion (secondary growth). During the polymerization, micelles size increases, the level of surface energy increases and new surfactant, coming from the not-visited micelles, covers the visited-micelles surface. In the end, the number of nanoparticles generated will be lower than the initial number of micelles and the final diameter of the nanoparticles will be larger (20-120 nm) than the initial micelles diameter (≤ 10 nm).⁷²

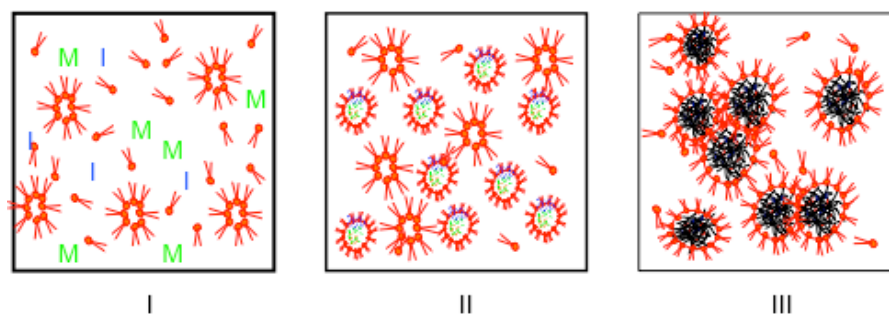


Figure 2.5: Candau, Leong and Fitch model for microemulsion polymerization. I: Micelles form and monomer and initiator move from the continuous phase to the dispersed phase; II: Polymerization starts inside some micelles. Visited micelles grow up at the expenses of non-visited micelles; III: Nanoparticles form inside the micelles.⁷¹

2.4 High-energy radiation-induced crosslinking

2.4.1 Interactions of high-energy radiation with matter

The term high-energy refers to energies greater than ionization energies of atoms and molecules, i.e. 9-15 eV per atom or molecule.⁷³

Both pulsed electron beam, a succession of short and intense pulses of electrons, and gamma radiation are two of the most common forms of high-energy radiation employed for research purposes and industrial applications. Gamma radiation is a steady-state process with typical time-averaged dose rate in the range of few kGy/h. Conversely, with pulsed e-beam very high time-averaged dose rate can be achieved (up to thousand of kGy/h).

The interaction between high-energy (ionizing) radiation and matter produces a multitude of chemical and physicochemical changes⁷³ and is completed within about 10^{-15} s. It gives rise to ions (positive ions and electrons) and electronically excited molecules that are concentrated in tracks along the path of ionizing species. The ions and excited molecules can be produced in small separated clusters (called *spurs*) or columnar *tracks*. The ions and excited molecules distribution observed in matter is function of the type and energy of the radiation source. Ions and excited molecules react/dissociate forming free radicals in covalently bonded systems and electrons solvated in polar media. In the very early stages of the reaction, these species are concentrated in the spurs, while at a later stage in the process, about 10^{-12} to 10^{-10} s after the initial events, any radicals that have not reacted diffuse from the tracks and become essentially homogeneously distributed in the medium.

At this point, the free radicals react with other molecules present in the system and chemical changes occurring in the material being irradiated are generally completed within few minutes or less in gaseous and liquid systems. Reactions are slower in most solid systems since the mobility of any reactive species formed is limited.

High-energy radiation sources are classified on the base of their energy and the rate at which they deposit the energy in the surrounding medium. In particular, the rate energy loss is described as the linear energy transfer (LET). Electron beam and electromagnetic (e.g. gamma and x-ray) radiation with energies in keV and MeV

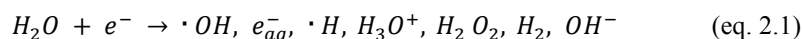
ranges are examples of low LET radiations, which typically deposit energy in small isolated clusters of ions and excited molecules, while slower electrons and large positively charged ions are examples of high-LET radiation which deposit a large fraction of energy in columnar tracks.⁷³⁻⁷⁵

2.4.2 Radiation-induced crosslinking of Poly-N-(vinylpyrrolidone)

In the present work, Poly-N-(vinylpyrrolidone)-based crosslinked structures have been generated irradiating polymer aqueous solutions using pulsed e-beams.

The energy deposited by the radiation in a multi-component material is distributed in proportion to the mass fraction of each component present in the system. Thus, in the case of diluted or semi-diluted polymer aqueous solutions the radiation energy is mainly absorbed by the most abundant component that is water.⁷⁵

Water undergoes radiolysis. The reactive species formed, within 10^{-7} - 10^{-6} s after deposition of energy, are hydroxyl radicals ($\cdot\text{OH}$), hydrated electrons (e_{aq}^-), hydronium ions (H_3O^+), protons (H^+) together with H_2O_2 , H_2 , OH^- (see eq. 2.1).⁷⁶



The amount of products formed upon radiation is expressed through the radiation chemical yield or G value. The G value ($\mu\text{mol J}^{-1}$) is defined as the moles of product produced or destroyed per joule of absorbed ionizing radiation energy or as the number of chemically changed molecules per 100 eV of absorbed energy. The SI unit of absorbed dose is the gray (Gy) which is defined as the amount of the absorbed energy in joules per unit mass (kg).⁷³⁻⁷⁵ The expression of the radiation chemical yield is as follows:

$$G(\mu\text{mol}/\text{J}) = \frac{C \cdot 10^6}{D \cdot \rho} \quad (\text{eq. 2.2})$$

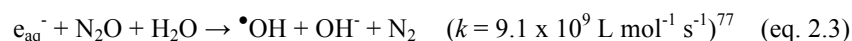
where C (mol/L) is the concentration of product formed or destroyed, D (Gy) is the absorbed dose, and ρ (kg/l) is the bulk density.

The G-values for the primary products of water radiolysis in the pH range 3 up to 11 are⁷³:

$$G(e_{aq}^-) = G(\bullet OH) = G(H_3O^+) = 0.27 \mu\text{mol J}^{-1}$$

$$G(H^\bullet) = 0.055 \mu\text{mol J}^{-1}; G(H_2) = 0.045 \mu\text{mol J}^{-1}; G(H_2O_2) = 0.068 \mu\text{mol J}^{-1}$$

In this study, before irradiation the solutions have been saturated with nitrous oxide (water solubility 25 mM at 20 °C) and all the e_{aq}^- have been converted into $\bullet OH$ by nitrous oxide (N_2O) by the following reaction:



In this condition the $\bullet OH$ radicals G value is doubled.

The products of water radiolysis interact with the solutes present in solution and chemical changes occur. This is a typical example of “indirect” effect of radiation on the matter. Direct effects predominate in systems where the reactive radicals cannot move freely (e.g. in the solid state) or where a particular species comprises a larger mass fraction of the total matrix.

Hydroxyl radicals are very reactive oxidizing species. In presence of organic monomers and macromolecules, $\bullet OH$ radicals readily abstract H from the C-H bonds to yield carbon-centered radicals. Due to this high reactivity, the H-abstraction by $\bullet OH$ is a non-selective process.⁷³ Besides H-abstraction, $\bullet OH$ add to unsaturated bonds with high rate constants, near to the diffusion-controlled limit:



The $\bullet OH$ predominantly reacts with polarized double bonds at the electron-rich center⁷⁸ due to its electrophilicity.⁷⁹ Since PVP does not have unsaturated carbon within its structure, H abstraction is expected to occur at the carbon in the aliphatic polymeric backbone as well as at the carbon in the pyrrolidone ring and produce carbon-centered free radicals as shown in Figure 2.6.^{80,81}

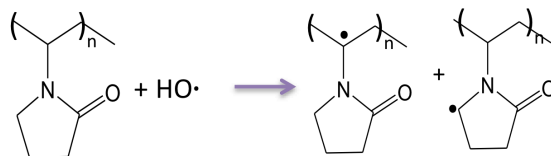
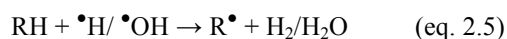


Figure 2.6. PVP-carbon-centered radicals formed upon the reaction of hydroxyl radicals with PVP.

H atoms can also contribute to the abstraction of molecular H, as follows:



where R represents alkyl or aryl group, $\text{R}\cdot$ represents each radical. The H atoms have a much lower yield than that of hydroxyl radicals (ca. 10% of the hydroxyl radicals in N_2O -saturated solutions) and the rate constants of reaction with polymer chains are lower.⁸²

The PVP carbon-centered free radicals formed can recombine both intra- and intermolecularly, undergo hydrogen transfer, disproportionation and chain scissions. Figure 2.7 is a schematic representation of all the possible macroradicals evolution reactions.

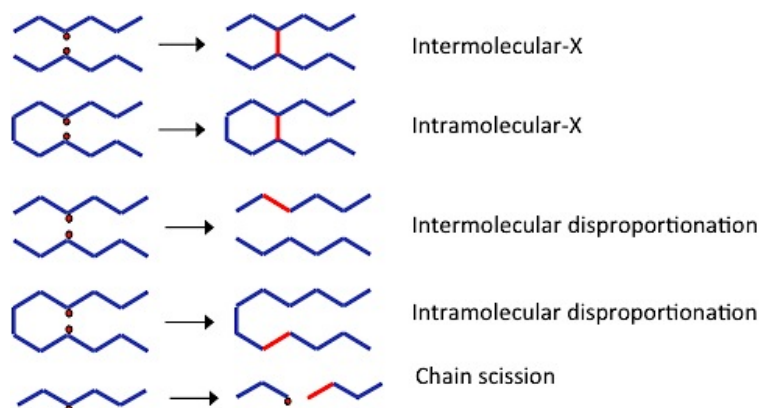


Figure 2.7: PVP-carbon-centered radicals evolution through various reaction pathways. Dots represent the radicals, blue segments represent the repetitive unit in the polymer chains; red segments represent new bonds formed upon radiation.

Crosslinking transforms a linear polymer as PVP into a 3D molecule and it can occur either between adjacent polymer chains (inter-molecular crosslinking) or within single polymer chain (intra-molecular crosslinking). Inter-molecular crosslinking is expected to increase the average size and molecular weight of starting polymer chains, whereas intra-molecular recombination does not affect the molecular weight, but it induces a contraction of the polymer coils reducing their dimension.

Macroradicals decay through inter-molecular crosslinking follows a classical II order kinetic. In particular, the reaction rate expression is:

$$-\frac{d[PVP^{\bullet}]}{dt} = k_2[PVP^{\bullet}]^2 \quad (\text{eq. 2.6})$$

where $[PVP^{\bullet}]$ is the instantaneous macroradicals concentration and k_2 is the II order kinetic constant. This is a diffusion-controlled process involving two separated entities that need to diffuse for encountering each other. Since it is a diffusion-controlled process one could expect that in the diluted regime the kinetic constant can be affected by both the polymer concentration in solution and its molecular weight. Indeed, when polymer concentration decreases (below the critical chain overlap concentration), the distance between polymer chains increases and they need to diffuse through a longer distance before approaching each other and recombine. Moreover, the diffusion coefficient varies at the variance of the polymer molecular weight and the diffusion of bigger macromolecules is slower. For high molecular weight PVP, the II order kinetic constant will be lower than that of low molecular weight PVP.^{83,84}

When macroradicals decay via intra-molecular crosslinking, a deviation from the homogenous II order kinetic has been observed for many systems.⁸⁵ In this case, the reactive entities are no longer independent since they belong to the same polymer chains. The kinetic is governed by the mobility of the segments on which radicals are located. The timescale and energy barrier of their mutual approach depend on their absolute and relative positions on the chain and the process cannot be described by a single value of activation energy, but by its distribution. Furthermore, the

formation of new bonds between the polymer segments reduces their mobility in the course of the reaction. Intra-molecular crosslinking kinetic can be modeled using a dispersive kinetics model⁸⁶:

$$k(t) = Bt^{\alpha-1} \quad (\text{eq. 2.7})$$

where $k(t)$ is the time-dependent kinetic constant, t the reaction time and B and α are parameters. α takes in account the deviation from a classical II order decay. Typical values observed for α are between 0.4 and 0.8. In particular, when α is equal to 1, the system follows a classical II order kinetic, while lower is α value, bigger is the deviation from it.⁸⁷ Figure 2.8 shows typical decay kinetics of PAA-derived radicals, in coordinates corresponding to classical second-order reaction. The experimental points do not follow a straight line. Instead, the momentary rate constant (the slope) decreases during the reaction. This is a typical feature of intra-molecular recombination.

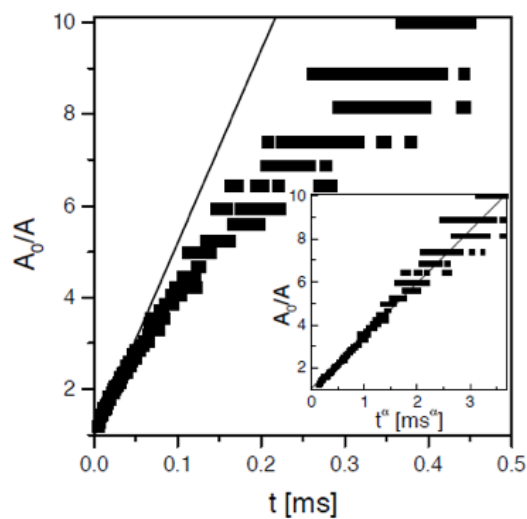


Figure 2.8: Pulse radiolysis of PAA (17.5%) in Ar saturated aqueous solution at pH=2.0. Exemplary second order kinetic plot of the decay of PAA radicals. Absorbance recorded at $\lambda=280\text{nm}$ after a pulse of 1.1 kGy. Inset: the same data plotted in coordinates resulting from the non-homogenous kinetics model (Eq. (2.7)), $\alpha=0.73$ (best fit).⁸⁷

Chain scission is a competitive reaction with cross-linking and it results in a reduction of the size and molecular weight of the polymer. It is well known that major chain-scission reactions happen when the lifetime of polymer radicals are relatively long and chain flexibility is limited, such as in poly(acrylic acid).⁸⁸ Conversely, PVP undergoes mainly crosslinking when irradiated in water solution and oxygen free atmosphere.⁸⁹ The rate of degradation induced by chain scission reactions follows a I order kinetic.⁷³

Hydrogen transfer reactions can also occur and they do not affect the polymer chemical structure, but disproportionation reactions (Figure 2.9) do.⁷⁵ In particular, disproportionation reactions introduce double bonds on the polymer networks. Disproportionation as well as crosslinking follows a II order kinetic, since it is a bimolecular process.⁹⁰

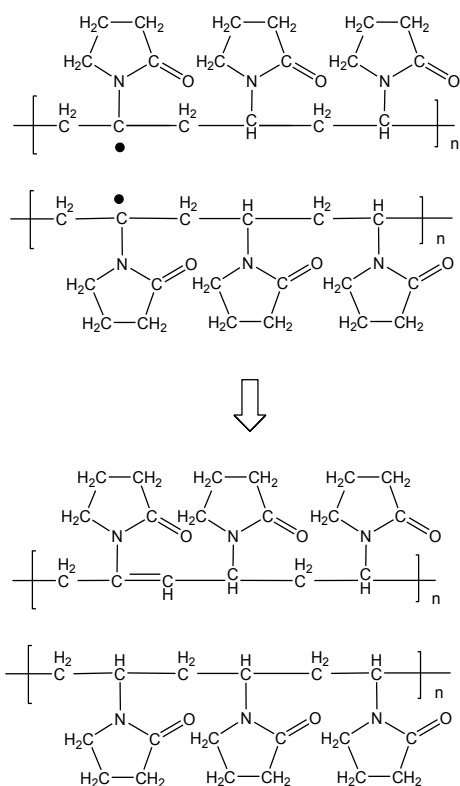


Figure 2.9. Disproportionation reaction mechanism of PVP carbon-centered free radicals.

2.4.3 Radiation-induced crosslinking of Poly-N-(vinylpyrrolidone) and simultaneous monomer grafting

PVP has been also irradiated in presence of acrylic monomers carrying reactive functional groups, such as acrylic acid (AA) and (3-aminopropyl)methacrilamide (APMAM). In presence of monomers, the reactions pathway becomes more complicated and further reactions such as monomer homopolymerization and monomer grafting to PVP may also occur. Indeed, upon irradiation, monomers undergo homolytic scission of their double bonds and the so formed monomer radicals can evolve through various bimolecular reactions. They can undergo either homopolymerization, transfer to the polymer and/or terminate by recombination with a polymer macroradical. The extent of each of these reactions is determined by both monomer concentration and solution pH. In particular, monomers homopolymerization is favored at high monomer concentrations. When the system is rich of unsaturated monomer molecules ($[M] \gg [\bullet\text{OH}]$), which are efficient radical scavengers, hydroxyl radicals will react preferentially with them. This can be explained in the light of eq. 2.8, which expresses the probability of reaction between $\bullet\text{OH}$ radicals and PVP:

$$\%(\bullet\text{OH} + \text{PVP}) = \frac{[\text{PVP}] \cdot k_2(\text{PVP} + \bullet\text{OH})}{[\text{PVP}] \cdot k_2(\text{PVP} + \bullet\text{OH}) + [\text{M}] \cdot k_2(\text{M} + \bullet\text{OH})} \quad (\text{eq. 2.8})$$

where, $\%(\bullet\text{OH} + \text{PVP})$ is the probability of reaction between PVP and $\bullet\text{OH}$ radicals; $[\text{PVP}]$ is the concentration of polymer reactive sites; $[\text{M}]$ is concentration of the monomer; $k_2(\text{PVP} + \bullet\text{OH})$ is the II order kinetic reaction for the polymer transient species built-up; and $k_2(\text{M} + \bullet\text{OH})$ is the II order kinetic reaction for the monomer transient species built-up.

As a result many monomer radicals will form and add to other monomer molecules. This picture is furthering complicated by the presence of ionizable groups in the monomer structures; the solution pH also governs the occurrence and extent of homopolimerization. In particular, monomer homopolimerization is not favored when its functional groups are in the ionized form; the mutual repulsion

between the charged monomer molecules impairs their recombination.⁸⁸ Furthermore, if oligomers and/or homopolymers form they mainly undergo chain scission. Indeed, it is reported in some works on high-energy radiation of poly(acrylic acid) (PAA)⁸⁷ that when this polymer is irradiated at pH neutral or alkaline, it assumes a rod-like shape, its segments become less flexible and the repulsive forces prevent radicals approach. Under such conditions, some radicals can survive even for hours and chain scission can occur to a high extent. What already discussed for PAA can be extended to other homopolymers with fixed charges on their chains, as poly-(aminopropylmethacrilamide).

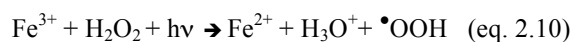
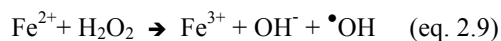
2.4.4 Radiation-crosslinked PVP-based hydrogels: from macro to nano. Overview of the state of the art.

Poly-N-(vinylpyrrolidone) hydrogels have been already produced using both high-energy radiation (pulsed e-beam and γ -radiation) and photo-induced crosslinking process. However, the possibility of introducing reactive functional groups on PVP networks has not been widely explored. Furthermore, the applicability of PVP-nanogels produced via radiation-crosslinking processing as delivery systems have not been assessed in any published study. Here, a brief overview of the background on radiation-crosslinked PVP-based hydrogels is attempted.

PVP crosslinking upon ionizing irradiation of aqueous solution has been first reported by Charlesby et al. in 1955.⁹¹ From the very beginning, these radiation-crosslinked hydrogels proved to be useful materials for medical and pharmaceutical applications since they are as born-sterilized materials.^{92,93} Therefore, many studies have been performed in the 80s-90s, in order to improve the physico-chemical properties of these macrogels and to understand how the irradiation conditions could affect the material properties. Since the 1990, radiation-crosslinked PVP hydrogels have been applied as wound dressing and commercialized under the trade names HDR® and Aqua-Gel®.^{93,94}

PVP macrogels have been also produced via photo-induced crosslinking reactions. Both direct ultraviolet irradiation of PVP aqueous solutions and photo-induced

crosslinking in the presence of crosslinking agents have been explored.^{95,96} The first approach leads to crosslinked networks through pyrrolidone moiety photolysis. In order to obtain macrogels with suitable mechanical properties, prolonged irradiations, i.e. high doses, are requested. Conversely, using crosslinking agents, such as hydrogen peroxide, and photo-Fenton reactants, PVP networks can be obtained in correspondence of lower doses. Indeed, it is reported that, in the presence of H₂O₂, the radiation doses necessary to form UV-crosslinked PVP hydrogels are typically one order of magnitude lower. In detail, upon UV irradiation, hydrogen peroxide undergoes photo-homolysis and generates hydroxyl radicals, which quickly react with macromolecules in solution. Macroradicals then can both recombine or undergo chain scission. Since the photolysis of H₂O₂ generates hydroxyl radicals, this process mimics that of high-energy radiation and leads to similar structures at the macro scale. Feasible sources for hydrogen peroxide photo-induced crosslinking are restricted to low pressure mercury lamps, which are relatively expensive devices with almost monochromatic sources ($\lambda=254$ nm). Little is known about the structure and crosslinking mechanisms of the PVP hydrogels generated by UV light irradiation. Zhu et al. proposed a reaction mechanism for hydrogels obtained by UV-irradiation of PVP-H₂O₂ solutions. In their approach, complementary spectroscopic analyses have been used for the determination of the relationships between macroscopic function, molecular structure and process.⁹⁷ An alternative approach is represented by photo-Fenton reactions. A Fenton system involves hydrogen peroxide and ferrous salts, which can generate highly reactive hydroxyl radicals (as shown in eq. 2.9). The rate of hydroxyl radicals production can be enhanced by UV radiation via the reaction shown in eq. 2.10.



In this approach, less energetic and inexpensive sources, i.e. UVA-visible radiation (290–400 nm) can be used. However, the doses necessary for obtaining a hydrogel with properties similar to that obtained in the absence of ferrous salts, is three times

higher than that requested by hydrogen peroxide photo-induced crosslinking. PVP photo-crosslinking reaction can be a feasible process for macrogels production since UV radiation is safe, portable and cost-viable process. However, this process cannot be easily scaled at industrial level, in consideration of the low penetration depth of UV rays.

At the best of my knowledge, only few studies on the possibility of generating nanogels using photo-induced crosslinking reactions have been reported in the literature. Xu et al. reported that polyethyleneimine (PEI) nanogels can be produced via photo-Fenton reaction.⁹⁸ In particular, these nanogels have been obtained starting from a commercial PEI and showed controlled particles size, homogeneous structure, good dispersion in water and high stability. Conversely, high-energy radiation crosslinking has been extensively proposed for the generation of gels with controlled particles size at the micro and nanoscale.^{81,99,100}

Rembaum et al. in the 1976 reported for the first time that is possible to obtain polymeric microspheres using high-energy radiation¹⁰¹ and radiation-induced dispersion polymerization to form polymer micro and nanoparticles is widely reported in the literature. In the 1998 Ulanski et al. reported, for the first time, that nanogels can be generated by irradiating semi-diluted poly(vinyl alcohol) (PVA) aqueous solutions at high dose per pulse (1100 Gy/pulse) and low deposited dose (1.1 kGy) with no recourse to surfactant, as template agents.¹⁰⁰ The authors selected the irradiation conditions that could enhance intra-molecular crosslinking among all the possible termination reactions that may occur upon irradiation. In particular, it has been highlighted that the main factor that influences the kinetics of recombination reactions is the number of radicals formed simultaneously on the same polymer chain (Z_{R0}), that in turn depends on the intensity of radiation or dose-rate (more precisely, on the dose per pulse). If this number is lower than 1, the probability of carbon-carbon intra-molecular crosslinking is very low. On the other hand, if $Z_{R0} < 1$, the concentration of the polymer is above the critical chain overlap concentration, ($C_p > C_p^*$), and the total dose D is higher than a threshold value, called the “gel dose” (D_g), macroscopic polymer networks can form. Contrariwise, if $Z_{R0} \gg 1$ carbon-carbon intra-molecular crosslinking is the prevailing termination

reaction and nanogels can be obtained as a result. Therefore, by a proper choice of the experimental parameters, i.e. composition of the reaction feed and irradiation conditions, the average distance between radicals present simultaneously on the same polymer chains can be controlled and as a result, also their final fate can be governed.

In the past, pulsed electron beam irradiation of semi-diluted PVP solutions has been generally performed at high dose per pulse (320-1000 Gy/pulse) and integrated low doses (<5 kGy). In these conditions, intra-molecular crosslinking dominates and PVP-based nanogels have been generated. These nanogels showed a decrease in the radius of gyration (R_{gyr}) while maintaining the same weight averaged molecular weight (M_w) of the non-irradiated PVP (Figure 2.10).⁸²

More recent studies, including my PhD dissertation, suggest that several experimental parameters can contribute to the final structure of radiation-induced crosslinked PVP nanogels. In particular, nanogels physico-chemical and structural properties can be further tuned by varying:

- The dynamics and diffusion kinetics of polymeric segments in solution, i.e. the *temperature, nature of the solvent, polymer molecular weight distribution, etc.*;
- The nature and half-life of formed macroradicals;
- The duration of each single pulse, i.e. *pulse width*;
- *The pulse repetition rate (or frequency)*;
- *The total dose deposited.*

An et al. have demonstrated that the temperature at which the irradiation is performed can affect nanogels hydrodynamic size and the molecular weight: nanogels with smaller molecular weight have been obtained when the irradiation is performed at higher temperatures.⁸¹ Indeed, the conformation of PVP chains in aqueous solution and their diffusion coefficient are sensitive to temperature. As the temperature increases, PVP-water hydrogen bonds are destroyed, thereby the polymer shifts from chain-extended to coiled conformation. The shrunken form of PVP at high temperature (77 °C) favors intra-molecular crosslinking since it leads to shorter inter-radical distances when radicals form on the same chain.

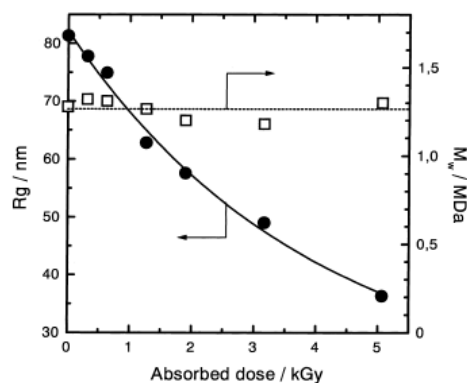


Figure 2.10. Properties of PVP in aqueous solution as a function of the average absorbed dose; M_w of PVP = 1.3×10^6 g mol⁻¹, dose/pulse = 320 Gy, pulse frequency = 0.5 Hz, pulse duration (width) = 2 μ s.⁸²

All the approaches described above do not allow an independent control of molecular weight and particles size, i.e. both of hydrodynamic and gyration radius. In order to increase the design flexibility, a two-steps synthetic approach has been proposed by Kadlubowski et. al.¹⁰² In particular, in the first stage a “concentrated” PVP aqueous solution, i.e. above its critical chain overlap concentration has been irradiated in a gamma chamber. Continuous irradiation at a low dose-rate has been used in order to induce mainly intermolecular crosslinking and to obtain nanogels with tailored molecular weight. The so produced nanogels have been then diluted and further irradiated using e-beam at a high dose per pulse (1000 Gy/pulse) and low dose (5-6 kGy). In these conditions, intra-molecular crosslinking occurs and nanogels coils shirked, without significant modifications of their molecular weight.

All the systems described above show some favorable properties as nanocarriers, i.e. controlled particles size, however they suffer from the lack of specific reactive functional groups that can be exploited for bioconjugation purposes. A viable strategy to generate highly functionalized PVP-based nanogels using radiation-induced crosslinking is to perform the irradiation in the presence of polymers/monomers carrying reactive functional groups. Carboxyl functionalized

PVP-based nanogels have been produced using high-energy radiation both irradiating PVP/PAA and PVP/AA solutions. PVP/PAA solutions have been irradiated using both pulsed e-beam¹⁰³ and γ -ray radiation.^{104,105} Nanogels with controlled particles size have been obtained in both cases. In these approaches the authors exploited the ability to form complexes of PVP and PAA. Indeed, it is well known that PVP and PAA form interpolymer complexes based on multiple hydrogen bonding at pHs close to AA pKa. In particular, PVP acts as a proton donor and PAA is a proton acceptor.¹⁰⁶ Polymers interact in a cooperative way, which depends on molecular weight of individual components, their concentration as well as degree of dissociation of charge-bearing polymer, and on the character of solvent. The attractive character of the interaction causes shrinkage of complexed macromolecules and the obtained supramolecular structures can be fixed into nanogels using radiation-induced covalent crosslinking reactions. It has been demonstrated in both the approaches that nanogels particles size can be controlled by varying the ratio between PVP/PAA and the total deposited dose. PVP-graft-AA nanogels of narrow size distributions have been also prepared by gamma radiation-induced polymerization of acrylic acid in PVP aqueous solution. In this approach, AA homopolymerization is carried out in the presence of PVP, which acts as a template polymer. The authors proposed the following reaction mechanism. AA homopolymerization starts in the bulk and when AA oligomers reach a critical length, they can form complexes with PVP and adsorb on the template. Now the polymerization proceeds by adding monomer from solution onto the growing chain adsorbed on the template. After most of monomer molecules are polymerized and nanoparticles are formed, radicals can form on the polymer chains (both PVP and PAAc) and recombine, fixing the structure. Nanogels size can be affected by the pH of the feed solution, the ratio between AA and PVP and the irradiation conditions. In order to form nanogels, the pH has to be below 4. Furthermore, smaller and more stable nanogels can be produced by irradiating a feed solution containing about 50 to 75 mol% of AAc and using PVP of high molecular weight.¹⁰⁷

2.5 Poly-N-(Vinyl-Pyrrolidone)-based composite nanodevices for tumor-targeted delivery and imaging

In order to show the potential of the generated nanogels, poly-N-(vinyl-Pyrrolidone)-based nanostructures have been used as building blocks for the assembly of tumor-target composite nanodevices. Ligands with various functions have been conjugated to nanogels. Each of these ligands has distinct features and biological activity, which is expected to be transferred to the nanogels after the coupling reaction. In the following, a brief description of the properties and functions of each ligand is reported.

2.5.1 Fluorescent probes

Fluorescent dyes have been used for labeling and tracking nanogels during *in-vitro* localization studies in cell cultures (via fluorescence and confocal laser scanning microscopy). In particular, fluorescein-isothiocyanate (FITC) and aminofluorescein (AmFluor) have been covalently attached on amino- and carboxyl-functionalized nanogels, respectively. Indeed, FITC is reactive towards primary amino groups to form a thiourea linkage, while AmFluor is reactive towards carboxyl groups to form an amide bond.¹⁰⁸ Both the probes are fluorescein derivatives and present similar properties. In particular, their UV-vis absorption maximum is around 490 nm and their of UV-vis emission maximum is around 520 nm in aqueous solution.

2.5.2 Folic acid as a model targeting moiety

Folic acid (FolAc) has been conjugated to carboxyl-functionalized nanogels as tumor-targeting moiety. Folic acid has been chosen since the folate receptor, a 38 kDa glycosyl-phosphatidylinositol-anchored glycoprotein, is one of the most highly investigated targets for cancer therapeutics. It has been reported that the folate receptor is significantly up-regulated on ovarian, lung, brain, head and neck, renal cell, and breast cancers compared to normal tissue, in some cases by two orders of magnitude. In addition, normal cells do not transport folate conjugates of any type

across their membranes, while malignant cells transport folate conjugates within the cytosol through the folate receptor.^{37,109} Furthermore, folate ligands are inexpensive, nontoxic, non-immunogenic and easy to conjugate to carriers. They retain high binding affinity and are stable upon storage and in circulation in the blood.¹¹⁰⁻¹¹²

2.5.3 Biomolecules for the generation of biohybrid nanogels

Biomolecules such as bovine serum albumin (BSA), oligonucleotides and antibodies have been conjugated on nanoparticles in order to generate biohybrid nanogels. Biohybrid products show versatility and specificity since they combine the properties of the nanoparticles themselves with the specific and selective recognition ability of the biomolecules attached onto them.¹¹³

Many studies have shown that a range of biomolecules, such as proteins (BSA, transferrin, lectins, cytokines, fibrinogen, thrombin), antibodies, oligonucleotide DNA, plasmids and siRNA, can be used either as targeting moieties or as therapeutics.³⁹ In general, when the biomolecule is used as targeting moiety, direct conjugation on the nanoparticles surface is preferred among physical encapsulation. Conversely, when the biomolecule is used as a therapeutic agent either physical encapsulation or chemical conjugation to nanoparticles, often through cleavable bonds are explored. The clear advantage of using covalent linkages compared to physical adsorption is that the linkage prevents the competitive displacement of the adsorbed biomolecule by blood components, and its fast and not-specific release. Some key design factors have to be considered in the development of biomolecules-conjugated nanoparticles, such as the conformation of the biomolecules, their origin and the modalities by which these are attached to the nanoparticles. Preserving the structure (primary, but also secondary and tertiary) of the biomolecule upon the conjugation is fundamental in order to preserve its activity and function.

Here, conjugation experiments using bovine serum albumin (BSA) as a model protein have been performed, with the purpose of developing suitable approaches to stably bind proteins to our nanogels.

Furthermore, two different antibodies, C-37 and Anti- $\alpha_v\beta_3$ integrin, have been attached to nanogels. In particular, $\alpha_v\beta_3$ integrin is one of the main angiogenic targets explored for anticancer therapy.³⁹ The angiogenesis appears to be one of the most crucial steps in tumor translation to the metastatic form, capable of spreading to other parts of the body. This is because tumors growth is dependent upon the possibility of the tumor mass to get an adequate blood supply. By exploiting the specific recognition ability of the anti- $\alpha_v\beta_3$ integrin, the release of a given therapeutic agent in correspondence of the angiogenic target can be achieved. The therapeutic agent, either a cytotoxic drug or a siRNA, impairs the growth of blood supply, thereby the size and metastatic capabilities of tumors can be regulated.¹¹⁵

A carboxyl functionalized-PVP nanogel system has been decorated with an amino-modified oligonucleotide. The chemical attachment has been proposed as an alternative approach to complexation. More commonly nanogel-DNA complexes are prepared in physiological buffers through cooperative systems of salt bonds between the functional groups of a cationic polymer nanoparticle and the phosphate groups of DNA. These systems suffer from some short-comes. Indeed, sometimes the interactions are so strong that the genetic material cannot be released and exploit its function or the interactions are too weak and the genetic material is released quickly and in the wrong body compartments. Furthermore, the functional groups responsible of the recognizing ability towards the complementary strand are not available since they are used for the formation of the complexes or steric hindered.¹¹⁴

2.5.4 Doxorubicin as a model drug

Doxorubicin (DOX) is one of the most effective chemotherapeutic anticancer drugs available nowadays and it is crucial for the treatment of a range of neoplasms including acute leukemia, malignant lymphoma, and breast cancer.¹¹⁶ Like all other anticancer agents, however, the high efficacy of DOX is associated with high systemic toxicity to healthy tissue.

Several nanocarriers-based DOX-delivery systems have been proposed in

literature. Usually, DOX is physically encapsulated^{17,118} or covalently bonded to nanoparticles.^{119,120} However, when physically encapsulated, DOX rapidly diffuses out from the nanoparticles, likely due to its small size.^{121,122} On the other hand, when DOX is directly linked to nanoparticles, its activity is decreased due to nanoparticles steric hindrance.

A new approach has been used in the present work. DOX has been linked to the nanogels through a linker containing a cleavable disulphide bridge, aminoethyldithiopropionic acid (AEDP), in order to realize a stimulus-responsive release of the drug.^{123,124} The release mechanism is based on the existence of a large difference in the redox potential between the mildly oxidizing extracellular milieu and the reducing intracellular fluids. The reducing agent is glutathione (GSH) that is found in the blood plasma of humans with micromolar concentrations, whereas it is around 10 mM in the cytosol. The concentration level of cytosolic GSH in cells with an enhanced level of oxidative stress, as in tumor cells, is several times higher than that in normal cells.¹²⁵

2.5.5 Gadolinium for imaging purposes

Gd³⁺ low molecular weight chelates represent an important class of contrast agents (CAs) for T1-Magnetic Resonance Imaging (T1-MRI). High dosages of Gd³⁺ are required for MRI of tumors in order to overcome the limitations due to their low sensitivity and inefficient accumulation at the target site. At these concentrations, potential toxicity, adverse side effects or even severe reactions to CAs may occur.¹²⁶ It is known that Gd³⁺ ion is highly toxic by disrupting critical Ca²⁺ signaling in cells. Gadolinium CAs should be avoided in patients with reduced kidney function or kidney failure and hepatorenal syndrome.¹²⁷

Alternatively to low molecular weight chelates, nanocarriers can incorporate a high number of Gd³⁺ atoms and restrain their mobility, thus leading to significant shortening of relaxation times and increased contrast. Furthermore, by displacing targeting ligands on nanoparticles surface, the CA may be preferential accumulated at the target site.¹²⁸⁻¹³⁰

Here, carboxyl-functionalized NGs have been modified using a chelating agent, diethylenetriaminepentaacetic (DTPA) and these NGs-mod DTPA systems have been used for complexing Gd^{3+} ions.

3 Experimental

3.1 Materials

1-Vinyl-2-pyrrolidone (VP, Aldrich) monomer has been freshly distilled before polymerization. N,N' methylen-bisacrylamide (MBA, Aldrich), fluorescein diacrylate (FDA, Aldrich), (3-aminopropyl)methacrylamide hydrochloride (APMAM, Polyscience), ammonium persulfate (APS, Aldrich), N,N,N',N'-tetramethylethylenediamine (TEMED, Aldrich), N-hexane (Aldrich), docusate sodium salt (AOT, Aldrich), Brij 30 (Aldrich), PVP k60 (Aldrich, $M_n=1.60 \times 10^5$ g/mol, $M_w=4.1 \times 10^5$ g/mol and radius of gyration, $R_{gyr} = 27$ nm the last two from static light scattering measurements¹³¹), acrylic acid (Aldrich, AA), 1-ethyl-3-(3-dimethylaminopropyl)carbodiimide (Aldrich, EDC), N-Hydroxysulfosuccinimide (Aldrich, Sulfo-NHS), 2-(N-morpholino)ethanesulfonic acid (Aldrich, MES), fluorescein isothiocyanate (Research Organics, FITC), amino-fluorescein (Aldrich, AmFluor), Folic Acid (Aldrich, FolAc), FAM-FW-N (Eurofins, FAM-5'-AAA ACT GCA GCC AAT GTA ATC GAA-3'-NH₂), C37^{TRITC}¹³², glutathione (Aldrich, GSH), aminoethyldithiopropionic acid (VWR, AEDP), doxorubicin (Aldrich, DOX), gadolinium(III) chloride hexahydrate (Gd³⁺, Aldrich), 1,5 diaminopentane-Boc (N-Boc-cadaverine, Aldrich), diethylenetriaminepentaacetic-penta-t-But ester (DTPA-tBut₅ ester, Brasco) and Arsenazo III (Fluka), have been all used as received, without further purification.

3.2 Samples preparation

3.2.1 PVP-based nanogels obtained via chemical radical polymerization in inverse microemulsion

Preparation of base PVP nanogels and fluorescein functionalized variants.

In a typical preparation for non ionic nanogels (VP-MBA; VP-MBA-FDA), 120 ml of 0.03 M AOT solution in hexane has been carefully deoxygenated with gaseous nitrogen (99.99%) and sequentially added of a solution (2.52 ml) containing freshly

distilled VP and MBA (2.7 mg/ml), FDA (2.3 mg/ml) when present, and TEMED (45 μ l). The mixture has been homogenized (UltraTurrax T25 basic) resulting optically transparent. Then, 120 μ l of aqueous APS (20% w/v) has been added drop-wise at 0-4 °C while stirring. Polymerization has been carried out at 37°C under gaseous nitrogen with continuous stirring for 48 h.

Hexane has been evaporated in a rotary evaporator and the dry mass has been resuspended in 10 ml of water. Purification from surfactant has been carried out as follows (method 1): 1 ml aliquots of 30% w/v calcium chloride solution have been added drop-wise while continuous stirring to precipitate the water-insoluble surfactant, AOT, as calcium salt by centrifugation.⁷⁰ Two distinct phases have been obtained upon centrifuging: an aqueous solution containing most of the cross-linked nanoparticles and an AOT salt cake, which may contain some of the nanoparticles. The precipitate has been dissolved in 15 ml of hexane and residual nanoparticles have been extracted using water. The phase-separated aqueous layers have been drained out and added to the previously centrifuged aqueous supernatant solution. The surfactant-free nanogel dispersions have been subjected to dialysis (12kDa MWCO) against water to remove any eventual low molecular weight hydrophilic residues. The total aqueous dispersions of nanoparticles have been then sub-divided in aliquots and either reduced in volume to produce nanoparticles concentrates or to a completely dry powder by freeze-drying.

Preparation of amino-functionalized PVP nanogels.

When APMAM has been present in the feed both the reaction conditions and the purification procedure have been modified. Briefly, the recourse to a non-ionic co-surfactant (Brij 30) has been made to increase the ease of emulsification and the inverse microemulsion stability⁷², and the initiator concentration has been decreased to reduce the overall system reactivity. A different purification procedure has been also developed (method 2). In this case, after hexane evaporation, the mass of dry product has been resuspended in ethanol and subjected to extensive dialysis (12kDa MWCO) against water/ethanol solution (20% v of water). At the end of the dialysis,

ethanol has been evaporated and the dry product has been resuspended in a note volume of water.

3.2.2 PVP-based nanogels obtained via high-energy radiation induced radical crosslinking

PVP-based nanogels synthesis.

PVP aqueous solutions at different concentrations within the range 10 to 0.05 wt% have been prepared by overnight stirring, filtered with 0.22 μm pore size syringe filters, and bottled in glass vials sealed with rubber septa and aluminum caps. Samples have been carefully deoxygenated with gaseous nitrogen and individually saturated with N_2O ($\text{N}_2\text{O} \geq 99.99\%$) prior to irradiation in order to increase the concentration of hydroxyl radicals formed from water radiolysis during irradiation. Base PVP nanogels have been coded after as P*X.

PVP aqueous solutions at 0.1 wt % (equivalent to $\sim 0.9 \times 10^{-2}$ mol of repetitive unit (RU) per liter, respectively) with APMAM (0.045, 0.09, 0.18, and 0.36 mM, corresponding to 1:200, 1:100, 1:50, and 1:25 APMAM/PVP's RU molar ratios, respectively) and PVP/AA aqueous solutions with three concentrations of PVP, 0.1, 0.25 and 0.5 wt% (equivalent to ~ 9.0 , 22.5 and 45 mM of repetitive unit (RU), respectively) and two molar ratios between PVP's RU and AA, precisely 25 and 50, have been also prepared in the same conditions as described above. Amino-functionalized PVP nanogels have been coded as P*0.1-g-AY; carboxyl-functionalized nanogels have been coded as P*X-g-AA Y, where X is the polymer concentration in the feed and Y is the molar ratio between PVP's RU/monomer (A or AA).

After irradiation samples have been dialyzed (100kDa MWCO) against distilled water for 48 h to remove eventual low MW polymer chains, unreacted monomer and/or oligomers, and re-equilibrate the pH. In facts, all formulations had a pH of about 6.0 prior to irradiation, which turned to be in the range 4-4.5 after irradiation and between 5-5.8 after dialysis.

Electron beam irradiation has been performed using two 10 MeV liner accelerators located at the ICHTJ of Warsaw (Poland), LAE 13/9 and Elektronika 10/10.

For irradiation runs with LAE 13/9, parameters have been set to have pulse length of 10-12 μ s and:

1. average beam current of 0.08 μ A and pulse repetition rate of 37.5, corresponding to a dose-rate of 100 kGy/h and dose per pulse of 0.74 Gy;
2. average beam current of 0.4 μ A and pulse repetition rates of 75 kGy, corresponding to a dose-rate of 500 kGy/h and dose per pulse of 1.8 Gy.

Samples irradiated with LAE 13/9 have been named after “LX-100” and “LX-500”, where X is a number indicating the total absorbed dose in kGy. The homogeneous dose distribution and the integrated absorbed dose by the sample have been measured using cellulose triacetate film dosimeters, on a basis of absorbance at 298 nm. Sample vials have been placed horizontally in front of the electron emission port in a suitable container filled with ice. Temperature during irradiation has been measured to be maintained between 5-10°C.

Irradiation with Elektronika 10/10 has been carried out at an average beam current of 450 mA, pulse length of 4.5 μ s and pulse repetition rate of 300 Hz. In this case, dosimetry has been performed using a graphite calorimeter; the measuring error \pm 4%. Samples have been horizontally placed in a box filled with ice and conveyed under the beam via a transporting belt at a speed of 0.3 m/min. An integrated dose of 20 or 40 kGy has been supplied with a single pass, while the higher dose here investigated, 80 kGy, has obtained with a double-pass exposure of 40 kGy for each. The total absorbed dose results from a combination of e-beam accelerator’s set-up parameters and speed of the conveyer’s belt. From a measurement of the residence time of the vials under the beam (\sim 10 s), an approximate absorbed dose per pulse of \sim 13 Gy has been estimated. Samples irradiated in this conditions have been named after “EX”, where X is the total absorbed dose in kGy.

The irradiation set-ups and the samples codification are summarized in Table 3.1.

Accelerator	Elektronika 10/10	LAE	
Av. Beam Current (μA)	450	0.08	0.4
Frequency (Hz)	400	37.5	75
Pulse Length (μs)	5.5	10-12	10-12
Dose-rate (kGy/h)	13,000	100	500
Dose per pulse (Gy/pulse)	13	0.74	1.8
Sample code	EX	LX-100	LX-500

Table 3.1 Summary of the irradiation conditions and sample codes

3.2.3 Preparation of PVP-based NGs composite nanodevices.

Preparation of nanogels fluorescent variants

Amino-functionalized NGs, produced via both the synthetic approaches, have been conjugated with a fluorescent probe, FITC. The conjugation has been performed accordingly to an in-house established protocol. Briefly, the reaction has been carried out in Borax (pH 9.3) at 37°C while stirring for 2 hrs. The molar ratio between NGs' theoretical functional groups and probe has been equal to 5. FITC conjugated nanogels have been then dialyzed against pH 7.4 PBS for 120 hr, using 12 kDa cutoff dialysis tubes. Both reaction and dialysis have been carried out in dark conditions.

Carboxyl functionalized NGs have been conjugated with AmFluor using an EDC based protocol.¹⁰⁸ Briefly, the reaction has been carried out in MES (pH 5.5) at 25°C while stirring for 4 hr. The molar ratio between NGs' theoretical functional groups and probe has been equal to 5. Probe-conjugated NGs have been then purified through prolonged dialysis against water, using 12 kDa cutoff dialysis tubes. Both reactions and purifications have been performed in the dark.

Preparation of NGs folate variants.

Carboxyl-functionalized NGs have been conjugated to folic acid using a two steps EDC/Sulfo-NHS based standard protocol.¹⁰⁸ In particular, folic acid has been first dissolved in a 10 wt% sodium carbonate solution (1 mg/ml) and then diluted 5 fold with pH 5.5 MES. The other reagents have been added FolAc in MES solution and the reaction has been carried at 25°C, while stirring. The molar ratio between NGs' theoretical functional groups and FolAc has been equal to 5. Folic acid conjugated NGs have been then purified through extensive dialysis against water, using both 12 and 100 kDa cutoff dialysis tubes.

Preparation of biohybrid NGs Variants.

Amino-functionalized NGs, produced via both the synthetic approaches, have been conjugated with BSA using a BORAX-based protocol. The reaction has been carried out at 37 °C for 2 h, while shaking. Afterward, the conjugated systems have been thoroughly dialyzed against PBS using 100 kDa membranes.

E-beam crosslinked P*-g-A have been also conjugated with an antibody, C37^{TRITC}, using an EDC/Sulfo-NHS based protocol. The reaction has been carried out in MES (pH 5.5) at 25°C, while stirring. The molar ratio between NGs' theoretical functional groups and C37 antibody has been equal to 5. Conjugated NGs have been then separated from not-conjugated NGs by multiple washings using centrifuge filter device 300 kDa cut-off (1000 rpm).

P*-g-AA NGs have been conjugated with modified ODN, FAM-FW-N (FAM-5'-AAA ACT GCA GCC AAT GTA ATC GAA-3'-NH₂). FAM-FW-N has been directly attached to the carboxyl groups of nanogels through the C3-amine modified link at 30 end using an EDC/Sulfo-NHS coupling solution. The conjugated has been thoroughly dialyzed against water using membranes with MWCO 14 kDa, to remove the not-conjugated oligonucleotide.

Preparation of AEDP-DOX stimulus-responsive NGs:

P*-g-AA NGs have been conjugated first conjugated with AEDP and then the AEDP-mod-P*-g-AA NGs have been linked to DOX. For both the conjugation reactions, the standard EDC/Sulfo-NHS based protocol has been used.¹⁰⁸ Briefly, the reactions have been carried out at 25°C, in pH 5 MES buffer, in excess of ligands with respect to the carboxyl groups and under continuous stirring. After each step of conjugation, the conjugated systems have been purified through prolonged dialysis against water, using 12 kDa cutoff dialysis tubes.

Preparation of Gd³⁺-DTPA-mod-NGs

Gd³⁺-DTPA-mod-NGs have been generated by a multi-steps conjugation protocol. In particular, P*-g-AA NGs have been first conjugated with 1,5 diaminopentane-Boc, in order to convert NGs carboxyl groups in amino groups. After that, a deprotection reaction has been carried out in order to make available the amino group introduced on nanogels. The deprotected amino groups of nanogels have been then exploited for the conjugation with DTPA-tBut ester. Finally, the 5 carboxyl groups of NGs-mod DTPA-tBut ester have been deprotected. All conjugation reactions have been performed in pH 7.4 PBS, under stirring at room temperature following a EDC/Sulfo-NHS-based protocol. The molar ratio between NGs theoretical carboxyl groups and the ligands has been 1. For the deprotection reactions, the pH have been dropped down to pH 2-3, using H₃PO₄. Each of these reaction steps has been followed by a purification step of extensive dialysis against water.

DTPA-mod-NGs have been then mixed with a gadolinium salt aqueous solution. The amount of Gd³⁺ complexed has been estimated by a complexometric titration using Arsenazo III.¹³³

3.2.4 Amino Fluorescein in vitro release studies

AmFluor solution has been placed into a dialysis tubing (MWCO 12 kDa) with NGs or without, as control, and immersed in 5 ml of water. The systems have been

kept at RT under shaking (200 rpm). At predetermined time intervals (1, 2, 4, 6, 8, 24, 150 ml h), all the external aqueous solutions have been withdrawn and replaced with 5 ml of fresh water.

3.2.5 Doxorubicin in vitro release studies

NGs-AEDP-DOX NGs have been placed into a dialysis tubing (MWCO 12 kDa) with 10 mM of GSH or without, as control, and immersed in 20 ml of phosphate buffered saline (PBS) (pH 7.4). The systems has been kept at 37°C under shaking (200 rpm). At predetermined time intervals (1, 2, 4, 6, 8, 12, 24 h), 1 ml of external buffer solutions have been withdrawn and replaced with 1 ml of fresh PBS.

3.3 Characterizations

3.3.1 Yield

Macroscopically gelled systems have been separated from their soluble portions by immersion for 72 h in excess double-distilled water at 40°C and successively freeze-dried. Conversely, nanogels and microgels have been dialyzed against distilled water for 48 h and then freeze-dried. The yield of the process has been determined gravimetrically by comparing the dry weight of the polymer in the sample before and after irradiation followed by dialysis.

3.3.2 Gel fraction

For PVP hydrogels obtained upon irradiation at high concentrations (10-2 wt %), the gel fractions have been determined by Soxhlet extraction for 24 hours, using water as solvent. The gel fraction has been estimated as ratio of the water-insoluble part with respect to the total amount of the dry sample before extraction. The reported results are the average of minimum three independent measurements and the experimental error was $\pm 2\%$.

3.3.3 Hydrogels Morphology from SEM and liquid-phase AFM

The morphology of both linear unirradiated PVP and PVP hydrogels has been investigated by a field emission scanning electron microscopy (FESEM) system (JEOL) at an accelerating voltage of 10 kV. Samples have been deposited on aluminum stubs and air dried before being gold sputtered with a JFC-1300 gold coater (JEOL) for 30 s at 30 mA.

Liquid-AFM studies have been performed on selected NGs systems to determine their morphology. In detail, nanogels have been deposited on amino-functionalized mica substrates for 5 min and then washed four times with water. In particular, 3-aminopropyltriethoxy silane (APTES) has been covalently bond on mica surface in order to generate positive charges on it. These amino groups become positively charged after the exposure to a water solution in a wide pH range (pKa APTES=10.5). The mica has been functionalized through a vapor phase reaction.¹³⁴ Samples have been examined under water in tapping mode at 2 Hz scanning rates with 256 points and lines per image using a MFP3D AFM (Asylum Research) and MSNL D tips (Bruker Nano Inc) with nominal resonance frequencies of 10 - 20 kHz and spring constant $k \sim 30$ pN/nm.

3.3.4 Swelling

Swelling measurements have been carried out accordingly to an established methodology.¹³¹ Rehydration ratio is defined as $RR = w_s/w_d$, where w_s and w_d are the measured weight of the hydrogel in the swollen and dry state, respectively.

3.3.5 Rheology determination

Dynamic-mechanical properties of the hydrogels have been assessed by small-amplitude shear experiments (stress controlled). Tests have been performed using a Stress-controlled Rheometer Ar 1000 TA Instruments with an aluminum plate geometry (diam. 20 mm), gap of 1000 mm temperature of 25 ± 1 °C. The mechanical response of the material is expressed in terms of shear storage or elastic modulus,

G' , and shear loss modulus, G'' , as a function of the frequency. Frequency sweep tests have been performed in the LVR at frequency values ranging from 0.01 to 200 rad/s at the controlled stress of 10 Pa, as determined by preliminary strain sweep tests over the range 1-1000 Pa.

3.3.6 Hydrodynamic size from DLS

Hydrodynamic diameters (D_h) of NGs' dispersed in bidistilled water, water solutions of different pH and same ionic strength or in PBS buffers at different pH, have been measured by dynamic light scattering (DLS). Samples, placed in the quartz cell, have been put in the thermostated cell compartment of the instrument at $20 \pm 0.1^\circ\text{C}$. Intensity autocorrelation function at the scattering angle of 90° and time autocorrelation function have been measured by using a Brookhaven BI-9000 correlator and a 50 mW He-Ne laser (MellesGriot) tuned at $\lambda = 632.8$ nm. The correlator has been operated in the multi- τ mode; the experimental duration has been set to have at least 2000 counting on the last channel of the correlation function. All irradiated samples have been analyzed without filtration to minimize artifacts. Particular care has been paid in treating the samples in a clean environment to reduce contamination. In consideration of the fact that samples showed a monomodal size distribution, DLS data have been analyzed by the method of cumulants. According to this method, the logarithm of the field-correlation function is expressed in terms of a polynomial in the delay time τ , with the first and second cumulant providing information on the mean value and standard deviation of the distribution of nanoparticles hydrodynamic size.^{135,136} Measurements have been carried out on a minimum two samples from three independent runs.

3.3.7 Weight average molecular weight from SLS

Weight average molecular weight (M_w) of nanogels were estimated from multi-angle static light scattering (SLS) measurements at $25^\circ\text{C} \pm 0.1^\circ\text{C}$ in aqueous solution. The refractive index increments (dn/dc) of PVP in aqueous solution have been measured by using a Brookhaven Instruments differential refractometer at $\lambda =$

620 nm. It has been obtained the value of 0.18 ± 0.004 mL/g in good agreement with a literature value.¹³⁷ The SLS data have been analyzed according to the Zimm plot method using the dn/dc value measured for the linear PVP.

3.3.8 Weight average molecular weight from GFC

Estimation of molecular weight distribution has been also performed using two Shodex SB HQ columns in series (806 and 804) thermostated at 20 °C with an Knauer oven, connected to a HPLC device (LC-2010 AT Prominence, Shimadzu, Kyoto, Japan) equipped with a 50 μ l sample loop. All samples have been eluted with 0.02% sodium azide solution at 0.5 ml/min; the refractive index has been recorded with a Smartline RI detector 2300 Knauer.

3.3.9 Surface charge density from Photo Crosslinking Spectroscopy

Surface charge density of nanogels dispersed in bidistilled water, in water solutions of different pH and same ionic strength or in PBS buffers at different pH has been measured at 25°C using a ZetaSizerNano ZS (Malvern Instruments Ltd, Malvern, UK) equipped with a He-Ne laser at a power of 4.0 mW. For systems characterized by a monomodal ζ -potential distributions, the mean ζ -potential and the relative distribution width are reported. Conversely, for systems that show a more heterogeneous surface charge density, i.e. multimodal ζ -potential distributions, mean ζ -potential values and relative widths of the different modes are reported. As for particle size distribution, also ζ potential measurements have been carried out on minimum two samples from three independent runs.

3.3.10 Chemical structure from FT-IR

FTIR analysis was carried out with Perkin Elmer-Spectrum 400 apparatus by dispersing the dry product in potassium bromide and compressing into pellets. Spectra were recorded at 30 scans per spectrum and 1 cm^{-1} resolution in the 4000-

450 cm^{-1} range. All spectra have been normalized with respect to the peak correspondent to the stretching of methylene groups (2956 cm^{-1}).

3.3.11 Chemical structure from NMR

^1H NMR spectra were recorded in D_2O solution by using a Bruker Advance series 300 MHz spectrometer.

^{13}C $\{^1\text{H}\}$ CP-MAS NMR analysis has been performed on solid samples with BrukerAvance II 400 MHz (9.4 T) spectrometer operating at 400.15 MHz for the ^1H nucleus and 100.63 MHz for the ^{13}C nucleus with a MAS rate of 13 kHz, 1024 scans, a contact time of 1.5 ms and a repetition delay of 2 s. The ^1H pulse was optimized to a value of 4.25 μs . The optimization of the Hartmann-Hahn condition has been obtained using an adamantane standard. All samples have been placed in 4 mm zirconia rotors with KEL-F caps. Silica has been used come as filler in order to avoid inhomogeneities inside the rotor. Chemical shifts of pure PVP and APMAM have been determined according to literature data^{98,138} and are reported in Table 3.2.

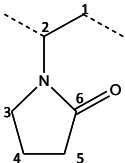
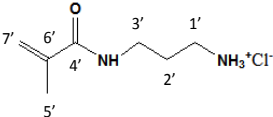
PVP	Carbon	Chemicalshift
	C_6	176,1
	$\text{C}_2 - \text{C}_3$	43,7
	C_1	36,3
	C_5	32,7
	C_4	19
APMAM		
	$\text{C}_{1'}$	39
	$\text{C}_{2'}$	27,8
	$\text{C}_{3'}$	40,3
	$\text{C}_{4'}$	169,45
	$\text{C}_{5'}$	20,4
	$\text{C}_{6'}$	122,5
	$\text{C}_{7'}$	138,8

Table 3.2: Attribution of main carbon chemical shifts of non-irradiated (linear) PVP and APMAM.

Cross polarization times, T_{CH} , values for were obtained through variable contact time (VCT) experiments.¹³⁹ Contact times used in the VCT experiments were 0.05, 0.1, 0.2, 0.3, 0.4, 0.5, 0.6, 0.8, 1.0, 1.2, 1.5, 2.0, 2.5, 3.0, 3.5, 4.0, 4.5, 5.0, 6.0 and 7.0 ms. Proton spin–lattice relaxation times in the rotating frame, $T_{1\rho}(H)$, were indirectly determined, with the variable spin lock (VSL) pulse sequence, by the carbon nucleus observation using a 90° – τ –spin-lock pulse sequence prior to cross-polarization.¹⁴⁰ Data acquisition was performed by 1H decoupling with a delay time, τ , ranging from 0.1 to 7.5 ms and a contact time of 1.5 ms.

3.3.12 Chemical structure from Raman Spectroscopy

Raman spectra have been recorded on a Renishaw 1000 micro-Raman spectrometer in the 200-2200 cm^{-1} range with 100 s integration time. A 785 nm diode laser served as excitation source, which has been focused into a spot having diameter of 1 micron. The laser intensity on the sample surface has been around 8 mW. A baseline correction has been performed on the experimental data in order to remove the background signal due to photoluminescence, followed by normalization to the intensity of the methylene deformation band. The parameters of the peaks have been determined by fitting with Gaussian functions.

3.3.13 Surface chemical composition from XPS analysis

Surface chemical composition of the samples has been investigated by XPS in an ultrahigh vacuum (UHV) chamber with a base pressure in the range of 10^{-8} Torr during data collection. Photoemission spectra have been collected by a VG Microtech ESCA 3000 Multilab spectrometer, equipped with a standard Al K_{α} excitation source ($h\nu = 1486.6$ eV) and a nine-channeltrons detection system. The hemispherical analyser operated in the CAE mode, at a constant pass energy of 20 eV. The binding energy (BE) scale has been calibrated by measuring C 1s peak (BE = 285.1 eV) from the surface contamination and the accuracy of the measure has been ± 0.1 eV. Photoemission data have been collected and processed by using the VGX900 software. Data analysis has been performed by a nonlinear least square

curve-fitting program using a properly weighted sum of Lorentzian and Gaussian component curves, after background subtraction according to Shirley and Sherwood.¹⁴¹ Surface relative atomic concentrations have been calculated by a standard quantification routine, including Wagner's energy dependence of attenuation length¹⁴² and a standard set of VG Escalab sensitivity factors. The uncertainty on the atomic concentration is of the order of 10%.

3.3.14 Conjugation degree from UV-vis absorption and emission

Conjugation degrees have been estimated by UV-visible absorption measurements with Shimadzu 2401-PC spectrofluorimeter (scan speed 40 nm/min, integration time 2 sec, bandwidth 1 nm) at room temperature.

Fluorescence spectra have been acquired with a JASCO FP-6500 spectrofluorimeter, equipped with a Xenon lamp (150W). Emission spectra, at the required excitation wavelength, have been obtained with emission and excitation bandwidth of 1 nm and 3 nm, respectively.

4 Nanogels obtained via chemical radical polymerization in inverse microemulsion

This chapter is dedicated to the synthesis and characterization of poly(N-vinyl pyrrolidone)-based nanogels using chemical radical polymerization in inverse microemulsion.

4.1 Physico-chemical properties of PVP-based nanostructures

N-vinyl pyrrolidone (VP) have been polymerized and simultaneously crosslinked inside the aqueous pods of a w/o microemulsion in the presence of a water-soluble monomer (3-aminopropyl) methacrylamide (APMAM), using a crosslinker (MBA) and an initiator (APS). Reverse micelles have been prepared by dissolving an ionic surfactant, AOT, in a given volume of n-hexane at a concentration higher than the critical micellar concentration. In this approach the reverse micelles act as template and their initial size and number determined the particles size of the nanogels generated. Different molar ratios between VP and APMAM have been explored in order to obtain PVP functionalized variants (VP-MBA-APMAM) with different physico-chemical properties and degree of functionalization. Base PVP nanogels (VP-MBA) and their fluorescent variants (VP-MBA-FDA) have been also generated.

The success of this synthetic approach, both in terms of yield of recovered product and control of particle size, is very much dependent on the optimal combination of synthetic and purification procedures. Indeed, when VP polymerization has been performed in the presence of APMAM, both the reaction conditions and the purification have been modified. In particular, the composition of the different formulations investigated and the separation method used are described in paragraph 3.2.1 and summarized in Table 4.1.

<i>Syst.;</i> <i>Purif.</i>	<i>Description</i>	<i>VP</i> <i>APMAM</i>	<i>VP</i> <i>APS</i>	<i>AOT</i> <i>(M)</i>	<i>Brij 30</i> <i>(M)</i>
#1; 1	VP-MBA	-	150	0.03	-
#2; 1	VP-MBA-FDA	200	150	0.03	-
#3; 1	VP-MBA-APMAM (200)	200	150	0.03	-
#4; 2	VP-MBA-APMAM (200)	200	25	0.09	0.2
#5; 2	VP-MBA-APMAM (50)	50	25	0.09	0.2
#6; 2	VP-MBA-APMAM (10)	10	25	0.09	0.2

Table 4.1: Feed composition of base, fluorescent and amino functionalized PVP nanogels

The total yield of the process, in terms of recovered product after the purification steps, has been evaluated gravimetrically for each system. Nanogels hydrodynamic radii and relative PDI, evaluated through DLS measurements at fixed angle (90°) and temperature (25°C) in water, are reported in Table 4.2. Surface charge density of nanogels is also reported as ζ -potential values.

<i>System; Purif. Method</i>	R_h (nm)	<i>PDI</i>	ζ -potential (mV)	Width (mV)
#1; 1	96	0.30	-19.5	5.94
#2; 1	367	0.88	-30	10.7
#3; 1	237	0.73	-26	9.6
#4; 2	131	0.99	-29	8.2
#5; 2	111	0.43	-40.6	6.55
#6; 2	92	0.20	15.8	7.8

Table 4.2: Average hydrodynamic radius, PDI and ζ -potential of nanogel systems in water

The gravimetrically yield estimated for the base (VP-MBA) systems is about 25 wt %. These nanogels show the target value of 96 nm for the radius, which is an optimal starting value for what it may constitute the core of e.g. an antibody-decorated bio-

hybrid nanogel. In fact, nanocarriers with an average diameter of 200 nm are suitable for intravenous administration and cellular uptake. Smaller nanocarriers may not reside in the cytoplasm enough to accomplish their function and they may not provide adequate surface or internal volume for the cargo or for the targeting moieties to be attached.¹¹ When the reaction feed is modified, e.g. by introduction of FDA, the yield of the recover product decreases significantly (< 10%), the average particle size increases and the particle size distribution widens (#2).

Also in the presence of APMAM, the yield of the recover product decreases and the particle size increases (#3). Considering that initiation and propagation rate constants of APMAM are significantly higher than VP's¹⁴³, the loss in recovered product cannot be attributed to a reduced reactivity of the reaction feed. Furthermore, homopolymerization of APMAM and formation of linear chains is not favored at the synthesis pH (5.5), owing to the electrostatic mutual repulsion between positively charged APMAM molecules (APMAM pKa is 8.5¹⁴⁴). The purification step is the critical step when polymerization is carried out in the presence of APMAM since the cationic monomer localizes preferentially at the water/surfactant interface due to the electrostatic interaction with the anionic surfactant and the separation of the nanogels from AOT becomes complicated.

In order to improve the product recover, a non-ionic surfactant, Brij 30, has been introduced. Also, the amount of APS has been reduced. The recovery of VP-MBA-AMPAM(200) increased and separation of nanogels from AOT/Brij has been quantitative, although not excellent. A product recovery of ~20% w has been consistently reached for VP-MBA-APMAM(50), this value being somewhat lower for VP-MBA-APMAM(10). A contextual improvement in particle size control has been achieved by the modification of both the reactor feed and the purification procedure. All the amino-functionalized variants synthesized using the new procedure, show lower particles size and for the system with higher APMAM content also the PDI decreases.

SEM analysis on the air-dried nanoparticles clearly supports the hypothesis that the separation procedure is not efficient in the presence of APMAM, and aggregates form. Figure 4.1a-b shows the comparison between VP-MBA (#1) and VP-MBA-

APMAM(200) (#3) systems. Dry VP-MBA nanoparticles have a diameter of about 10 nm (Figure 4.1a), which is approximately twenty times smaller than the hydrodynamic diameter when the nanogels are swollen in the aqueous media and move with their hydration water shell. Big aggregates are clearly visible for dry VP-MBA-APMAM(200) at the micron scale (Figure 4.1b). These aggregates are nanogel-surfactant aggregates and their presence likely affects the measured R_h values. VP-MBA-APMAM(50) SEM analysis (Figure 4.1c-d) shows a deposit of dry nanoparticles characterized by a fairly uniform particle size, similarly to the base VP-MBA system (Figure 4.1a). For this system no aggregates are present.

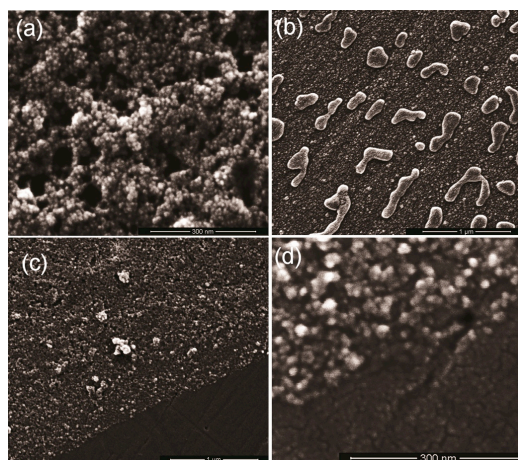


Figure 4.1a-d: SEM micrographs of an air-dried deposit of (a) VP-MBA (formulation #1 - purification method 1); (b) VP-MBA-APMAM(200) (formulation #3- purification method 1); (c) VP-MBA-APMAM(50) (formulation #5- purification method 2); (d) detail of (c) at higher magnification. Both in (c) and (d) dry nanogels particles cover only part of the stub to evidence the difference in morphology with the gold sputtered substrate.

The surface charge density of linear PVP has been evaluated and the ζ -potential distribution curve is reported in Figure 4.2. Semi-diluted linear PVP in aqueous solution (0.1 wt%) shows a bimodal distribution of ζ -potential values, with a main peak close to neutrality and a second peak at about -20 mV. They can be explained in

the light of the keto-enolic tautomerism and possible partial pyrrolidone ring opened, respectively.^{106,145}

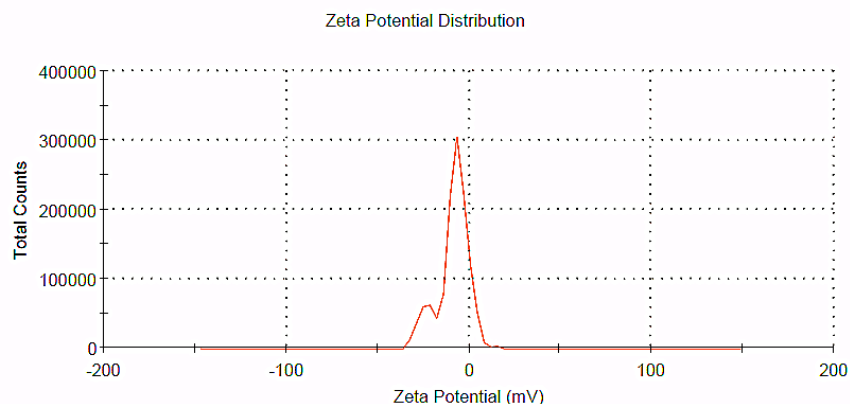


Figure 4.2: ζ -potential curves for PVP in water.

Surface charge density of nanogels has been also determined through ζ -potential measurements and the relative values are reported in Table 4.2. VP-MBA nanogels in water shows a slightly negative surface charge, similarly to the linear polymer. Unexpectedly, for VP-MBA-APMAM(50) the anionic character increases. Even though a cationic monomer has been grafted onto PVP crosslinked network, the positive charges of APMAM are shielded by chlorine counter ions, since APMAM is added to the feed as a chlorine salt. When the content of APMAM is further increased, as for the VP-MBA-APMAM(10) system, the average ζ -potential becomes slightly positive. The proximity of many amino propylene grafts on the NG surface may render the charge shielding by the counter ions less effective and the overall charge density becomes more affected by the fixed positive charges from the protonated amino groups.

4.2 Colloidal stability and redispersability of PVP-based nanostructures

In order to prove that amino-graft PVP nanogels are colloiddally stable and redispersable from the dry physical form, DLS and ζ -potential measurements have

been carried out both in water and in buffer and at the variance of pH, temperature and time.

In particular, freeze-dried amino-graft-PVP nanogels have been redispersed in PBS buffers with similar ionic strength (0.2 M) and different pH, and characterized for their particle size and surface charge distributions, both at room temperature (25°C) and at body temperature (37°C). DLS and ζ -potential data are reported in Table 4.3. The NGs hydrodynamic size, measured at room temperature and in PBS at pH around neutrality, have been very similar to those of the as prepared NG dispersions in water, thus proving their excellent redispersability from the dry form.

No evident influence of pH on particle size has also been observed between 4.5 and 7.4, while at pH 8 NGs are slightly bigger (see Table 4.3). Conversely, at pH=2.5 and lower, aggregation and precipitation occurred in a temporal window of few hours. The hydrodynamic radius reported for pH 2.5 in Table 4.3 refers to freshly prepared dispersions, but this value increases with time at 25 °C up to the onset of precipitation, when the scattered light intensity drops to very low values.

The increase of temperature from 25 °C to 37°C did not affect hydrodynamic size in a systematic way, but it generally increased the PDI, for the pH values within the NGs colloidal stability range (4.5 - 8). It can be speculated that the increase of temperature has the effect of better evidencing the inherent variety of chemical structures of the system, in terms of distribution of functional groups, their protonation states and/or extent of interactions with the solvent (i.e. swelling degree). A contribution coming from nanoparticles aggregation cannot be ruled out in consideration of the relatively low absolute ζ -potential values of these nanoparticles. Indeed, faster aggregation kinetics are responsible for the significant higher R_h value at 37°C for pH 2.5.

Z-potential values for the various pHs and T=25°C (Table 4.3) show that the anionic character is attenuated when NGs are in buffer at pH 7.4 with respect to water (-26.3 mV vs. -40.6 mV), probably due to ions exchange between nanogels and medium, with substitution of the chlorine ions of APMAM with loosely bound phosphate anions. This evidence indirectly confirms the role that chlorine counter ions have in determining the fairly strong negative surface charge of the original nanogels dispersions in water. A change of pH, in the range 2.5 – 8, essentially affects the

contribution of pyrrolidone rings to NGs charge density, being the pH always below the pKa of APMAM. At pH 2.5 NGs become almost non-ionic, with a maximum in anionic character at pH 7.4 and slight decrease at pH 8. No appreciable effects on NGs surface charge density are observed at the increase of temperature.

VP-MBA-APMAM (50)								
pH	25 °C		37 °C		25°C		37°C	
	R _h (nm)	PDI	R _h (nm)	PDI	ζ-potential (mV)	Width (mV)	ζ-potential (mV)	Width (mV)
2.5	115	0.51	150	1	-5.2	3.2	-5.0	6.4
4.5	99	0.57	97	0.76	-13.6	5.8	-14.3	9.1
6.8	93	0.38	125	0.66	-21.8	6.7	-23.8	4.2
7.4	110	0.35	130	0.50	-25.2	5.4	-26.3	7.5
8	120	0.46	91	0.49	-13.8	8.4	-16.1	10.4

Table 4.3: Average hydrodynamic radius and ζ-potential for an amino-graft crosslinked VP nanogels redispersed in PBS, as function of pH and temperature.

4.3 Internal structure of PVP-based nanostructures

A thorough structural characterization of the nanoscalar networks has been performed via ¹H-NMR and solid-state ¹³C-NMR spectroscopies. Further information on polymer network density has been collected through solid-state NMR relaxation time measurements. Figure 4.3a shows solid state ¹³C {¹H} CP-MAS NMR spectra of VP-MBA-APMAM(50) nanogels after purification and freeze-drying, compared with the spectra of linear PVP.

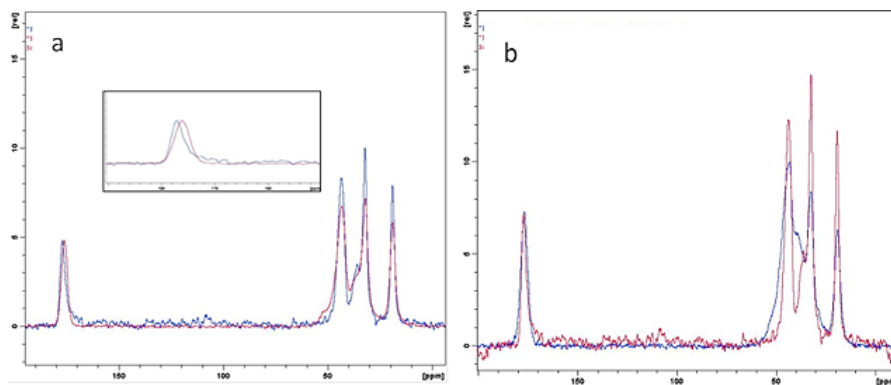


Figure 4.3a-b: ^{13}C { ^1H } CPMAS NMR overlaid spectra of (a) linear PVP (red) and VP-MBA-APMAM(50) nanogels (blue) with expansion of carbonyl region in the inset; (b) VP-MBA-APMAM(50) nanogels (blue) and VP-MBA-APMAM(10) macrogel (red).

Peaks attribution for linear PVP and APMAM is reported in paragraph 3.3.11. It is evident that the chemical structure of the nanogel closely resembles that of the linear PVP. No evidence of residual surfactant or unreacted monomers is present, thus confirming the effectiveness of the purification procedure. The bands for the nanogels are narrower than those of the linear polymer, for the higher level of rigidity of macromolecular segments in the nanoscalar network. The carbonyl carbon chemical shift is positioned at higher values and the band shows a shoulder stretching to lower fields. This behavior can be associated to a variety of carbonyls, attributable to PVP's pyrrolidone and secondary amides of MBA and APMAM. The spectrum of VP-MBA-APMAM(50) has not allowed to obtain a spectroscopic evidence of the presence of the APMAM, for the low concentration of the monomer and the small quantities of materials produced at the laboratory scale. An indirect confirmation of the occurrence of copolymerization between VP, MBA and APMAM in the selected reaction conditions has been obtained by preparing the “equivalent” macrogel of the 10:1 formulation, named after “VP-MBA-APMAM(10) macro”. For this macrogel, polymerization and crosslinking has been carried out starting from the same composition of the aqueous phase as the corresponding microemulsion. Purification from unreacted monomers has been performed by extensive washings with water and the insoluble fraction was freeze dried and analyzed. Figure 4.3b shows the overlaid

spectra of macrogel and linear PVP. A new band appears at 39 ppm, that can be attributed to APMAM. $^1\text{H-NMR}$ spectrum of VP-MBA-APMAM(50) nanogels confirms the above discussed findings. Attribution of proton chemical shifts for the nanogel and linear PVP^{146,147} is reported in Table 4.4.

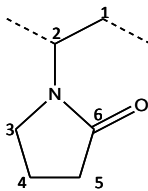
	Linear PVP	VP-MBA-APMAM(50)
	3.6702	3.7097
	3.5112	3.5674
C3	3.1784	3.2249
	3.0301	3.0616
C5	2.1450	2.1658
	2.1793	2.2290
	2.3161	2.3660
C4	1.8931	1.9392
C1	1.6139	1.6493

Table 4.4: $^1\text{H-NMR}$ proton chemical shifts (ppm)

In Table 4.5 the proton spin lattice relaxation times in the rotating frame ($T1\rho\text{H}$) are reported, for the VP-MBA-APMAM(10) formulation both in the form of macrogel and nanogel and with specific reference to the characteristic chemical shifts of the PVP repeat unit in the network. It is known that $T1\rho\text{H}$ values are sensitive to the molecular motions which occur in the kHz regions, associated with cooperative polymer backbone rearrangements, thus enveloping the collective motions of a large number of monomer units. As a general consideration, $T1\rho\text{H}$ values are much higher for the macrogel than for the corresponding nanogels, with the only exception of the carbonyl carbon. This indicates that the local motions are more hindered in the 3D-extended macroscopic network, especially at the C1 position, which is the most

affected by the proximity to T- and X- type crosslinks formed by MBA. For the nanogels, we would be inclined to think that the overall average crosslinking density is lower. In consideration of the fact that the size of the domains where spin-lattice relaxation times are averaged is of the same order of magnitude of the size of nanogel dry particles (tens of nanometers), the increase of mobility may reflect a significant contribution of polymer segments at the particle surface, which is the richest in polymer loose loops and flexible chain ends. Carbonyl groups, which are strongly interacting with bound water, show much closer values.

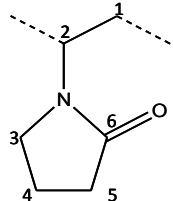
	$T_{1\rho H}$ (ms)	
	Macrogel	Nanogel
C6	7.4	8.8
C2 e C3	13.3	8.4
C1	16.4	6.8
C5	13.3	6.0
C4	12.2	5

Table 4.5: ^{13}C $\{^1\text{H}\}$ CP-MAS NMR- Proton spin-lattice relaxation time in the rotating frame ($T_{1\rho H}$)

4.4 Biological evaluations on PVP-based nanogels

The total absence of *in-vitro* toxicity and immunogenicity has been ascertained first. Both base PVP nanogels and functionalized variants have shown of being biocompatible.

Furthermore, cell localization studies in cell cultures using the nanogels fluorescent variants have been performed. In particular, VP-MBA-FDA and VP-MBA-APMAM(50)FITC have been used. As already reported above, VP-MBA-FDA particles have a hydrodynamic diameter of about 370 nm and their surfaces are

negative charged. VP-MDA-APMAM(50)FITC variant has been produced by covalently linking FITC on nanogels. They have a hydrodynamic radius of 110 nm and do not show a net surface charge density, as result of conjugation reaction with FITC (average z-potential=-1.0 mV, width=5mV; see paragraph 8.1.1). Both the nanogels systems show a similar behavior and high affinity towards cells. They rapidly and quantitatively bypass the cellular compartments, to accumulate in specific cell portions for the first 4-6 hours, then being released from the cells after 24 h. A full description of the biological assays performed is reported in Paper VI.

4.5 BSA conjugation to PVP-based nanogels

BSA has been conjugated on nanogels surface as model bulky protein in order to verify if the grafted amino groups were available for conjugation reactions with biomacromolecules. The conjugation has been successful as assessed by UV-Vis spectrophotometry. Absorption spectra, reported in Figure 4.4, show that the BSA-conjugated NG spectrum has a peak at 280 nm, which coincides to the one of free BSA used as reference; while no absorption peaks have been observed in the non-conjugated system. The interaction between BSA and nanoparticles is fairly strong, as it survives upon extensive dialysis and repeated washings. In consideration of the dimensions of BSA, we expect the protein to be essentially located at the nanoparticles' surface.

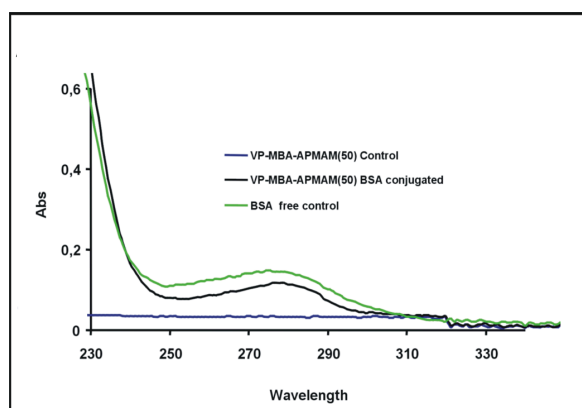


Figure 4.4: UV-vis spectra for VP-MBA-APMAM(50) and VP-MBA-APMAM(50)BSA.

4.6 Conclusions

Biocompatible NGs have been produced via inverse emulsion free radical polymerization of VP and a primary amino group carrying monomer (APMAM). By a proper selection of reaction and purification conditions, nanogels showed controlled particles size, high stability in aqueous solutions and redispersibility from the dry physical form.

The comparison between the proton spin-lattice relaxation times in the rotating frame for one of the nanogel variants and the corresponding macrogel “analogue” suggests that the overall average crosslinking density is lower for the nanogels than for the macrogel obtained from the same monomer mixture, likely due to a greater contribution in macromolecular segments mobility from polymer loose loops and flexible chain ends at their surface.

Nanogels have been proved not to be cytotoxic and genotoxic, and they showed good affinity for cells. Chemically crosslinked NGs have been also successfully linked to fluorescent probes and biomolecules, such as BSA. However, this synthetic approach presents some limitations related to the low product recovery from purification for the difficulty in removing the surfactant. Furthermore, the scale up of this process at industrial level is not appealing. For these reasons a surfactant-free alternative approach has been pursued, as it will be described in the following chapter.

5 Base PVP nanogels obtained via high-energy radiation induced radical crosslinking

In chapter 4, PVP-based NGs synthesized via chemical-radical polymerization in inverse microemulsion have been described. These NGs couple the advantages stemming from PVP structure, such as biocompatibility, affinity towards cells and escape ability from the body through natural pathways, with the opportunities arising from being nanoparticles with a controlled size. However this conventional synthetic approach is not particularly appealing for a scale-up for the low yields of recovered product attained after several time-consuming purification steps.

Here, the possibility of obtaining PVP-based NGs using high-energy radiation-induced radical crosslinking as an alternative approach is explored. This synthetic route has been first applied for the generation of base PVP NGs and, then, further developed for the production of their functionalized variants.

Since the main goal of these synthetic efforts is the generation of a family of functional nanocarriers, a preliminary assessment of the validity of any approach proposed has to be performed with reference to the capability of the technology to grant a satisfactory particles dimensional control.

On the account of the already published studies, it is expected that irradiating PVP solutions at concentration below the polymer critical chain overlap concentration (C^*) micro-/nanoparticles are obtained.⁸² For this reason, semi-diluted PVP aqueous solutions have been irradiated using pulsed e-beams. In Figure 5.1 the average hydrodynamic radii of the NGs obtained for PVP concentrations below $C^* \sim 1$ wt%¹³¹ (0.1, 0.25 and 0.5 wt%), at the variance of dose and dose-rate, is provided. Relative widths of nanoparticles size distributions are also reported as error bars. Three different dose-rates have been selected (100 kGy/h, 500 kGy/h and 13,000 kGy/h) and each panel of Figure 5.1 refers to a different dose-rate. The variation of the dose rate has been achieved by varying both the dose per pulse and the pulse repetition rate. The total doses delivered to the materials have been 20, 40 and 80 kGy. The two lower doses are the upper and lower limits of the sterilization dose range. Samples have been

irradiated also at twice the maximum sterilization dose, to investigate the effects of higher doses on the structure and properties of these polymer nanoparticles.

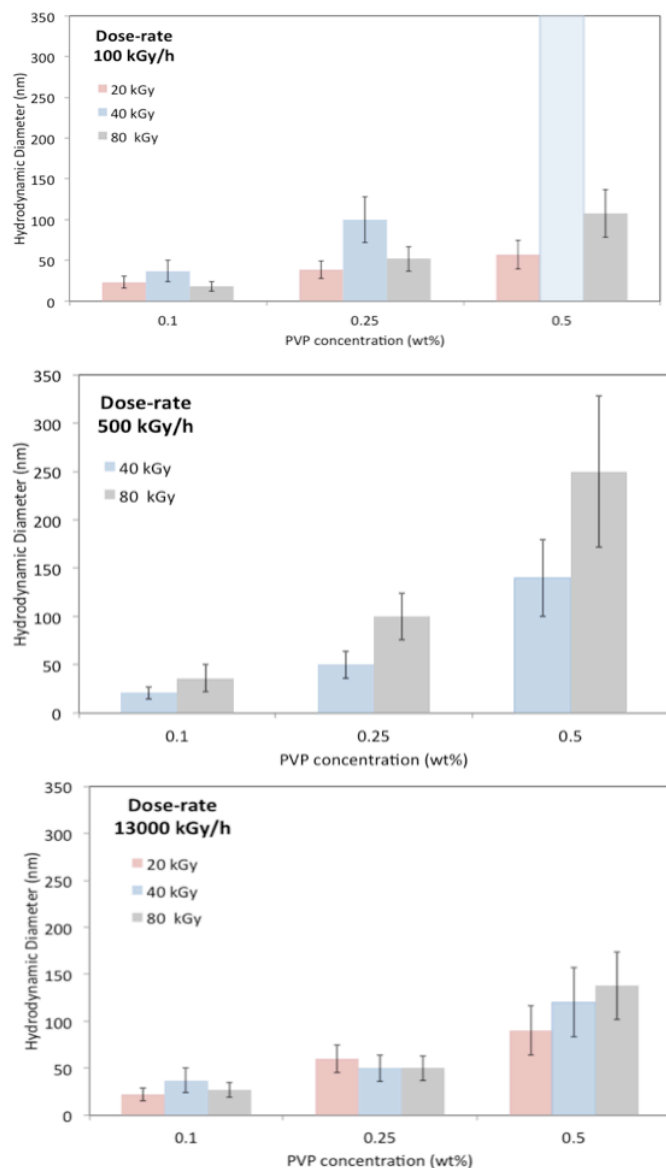


Figure 5.1a-c: Hydrodynamic radii of nanogels obtained for three PVP concentration, 0.1, 0.25 and 0.5 wt%, at the variance of dose, for the dose-rates of a) 100 kGy/h; b) 500 kGy/h and c) 13000 kGy/h. Error bars represent the width of the size distribution.

Generally e-beam crosslinked PVP NGs have particles size below 100 nm and not smaller than 20 nm. Furthermore, narrow particles size distributions have been obtained. Only for the 0.5 wt% systems, in given irradiation conditions, particles size control has not been achieved. In particular, macrogel flakes form in a continuous “sol” phase for the system at 0.5 wt% irradiated at 100 kGy/h and 40 kGy. At all irradiation conditions, a strong influence of polymer concentration on particle size is evident. In particular, at the increase of polymer concentration the hydrodynamic radius increases. Furthermore, dose and dose-rate affects nanogels particles size, the more the higher is the polymer concentration.

This preliminary study evidences one advantage of this synthetic route that is the possibility to fine-tune the size of the polymer nanoparticles by controlling - independently - the composition of the irradiated systems, the dose-rate and the total absorbed dose. These preliminary results have encouraged performing a deeper exploration of this methodology. A detailed product analysis on selected systems has been carried out in order to identify the main correlations between process variables and physicochemical and molecular properties of the products, which will be the subject of this chapter.

5.1 Effect of PVP concentration on dimensional control and properties of base NGs

The influence of PVP concentration in water on the organization and dynamics of the formed networks upon irradiation has been systematically investigated in a wide concentration range (0.05-10 wt%), from well above to below the critical chain overlap concentration ($C^* \sim 1$ wt%). For the purpose, the integrated dose of 40 kGy has been deposited at the lowest dose rate (100 kGy/h) and controlled temperature 0-4°C.

In the chosen irradiation conditions, the instantaneous concentration of formed hydroxyl radicals after each pulse is about $4 \cdot 10^{-7}$ M, as estimated by the known hydroxyl and hydrogen radical yields ($G(\cdot\text{OH})_{N_2\text{Osat}} = 0.54 \mu\text{MJ}^{-1}$, $G(\cdot\text{H}) = 0.055 \mu\text{MJ}^{-1}$), and dose per pulse (0.74 Gy/pulse). $\cdot\text{OH}$ ($\cdot\text{H}$) radical-radical recombination is not favored when these water radiolytic products are formed in the presence of radical

scavenging substrates, such as the methylene groups of polymer. They prevalently transfer to the polymer by hydrogen abstraction, forming carbon-centered polymer radicals.^{81,82}

In the concentrated regime, when $C \gg C^*$, linear PVP in water forms a transient network where labile junctions are represented by chain entanglements, van der Waals interactions and water-mediated hydrogen bonds. The network dynamics are highly cooperative, i.e. characterized by the coordinated motion of many macromolecular segments. In addition, independent Brownian motions of “contracted” polymer coils or loose ends can be observed.¹³¹

In this concentration regime, the number of primary radicals instantaneously formed upon each pulse is well below the number of possible reactive sites on the polymer chains and, on the average, even below one per polymer chain. Therefore, the polymer can efficiently scavenge all the primary radicals formed upon radiolysis. The formed macroradicals can terminate mainly by inter-molecular recombination (leading to crosslinks formation) or disproportionation reactions. In principle, also monomolecular termination via chain scission cannot be ruled out.

In semi-dilute conditions, when $C < C^*$, solution dynamics are characterized by the independent motion of many objects, essentially constituted by individual polymer chains. The hydrodynamic radius (R_h) of linear PVP is ~ 20 nm, at all the low concentrations investigated. From the measured gyration radius (R_{gyr}) value through SLS, a shape factor, $\rho = R_{gyr}/R_h$, of ~ 1.35 can be estimated, which suggests a slightly chain-extended conformation, probably due to hydrogen bonding of polymer with water and charge repulsion owing to the slight zwitterionic character of PVP (see paragraph 4.2).

At these concentrations, provided that PVP concentration is not extremely low, the average number of radicals that can form on each chain can be higher than two and if they are in a favorable position, they can recombine intra-molecularly.

5.1.1 Physico-chemical and rheological properties

At a preliminary visual inspection upon irradiation, the systems at 10, 8 and 6 wt% appear completely macroscopically gelled, while systems at 4, 2 and 0.5 wt% present

both macrogel islands and a separated aqueous phase. At lower concentrations, all irradiated systems appear optically transparent liquids that would be “traditionally” classified as “sols”.

The yield of crosslinking reactions has been estimated gravimetrically for all the systems. In particular, macroscopically gelled systems have been separated from their soluble portions and successively freeze-dried. The “gel fraction” values estimated for these gels are reported in Table 5.1. Systems from 10 to 2 wt% have similar high gel fraction values (above 85 %), while the “0.5 wt %” system has a lower but still significant gel fraction (about 55 wt%). For this last system, the sol fraction has been first separated from the gel-fraction and then dialyzed and freeze-dried as well as low concentration systems (0.05-0.25 wt%). For these systems, the yield in term of recover product has been always higher than 90 %.

Pol. conc. (wt%)	GF (%)	G' (Pa)	G'' (Pa)	M _c (Da)	ξ (nm)	RR _{plateau}
10	91.2	1974	21	48848	11.5	25.3
8	92.8	2811	33.5	37468	11.4	27.5
6	94	3385	70	28343	11.4	21.3
4	93.5	2260	76.	33007	12.6	20.4
2	86	1740	75	32900	14.0	16.5

Table 5.1: Gel fraction (GF), shear storage modulus (G'), shear loss modulus (G'') at 1 rad/s, molecular weight of the polymer chain between two neighboring crosslinking points (M_c), network mesh size (ξ), rehydration ratio at plateau (RR_{plateau}).

Conventional swelling and rheological characterizations have been applied to the obtained macrogels. The dynamic storage, G' , and loss moduli, G'' , as function of frequency are shown in Figure 5.2a-b. G' and G'' values at 1 Hz are also reported in Table 5.1. It can be observed that, in the investigated angular frequency range, G' values are almost constant and higher than the corresponding G'' values. This indicates that gels formed by irradiation in these conditions are typical “strong gel”, i.e. with prevalent elastic behavior.¹⁴⁸ Looking closer at the influence of the polymer concentration, from 2 to 6 wt%, G' increases, while G'' is almost constant. At higher concentration (8 and 10 wt%) a decrease of both G' and G'' occurs. The G' increase for systems ranging from 2 to 6 wt% can be attributed to the increase of crosslinking density. Above 6 wt% the crosslinking density may locally further increase, but at the expenses of the spatial network homogeneity yielding to very compact but weakly

interconnected clusters. Accordingly, G'' decreases: the reduction of dissipative phenomena, evidenced by the decrease of G'' , can be explained with the relative easiness of mutual slipping of neighboring densely crosslinked clusters. The average molecular weight between two adjacent crosslinks, M_c , and the average distance between crosslinks or mesh size, ξ , have been calculated from well known equations derived from the general theory of rubber elasticity¹⁴⁹⁻¹⁵¹ and reported in Table 5.1. The lowest M_c pertains to the macrogel at 6 wt%. Increases of M_c , as well as of network mesh size for concentrations below this value may reflect a looser networked structure. Conversely, hydrogels at 8 and 10 wt% combine lower ξ values with higher average molecular weight between adjacent crosslinks. In the aforementioned hypothesis of spatial heterogeneity of the networks for these two systems, the two average molecular parameters calculated from a bulk macro-mechanical behavior found the limit of their usefulness.

The RR plateau values are well in agreement with the above-discussed hypothesis on the network organization of macrogels. The poorly developed network of the 2 wt% system, upon freeze-drying, collapses into a non-porous solid (see Figure 5.3b) that cannot be fully rehydrated. The yet limited number of crosslinking points, in fact, reduces the polymer chains mobility, thus preventing full hydration of PVP polar groups and activation of the typical hydrogel swelling driving forces, such as capillary and osmotic forces.¹⁵² The 4 and 6 wt% systems can be considered proper “wall to wall” macrogels that optimally combine chain elasticity and network permeability, thus ensuring “reversibility” of the freeze-drying/rehydration processes. Finally 8 and 10 wt% show high RR values at plateau. For the postulated inhomogeneity in the distribution of crosslink points, the RR measured see the modest contribution of the highly cross-linked regions, and a most conspicuous contribution of the looser tie zones.

The soluble part of the 0.5 wt% system and all the other systems produced at lower polymer concentration have been investigated though dynamic light scattering. In Table 5.2 the calculated average hydrodynamic radii and relative standard deviations are reported.

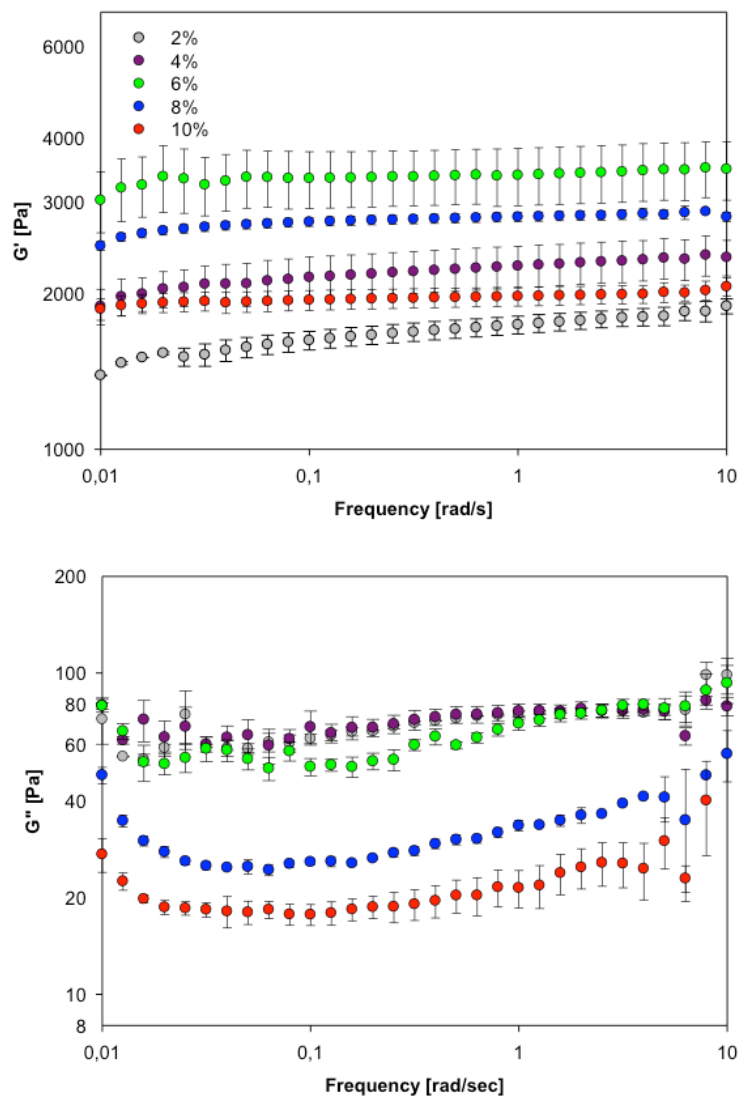


Figure 5.2a-b: Storage modulus, G' , (a) and loss modulus, G'' , (b), as function of the frequency for macrogels obtained at the variance of polymer concentration in water.

The 0.5 and 0.25 wt% systems present nanoparticles with average hydrodynamic radii of 32 and 50 nm, respectively, that are higher than those of the unirradiated PVP coils ($R_h=20$ nm). This can be due to the occurrence of both intermolecular and intramolecular crosslinking. On the contrary, nanogels obtained from 0.1 and 0.05

wt% solutions have hydrodynamic radii lower than that of the corresponding unirradiated systems. In this case, intramolecular crosslinking may be the prevailing phenomenon, according to the already reported effect of polymer concentration on the nanogels size.⁸² Standard deviations are only slightly higher at the lowest values in the range. Measurements carried out at the variance of the scattering angle, in the range 30-150°, lead always to the same average hydrodynamic diameters pointing out a spherical geometry for the investigated systems.

For all NGs, the weight average molecular weight has been determined through SLS measurements and it is reported in Table 5.2. An increase of weight average molecular weight with respect to that of linear PVP ($M_w=0.5$ MDa) is always observed. This points out that intermolecular crosslinking occurs for all systems; the more the higher is the concentration.

Polymer (wt%)	$N_{rad} : N_{chains}$ per pulse	R_h (nm)	Err (nm)	M_w (MDa)	Err (MDa)
0.5 (sol)	1:12	32	8	-	-
0.25	1 : 5-6	60	14	9.50	0.078
0.1	1:3	15	4	1.23	0.18
0.05	1 : 1	13	4	0.65	0.15

Table 5.2: The average number of radicals per chain per pulse ($N_{rad} : N_{chains}$ per pulse), hydrodynamic radius (R_h) and corresponding weight average molecular weight (M_w) of nanogels.

In particular, in the selected experimental conditions, the *average* number of radicals per chain per pulse, calculated by equally distributing the instantaneous concentration of $\bullet OH$ ($\bullet H$) over the total number of polymer chains, is always below two (see Table 5.2), therefore macroradical recombination through intra-molecular crosslinking is not the dominant process both in the initial pulses and throughout the process.

Extensive intra-molecular crosslinking is not pursued either, because it would freeze the polymer conformation in water, thus restraining segmental mobility and coil flexibility. Furthermore, from a picture of the spatial distribution of the polymer in the aqueous medium, it comes out the probability of two polymer chains overlapping in

this concentration range being small but not negligible⁸¹, therefore inter-molecular recombination can also concur.

It must be said that the estimation of the number of radicals per chain and per pulse from the radiation yield of $\bullet\text{OH}$ ($\bullet\text{H}$) in water implies a number of simplifying assumptions. The first simplification is in the use of the G-values determined for the radiolysis of pure water (i.e. neglecting direct effects of radiation to the polymer and the influence that a solute can have to the G-values). One other simplification is neglecting that radicals can survive the time between pulses and that other possible reactions consuming primary radicals, that are not radical transfer reactions to the polymer, can also concur especially when the concentration of polymer is very low.

In a more realistic picture, macroradical termination modality would be affected by the polymer concentration, the number of radicals instantaneously formed per chain, radical stability, polymer chain flexibility and by the way the chemical structure and, in turn, radical stability and chain flexibility modifies during irradiation, as well as by the probability of having more reactive species (different type of macroradicals or water-radiolysis products) in the same “reactive volume”.

Therefore, it can be concluded that inter and intra- molecular recombination of carbon-centered radicals both occur and compete, but it shall be anticipated that they may not suffice to describe all the final structure and molecular architecture of the nanogels. This last consideration is supported by the evidence gathered from the structural characterization of the obtained nanogels particles that will be discussed in the following paragraph.

5.1.2 Base PVP hydrogels morphology

SEM morphology of PVP macro and nanogels can be observed in Figure 5.3a-d. In particular, the dry nanogel particles of the 0.25 wt% system form a thin layer of sub-micron globular aggregates (Fig 5.3a). Freeze-dried residues of macrogels obtained at 2, 4 and 8wt% are shown in Figure 5.3b-d. While at 2 wt% the xerogel does not present porosity, at increasing polymer concentration, up to 6 wt%, a fairly regular porous structure is evidenced. Above this value, porosity is reduced in size with evident heterogeneity in size distribution.

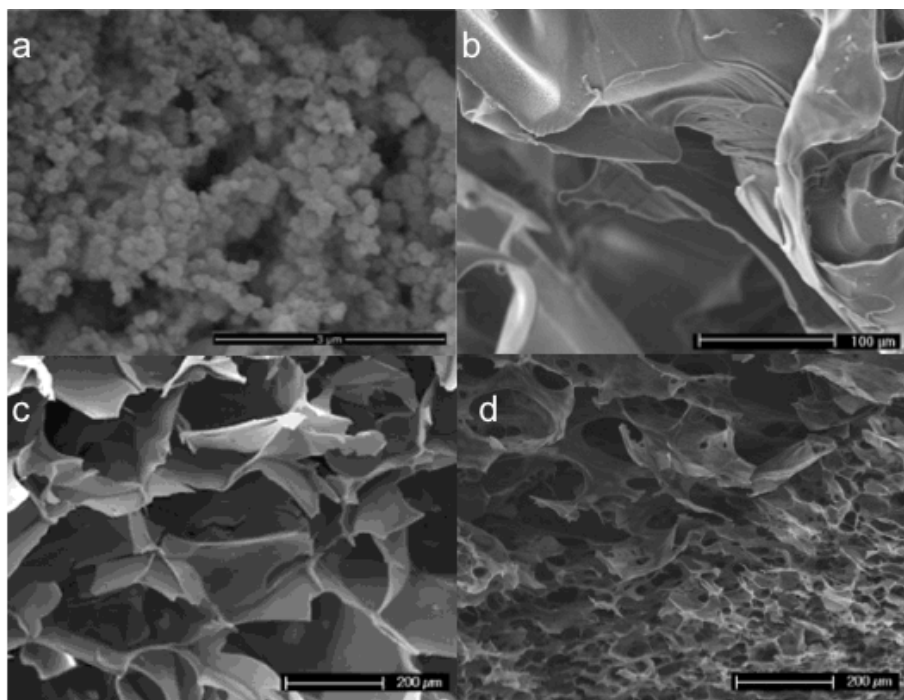


Figure 5.3a-d: SEM images of dried residues of hydrogels obtained at the variance of polymer concentration in water: (a) 0.25 wt%; (b) 2 wt%; (c) 4 wt% (d) 8 wt%.

By combining the results from the light scattering analysis on the semi-diluted systems before and after irradiation with rheological characterizations on the concentrated regimes, the overall picture that comes out is that: at the top of the concentration range (10-8 wt%) clusters of densely networked micro/macro gel particles loosely tied together form; for 6-4 wt% systems, long-range interconnected networks form; macro/microgel islands for concentrations (2-0.5 wt%) that span across the critical chain overlap concentration ($C^* \sim 1$ wt%) are generated; mainly intermolecularly crosslinked nanogels just below C^* and predominantly intra-molecularly crosslinked nanoparticles at 0.1 wt % and below are produced. These different structures are depicted in Figure 5.4a-e.

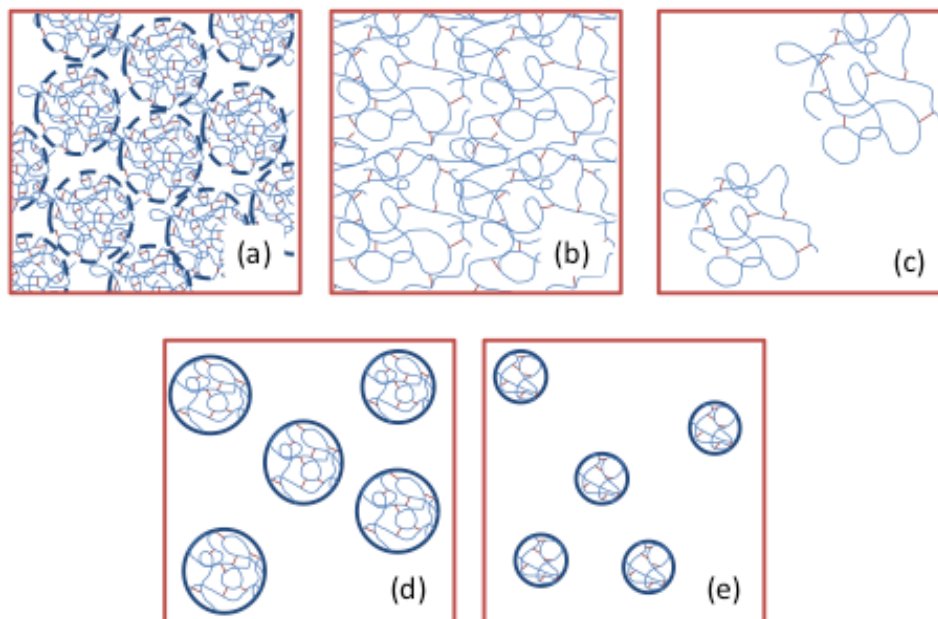


Figure 5.4a-e. Schematic representation of network organisation for the different polymer solutions: (a) densely networked micro/macro gel particles loosely tied together (10-8 wt%); (b) long-range interconnected networks (6-4 wt%); (c) macro/microgel islands (2-0.5(gel) wt%); (d) mainly inter-molecularly crosslinked nanogels (0.5(sol)-0.25 wt%); (e) predominantly intra-molecular crosslinking nanogels (0.1-0.05 wt%). Representation is not in scale.

5.1.3 Structural modification of PVP networks from macro to nano

At the best of my knowledge, all published studies in the field of high energy radiation crosslinking of PVP mainly focus on low irradiation doses and high dose per pulse. In particular, PVP macrogels have been obtained at doses up to 20 kGy (the gel dose when $C_{\text{polym}} > C^*$ is about 15-20 kGy¹⁵³, while PVP nanogels have been generally produced at lower doses (5-10 kGy) when high doses per pulse are applied.^{81,102} In none of these cases modification of PVP chemical structure, beside C-C crosslinking, is documented.

In the approach here presented, the irradiation conditions explored are different, i.e. the dose per pulse is relatively low as well as the pulse repetition rate, and the integrated dose is high, to be within the sterilization dose range. As a consequence, it cannot be ruled out that PVP chemical modification upon irradiation may occur.

FTIR spectra of dry networks are here compared to that of the linear PVP, as shown in Figure 5.5a-c for macro-systems. All the characteristic peaks of linear PVP are present in the macrogels spectra with no evident shifts. More in detail, bands at 3700-3000 cm^{-1} , referring to hydroxyls and amidic groups (νOH and νNH^+) in linear PVP for its partially zwitterionic nature and the presence of open rings, are generally broader and lower in intensity for macrogels. Furthermore, the band shifts toward the lower wavenumbers and this can be due to the contribution from alkene C-H stretch vibrations at $\sim 3100\text{-}3000 \text{ cm}^{-1}$ accompanied by the correspondent increase of absorptions at 2450-1980 cm^{-1} . Absorptions in this last region may come from unsaturated groups involving both carbon and nitrogen,¹⁵⁴⁻¹⁵⁵ that, in this context, may originate by carbon centered macroradical termination via disproportionation reactions.

Pyrrolidone carbonyl stretching peak ($\nu\text{CO } 1662 \text{ cm}^{-1}$) also broadens and systematically reduces in intensity at the decrease of PVP concentration up to 2 wt%. Crosslinking through recombination of carbon centered radicals, as well as disproportionation, may generate a variety of states for carbonyl groups that results in significant band broadening. Bound water molecules may also contribute when the network is sufficiently loose. Special consideration should be paid to the 0.5 wt% gel, that shows high absorption peaks and broad bands. In particular, the pyrrolidone carbonyl peak shows a shoulder at 1769 cm^{-1} , which is also characteristic of the nanogels described in the following.

Spectra of nanogels with respect to linear PVP are shown in Figure 5.6a-c. Absorptions from hydroxyls and amidic groups at 3700-3000 cm^{-1} increase and the more the lower is the concentration of polymer in the parent solution. The characteristic carbonyl peak of PVP becomes a multi-band envelope, which stretches both toward the higher and lower wavenumbers. Two new peaks appear, at 1769 and 1698 cm^{-1} , near the amide I band of the pyrrolidone ring. These peaks are generally associated to C=O symmetric and asymmetric stretching vibrations, respectively, of 5-

members cyclic imides. Also, the appearance of a small band at 820 cm^{-1} , attributable to the ring CH_2 twisting of succinimide, supports the aforementioned structure. The band at 1698 cm^{-1} becomes dominant over that of 1660 cm^{-1} absorptions from CH_2 groups in the region between 1496 and 1424 cm^{-1} at the lowest concentration in the range (0.05 wt%), when also absorptions from CH_2 groups in the region between 1496 and 1424 cm^{-1} are significantly reduced. In the lower wavenumber range, beside to the band at $\sim 1290\text{ cm}^{-1}$ due to ring C-N stretching coupled with ring CH_2 wagging, new bands at about 1397 , 1384 , 1058 and 986 cm^{-1} appear. Peaks at 1397 and 1384 cm^{-1} can be associated to the presence of carboxylate anions, which may be also responsible for the enlargement of the carbonyl band toward 1600 cm^{-1} . Bands at 1058 and 986 cm^{-1} suggest the formation of oxygen atoms mediated crosslinks, which results from PVP hydroxylation. Similar absorptions have been recently observed by Zhu et al. in photo-crosslinked PVPs macrogels obtained in the presence of substantial amounts of hydrogen peroxide.⁹⁷

It is also worth pointing out that no increased absorptions are present in the 2450 - 1980 cm^{-1} region, differently from the macro-analogues, as it would be expected in dilute systems where bimolecular disproportionation reactions are less probable. Intra-molecular disproportionation cannot be ruled out, but any eventual double bond formed would be then depleted by either direct or indirect ($\bullet\text{OH}$ radicals-mediated) interaction with ionizing radiation, as there is not any spectroscopic evidence of residual double bonds.

The new species that have been identified in the nanogels suggest that when the probability of intermolecular recombination of polymer macroradicals is very low and intra-molecular recombination or disproportionation becomes hindered by progressive chain mobility reduction, then other reactions leading to hydroxylated and carboxylated PVP networks occur.

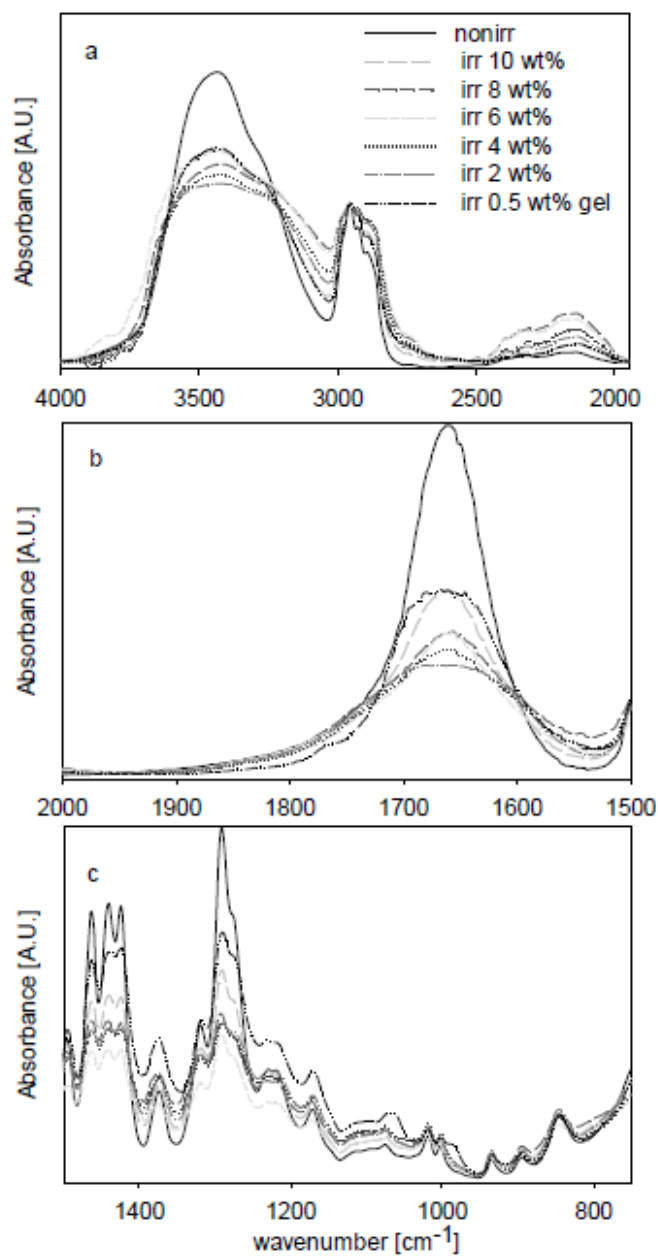


Figure 5.5a-c: FT-IR spectra of nonirradiated PVP and macrogels at different concentrations. All spectra were normalized with respect to the peak at 2956 cm^{-1} .

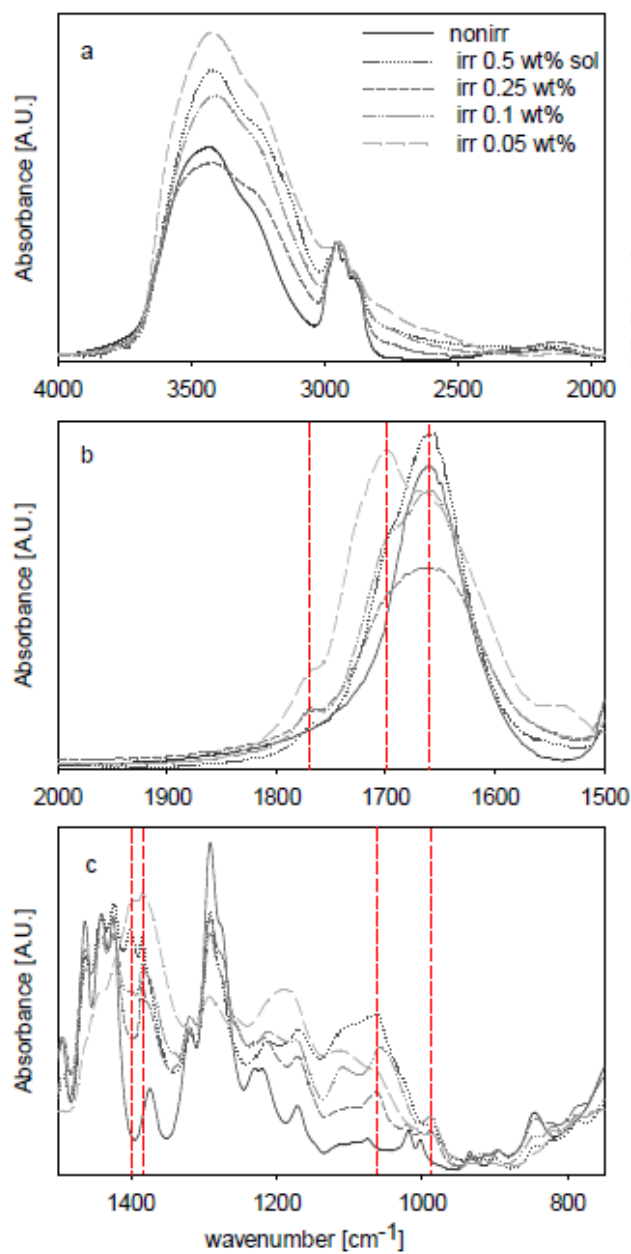


Figure 5.6a-c: FT-IR spectra of nonirradiated PVP and nanogels at different concentrations. All spectra were normalized with respect to the peak at 2956 cm^{-1} . Vertical dashed lines correspond to the following peaks: 1769 , 1698 , 1662 , 1397 , 1384 , 1058 and 986 cm^{-1} .

In Figure 5.7, 785 nm excited Raman spectra of irradiated PVP systems are shown. The spectra have been normalized to the 1432 cm^{-1} main chain methylene deformation. Peaks at 934 , 1671 and 1775 cm^{-1} , which correspond to the pyrrolidone ring breathing mode, vibrations of the amide I group of the pyrrolidone ring and to the C=O stretching of succinimide rings, respectively, have been investigated in detail.

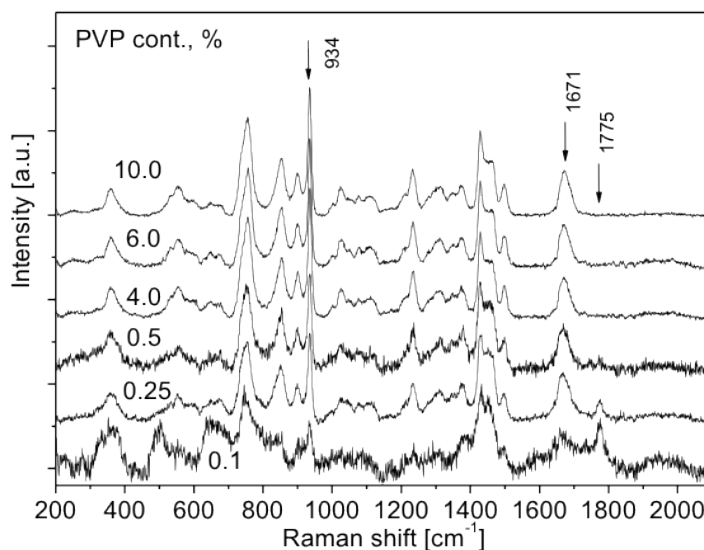


Figure 5.7: Raman spectra of irradiated PVP at different concentrations. All spectra were normalized with respect to the peak at 1432 cm^{-1} .

The intensity of the band at 934 cm^{-1} decreases rapidly when the PVP content is lowered to below the critical chain overlapping concentration (see Figure 5.8a) and correspondently the width of band suddenly increases (Figure 5.8b). This last evidence can be explained with a conformational modification of polymer chains, whereas the attenuation of the band, accompanied by an increase of succinimide peak intensity at 1775 cm^{-1} (Figure 5.8f), can be explained with the formation of such structure, because the presence of the additional oxygen on the ring suppresses the pyrrolidone ring breathing mode.

With reference to the band peaking at 1671 cm^{-1} , peak shifts (Figure 5.8c) to lower wavenumbers with the decrease of PVP content are observed. This shift can be

attributed to the transformation of the C=O group from mainly non-hydrogen bonded to mainly hydrogen-bonded state. Band width (Figure 5.8d) first increases and then, when succinimide forms, decreases.

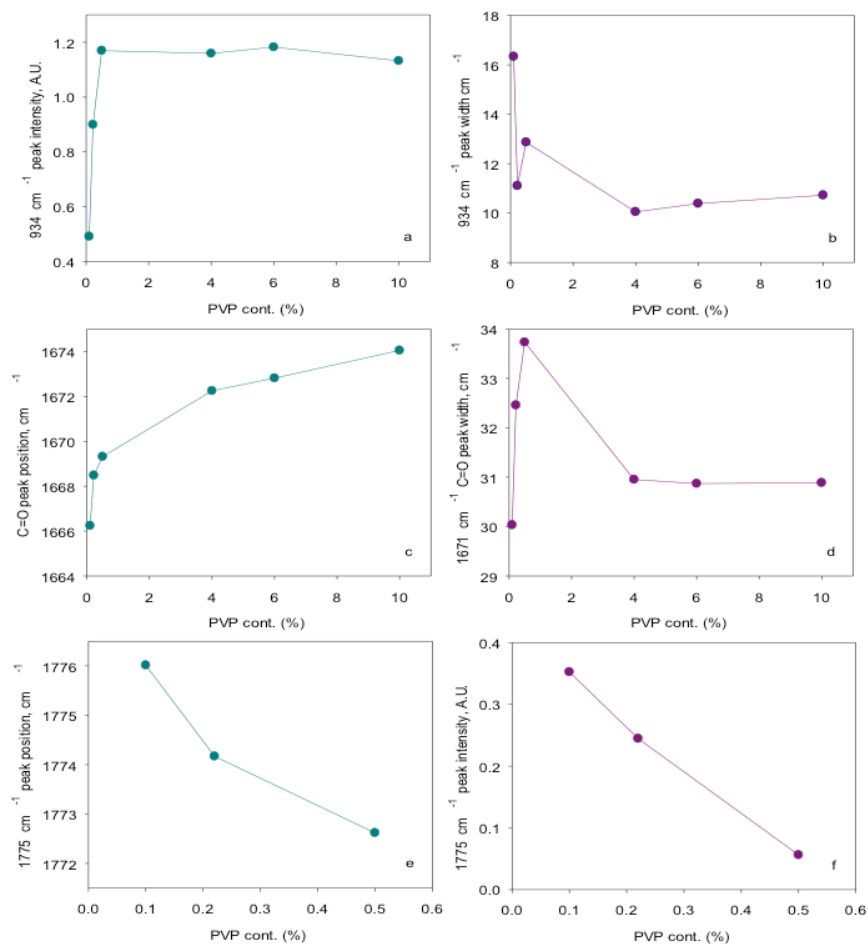


Figure 5.8a-f. Modification of Raman spectra of irradiated aqueous PVP at different concentrations: peak intensity and band width for the pyrrolidone breathing mode (a-b); peak position and band width for pyrrolidone amide I band (c-d); peak position and intensity for formed succinimide at low concentration (e-f).

The succinimide peak at 1775 cm⁻¹ appears for the low concentrations, in analogy with FTIR spectra (see Figure 5.6). An upshift in peak position is observed at the

decrease of polymer concentration and it may be related to the same effect as the downshift of 1671 cm^{-1} band (Figure 5.8 4e). Peak intensity (Figure 5.8f) increases linearly reducing PVP concentration.

It appears as, when irradiation is carried out at low concentration, concomitantly with the appearance of an additional C=O group on the pyrrolidone ring, transforming it into succinimide, there is evidence of pronounced hydrogen bonded carbonyls. This can support the already proposed hydroxylation and carboxylation of the polymer as well as suggest an easier organization of the surrounding water. Whereas increasing PVP concentration, there is no longer succinimide formation and the hydrogen-bonded amide groups progressively decrease. Intermolecular crosslinking through recombination of carbon-centered macroradicals may cause rings to be close to each others, thus limiting the presence of bound water. This is also supported by previous studies carried out with hydrophobic fluorescent probes, suggesting the presence of hydrophobic pockets in such crosslinked networks.¹⁵

$^{13}\text{C}\{^1\text{H}\}$ CP-MAS NMR spectra of all the irradiated systems are reported in Figure 5.9 (A-D). Chemical shift assignments have been performed according to literature and are reported in chapter 3.^{97,156} The characteristic bands of linear PVP are present in the macrogel systems with no significant modification. Figure 5.9A shows the enlargement of the spectral zone from 160 to 190 ppm. Peak at ~ 177 ppm is related to the carbonyl carbon (C1). It can be noticed a downfield shift of this signal when PVP concentration decreases below C^* . In the enlargement of the spectral zone from 0 to 70 (Figure 5.9C) the peak at 43.5 results from the overlapping of CH (C5) and CH_2 (C4) signals, peak at 36.6 ppm is due to the CH_2 (C6) of the backbone chain, peak at 32.2 ppm is related to the CH_2 (C2) of the pyrrolidone ring near the carbonyl carbon and peak at 18 ppm is due to the CH_2 (C3) in the pyrrolidone ring. In the irradiated systems at 0.25 and 0.1 wt% a new shoulder at 29 ppm and a concomitant decrease of signal intensities at 18 ppm and 43.5 are detectable. In particular, the band at 29 ppm is attributable to the CH_2 groups of succinimide ring. The trends of the carbonyl shift and of the decrease of C4 peak as a function of PVP concentration are reported in Figure 5.9B and D, respectively. These evidences further confirm the imidization of pyrrolidone rings in crosslinked PVP gels when networks are approaching the

nanoscale. Furthermore, for the 0.1 wt% system a distinct shoulder at 180 ppm is also present and supports the already proposed formation of carboxylate groups.¹³⁸

Finally, the PVP 0.1 wt % system shows also a signal at 83 ppm (indicated by the arrow in Figure 5.10). This band, together with the already observed increase of FTIR broad band at $3700\text{-}3000\text{ cm}^{-1}$, suggests PVP hydroxylation. Moreover, a not well resolved group of signals in the spectral zone around 73 ppm may be attributable to C-O-C crosslinking bonds involving the C4 and C5 bonds.⁹⁷

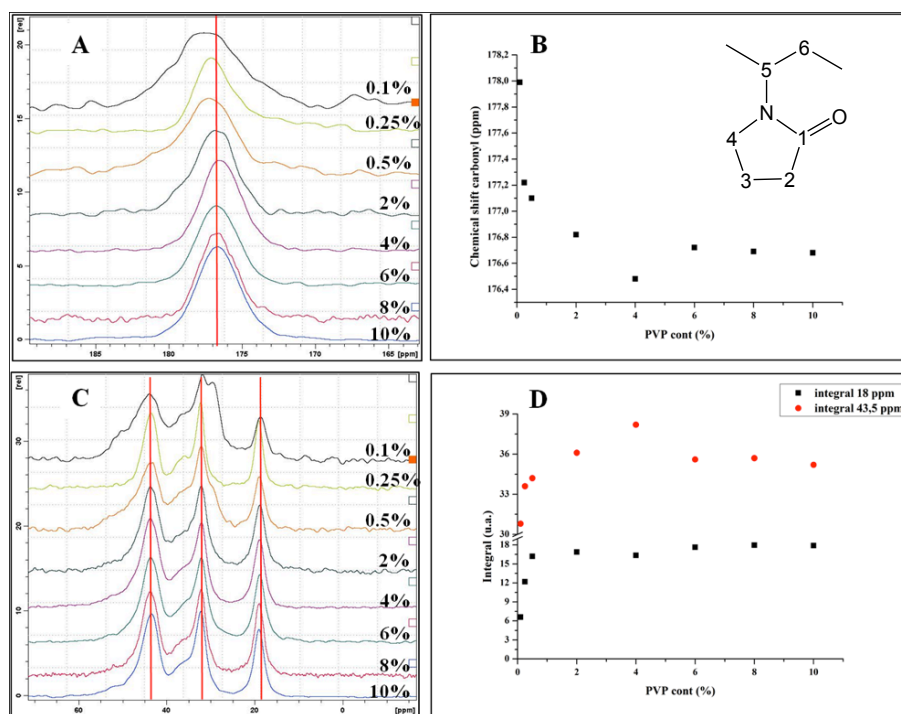


Figure 5.9A-D. ^{13}C $\{^1\text{H}\}$ CP-MAS NMR spectra of irradiated systems: enlargement of the spectral zone from 160 to 190 ppm, (A); carbonyl peak chemical shift, (B); enlargement of the spectral zone from 0 to 70 ppm, (C); C3 and C4 peaks integrals, (D).

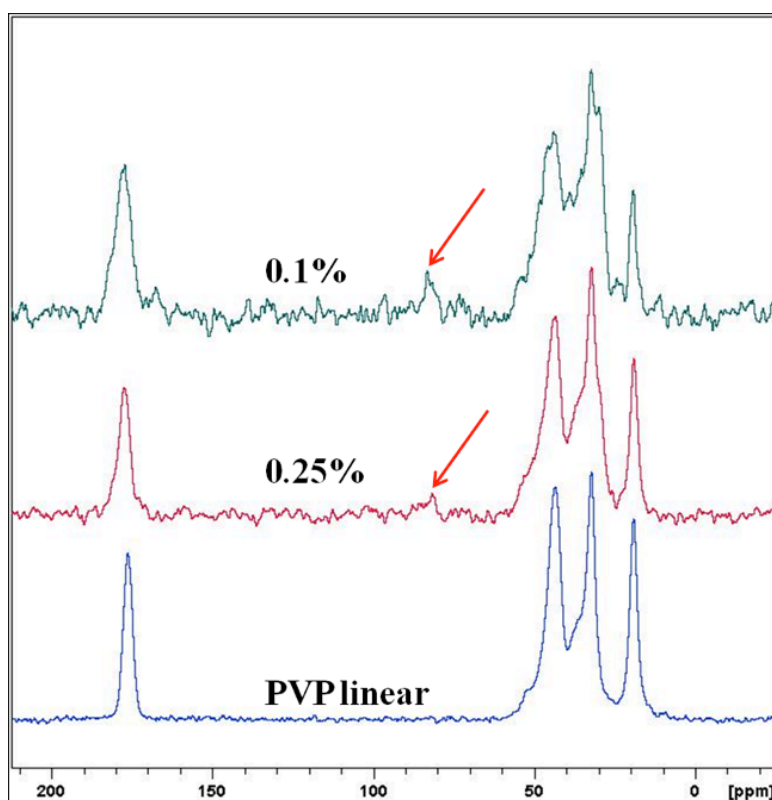


Figure 5.10: ^{13}C $\{^1\text{H}\}$ CP-MAS NMR spectra of nanogels and non irradiated PVP for comparison. The arrow points the chemical shift of C bonded to hydroxyl group.

5.1.4 Solid state ^{13}C NMR relaxation spectroscopy

^1H spin lattice relaxation times in the rotating frame, $T_{1\rho\text{H}}$, and cross-polarization times, T_{CH} , have been determined for the different investigated systems. The spin lattice relaxation time in the rotating frame ($T_{1\rho}$) is sensitive to molecular motions, which occur in the kHz region. In particular, it is inversely proportional to the spectral density of motion in the kHz frequency region. These motions reflect the dynamic behavior of a polymeric chain segments in a range of a few nanometers. An increase of rigidity in a polymer results in longer $T_{1\rho}$ values.¹⁵⁷⁻¹⁵⁸ In Figure 5.11a-b $T_{1\rho\text{H}}$ values relative to carbonyl carbon (C1) and methylene carbon (C3) of pyrrolidone ring are reported, respectively.

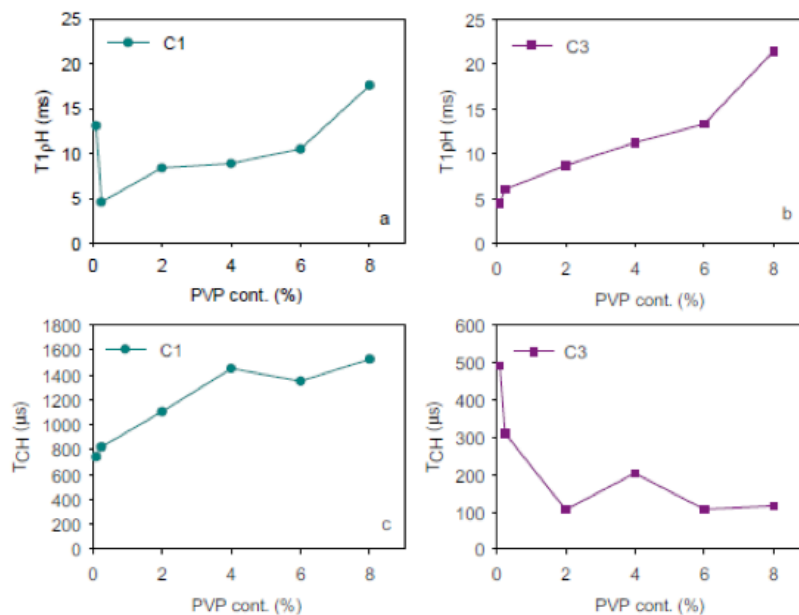


Figure 5.11a-d. Proton spin-lattice relaxation times in the rotating frame, $T_{1\rho H}$, and cross-polarization times, T_{CH} , for PVP networks spanning across different scales, from macro (2, 4, 6 and 8 wt%) to nano (0.1 wt%): $T_{1\rho H}$ and T_{CH} for the pyrrolidone ring carbonyl carbon (C1), (a) and (c), and for the methylene carbon (C3), (b) and (d), respectively.

The plots indicate that as the polymer concentration increases the cooperative motions, which allow the protons to relax involve increasingly larger portions of the PVP lattice. This is an evidence that PVP network's stiffness increases with the concentration due an increasing extent of crosslinking.

The very high value of $T_{1\rho H}$ observed for the carbonyl carbon of system at 0.1 wt% could be related to the proposed hydrogen-bonded state of C=O groups in such nanogels as well as to intra-molecular crosslinking which hinder chain motions.

Conversely, C3 shows $T_{1\rho}$ values monotonically increasing with concentration. This relaxation refers to pyrrolidone groups, which have not been chemically modified upon irradiation and that, presumably both for steric hindrance and reduced mobility, are less affected by hydrogen bonding.

T_{CH} values are an indication of the rate at which the magnetization transfer from protons to carbons takes place. The magnetization transfer is due to the 1H - ^{13}C dipolar coupling. In particular, the higher is this interaction the shorter is the T_{CH} value.

T_{CH} are reported in Figure 5.11c-d for C1 and C3, respectively. With reference to C1, we can observe that T_{CH} values decrease as the polymer concentration increases. This suggests a reduction of proton density around the carbonyl carbon at the increase of concentration, in excellent agreement with previous findings. Conversely, the proton density around the aliphatic carbons (see Figure 5.11d) does not significantly change except for the nanogels where it significantly increases. This phenomenon can be explained under the light of both the proposed structural modifications of PVP when forming nanoscalar networks: chain folding and intramolecular crosslinking as well as hydroxylation.

5.2 Effect of the dose-rate on base PVP NGs properties.

As already discussed in chapter 2, the main factor that influences the nature and kinetics of macroradicals termination reactions is the *distance between radicals* existing simultaneously on the polymer chains. The dose per pulse, in addition to the concentration of polymer in solution, governs this instantaneous distance and it can be used as a tool for tailoring nanogels size and molecular weight.

Furthermore, the pulse repetition rate, that is the time between two successive pulses, can affect the kinetics of termination reactions and, in turn, the final properties of NGs. In particular, the time between two successive pulses has to be compared with the half-life of the formed macroradicals. If the time between two successive pulses is longer than the half-life of the macroradicals, radicals disappear in intra-pulse reactions. Conversely, if the time between two successive pulses becomes shorter, each pulse cannot be considered independent and some of the macroradicals can survive until the successive pulse. The “survived” macroradicals can then terminate with the new macroradicals formed. This condition “virtually” reduces the average distance between radicals.

For the purpose of the study presented hereafter, irradiations have been performed using two different accelerators with “fixed” set-ups. The dose per pulse and the

pulse repetition rate have been varied simultaneously and the lowest dose per pulse has been obtained in correspondence of the lowest pulse repetition rate (0.74 Gy/pulse and 37.5 Hz – average dose rate of 100 kGy/h). In these conditions a quite low instantaneous radicals yield and a sufficient long time between two successive pulses have been achieved, so that the final effect has been an increased distance between radicals. Conversely, the highest dose per pulse has been obtained in correspondence of the highest pulse repetition rate (13 Gy/pulse and 300 Hz – average dose rate of 13,000 kGy/h), therefore in these last conditions the distance between radicals has been reduced.

In Figure 5.12a-b, the average hydrodynamic diameters and molecular weights for nanogel systems irradiated at the variance of the polymer concentration at the two dose-rates are reported. A total dose of 40 kGy has been deposited.

It can be observed that all systems are nanoscalar in size, except for P*0.5L40-100, which is a macrogel. The molecular weight of the generated NGs is always higher than that of the linear polymer (0 kGy/h) and the observed increase of the molecular weight is more pronounced at the lowest dose-rate. Furthermore, at the highest dose rate, nanogels with the smallest size have been obtained at all concentrations. Particles size distribution (PDI) is always around 0.3.

More in detail, at the increase of dose-rate P*0.5 system, that is a macrogel at the lowest dose rate, becomes a transparent dispersion of polymer nanoparticles; at 0.25 wt% both the hydrodynamic diameter and the molecular weight decrease; at 0.1 wt% only a slight reduction of both the hydrodynamic size and molecular weight is observed.

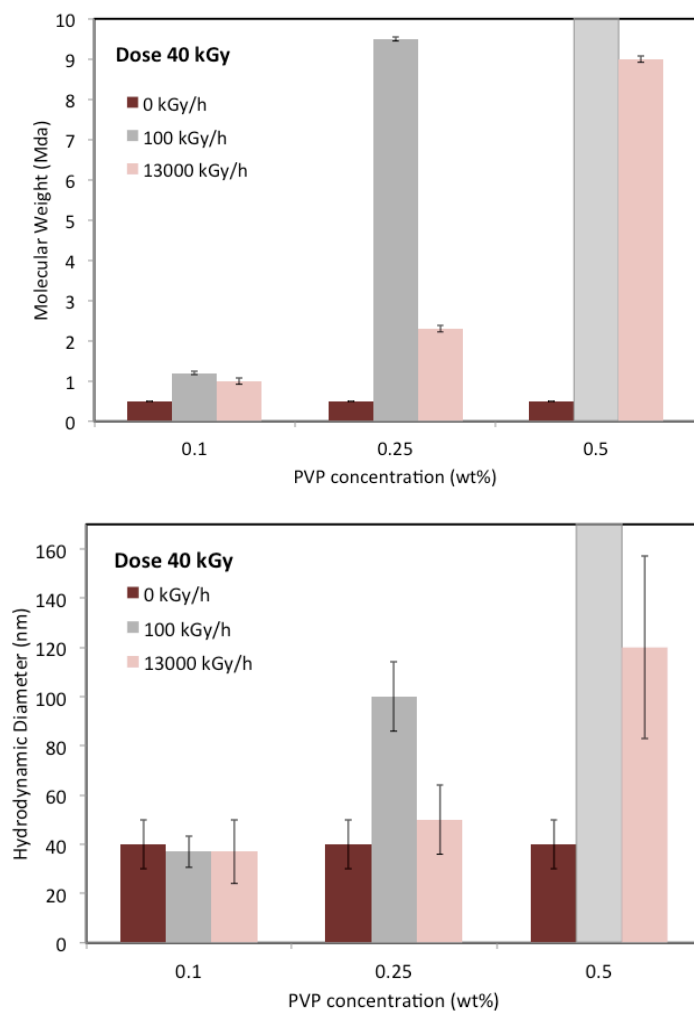


Figure 5.12a-b: a. Hydrodynamic diameter and b. molecular weight, at the variance of the polymer concentration for two dose-rates. Error bars represent the width of the distributions.

All the evidences gathered suggest that inter-molecular crosslinking always occurs and the extent of inter-molecular crosslinking increases with the increase of polymer concentration and the decrease of dose-rate. These effects can be discussed in terms of the instantaneous average number of radicals formed per each polymer chain, calculated on the account of the dose per pulse and the assumption that primary

radicals formed are all transferred to the polymer (see also paragraph 5.1.1). In Table 5.3 the average number of radical sites per polymer chain per pulse is reported.

Irradiation set-up	LAE 100 kGy/h [HO·] _L = 4.6 10 ⁻⁷ M	Elek. 13000 kGy/h [HO·] _E = 8.3 10 ⁻⁶ M
Polymer conc.	N _{rad} : N _{chains} per pulse	N _{rad} : N _{chains} per pulse
0.5 wt%	1 : 12	1:2
0.25 wt%	1 :5-6	1:1
0.1 wt%	1 :1	4:1

Table 5.3: Instantaneous average number of radicals formed per each polymer chain for LAE 100 kGy/h and Elektronika 13,000 kGy/h.

The approximate average number of radicals for macromolecule is low in both the irradiation conditions. In none of these conditions intra-molecular recombination of polymer radicals is expected to be the predominant termination reaction. When the polymer concentration decreases, the instantaneous average number of radicals for macroradicals increases and intra-molecular crosslinking is more favored.

As described in paragraph 5.1, intra- and inter-molecular crosslinking reactions may not be the only reaction occurring when substantial doses of irradiation are imparted (e.g. 40 kGy). Indeed, at these doses, the nature of the macroradicals as well as their mobility changes and other reactions take place leading to chemical modifications of the PVP structure.

FT-IR analyses have been carried out on P*0.1 nanogels generated at different dose-rates and the full spectra are reported in Figure 5.13. Linear PVP spectrum is also reported in Figure 5.13 as reference. In Figure 5.14a-b two portions of the same spectra are shown. The nature of chemical modifications occurring upon irradiation

for P*0.1L40-100 have been already described in detail in paragraph 5.1. The comparison between the spectra of the P*0.1 systems produced at the two dose-rates reveals that the dose-rate does not significantly affect the NGs chemical structure modification in terms of new functional groups formed but it changes their relative concentration. In particular, since the spectra have been normalized with respect to methylene groups, the observed increases of the hydroxyl and carboxyl absorptions point to a reduction of methylene groups, likely due to a higher crosslinking formation.

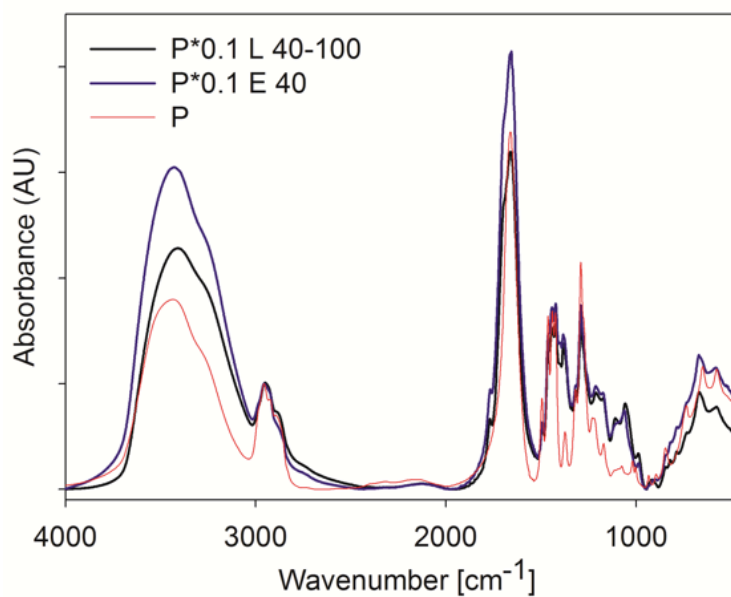


Figure 5.13: FT-IR spectra of P*0.1L40-100 and P*0.1E40. All spectra have been normalized with respect to the peak at 2956 cm⁻¹.

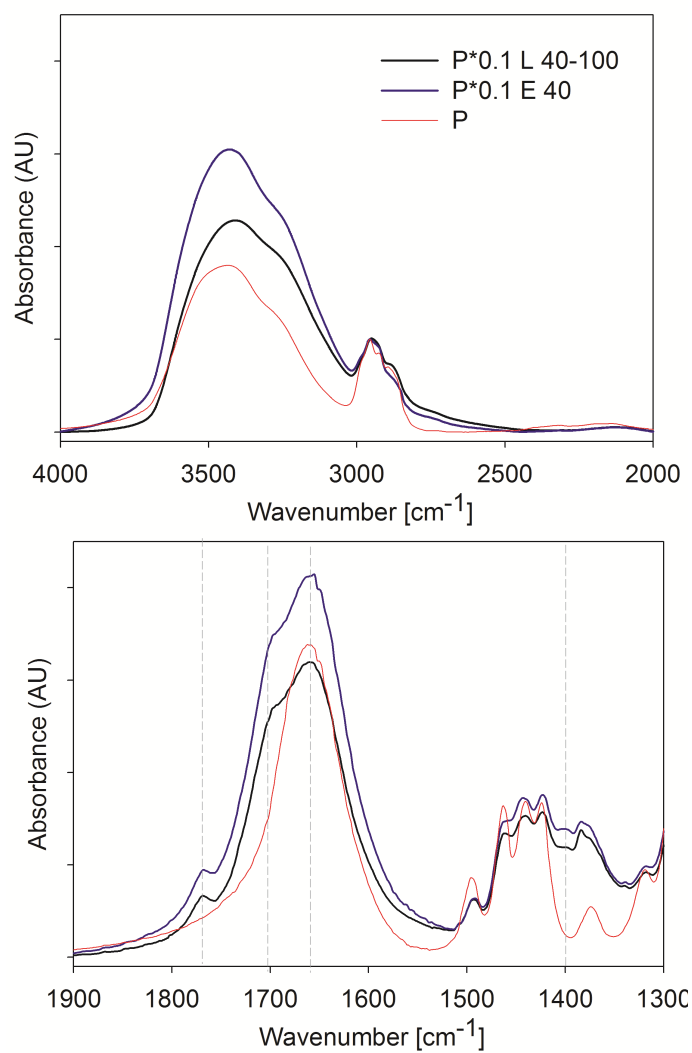


Figure 5.14a-b: FT-IR spectra of P*0.1L40-100 and P*0.1E40. All spectra have been normalized with respect to the peak at 2956 cm^{-1} . Vertical dashed lines correspond to the following peaks: 1769 , 1698 , 1662 and 1400 cm^{-1} .

5.3 Base PVP nanogels: effect of the deposited dose on NGs properties.

For two selected PVP concentrations, 0.1 and 0.25 wt%, the effects of the total deposited dose on hydrodynamic size, molecular weight, surface charge density and chemical structure are here discussed. In particular, data relative to the irradiation performed at the highest “dose-rate” (both the highest dose per pulse and the highest pulse repetition rate in the investigated range) and at three total doses, 20-40-80 kGy, are shown.

In Figure 5.15a-b nanogels’ hydrodynamic size and molecular weight are reported. P*0.1E20 shows smaller hydrodynamic size and similar molecular weight to linear PVP (0 kGy). Increasing the dose up to 40 kGy the average hydrodynamic diameter increases as well as the molecular weight. For the 80 kGy particle size slightly decreases while molecular weight is almost constant. Conversely, for P*0.25E20 both the hydrodynamic diameter and the molecular weight values are significantly higher than those of the linear polymer and relatively little affected by the increase of dose up to 40 kGy. By prolonging irradiation up to 80 kGy the size maintains almost constant and the molecular weight increases of about 20%.

In conclusion, the most relevant molecular and dimensional modifications of PVP occur already within the first 20 kGy of absorbed dose, whereas irradiation at high doses seems to lead to denser structures.

In Figure 5.16, ζ -potential distribution curves for P*0.1 systems are reported. The average ζ -potential values and hydrodynamic diameters are also plotted as function the dose in Figure 5.17. Error bars in the plots represent the standard deviation of the distributions. From this last figure it can be observed that the trends of D_h and ζ -potential are at all similar. When particle size decreases with dose, the anionic character is enhanced; when size increases the surface charge density becomes lower. Therefore, by increasing the particle size, thus decreasing the overall surface area (total mass is constant for all systems), the density of anionic groups on the surface is lower. Interestingly, the charge distribution is fairly narrow with a main peak at about -40 mV after 20 kGy of irradiation. The distributions become wider and wider at the increase of dose up to 80 kGy. Indeed, irradiation at the lowest dose (20 kGy) is

responsible for ionizable groups formation (e.g. carboxyl groups from ring opening reactions). These groups may be involved in inter-complexes formation and/or ionic interactions when particles grow in size (40 kGy) until the polymer chains have sufficient flexibility. When the nanoparticles are further irradiated a higher heterogeneity of negatively charged and non-ionic nanoparticles is evidenced.

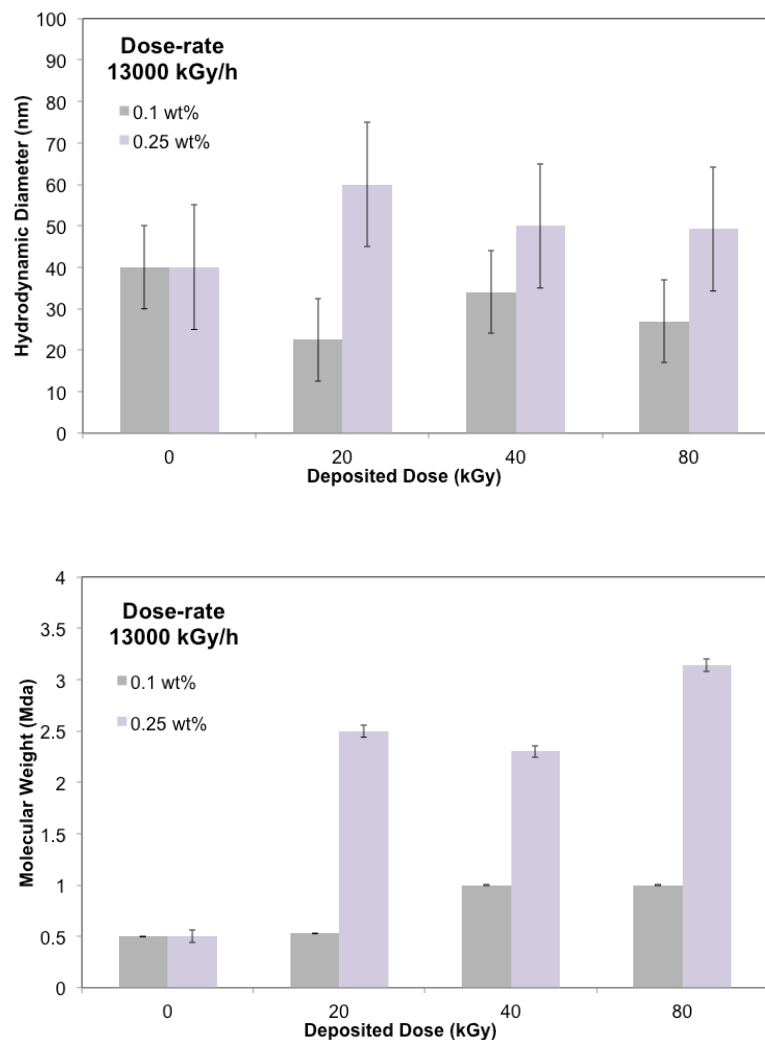


Figure 5.15a-b: a) Hydrodynamic size and b) molecular weight for P*0.1 and P*0.25 system obtained at the highest dose-rate (13000 kGy/h) for the three integrated doses of 20, 40 and 80 kGy. Error bars represent the width of the distributions.

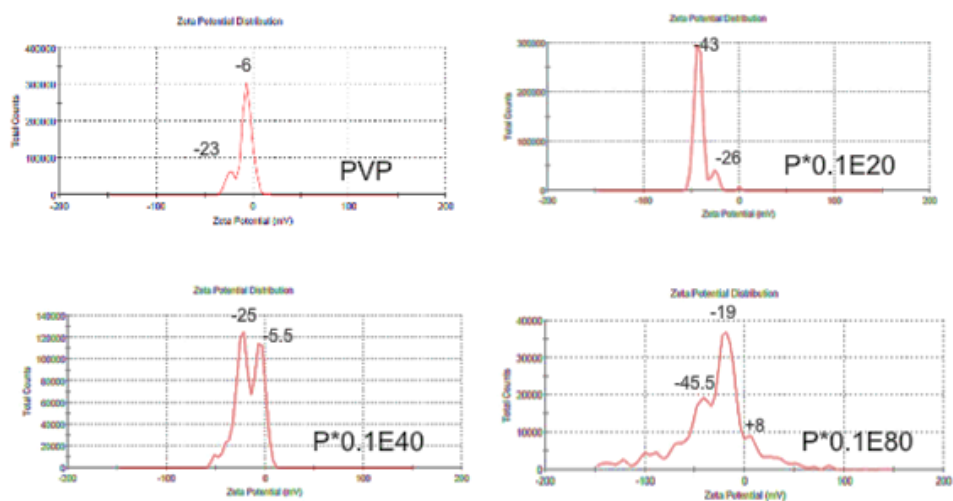


Figure 5.16: ζ -potential distribution curves for linear PVP and P*0.1 systems. The mean value of each peak is reported in the figure as a tag.

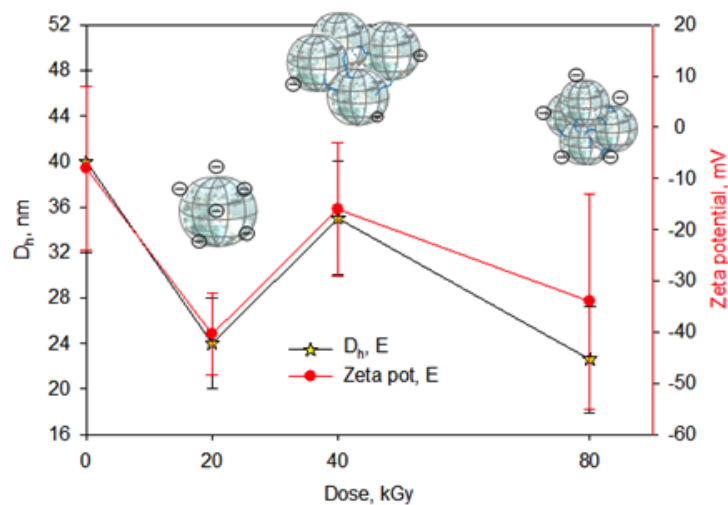


Figure 5.17: Average hydrodynamic size and ζ -potential values with their relative standard deviations for P*(0.1) system obtained at the highest dose-rate for the three integrated doses of 20, 40 and 80 kGy.

FT-IR spectra have been collected both for P*0.1 and P*0.25 at the three doses. In Figure 5.18 the full spectra of P*0.1 systems and linear PVP are reported, while in Figure 5.19 a and b, the portions of spectra between 2000-4000 cm^{-1} and between 1900-1300 cm^{-1} , for the P*0.1 systems and linear PVP are reported. The NGs spectra show qualitatively similar chemical modifications with respect to the linear polymer to those of the systems already described in paragraph 5.1 and 5.2.

With reference to the band at 3700-3000 cm^{-1} (Fig 5.19a), associated to the stretching of hydroxyl and amidic groups, all irradiated systems show a more pronounced and wider absorption band. The carbonyl absorption is always a multi-band peak with a contribution from absorptions at 1769 and 1698 cm^{-1} that is higher the higher is the irradiation dose. A systematic increase of absorptions at 1400 cm^{-1} , related to carboxylated ions, is also observed.

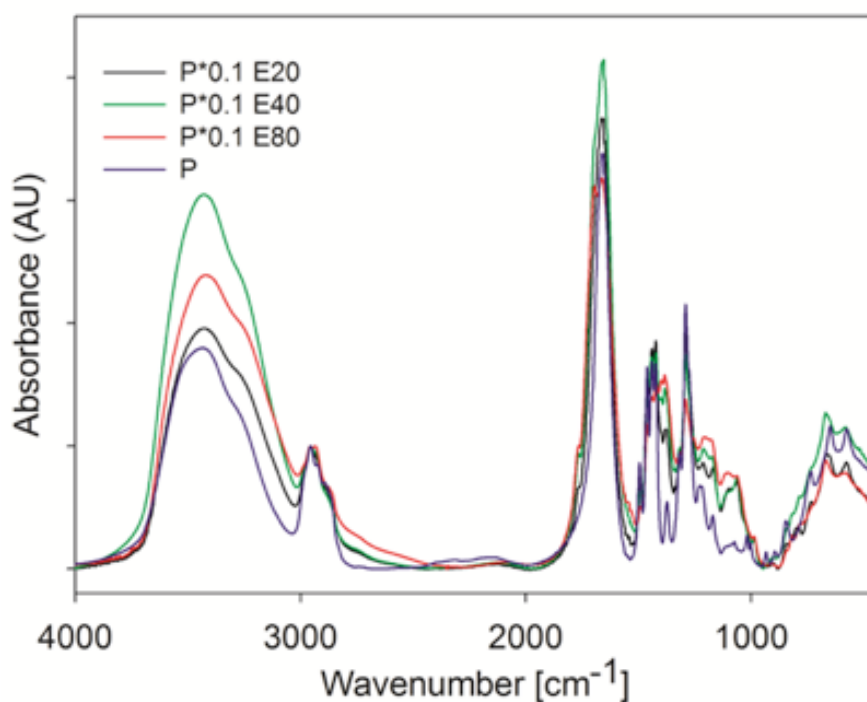


Figure 5.18: FT-IR spectra of linear PVP, P*0.1 E20, E40 and E80. All spectra have been normalized with respect to the peak at 2956 cm^{-1} .

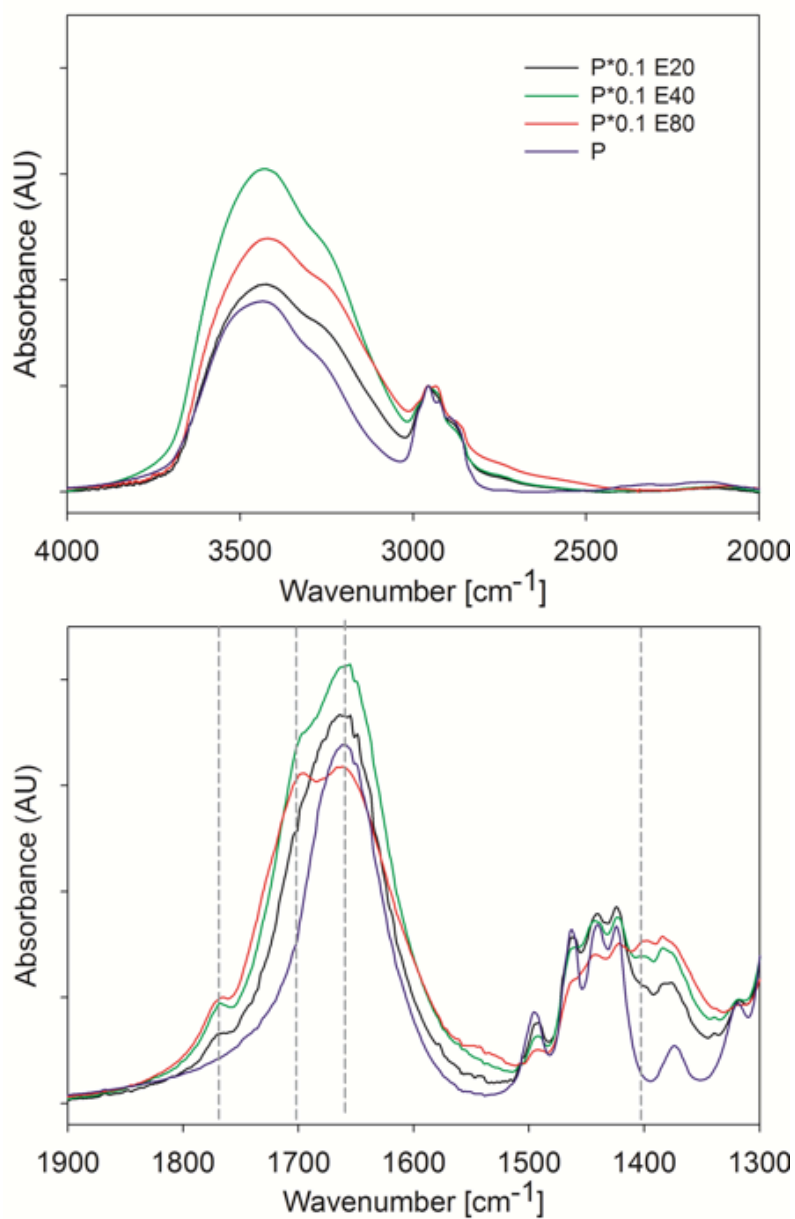


Figure 5.19a-b: FT-IR spectra of P*0.1 E20, E40 and E80. All spectra have been normalized with respect to the peak at 2956 cm^{-1} . Vertical dashed lines correspond to the following peaks: 1769, 1698, 1662 and 1400 cm^{-1} .

In Figure 5.20 the full spectra of P*0.25 systems and linear PVP are also reported, while in Figure 5.21 a and b, the portions of spectra between 2000-4000 cm^{-1} and between 1900-1300 cm^{-1} , for the P*0.25 systems and linear PVP are reported. . With respect to P*0.1 systems, the effect of the irradiation on the chemical structure of P*0.25 NGs is at all similar to that observed for NGs produced at the lowest dose rate (L40-100), that have been already described in paragraph 5.1. Briefly, all absorption bands are broader and lower in intensity with respect to those of the linear polymer. The nature and extent of structural modification is not as much affected by the dose as for P*0.1 systems

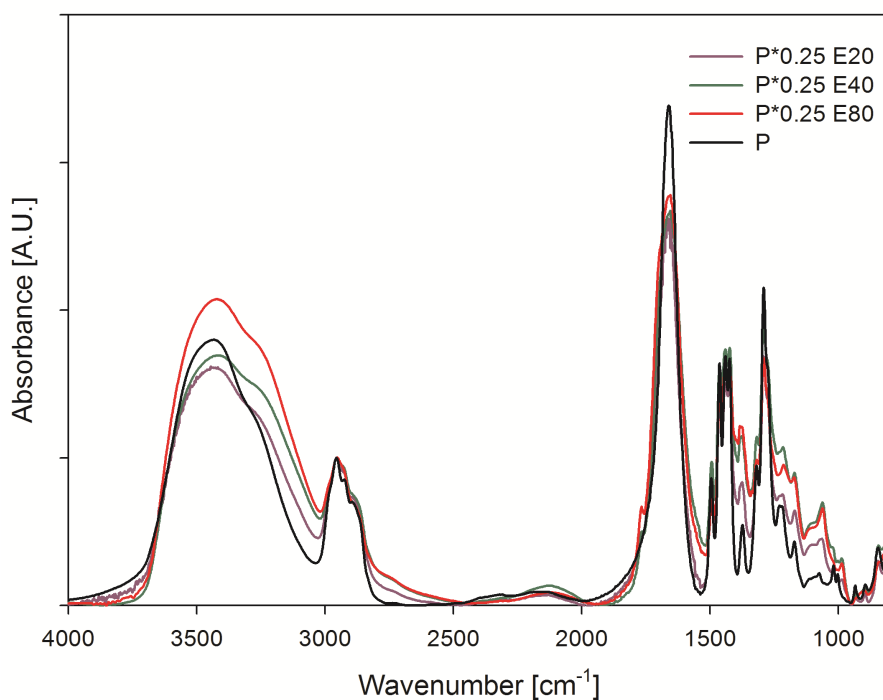


Figure 5.20: FT-IR spectra of linear PVP, P*0.25 E20, E40 and E80. All spectra have been normalized with respect to the peak at 2956 cm^{-1} .

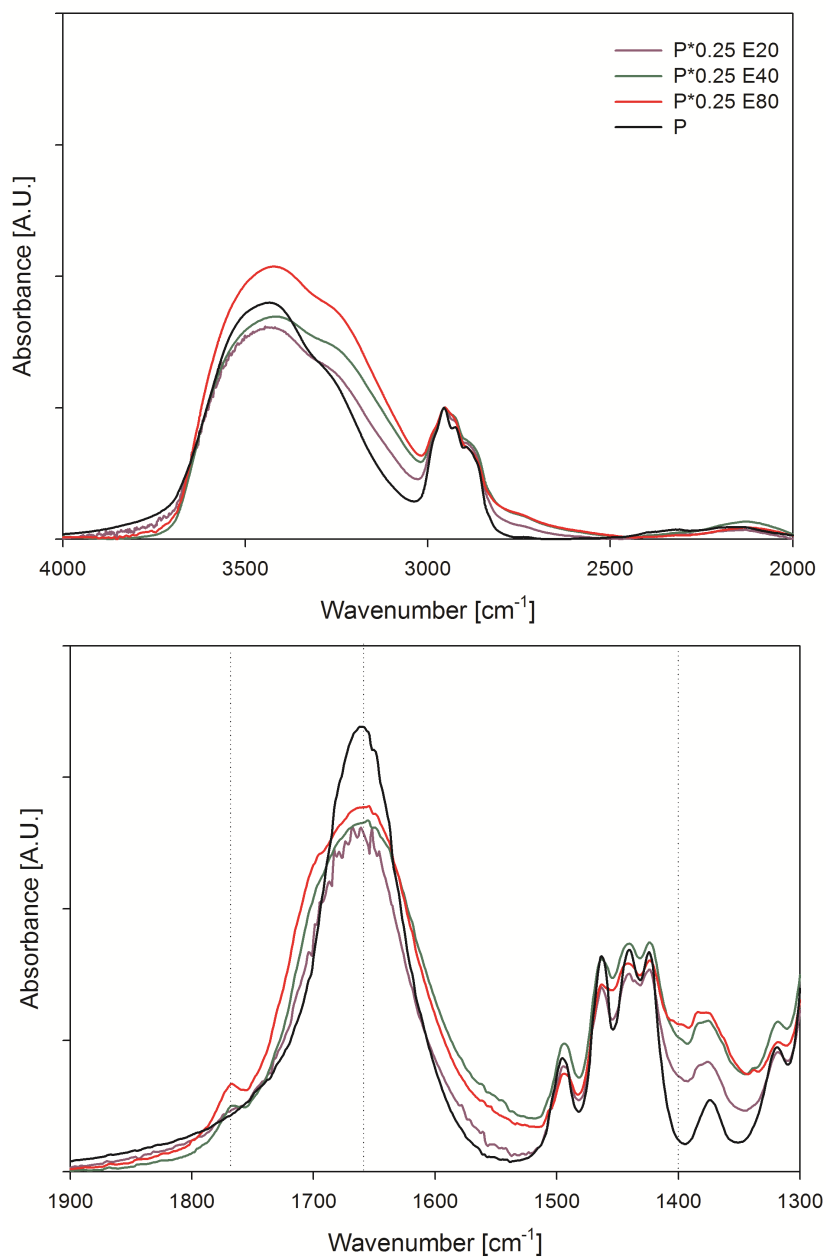


Figure 5.17a-b: FT-IR spectra of P*0.25 E20, E40 and E80. All spectra have been normalized with respect to the peak at 2956 cm^{-1} . Vertical dashed lines correspond to the following peaks: 1769, 1662, 1400 cm^{-1} .

The evidences collected here suggest that cyclic imide and carboxylate groups formation is already occurring within the first 20 kGy of total deposited dose and occur to a higher extent when the material is irradiated at low concentration and for a prolonged time.

5.4 Conclusions

Pulsed electron beam irradiation of PVP aqueous solutions leads to the formation of either macrogels or nanogels with high yields (~90%). Macrogels form at high polymer concentration ($C > C^*$) and at all the investigated dose-rates, being the total doses imparted always above the gel dose. Conversely, when $C < C^*$, nanogels can be obtained depending on the irradiation conditions. A general feature observed for all the generated nanogels is that they grow in molecular weight with respect to that of the linear polymer. This suggests: (i) PVP undergoes inter-molecular crosslinking up to some extent, even if $C < C^*$; (ii) chain scission is not significantly occurring even when substantial doses (up to 80 kGy) are imparted to the materials. Polymer concentration and irradiation conditions can be used as independent tools to tune the size and molecular weight of PVP nanoparticles. In particular, at the increase of the polymer concentration, nanogels' hydrodynamic size and molecular weight both increase, as inter-molecular crosslinking is enhanced with respect to intra-molecular crosslinking. Moreover, dose and dose-rate affect NGs physico-chemical properties, the more the higher is the concentration of the polymer.

PVP NGs show a marked anionic character with respect to non-irradiated PVP, suggesting that the chemical structure of PVP is modified upon irradiation. A detailed structural characterization of materials reveals that the more the networks approach the nanoscale, the higher is the extent of chemical modification. In particular, the new chemical functionalities found are succinimide groups and C-O-C type of crosslinks. An enhanced concentration of hydroxyl and carboxyl groups is also present. These last results suggest that the final structure and molecular architecture of the nanogels is the result of a complex reaction pathway, involving not only inter and intra-molecular recombination of carbon-centered radicals, but also disproportion and termination reactions with water radiolysis primary products. It can be argued that

when the probability of inter-molecular recombination of polymer macroradicals is low (i.e. for low PVP concentration and high dose-rate) and intra-molecular recombination becomes hindered by progressive chain mobility reduction (high dose-rate), termination reactions leading to more hydroxylated and carboxylated PVP networks take place. The concentration of polymer in solution appears to significantly affect both the type and extent of chemical modification, whereas both absorbed dose and dose-rate determine only a change in the relative concentrations of the formed groups.

It must be pointed out that the effect of the deposited dose and dose-rate on NGs physico-chemical properties is not completely clarified yet, as these two parameters could not be systematically varied in a wide range, independently. In particular, the recourse to industrial-type accelerators have advantages and disadvantages. The advantage is the possibility of a straightforward scale up of the process. The disadvantages are related to the limited flexibility offered by these accelerators in terms of selection of operative parameters. For this reason, relatively high total doses have been deposited on the materials, therefore the radiation is interacting with a material that is continuously changing. Furthermore, the use of these irradiation setups has impaired to vary the dose per pulse and the pulse repetition, independently, and to clarify how these parameters affect the NGs' properties. A more fundamental study carried out using research-type accelerators can offer the opportunity of a better understanding of the correlations between process and properties for a fine-tuning of the nanogels physico-chemical properties, and the acquired new knowledge can be then transferred to the manufacturing process at large scale. Notwithstanding the limitations in the irradiation conditions, "as borne" sterile nanogels have been produced with high yields, tailored particles size and narrow size distributions, without making recourse to surfactants, with clear advantages both in terms of product and process performance.

6 Amino-functionalized e-beam crosslinked nanogels

In the previous chapter it has been demonstrated that radiation-induced crosslinking can be a viable synthetic strategy for the production of PVP-based NGs with tailored physico-chemical and molecular properties. These PVP-based NGs, if appropriately derivatized with functional groups reactive towards specific bio-active ligands, can be used as building blocks for the assembly of composite nanodevices.

In this chapter, the possibility of generating as-borne sterile, amino-functionalized NGs, by simultaneously crosslinking PVP and grafting a monomer carrying amino groups to the crosslinked particles, has been explored. In particular, PVP/APMAM dilute aqueous solutions have been irradiated at the variance of APMAM concentration and irradiation conditions, i.e. dose-rate and total deposited dose. Irradiation has been carried using both with Elektronika 10/10 and LAE 13/9 at different dose-rates, i.e. 500 and 13,000 kGy/h, and depositing different total doses, i.e. 40 and 80 kGy. For all the formulations, PVP concentration is 0.1 wt%.

6.1 Amino-functionalized NGs physico-chemical properties

For all irradiation conditions and formulations, the yield of the process has been estimated gravimetrically and it has been always above 98 % wt.

Particles with different hydrodynamic sizes have been obtained at the variance of APMAM concentration and the irradiation conditions. In Figure 6.1 the average hydrodynamic diameters and their relative standard deviations for both linear PVP (P), base PVP NGs and amino-functionalized NGs, are shown. Base PVP NGs (P*) have been already described in the previous chapter and here some of them are included as reference. Poly(N-vinylpyrrolidone)-grafted-(aminopropyl) methacrylamide microgels (MGs) or NGs are coded P*-g-A(X), where X=200, 100, 50, 25 depending on the APMAM:PVP's RU molar ratio.

6.1.1. Influence of APMAM concentration

Figure 6.1a refers to nanogel dispersions obtained after e-beam irradiation at the integrated dose of 40 kGy and the highest average dose-rate (13,000 kGy/h). The hydrodynamic diameter of the linear polymer in the presence of APMAM (P+A) is also reported in Figure 6.1a. It can be observed that the addition of APMAM to a PVP solution (at the molar ratio 1:50 with respect to PVP RU) is causing a slight reduction of PVP hydrodynamic size already prior to irradiation. The observed shrinkage of PVP coils can be attributed to the shielding effect exerted by the protonated amino groups of APMAM toward the anionic charges of PVP (see Figure 4.2).

As already pointed out in paragraph 5.2, no appreciable differences between the linear polymer (P) and P*0.1E40 (P*) can be observed. The average hydrodynamic diameters (D_h) of the particles obtained upon irradiation, at the variance of APMAM content, are also reported in Figure 6.1a. Increasing APMAM content from 1:200 to 1:100, D_h only slightly increases, always leading to nanogels of comparable size to the P*'s. At 1:50 ratio particle size suddenly rises to few microns. This sudden increase of D_h can be associated to a step change in the main type of crosslinking reactions upon irradiation. When e-beam irradiation of the aqueous solutions of PVP with APMAM is carried out with both components present at low concentration, grafting of APMAM to individual PVP nanoparticles likely occurs, while at the increase of APMAM content inter-particle bridging may concur (Figure 6.2). As a consequence, the step-wise increase in particles size is observed and microparticles are formed.

6.1.2 Influence of dose and dose-rate

Figure 6.1b compares the dimensions of particles obtained at the same dose-rate (13,000 kGy/h), for two integrated doses: namely, 40 and 80 kGy. As already described in the paragraph 5.3, the effect of increasing the dose, from 40 to 80 kGy, for the base PVP system at 0.1 wt% is in the direction of reducing the nanogels' particle size and narrowing the particle size distribution without affecting the

molecular weight. Conversely, when it comes to compare hydrodynamic diameters of systems obtained by irradiation of PVP in the presence of APMAM, higher doses generally lead to bigger particles, that are still in the nanoscale range for the lower molar ratios (1:200 and 1:100), while they become micron-sized for the 1:50 ratio, with concomitant broadening of the particle size distribution.

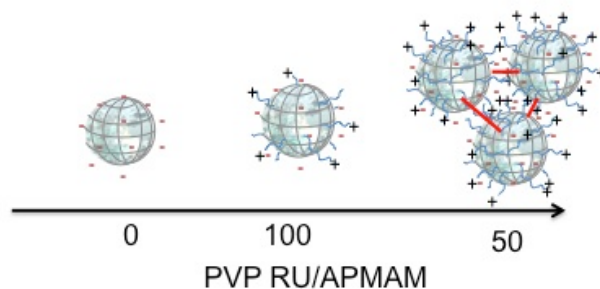


Figure 6.2: Schematics of a typical base PVP nanogels (PVP RU/APMAM=0) with its network and negative surface charges; of an amino-grafted PVP (P*-g-A) nanogel (PVP RU/APMAM=100) and of a microgel (PVP RU/APMAM=50). The curly blue lines represent grafted APMAM carrying a primary amino group. Bold red lines represent APMAM monomers or oligomers bridging crosslinked PVP coils.

It has been demonstrated already that the dose-rate does not significantly affect the hydrodynamic diameter of the 0.1 wt% base NGs, and this is still true for the amino-functionalized variants (see Figure 6.1c) when APMAM concentration is low, such as for P*-g-A (200). However, the effect of the dose-rate becomes quite important at a higher APMAM contents: the switch from mainly intra-molecular crosslinking to inter-particle bridging occurs already for the 1:100 PVP RU:APMAM molar ratio. Indeed, reducing the dose-rate (i.e. frequency) makes the time lag between two successive pulses comparable with the time-scale of encounters of radicals formed on different nanoparticles, thus favoring aggregation.

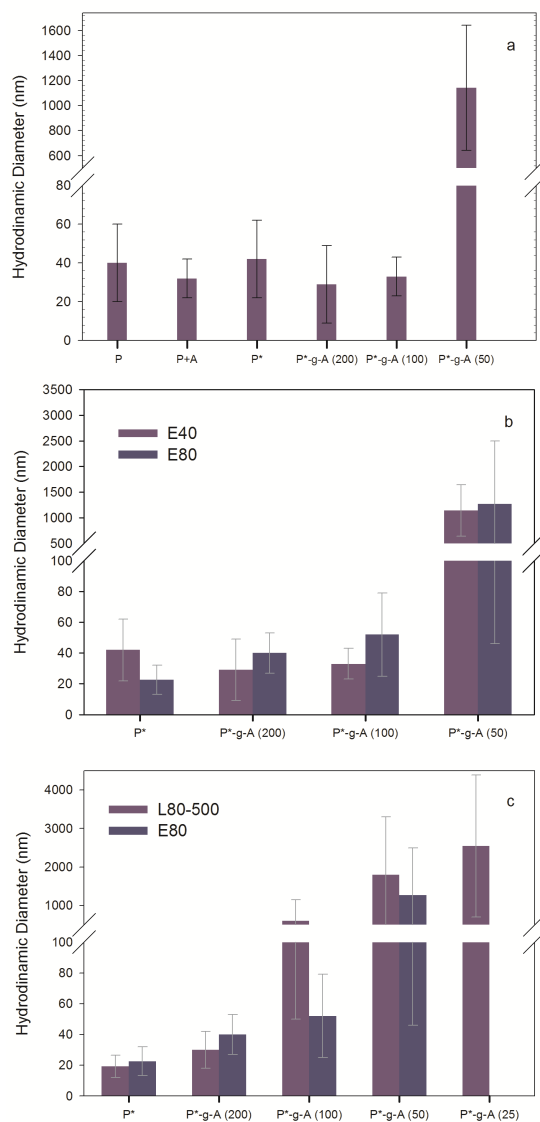


Figure 6.1a-c. MGs and NGs hydrodynamic diameters from DLS analysis at 20°C in water. (a) Systems irradiated with low dose-rate and the lower dose (E40). Non-irradiated aqueous PVP both in the presence and in the absence of APMAM are reported for comparison. (b) Influence of irradiation dose for the different formulations. (c) Influence of dose-rate for the different formulations. Error bars represent the variance of the particle size distribution.

6.2 Surface charge density of base and amino grafted PVP micro/nanogels.

In Figure 6.3 average ζ -potential values for E40 and E80 MGs/NGs are shown. All irradiated systems present a marked anionic behavior, more pronounced at the highest dose. The markedly anionic character observed for P*0.1E40 is due to PVP chemical modification occurring upon irradiation (see paragraph 5.3).

Nanogels obtained in the presence of increasing amounts of APMAM show a progressively reduced anionic character, likely due to the already proposed screening effect of the negative charges of PVP by the protonated amino groups of APMAM. Conversely, at the highest concentration of APMAM, when microgels are formed from aggregation of several PVP chains, this monomer and/or its oligomers are expectedly no longer preferentially located at the particles surface, but in their interiors, therefore ζ -potential values become comparable to that of the base PVP systems.

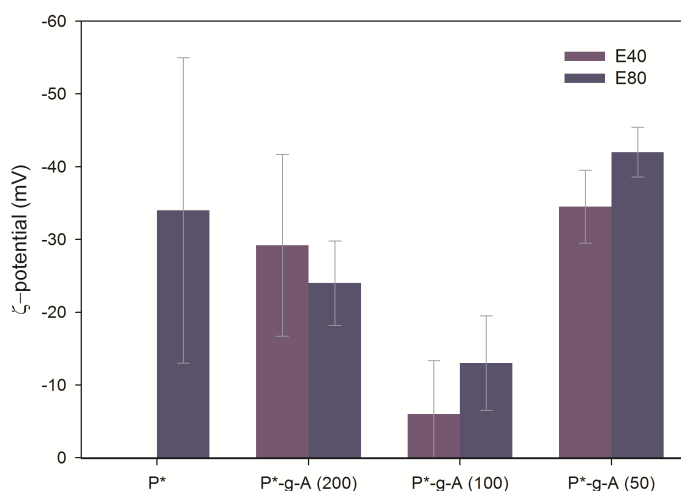


Figure 6.3: Surface charge density for the micro and nanogels produced at the different PVP RU:APMAM molar ratios and at the two doses of 40 and 80 kGy. Error bars represent the width of the surface charge distribution.

It is worth pointing out that, in general, amino-functionalized MGs or NGs show broad ζ -potential distributions, which reflect an inherent heterogeneity of charge density. In Figure 6.4, the ζ -potential distribution curve for a representative system, P*-g-A(50) E80, it is shown. For this particular system, the average surface charge density around -40 mV, with a wide distribution of values that span from -15 to -55 mV.

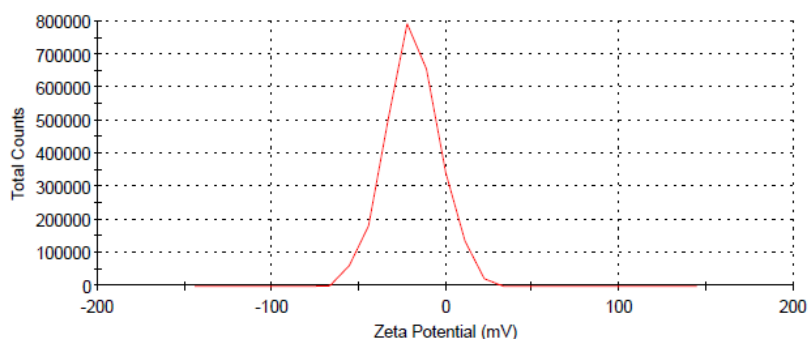


Figure 6.4: ζ -potential curves for functionalized nanogels (P*-g-A(50) E80) in water.

6.3 Structural characterization of amino-functionalized PVP micro/nanogels.

Spectroscopic confirmation of the chemical attachment of APMAM to PVP has been sought by a combination of different spectroscopic techniques. In particular, in Figure 6.5, FTIR spectra of not irradiated PVP, P*, P*-g-A(50) and P*-g-A(25) are presented. The spectrum of AMPAM is also reported for comparison.

FT-IR spectra of all the irradiated systems show the characteristic features of 0.1 wt% systems described in chapter 5. When irradiation is carried out in the presence of APMAM, differences with respect to the base P* system are subtle. A relative increase of the absorption related to the amide I band of PVP (1661 cm^{-1}) and a shoulder at 1537 cm^{-1} , probably due to the contribution of amide/amine bands of APMAM can be noticed.¹⁵⁴ The strong peak at 1610 cm^{-1} , that is present in the free monomer, and mainly related to double bond stretching vibration, is not present in any of the irradiated systems, so are not any of the corresponding characteristic

bands at 1013, 940 and 811 cm^{-1} . This last evidence supports the proposed radical addition reaction of APMAM to PVP.

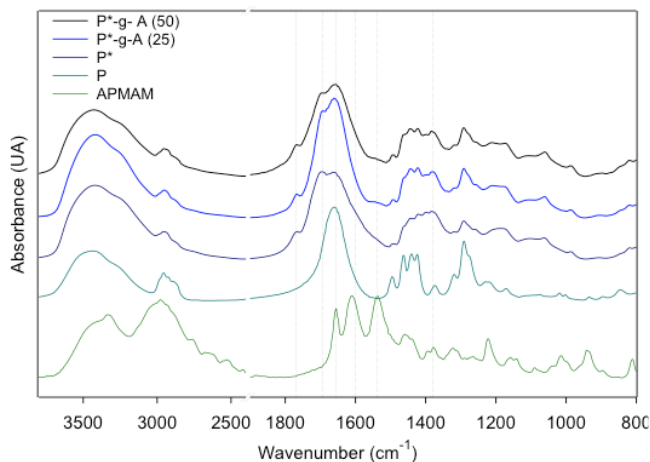


Figure 6.5: Comparison of FT-IR spectra of the non-irradiated PVP, base PVP nanogels (P*) and amino-functionalised variants irradiated with LAE 13/9 at 80 kGy. All spectra, except for APMAM, have been normalized with respect to the peak at 2956 cm^{-1} . Vertical dashed lines correspond to the following peaks: 1661, 1695, 1765, 1600, 1537 and 1388 cm^{-1} .

Solid state ^{13}C NMR has been carried out on the PVP-g-A(25) L80 and on the linear PVP and monomeric APMAM, as reference (see Figure 6.6 and Table 6.1). Chemical shifts with reference to those of both pure PVP and APMAM have been assigned according to literature data¹³⁸ and are reported in paragraph 3.3.11. In Table 6.1, the major peaks for P*-g-A(25)L80-500 MGs are reported. Modification of the spectral features of the MG with respect to the linear PVP is evident in all the different carbon sites. Although the obtained spectrum is not suitable for an exact identification and quantification of the different species, the evident shift of the carbonyl band toward the higher chemical shifts is in good agreement with the proposed structural modifications of PVP.

The influence of the electron beam irradiation on the surface chemical composition of the produced MGs and NGS has been also investigated by X-ray photoelectron spectroscopy (XPS), due to its ability to provide surface quantitative elemental and chemical state information.

P*-g-A(25)L80	Carbon	Chemical shift
	C ₆ as in PVP	177,1
	C ₂ _ C ₃ as in PVP	45,4
	C ₂ 'as in APMAM	29,5

Table 6.1: Attribution of main ¹³C NMR chemical shifts of P*-g-A(50) L80 MG.

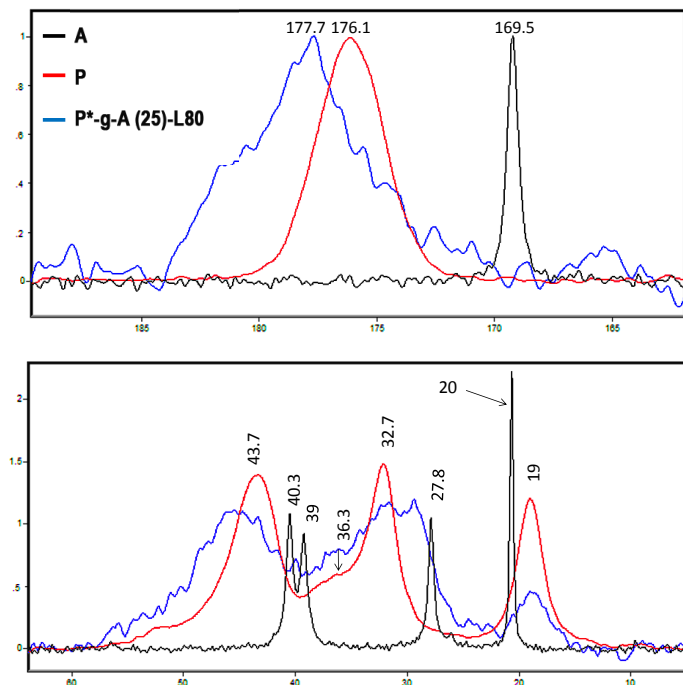


Figure 6.6. Overlaid ¹³C {¹H} CP MAS NMR spectra of not irradiated PVP (P), APMAM monomer (A) and amino-functionalized nanogels (P*-g-A (25)-L80) in expanded scale. Spectra are normalised with respect to the carbonyl peak.

The surface chemical composition of the investigated samples is reported in Table 6.2 and quantitative results are expressed as atomic percentage (at. %). A sample of non irradiated PVP has been taken as reference. Differences in atomic percentage are detected before and after irradiation of aqueous PVP. A noticeable increase in

the oxygen concentration and a slight decrease in the carbon and nitrogen amounts are evidenced on the surface of the irradiated PVP samples (P*). The value of the O/C ratio increases from 0.169 to 0.327 after irradiation with LAE at 80 kGy and the N/C decreases from 0.144 to 0.094, as reported in Table 6.2. These results confirm an increased level of PVP oxidation upon irradiation, which is consistent with the findings of the other spectroscopic techniques applied. No significant differences have been observed in surface quantitative analysis among the samples subjected to irradiation at different dose-rates or in the presence of APMAM, with the only exception of P*-g-A (100) E80. This sample shows the highest O/C ratio and a slightly higher N/C with respect to P*-g-A (50) E80, despite of the fact that it comes from a halved amount of APMAM in the feed.

A nonlinear least-square curve fitting routine has been used for the analysis of XPS spectra, separating elemental species in different oxidation states. In all the investigated samples the N 1s photoelectron peak consists of a single component located at BE = 400.1 eV that can be attributed to nitrogen species in the amide group $\text{N}-\text{C}=\text{O}$.¹⁵⁹ In all the O 1s spectra, the component of the photoelectron peak corresponding to the binding energy of the carbonyl group is located at BE = 531.5 eV, which is assigned to oxygen species in $\text{N}-\text{C}=\text{O}$.^{159,160}

The curve-fitting of C 1s photoelectron peak revealed the presence of three components at BE = 285.1 eV, BE = 286.5 eV and BE = 288.1 eV, that can be assigned to carbon atoms in C-C, C-O and C=O bonds, respectively.^{160,161}

Results of the curve-fitting procedure of C 1s peak are reported in Table 6.3. A different content of $\text{N}-\text{C}=\text{O}$ carbon species, corresponding to C 1s component at BE = 288.1 eV, is detected in the base PVP samples before and after irradiation. Electron beam irradiation induces a significant increase in the concentration of carbon species in the amide group, coherently with the proposed formation of a cyclic imide. The increase of these species is confirmed by the already discussed increase of the $\text{N}-\text{C}=\text{O}$ species in the O 1s spectra.

SYSTEM	C 1s	O 1s	N 1s	O/C	N/C
PVP	76.1	12.9	11.0	0.169	0.144
P* L80	70.4	23.0	6.6	0.327	0.094
P*-g-A (50) L80	68.7	22.9	8.4	0.333	0.122
P* E80	70.7	22.0	7.3	0.311	0.103
P*-g-A (50) E80	72.9	20.1	7.0	0.276	0.096
P*-g-A (100) E80	61.2	31.4	7.4	0.513	0.121

Table 6.2. XPS surface quantitative analysis of the investigated samples. Elemental concentration is expressed as atomic percentage (at. %).

SYSTEM	C 1sBE (eV)		
	285.1	286.5	288
PVP	69.8	20.5	9.7
P* L80	67.8	12.9	19.4
P*-g-A (50) L80	64.6	16.9	18.5
P* E80	66.1	16.3	17.6
P*-g-A (50) E80	72.4	10.6	17.0
P*-g-A (100) E80	67.5	15.0	17.5

Table 6.3: XPS surface distribution of carbon species resulting from the curve-fitting of C 1s photoelectron peak. Carbon species are expressed as peak area percentage.

6.4 Biological evaluations on amino-functionalized PVP micro/nanogels.

Biological assays have been performed on cells treated with amino-functionalized NGs to verify their biocompatibility. All gathered data suggest a good degree of biocompatibility of the produced NGs. Furthermore, cellular-internalization experiments showed a significant cellular accumulation of nanogels, probably by an endocytotic pathway: a direct translocation process without observable cytotoxic processes. For a detailed description of all biological evaluations see Paper II.

6.5 Conclusions

Amino-functionalized PVP-based MGs and NGs have been produced via e-beam radiation processing. In the chosen experimental conditions, although APMAM has been successfully grafted on PVP, the possibility of obtaining variants of amino-functionalized PVP nanogels with different size or many available amino groups has been impaired by the attractive interactions occurring between the irradiated PVP and APMAM. These interactions promote nanoparticles coalescence and covalent bridging phenomena, the more the higher is APMAM concentration, depending on irradiation conditions. This issue can be overcome by using an APMAM variant with a protected amino group or, as it will be shown in the following, by producing carboxyl-functionalized PVP nanogels first, with better controlled particles size distribution (see chapter 7), and converting the radiation-grafted carboxyl groups in amino groups by a chemical reaction in mild conditions (see paragraph 8.5).

Nonetheless, a few amino-functionalized nanogels variants with controlled particles size ($D_n=35-60$ nm; PDI=0.2-0.3) have been generated, by keeping APMAM and PVP concentration low and by selecting proper irradiation conditions.

Moreover, these amino-functionalized nanogels have been proved not to be cytotoxic and they showed good affinity for cells. Indeed, cellular-internalization experiments showed a significant uptake of nanogels by cells, probably via an endocytotic pathway. It can be recalled that similar results have been obtained for the amino-functionalized PVP NGs produced via chemical radical polymerization in inverse microemulsion (see chapter 4).

7 Carboxyl-functionalized e-beam crosslinked nanogels

In chapter 6, it has been shown that biocompatible, “as borne” sterile, *functionalized* micro- and nanogels can be produced with high yields, by simultaneous polymer crosslinking and monomer grafting induced by pulsed e-beam irradiation. However, controlling the particle size distributions has been complicated by the opposite charges of PVP nanoparticles and monomer. In order to overcome this issue, PVP has been irradiated in the presence of an anionic acrylic monomer, precisely acrylic acid (AA). The carboxyl groups of AA, if grafted onto PVP nanogels, can be directly either used for bioconjugation purposes or converted first into amino groups if this functionality is specifically required, as it will be shown in chapter 8. In particular, PVP aqueous solutions in presence of acrylic acid have been irradiated at a relatively low dose per pulse (13 Gy/pulse), high dose-rate (average dose-rate 13,000 Gy/h) and at the integrated dose of 40 kGy, using Elektronika 10/10. Also the carboxyl-functionalized PVP nanogels have been obtained with high yields (above 98 % wt) in all the conditions explored.

7.1 Physico-chemical properties of carboxyl-functionalized PVP-based nanogels

7.1.2. Influence of PVP concentration on carboxyl-functionalized NGs size

NGs mean hydrodynamic diameters and relative distribution widths are reported in Table 7.1. All base PVP systems have been already described in detail in chapter 5, but some of these systems have been also included here, as a reference.

A remarkable feature of these systems is that in the presence of AA NGs dimensional control has been always achieved; a variety of carboxyl-functionalized NGs have been generated by varying the concentration of polymer in solution. More in detail, with the exception of the base PVP systems at the highest concentrations (0.25 and 0.5 wt%), the hydrodynamic size of all NGs is smaller than that of non-irradiated polymer coils. All carboxyl-functionalized PVP NGs show smaller hydrodynamic diameters than the corresponding base NGs. This behavior can be

attributed to the occurrence of acrylic acid-mediated intra-molecular crosslinking. Particle size distributions are monomodal and size variability is about 30% for all systems.

7.1.2. Influence of PVP concentration on carboxyl-functionalized NGs molecular weight

In Table 7.1 the refractive index increments and weight average molecular weight of the various systems are also reported. NGs molecular weights have been estimated from SLS measurements through Zimm Plot analysis and calculated using the dn/dc values reported in Table 7.1. The gyration radius cannot be estimated using multi-angle static light scattering because the radii of these nanoparticles are significantly smaller than the laser wavelength.¹⁶² All NGs show an increase in molecular weight with respect to that of the linear PVP and this observed increase is more pronounced for the most concentrated systems. Even in presence of acrylic acid, PVP mainly undergoes crosslinking, with inter-molecular crosslinking occurring to some extent although PVP concentration is below the critical chain overlap concentration. This effect has been already observed for the base PVP NGs (see paragraph 5.1). When PVP is irradiated in the presence of acrylic acid, the increase in molecular weight with respect to the linear polymer is less pronounced, suggesting a competition between acrylic acid grafting and inter-molecular crosslinking. In principle, monomer homopolymerization cannot be ruled out. However, irradiation is performed here at a pH higher than the AA pKa and the irradiated systems are diluted in monomer ($\approx 10^{-4}$ M), therefore homopolymerization of acrylic acid is not particularly probable (see paragraph 2.4.3) and AA radicals should preferentially graft to the crosslinked PVP nanoparticles, acting as soft-template. For PVP at 0.25 wt %, the effect of two different acrylic acid concentrations on NGs properties has been investigated; the two systems show similar values of molecular weight.

System	dn/dc		MW (MDa)		D_h (nm)	
	Mean	Width	Mean	Width	Mean	Width
Linear PVP	0.1805	0.0017	0.41	0.015	40	16
P*0.1	0.2127	0.00183	0.73	0.11	34	10
P*0.1 AA 50	0.1805	0.0016	0.65	0.07	14	5
P*0.25	0.1888	0.0046	2.3	0.024	50	14
P*0.25 AA 50	0.1866	0.0021	0.8	0.025	26	10
P* 0.25 AA 25	0.1873	0.0017	0.78	0.056	31	10
P*0.5	0.225	0.0019	7.5	0.34	150	45.7
P*(0.5) AA 50	0.1766	0.0065	4.5	0.24	40	16.4

Table 7.1. dn/dc , weight average molecular weight of the polymer (MW) from SLS, mean hydrodynamic diameter (D_h) from DLS and their relative distribution widths for linear PVP and NGs.

Gel filtration chromatography has been carried out to resolve the molecular weight distributions of the investigated systems. Chromatograms are reported in Figure 7.1a-d. The lack of polymeric standards with topological features similar to these nanogels impaired any meaningful determination of molecular weight distribution curves. Notwithstanding that, the elution curves for the various systems give a better picture of the molecular properties of the nanogels and some hints on their generation. At first, it can be noticed that the relative positioning of NGs chromatograms is in accordance with the molecular weight trends from SLS. It is quite remarkable that all irradiated systems show much narrower distributions than that of linear PVP (see Fig 7.1a), especially when NGs are formed at low polymer concentration (Fig 7.1a-b). It appears that the low molecular weight fractions mainly undergo intermolecular crosslinking, while the higher molecular weight fractions mainly undergo intra-molecular crosslinking. This is not surprising since radicals formed on smaller yet different chains have higher translational mobility, therefore

they have more chances to encounter each others and bind covalently. Conversely, larger macromolecules are more hindered in their translational motion and more likely to experience the simultaneous formation of many radical sites on the same chain, recombining intra-molecularly. When the polymer concentration increases inter-molecular crosslinking can also involve larger macromolecules, since the average inter-chain distance becomes smaller. The presence of AA does not shift the distributions, but it mainly changes the relative proportions between the different fractions. The GFC measurements also support the substantial identity, in terms of molecular properties, of the two carboxyl-functionalized systems obtained for the PVP at 0.25 wt% (see Fig 7.1c).

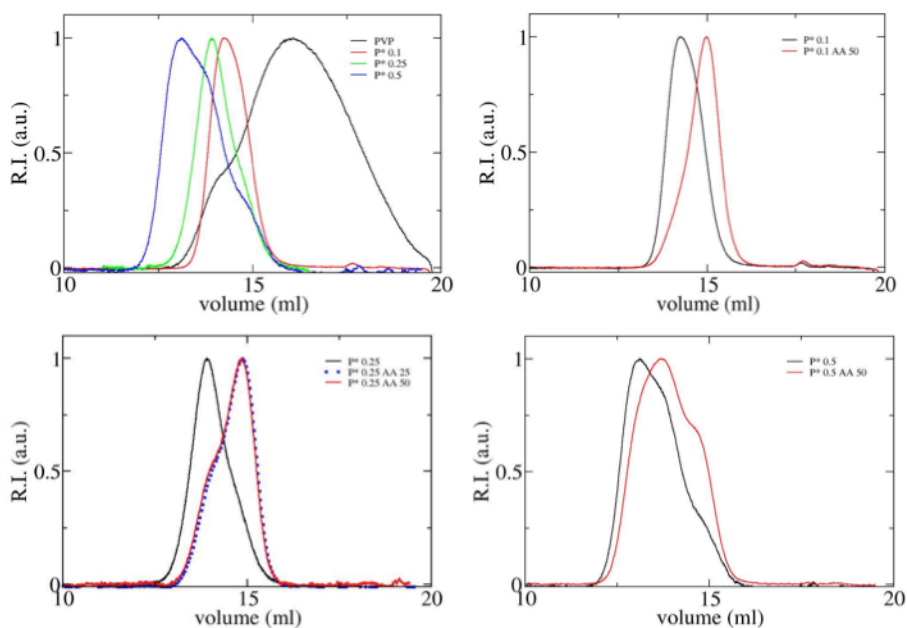


Figure 7.1a-d: Chromatograms from gel filtration chromatography for (a). linear PVP and base NGs; (b). P*0.1 and P*0.1AA50 NGs; (c). P*0.25, P*0.25AA50 and P*0.25AA25 NGs; (d). P*0.5 and P*0.5AA50 NGs.

7.1.3. Influence of PVP concentration on carboxyl-functionalized NGs surface charge density

NGs surface charge density has been evaluated by ζ -potential measurements and the results are reported in Table 7.2. In general, all irradiated nanogels present a distinct anionic character, owing to the chemical modifications of PVP induced by irradiation. In particular, for P*(0.1) the surface charge distribution is bimodal as well as for the linear polymer and the proportion between slightly charged and uncharged particles increases with respect to PVP (see Figure 5.16). P*0.25, P*0.5 and AA functionalized variants show monomodal distributions of charge densities. Moreover, both the AA-functionalized variants of P*0.25 and P*0.5 show a pronounced anionic character with zeta potential values of about $-40 \div -50$ mV, likely due to the contribution of acrylic acid's carboxyl groups grafted on the surface.

System	Mean (mV)	Width (mV)
P*(0.1)	-6; -20	5.54; 7.82
P*(0.1) AA 50	-21.9	8.40
P*(0.25)	-30.2	9.45
P*(0.25) AA 50	-40	9.26
P* (0.25) AA 25	-48.8	7.57
P*(0.5)	-10.8	3.8
P*(0.5) AA 50	-32	5.68

Table 7.2: Surface charge density and relative standard deviation for linear PVP, base and carboxyl-functionalized NGs.

7.2 Morphology of carboxyl-functionalized PVP-based nanogels

The topology of selected NGs systems has been analyzed by tapping mode AFM under water. Liquid-phase AFM has been preferred over air-AFM measurements. Indeed, it is fundamental to have information on nanogels morphology in watery environment. Furthermore, the size of these materials has been always determined through DLS measurements assuming that these particles have a “sphere-like” shape, on the account that no significant variability of size with the scattering angle has been observed. Nonetheless, a confirmation of the morphology in the liquid phase with a different analytical technique can further support the assumption made. Figure 7.2a-d refers to height profiles of APTES-mica substrate, P*0.1, P*0.5 and P*0.5 AA 50 NGs, respectively. The freshly cleaved bare mica in water has usually a roughness of ~180 pm, mostly due to liquid AFM noise. Conversely, the image of the APTES-mica shows some small aggregates (<2 nm) and a standard deviations in height of ~300 pm. The functionalization of mica has been successful and the substrate shows a uniform and smooth surface. The height of nanogels is higher than that of the functionalized substrates (~ 4 nm), as expected. Images of nanogels clearly show that they have a globular shape and confirm what already found through DLS measurements: P*0.1 and P*0.5AA50 nanogels are smaller than P*0.5 nanogels. In order to perform a quantitative particles size analysis using AFM images almost isolated nanoparticles are required. E-beam irradiated nanogels reveal a strong tendency to form a continuous deposit on the APTES-mica even if the concentration of the dispersions prepared for the deposition has been kept very low (5 ng/ml). This may be due to the strong interactions occurring between the APTES amino groups and the negative charges present on nanogels.

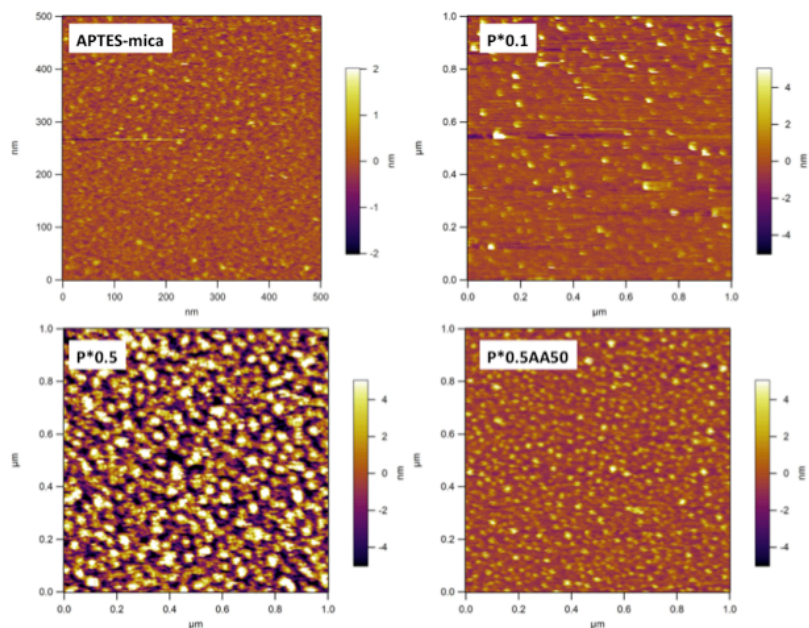


Figure 7.2a-d: Images from tapping mode AFM under water show height profiles for APTES-mica substrate, P*0.1, P*0.5 and P*0.5AA50 wt% systems. The color scale represents 2 nm for the height profile of a and 4 nm for the height profiles of b-c-d.

7.3 Structural properties of the bare carboxyl-functionalized PVP NGs

In Figure 7.3a-c FT-IR spectra for linear PVP, base and functionalized PVP NGs are shown. As already assessed in this work, PVP NGs have a slight different chemical structure with respect to the linear polymer and chemical modifications are the more pronounced the lower is the concentration of PVP.

The spectra of base systems have been already described (see chapter 5), so only the differences between base and carboxyl-functionalized NGs are here described. In particular, the spectra of P*0.1AA50 and P*0.5AA50 resemble the spectra of the parent base systems (see Fig 7.3 a e c). Conversely, slightly differences between the spectra of 0.25 wt% systems can be noticed. For P*0.25 NGs the carbonyl band enlarges mainly toward the lower wavenumbers at the expenses of its height. The spectrum of P*0.25AA25 system shows only a slight widening of the OH and carbonyl bands, while P*0.25AA50 NGs systems shows a substantial increase of

hydroxyl and carbonyl bands intensity. This result is in good agreement with the marked anionic character of 0.25 wt% functionalized systems.

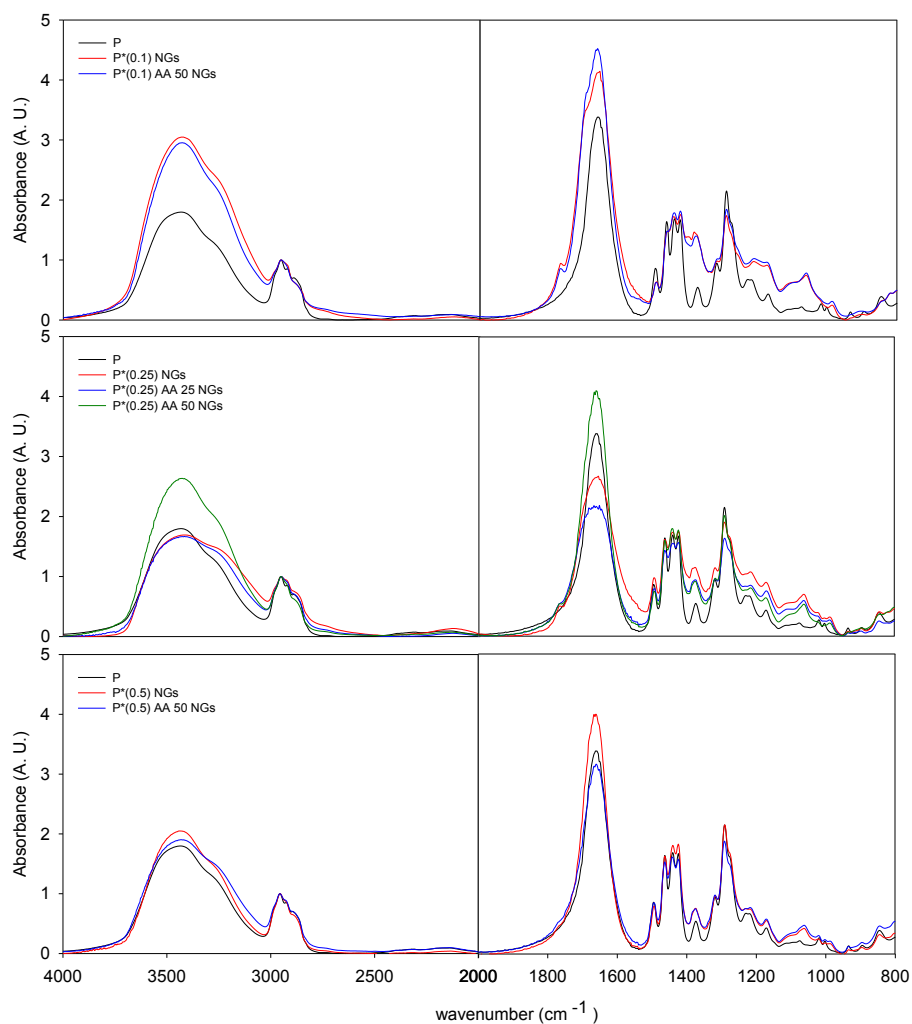


Figure 7.3a-c: Comparison of FT-IR spectra of the not irradiated PVP (P), base PVP nanogels and carboxyl-functionalized variants (a) P, P*0.1 and P*0.1AA50 NGs; (b) P, P*0.25, P*0.25 AA50 and P*0.1AA25 NGs; (c) P, P*0.5 and P*0.5AA50 NGs . All spectra have been normalized with respect to the peak at 2956 cm^{-1} .

7.4 Colloidal stability of NGs upon storage and as function of pH

DLS measurements have been carried out on NGs subjected to prolonged storage. In Figure 7.4 the decay curves of the scattered light intensity correlation, acquired after storage at 4°C for different times, are displayed for a representative functionalized system (P*0.5AA50). Even after prolonged storage (up to 18 months), no significant variation of nanoparticles size has been observed. Indeed, the small dimensions and the marked anionic character of NGs grant their excellent colloidal stability in the given conditions.

Hydrodynamic size and surface charge density have been also measured at different pH (2.5-10) and controlled ionic strength (1 mM). DLS data for two representative systems are shown in Figure 7.5.

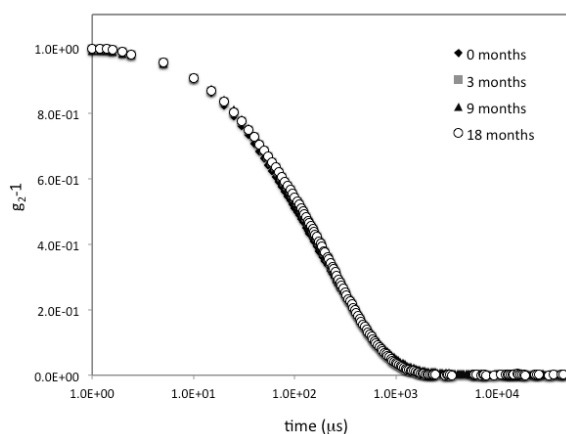


Figure 7.4: DLS autocorrelation function curves for P*0.5AA50, acquired after storage at 4°C for different times.

Hydrodynamic diameters and relative PDI are fairly invariant between pH 4 and 10. At pH<3.5 nanoparticles become slightly bigger due to the onset of aggregation phenomena. Below pH 2.5, aggregation leads to precipitation, thus impairing the measurement. This is because at pH<pKa for AA (pKa=4.75) a great proportion of NGs carboxyl groups are protonated and ζ -potential values become around 0 mV (see Figure 7.6). Therefore, the contribution from electrostatic repulsion to

stabilization ceases. At $\text{pH} > 2.5$, the ζ -potential values become negative and their absolute values increase with the pH due to progressive dissociation of carboxyl groups. Since the degree of dissociation of carboxyl groups does not affect NGs hydrodynamic size, but it does affect their surface charge density, we expect these groups to be preferentially located on the surface of NGs, as grafted arms, and/or to be attached to a tightly crosslinked core.

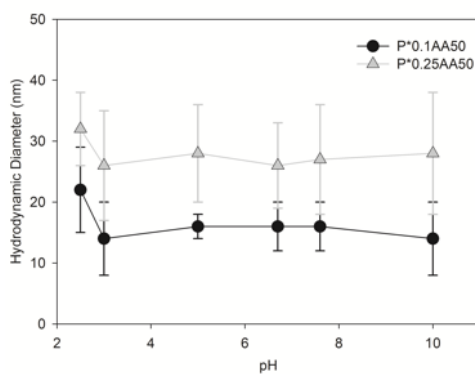


Figure 7.5 : Hydrodynamic diameter and relative standard deviation for P*0.1AA50 and P*0.25AA50 reported at the variance of pH and constant ionic strength (1mM).

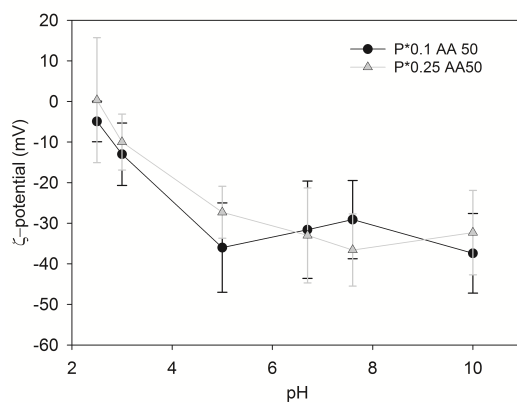


Figure 7.6: ζ -potential and relative standard deviation for P*0.1AA50 and P*0.25AA50 reported at the variance of pH and constant ionic strength (1mM).

7.5 Biological evaluations on carboxyl-functionalized NGs

Biological assays have been performed on cells treated with carboxyl-functionalized NGs to verify their biocompatibility. All gathered data suggest a good degree of biocompatibility of the produced NGs. Furthermore, NGs movements through the cell membrane and their internalization pattern at different times has been investigated. It has been found that after 3 h of incubation, nanogels start to internalize inside cells; after 6 h they are mainly localized in the perinuclear area of cells and after 24 h nanogels concentration inside cells decreases, probably due to excretion as waste products in the extracellular environment. For a more detailed description see Papers VII and VIII.

7.6 Conclusions

Radiation-induced PVP crosslinking and simultaneous monomer grafting has shown to be a viable synthetic approach for the generation of carboxyl-functionalized NGs with tailored properties. In particular, a variety of carboxyl-functionalized NGs with different hydrodynamic diameters varying from 10 to 50 nm with a narrow size distributions, colloidal stability in a wide pH range (3 - 9) and negative surface charge density (-30 mV) have been generated.

In vitro cell studies proved that the nanogels are biocompatible and able to quantitatively bypass cellular membrane, accumulating preferentially near the cellular nuclei during the first 6 hrs of incubation and being fully released within 24 hrs. A similar behavior has been observed for amino-functionalized variants produced with both the synthetic approaches. Indeed, in the absence of specific “biologically active” moieties, interactions with cells are mainly governed by nanoparticles size and surface charge density (see chapter 2), therefore it is not surprising that systems with comparable chemical structure and similar physico-chemical properties show similar behavior.

Carboxyl-functionalized NGs as well as amino-functionalized variants have been decorated with various ligands and this will be the subject of chapter 8.

8 PVP-based composite nanodevices for tumor-targeted delivery and imaging

Functionalized NGs have been derivatized with “model” (bio)molecules, such as fluorescent probes, targeting ligands, therapeutic and diagnostic agents.

All the conjugation reactions have been performed in aqueous solutions, at mild pH and temperature conditions, in order to preserve both NGs and (bio)molecules properties and activity. In particular, the conjugation protocols have been established using chemically/functionally more stable molecules, and then extended to biomacromolecules, which are more prone to denaturation and/or degradation. The use of ligands of different steric hindrance has enabled the assessment of the availability and accessibility of NGs reactive functional groups. Furthermore, it has been verified that each ligand conjugated to NGs has retained its specific function at biological level, so that it can appropriately interact with cells.

It is worth pointing out that this PhD dissertation has the intention of showing the potential and versatility of the generated nanocarriers without the ambition of proposing innovative “theranostic” approaches for the treatment of specific diseases.

8.1 Conjugation of fluorescent probes to functionalized PVP micro/nanogels.

Chemical conjugation of fluorescent probes to both amino-functionalized (P*-g-A) and carboxyl-functionalized (P*-g-AA) NGs has been attempted to generate NGs fluorescent variants for in vitro biological evaluations. Base-PVP nanogels (P*) have been also conjugated with the probes, as control systems. In principle it cannot be ruled out that probe physical adsorption to the nanoparticles may also occur in conjunction with its chemical attachment. Indeed, it has established that PVP macrogels produced through e-beam irradiation have hydrophobic pockets as a result of the crosslinking that favorably and also irreversibly, in some circumstances, house barely polar solutes present in water.¹⁵³

Fluorescein derivatives have been used for the purpose since they are important xanthene dyes widely used in the biosciences. In fact, they show large absorption in visible range and high quantum yield of fluorescence.¹⁰⁸

In particular, fluorescein isothiocyanate (FITC) has been conjugated to P*-g-A NGs using a pH=9.3 borax-based protocol, while aminofluorescein (AmFluor) has been conjugated to P*-g-AA NGs using a EDC-based protocol. The reaction mechanisms are reported in Figures 8.1 and 8.2 and their detailed descriptions are reported in paragraph 3.2.3. The success of conjugations has been assessed via both UV-visible absorption and emission spectroscopies.

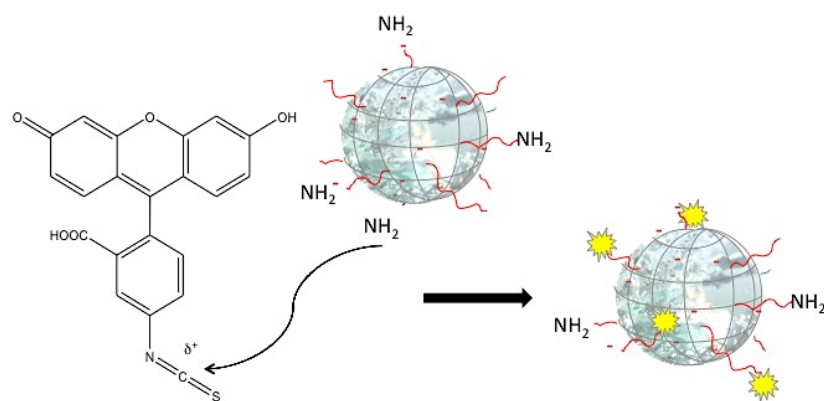


Figure 8.1: Scheme of a typical conjugation reaction between FITC and P*-g-A NGs via borax protocol.

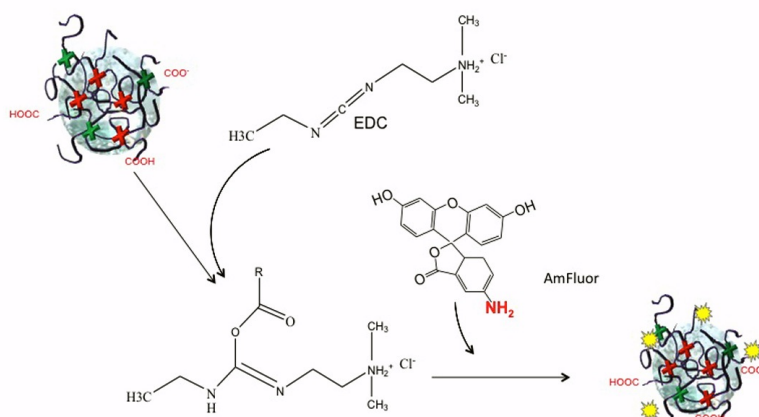


Figure 8.2: Scheme of a typical conjugation reaction between AmFluor and P*-g-AA NGs via EDC protocol.

8.1.1 P*-g-A fluorescent variants' properties

In Figure 8.3a the emission spectra of a representative fluorescent MGs (P*-g-A(50)^{FITC}) and NGs (P*-g-A(100)^{FITC}) are reported. FITC-conjugated base NGs (P*^{FITC}) and a representative bare NGs (P*-g-A) system are also shown. The bare NGs do not present any significant emission band when excited at 490 nm. The P*^{FITC} systems show a modest emission, while both the P*-g-A^{FITC} systems show intense emission peaks.

Figure 8.3b reports the normalized emissions of P*-g-A^{FITC}, P*^{FITC} and free probe. Normalization allows easier identification of shifts in λ_{peak} . It is evident that the emission band of a FITC-conjugated amino-grafted MG or NG is at all similar to that of the free probe, yet with a significant red shift (+5 nm) which confirms the formation of the thiourea bond.¹⁶³ Conversely, P*^{FITC} shows a peak at an intermediate position between that of the free and the bound probe and it may be likely caused by FITC physically entrapped in the crosslinked particles.

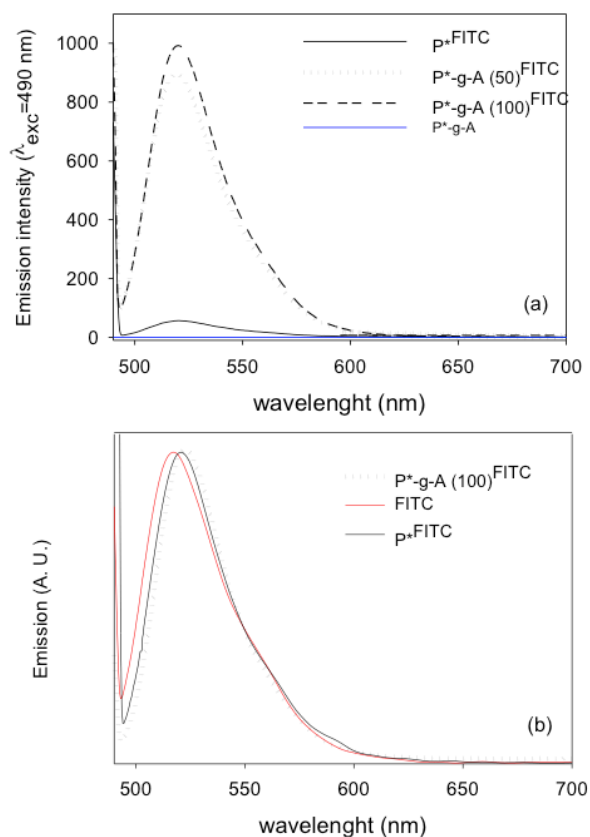


Figure 8.3a-b: UV-Vis emission spectroscopy of: (a) Non-conjugated amino-functionalized nanogels, two FITC-conjugated variants and corresponding FITC-conjugated base PVP nanogel (irradiation condition: E80); (b) Normalized emissions of a typical FITC-conjugated amino-grafted nanogels/microgel (P^*-g-A^{FITC}); FITC-conjugated base PVP nanogels (P^{*FITC}); free FITC aqueous solution (FITC).

The emission intensities at peak ($\lambda_{em}=520$ nm) for 1:100 and 1:50 P^*-g-A systems and corresponding base P^{*FITC} nanogels produced at the different irradiation conditions are reported in Table 8.1. In general, the emission intensity of the $P^*-g-A^{FITC}(100)$ is higher than that of $P^*-g-A^{FITC}(50)$, despite of the twofold increase of APMAM moles in the formulation for the latter. $P^*-g-A(100)$ systems are genuinely

nanogels, while P*-g-A(50) systems are microgels in all investigated irradiation conditions (see paragraph 6.1.2). If the formation of bigger particles is involving APMAM as a coupling agent, a relevant amount of the amino groups may not be accessible to FITC and/or may have been depleted by the establishment of strong interactions with PVP.

SYSTEM	Emission intensity at peak (A.U.)
P* E40	55
P*-g-A (100) E40	450
P*-g-A(50) E40	202
P* E80	50
P*-g-A (100) E80	990
P*-g-A(50) E80	890
P* L80	60
P*-g-A (100) L80	446
P*-g-A(50) L80	105

Table 8.1: Emission intensity at λ_{peak} for the FITC conjugated systems.

Absorption spectra for a representative P*-g-A conjugated systems and free FITC solutions are reported in Figure 8.4. As well as in the emission spectra, the maximum absorption peak of the conjugated is shifted with respect to the free FITC solution.

Furthermore, ζ -potential measurements carried out on all the P*-g-A^{FITC} conjugated systems show narrower charge distributions with respect to those of bar NGs, centered on neutrality, that suggest a modification of the surface charge distribution. In Figures 8.5 and 8.6 the ζ -potential distribution curves for a representative bare system (P*-g-A(50) E80) and for its FITC-conjugated (P*-g-

A(50)^{FITC} E80) are reported. All the evidences collected confirm the success of conjugation.

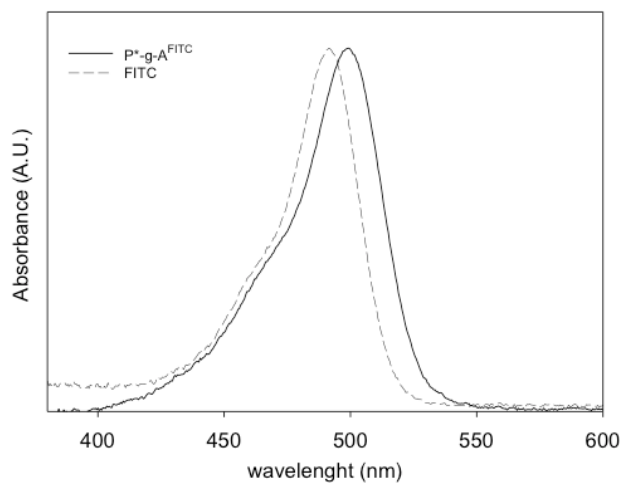


Figure 8.4: Normalized absorption spectra for a typical conjugated NG system and the free FITC solution.

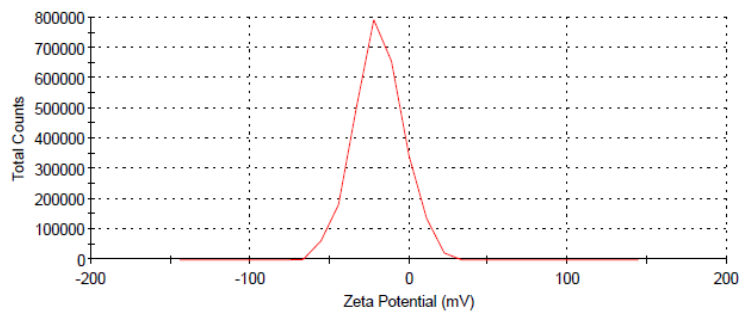


Figure 8.5: ζ -potential curves for functionalized nanogels (P*-g-A(50) E80) in water.

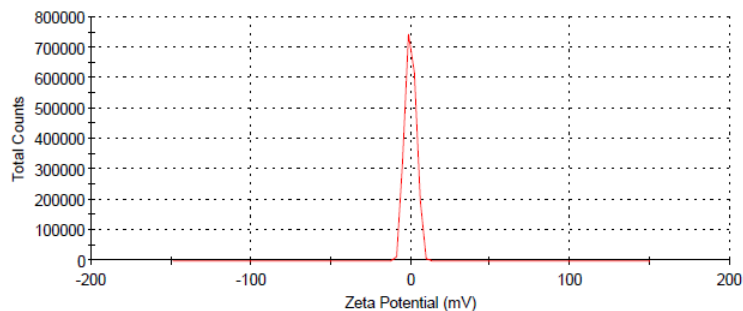


Figure 8.6: ζ -potential curves for conjugated nanogels (P^* -g-A(50)^{FITC} E80) in water.

Since both the emission and absorption spectra of the conjugated systems show a red-shift, it has been not possible to use the free-FITC molar extinction coefficient for the determination of the degree of conjugation.

8.1.2 P^* -g-AA fluorescent variants properties

Normalized absorption spectra for a representative P^* -g-AA system conjugated with AmFluor, a free AmFluor solution and the parent bare carboxyl-nanogels (P^* -g-AA) are reported in Figure 8.7. NGs do not show any absorption band in the wavelength range where AmFluor strongly absorbs. Conversely, the AmFluor-loaded system shows the characteristic absorption band of AmFluor, yet significantly red-shifted (+5 nm). These red-shift is similar to that already observed for P^* -g-A NGs conjugated to FITC.

The estimation of the amount of probe linked to nanogels is complicated by the chemical structure of fluorescein and its derivatives. In particular, fluorescein can exist in different structure forms depending on the surrounded environment. Each of these forms show different photophysical properties and give varied absorption spectra, fluorescence spectra, quantum yields and lifetimes, responding to the various pH^{164,165}, hydrogen-bonding power^{166,167} and polarity¹⁶⁸ of the environment. Some published studies show that the shape and intensity of the absorption and emission spectra of fluorescein change in the presence of micelles and that the nature of the micelles determines the extent of these changes.

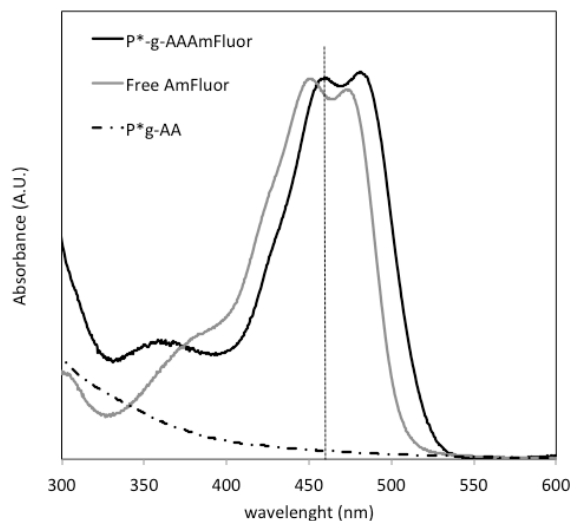


Figure 8.7: Normalized absorption spectra for a typical conjugated NG system, the free FITC solution and the bare P*-g-AA NGs.

It has already mentioned that crosslinked PVP has an inherent “amphiphilic” nature in the way that it offers hydrophobic pockets that can preferentially host hydrophobic molecules. It would be expected that the photo-physical properties of the probe hosted in the nanogels’ interiors have been somehow affected by their surroundings. In order to better understand the nature of the interactions between probe and nanoparticles and assess whether PVP-based nanogels deplete or enhance the absorption and/or emission properties of the probes, uptake and release experiments with AmFluor and carboxyl-functionalized NGs have been performed.

The absorption spectra of a typical “free” AmFluor solution and a typical solution of “free” AmFluor and carboxyl-functionalized NGs (P*-g-AA) are shown in Figure 8.8. Moreover, calibration curves have been built up both for the free probe in solution and for the free probe with nanogels. Calibration curves for both systems are reported in Figure 8.9. It can be noticed that, in the presence of nanogels, the absorption bands of the probe are partially quenched. It appears that the physical interactions between nanoparticles and probe reduce the intensity of the peaks, as these interactions make the ground state of the probe more stable than the excited form, without modifying their shape and position.

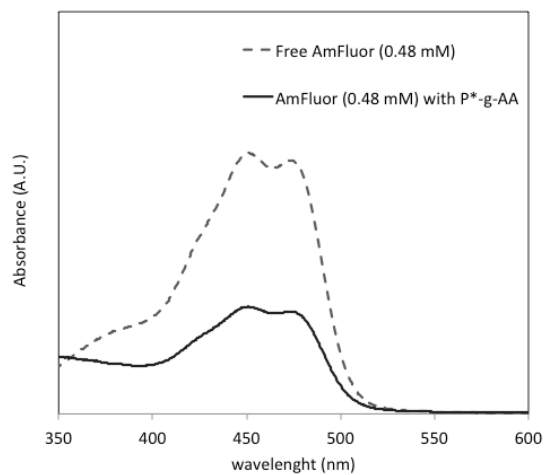


Figure 8.8: Absorption spectra of the free AmFluor (0.48 mM) in solution in the presence or not of carboxyl-functionalized NGs.

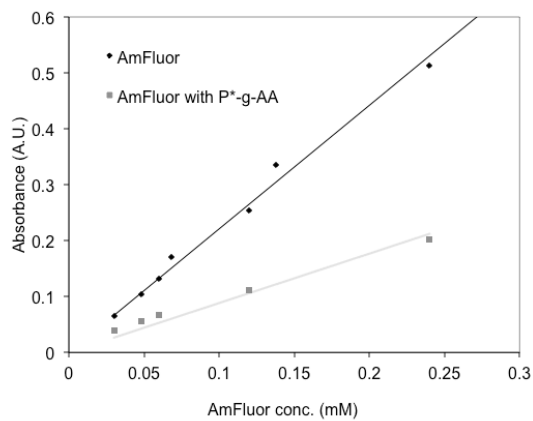


Figure 8.9: UV-vis calibration curves ($\lambda = 450$ nm) for free AmFluor in solution in the presence or not of carboxyl-functionalized NGs.

In order to assess the strength of these interactions, the release of the free probe out of a dialysis membrane both in the presence or not of P*-g-AA has been studied.

In Figure 8.10 the release profiles are reported. The two profiles are initially almost coincident, while they slightly diverge after 24 h. Approximately 50% of the total AmFluor diffuses out within the first 24 h. Then, the release rate of AmFluor in the presence of the nanoparticles becomes slower with respect to release rate of the free probe when it stands alone. In the long term (150 h) almost all AmFluor is released by both systems. It can be concluded that within the first 24 h it is mainly the non-interacting probe that diffuses out. Then, also the remaining part is released, thus suggesting that the strength of the interactions occurring between NGs and probe are not particularly strong.

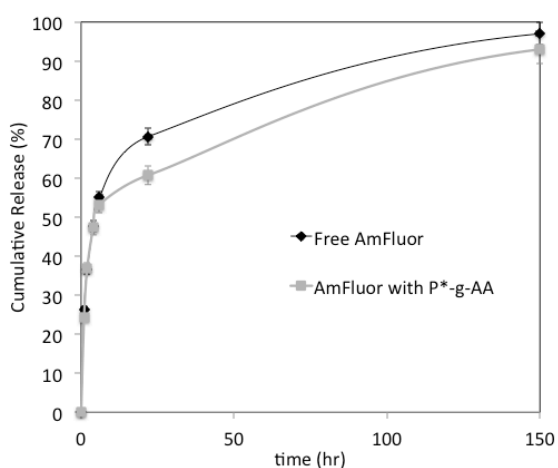


Figure 8.10: Release of AmFluor out of a dialysis membrane in the presence or not of carboxyl-functionalized NGs.

8.1.3 Estimation of the conjugation degree

The amount of probe linked to the nanogels could be estimated by performing a “detachment” reaction. In particular, by changing the pH of the solution the bond between the probe and the nanoparticles can be broken. The free probe can be then separated by filtration from the nanoparticles and quantified via UV-vis absorption measurements. If the probe is completely detached from the nanoparticles, the

quantification is easy. If only a portion of the probe is detached and nanogels recovered after the separation still present an absorbance peak in the same position of the one shown by the conjugated nanogels, the quantification becomes more complicated. In this latter case, a molar extinction coefficient for the “bound probe” can be calculated by a molar mass balance, as follows:

$$K_x = K_{probe} \frac{Abs_1 V_1 - Abs_2 V_2}{Abs_3 V_3} \quad \text{eq. 8.1}$$

where, K_x is the molar extinction coefficient of bound probe, K_{probe} is the molar extinction coefficient of the free probe, as determined by an experimental calibration curve made using probe solution at different concentrations, Abs_i is the maximum absorbance value for the i -th (1,2,3) systems, V_i is the volume of the i -th (1,2,3) solution read at a spectrofluorimeter, 1 refers to conjugated nanogel’s dispersion, 2 to dispersions of nanogels recovered from the filter and 3 to the solution of detached probe.

This approach works very well for FITC, since the thiourea bond can be easily broken by raising the pH up to 12. Conversely, it does not work for AmFluor, since the bond formed between the probe and the nanogels is an amide bond and it is very stable in a wide pHs range (3-12).

FITC detachment has been performed for P*-g-A(100)^{FITC} and P*-g-A(50)^{FITC} E80. A molar extinction coefficient for “bound FITC” has been experimentally determined using the approach described above and the moles of available amino-groups estimated ($4.4 \cdot 10^{-4}$ and $1.3 \cdot 10^{-4}$ mM) represent about 0.5% and 0.3% of the moles of APMAM charged in the feed for P*-g-A(100) and P*-g-A(50), respectively.

DLS analyses have been carried out both on the P*-g-A^{FITC} and P*-g-AA^{AmFluor} conjugated systems and they have shown that the conjugation reaction with the probe does not significantly affect the hydrodynamic size of the NGs. As exemplification, in Figure 8.11 the normalized decay curves for P*0.5AA50 and P*0.5AA50^{AmFluor} are reported. The decay curve for P*0.5AA50 NGs treated similarly to the P*0.5AA50^{AmFluor}, except for the absence of AmFluor in the reaction

system, is also reported, as a “negative control” system. The conjugated system is only slightly bigger than the bare NG system, while the control system shows almost the same decay curve of the bare NGs’ one. Z-potential measurements have been also performed and it has been found that the conjugation reaction with the probe affects NGs anionic surface charge densities, that become smaller after the conjugation (see Figure 8.6).

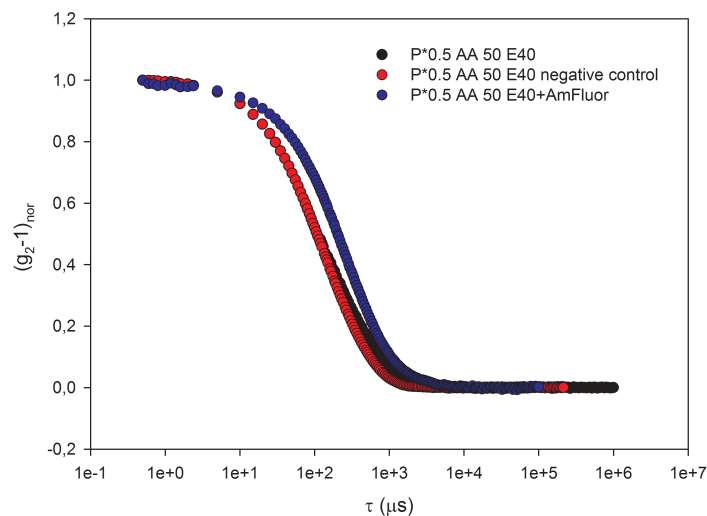


Figure 8.11: DLS autocorrelation function curves for P*0.5AA50 NGs, P*0.5AA50 NGs negative control and P*0.5AA50 NGs+AmFluor.

NGs fluorescent variants have been used for in vitro localization studies. In particular, P*-g-A 100^{FITC} and P*0.5AA50^{AmFluor} show ability to bypass the cell membranes and concentrate in the cytoplasm compartments, particularly in the perinuclear area. Moreover, after 24 h they are released by the cells in the culture medium. For further details, see Paper VII and VIII.

8.2 Folic Acid as model targeting moiety

Carboxyl-functionalized NGs have been decorated using folic acid as targeting agent. The conjugation has been performed in two steps using an EDC/Sulfo-NHS

protocol. In particular, in the first step, the carboxyl groups of NGs have been activated using both EDC and Sulfo-NHS, while in the second step a nucleophilic substitution reaction operated by the amino group of folic acid takes place. The reaction mechanism is shown in Figure 8.12 and a detailed description is reported in paragraph 3.2.2.

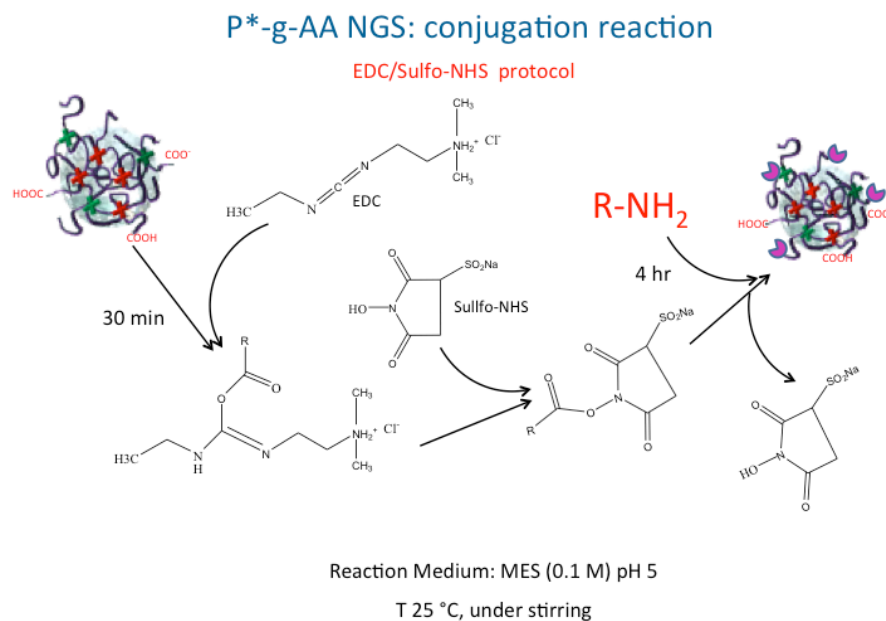


Figure 8.12: Scheme of a typical conjugation reaction between AmFluor and P*-g-AA NGS via EDC/Sulfo-NHS protocol. R-NH₂ represents folic acid.

8.2.1 Estimation of the conjugation degree for NGS folate-variants

Folic acid has both carboxyl and amino groups in its structure, thus homopolymerization may occur. In order to understand if homopolymerization has occurred up to a significant extent, purification of the conjugates through extensive dialysis has been carried out using two molecular weight cutoff (MWCO) dialysis tubes (12 kDa and 100 kDa). The amount of folic acid conjugated to NGS has been then quantified by UV-vis absorption measurements. In Figure 8.13, the absorption

spectra of P*0.25AA50 conjugated with folic acid after purification with either of the two MWCO membranes are reported. Folic acid and bare NGs absorption spectra are also shown, as reference. It can be noticed that P*-g-AA NGs do not absorb in correspondence of the folic acid absorption peaks ($\lambda=280$ nm and $\lambda=340$ nm). Conversely, the spectrum of the conjugated system dialyzed using a 12 kDa MWCO shows both the two folic acid peaks, yet blue-shifted (-5 nm). The spectrum of the same conjugate, dialyzed using a 100 kDa MWCO, shows only the peak at $\lambda=280$ nm, that is also blue-shifted. Dialysis using 100 kDa MWCO reduces also the intensity of the peak at $\lambda=280$ nm of about the 90%. This evidence confirms that folic acid undergoes homopolymerization. Similar effect has been observed also for other folic acid-conjugated systems. Therefore, all the results presented in the following will refer to systems purified with a 100 kDa MWCO.

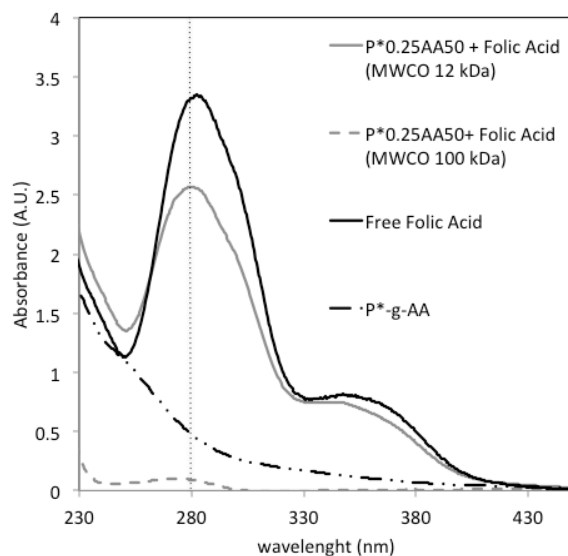


Figure 8.13: Absorption spectra of P*0.25AA50+FolicAcid purified using MWCO 12 kDa and 100 kDa membranes, free folic acid and the bare NGs (P*-g-AA).

In Table 8.2 the degree of conjugation of folic acid for three different NG systems, as determined through UV-vis measurements, is reported. P*0.1AA50 and P*0.25AA50 systems show similar moles of ligands per NG, while the P*0.5AA50

presents the highest molar ratio. However, all these systems have different hydrodynamic volumes, therefore in order to have an insight on their inherent conjugation propensity, the conjugation degree has been also expressed as weight ratio of ligand to NG. In these terms, the two most performing systems are P*0.1AA50 and P*0.5AA50, while the lowest efficiency of binding is observed for the 0.25 wt% system. It can be recalled that this latter system also showed the most pronounced anionic character (see paragraph 7.1.3), which may be considered responsible for the electrostatic repulsion toward folic acid (that is reacted in sodium salt form, see also paragraph 3.2.3) and, in turn, for the observed lower efficiency of binding.

System	FolAc/NG	FolAc/PVP (mg/mg)
P*0.1AA50	15.5	10.14
P*0.25AA50	12	4.76
P*0.5AA50	88	8.55

Table 8.2: Degree of conjugation for folic acid expressed as number of ligand molecules per NG (left) and weight ratio between ligand and NGs (right).

8.2.2 Localization of NGs folate variants in cell cultures

Localization studies in cell cultures have been performed through confocal microscopy in order to prove the targeting ability of folic acid decorated NGs. Since folic acid does not show good emission properties, P*-g-AA NGs have been first labeled with AmFluor, then conjugated with folic acid. This study has been performed using P*0.5AA50 NGs. AmFluor has been conjugated to the nanogels using the same protocol described in the previous paragraph (paragraph 8.1), but loaded at a lower amount in order to leave some free carboxyl groups for the subsequent conjugation step with folic acid. The success of conjugations has been verified testing the absorption properties of the conjugates after each reactive step.

In Figure 8.14 the full absorption spectra of P*0.5AA50+AmFluor and P*0.5AA50+AmFluor+Folic systems are reported.

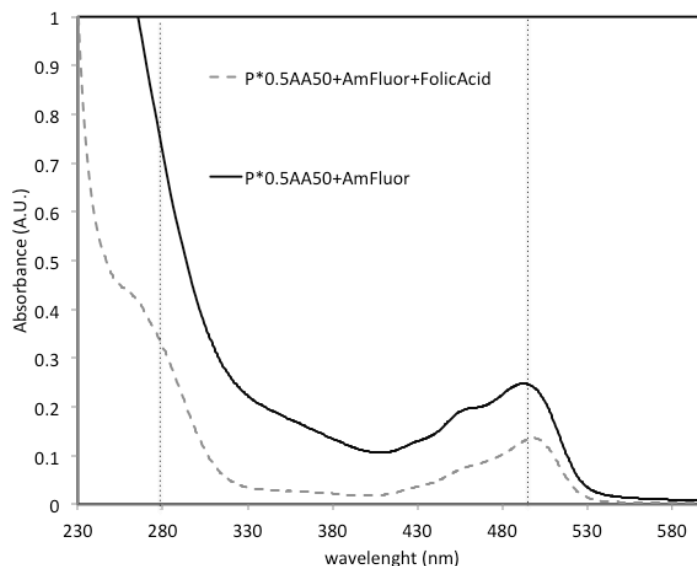


Figure 8.14: Full absorption spectra of P*0.5AA50+AmFluor and P*0.5AA50+AmFluor+Folic systems

In Figure 8.15, the absorption spectra of P*0.5AA50+AmFluor and P*0.5AA50+AmFluor+Folic systems in the 350-600 nm wavelength range are reported. Bare NGs (P*0.5AA50) and free AmFluor spectra are also shown. Both P*0.5AA50+AmFluor+FolicAcid and P*0.5AA50+AmFluor systems show the characteristic AmFluor maximum absorption peak at about 490 nm. For both conjugate systems the peak is shifted towards higher wavelengths with respect to the one of the free probe and this shift is more pronounced for P*0.5AA50+AmFluor+FolicAcid. The intensity of the peak for P*0.5AA50+AmFluor+Folic is lower than that of P*0.5AA50+AmFluor, due to the dilution of the sample during the second conjugation step.

In Figure 8.16 the absorption spectra of P*0.5AA50+AmFluor+FolicAcid, bare NGs and free folic acid in the 230-480 nm wavelength range are reported. P*0.5AA50+AmFluor+FolicAcid spectrum shows both folic acid peaks, but slightly shifted.

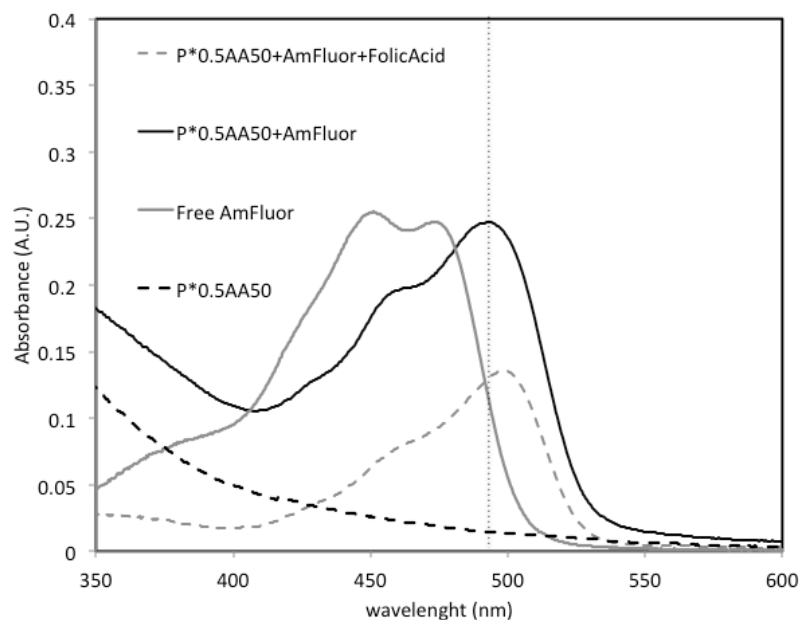


Figure 8.15: Absorption spectra of P*0.5AA50+AmFluor+FolicAcid, P*0.5AA50+AmFluor, free AmFluor and bare NGs (P*0.5AA50).

The intensity of the first peak ($\lambda=340$ nm) is very low and it shows only as a shoulder of the first peak, since in this range of wavelengths (200-350 nm) all the spectra are affected by the contribution from light scattering to the total absorption (see spectrum of bare NGs in Figure 8.13). The estimated degree of conjugation for folic acid, expressed as molecules of folic acid per NGs, is 50. The presence of the AmFluor on the same nanoparticle reduces the number of available carboxyl groups for the folic acid.

NGs dimensions after each conjugation step have been checked via DLS measurements and it has been found that the hydrodynamic size is not affected by the conjugation. As mentioned above, P*0.5AA50+AmFluor+FolicAcid NGs have been used for preliminary localization studies. These studies have been performed in collaboration with Prof. Ghersi's group, Dipartimento di Scienze e Tecnologie Biologiche, Chimiche e Farmaceutiche (STEBICEF), Università di Palermo. In

particular, Hela cells and NIH 3T3 cells have been co-cultured. It is well known that Hela are tumoral cells that overexpress the receptors for folic acid. Conversely, NIH3T3 cells do not express the receptors for folic acid.

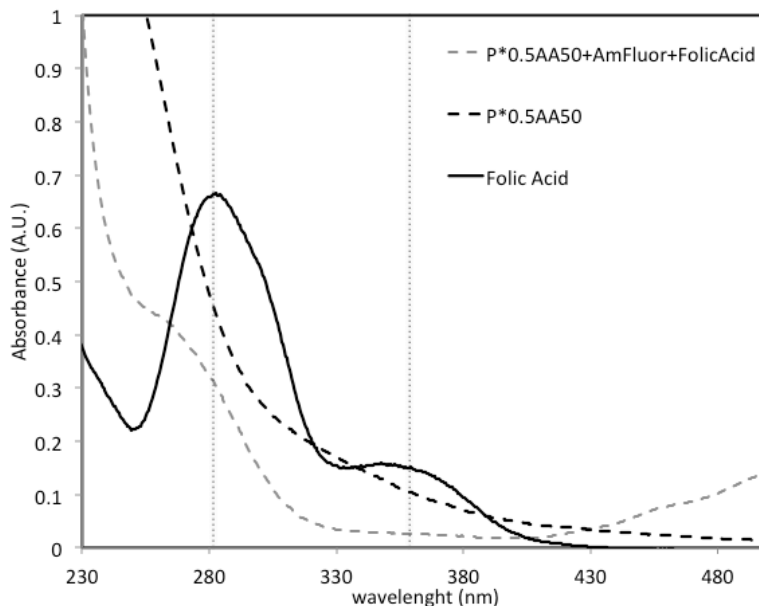


Figure 8.16: Absorption spectra of P*0.5AA50+AmFluor+FolicAcid, free folic acid and the bare NGs (P*0.5AA50).

Cells have been incubated for different times with a folate-NG derivative introduced with the culture medium. In Figure 8.17 the images acquired using the confocal microscopy at three different incubation times are reported. In the figure, the red color refers to the cells, while the green color refers to folate-NG variant that is also labeled with AmFluor. It can be noticed that the internalization of NGs is faster in Hela cells than in NIH 3T3. After 30 min, NGs are localized around the Hela cells and after 2 h they are fully internalized. This preliminary study shows that folic acid can regulate the uptake of NGs by the cells through a ligand-receptor mechanism. Furthermore, in the presence of the targeting moiety the internalization is faster than in its absence. Indeed, localization studies performed using the same

bare NGs labeled with AmFluor have shown that internalization occurs in 6 hr (see paper VII). All the generated NGs are internalized by cells, also in the absence of the targeting moiety, but when the uptake is not specific, this process appears to be significantly slower.

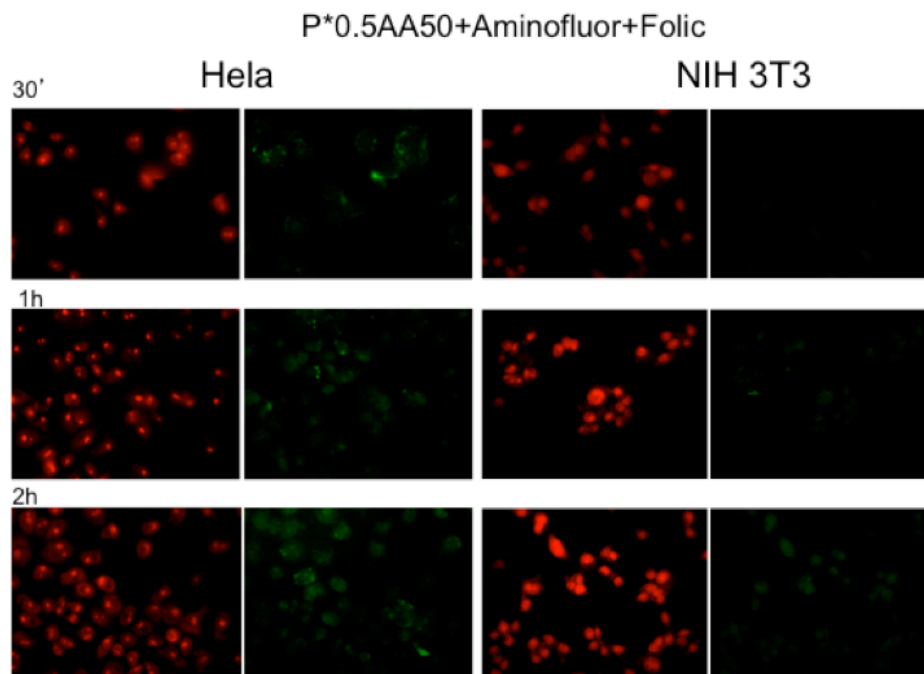


Figure 8.17: Localization studies in a co-culture of Hela and NIH 3T3 cells. The red color refers to the cells and the green color to P*0.5AA50+AmFluor+FolicAcid. The images have been taken at the confocal microscopy after different incubation times (30', 1h and 2 hr).

8.3 Conjugation of “model” biomolecules for the generation of biohybrid nanogels

“Model” larger biomolecules such as bovine serum albumin (BSA), an oligonucleotide and two different antibodies have been conjugated to the nanoparticles in order to generate biohybrid nanogels.

8.3.1 BSA as a model protein

In particular, BSA has been conjugated to P*-g-A 100 E80 nanogels using a borax-based protocol (see paragraph 8.1). Absorption spectra reported in Figure 8.18 show that the BSA-conjugated NG spectrum has a peak at 280 nm, which coincides to the one of free BSA. No absorption peak has been observed for the not-conjugated system. In consideration of the dimensions of BSA, it would be expected that the protein is preferentially located on the nanoparticles' surface. The interaction between BSA and nanoparticles is fairly strong as it survives upon extensive dialysis and repeated washings. In particular, it has been estimated that the weight percentage of retained BSA per polymer is about 30.

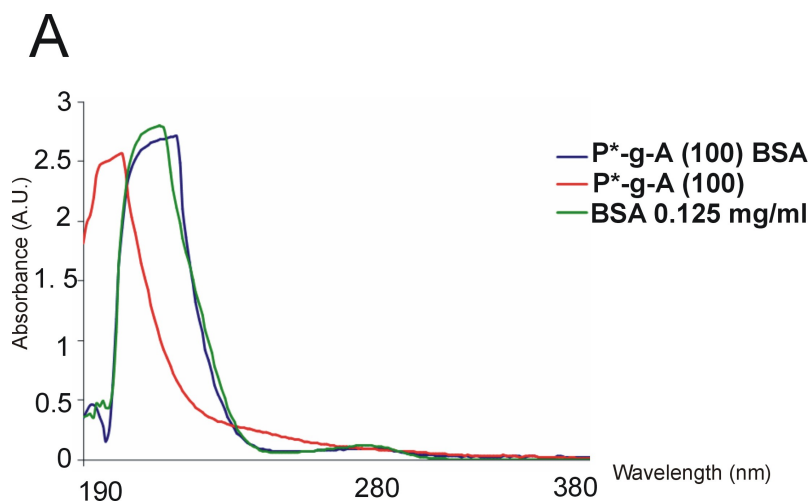


Figure 8.18. UV-Vis absorption spectra of BSA-conjugated P*-g-A(100) system; not conjugated P*-g-A(100) system as control; free BSA as reference.

8.3.2 C37 as a model antibody

P*-g-A NGs have been also conjugated with two antibodies, C37^{TRITC} and Anti- $\alpha_v\beta_3$ integrin. In particular, C37 has been used as a model antibody in order to develop a suitable conjugation protocol and perform preliminary co-localization studies, as it will be explained in the following. C37 is labeled with a red-emissive probe, tetramethylrhodamine-5-(and-6)-isothiocyanate (TRITC). A EDC/Sulfo-NHs protocol has been used for the conjugation to this antibody to the nanoparticles (see reaction scheme in Figure 8.12). A detailed description of the protocol is reported in paragraph 3.2.2.

The success of the conjugation has been assessed by UV-vis emission measurements. In particular, the emission spectrum ($\lambda_{exc}=280$ nm) of P*-g-A-C37^{TRITC}, P*-g-A and C37^{TRITC} are shown in Figure 8.19. It can be noticed that the bare nanogels do not show any emission if excited at 280 nm, while the conjugated ones shows an emission peak that it is similar to the emission peak of C37^{TRITC}, although somewhat blue-shifted

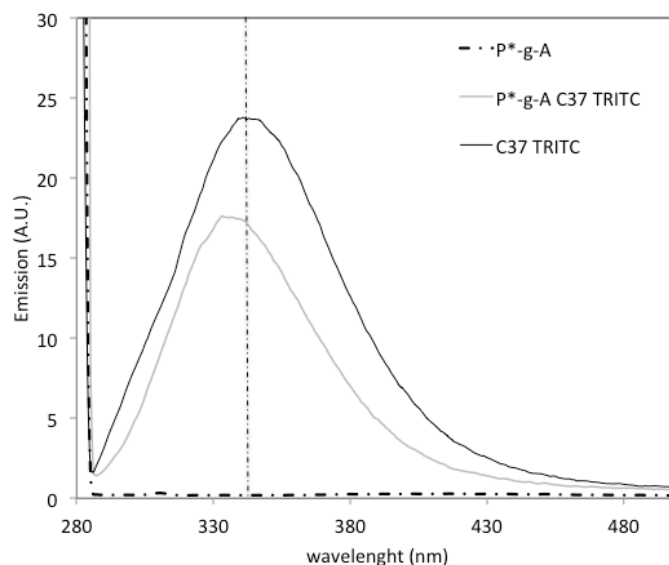


Figure 8.19: Emission spectra of non-conjugated NGs (P*-g-A), NGs conjugated with C37^{TRITC} (P*-g-AC37^{TRITC}) and the free antibody (C37^{TRITC}) in solution ($\lambda_{exc}=280$ nm).

The quantification of the antibody linked to the NGs has been performed thanks to the presence of TRITC ($\lambda_{exc}=550$ nm, $\lambda_{em}=570$ nm), since its emission is not affected by the conjugation. This is confirmed by the emission spectra shown in Figure 8.20. The conjugated system shows a maximum emission peak in the same position of the free $C37^{TRITC}$. It has been estimated that the concentration of $C37^{TRITC}$ in the conjugated system is 0.052 $\mu\text{g/ml}$.

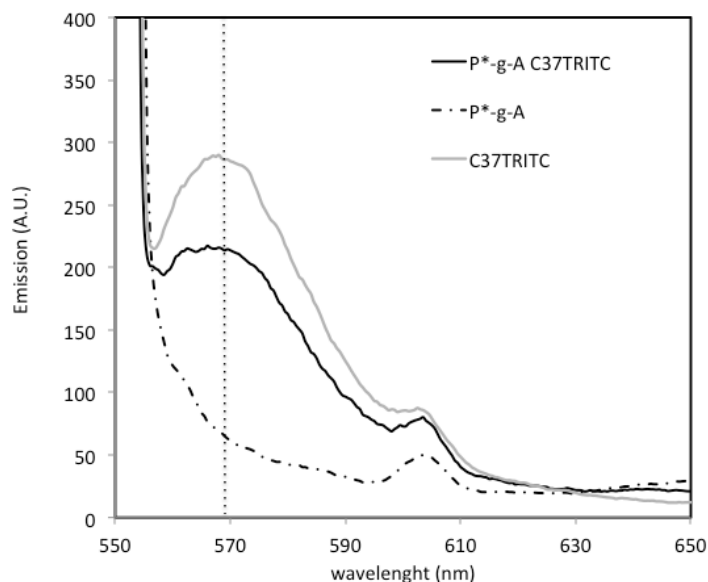


Figure 8.20: Emission spectra of NGs conjugated with $C37^{TRITC}$ ($P^*-g-AC37^{TRITC}$), non-conjugated NGs (P^*-g-A), and the free antibody ($C37^{TRITC}$) in solution ($\lambda_{exc}=550$ nm)

After conjugation and purification, the dispersion of conjugated NGs looks perfectly transparent; therefore, we do not expect any significant dimensional modification of the nanoparticles. Unfortunately, it has not been possible to determine the actual hydrodynamic size of the conjugated system, since the fluorescence of the TRITC impairs DLS measurements.

After the assessment of the success of conjugation, $P^*-g-A C37^{TRITC}$ has been used as a model system for *in vitro* localization studies, in order to verify if the presence

of the antibody enhances the uptake of nanogels by cells, as already observed for the folate-NG derivatives. In particular, for these studies P*-g-A NGs have been first labeled with a green-emissive probe (FITC) and then conjugated with the red-emissive C37^{TRITC}. The conjugation protocol between P*-g-A NGs and FITC has been already described in the previous paragraph. For this particular experiment, a lower amount of FITC has been used for the conjugation to leave some available amino groups for the conjugation with the antibody. The success of both the conjugation reactions has been verified through UV-vis emission measurements. In particular, P*-g-A^{FITC}C37^{TRITC} NGs have been excited first at 490 nm and then at 550 and the estimated concentration of FITC and C37^{TRITC} in the conjugated system are 0.081 $\mu\text{g/ml}$ and 0.019 $\mu\text{g/ml}$ (see Fig. 8.21 and 8.22).

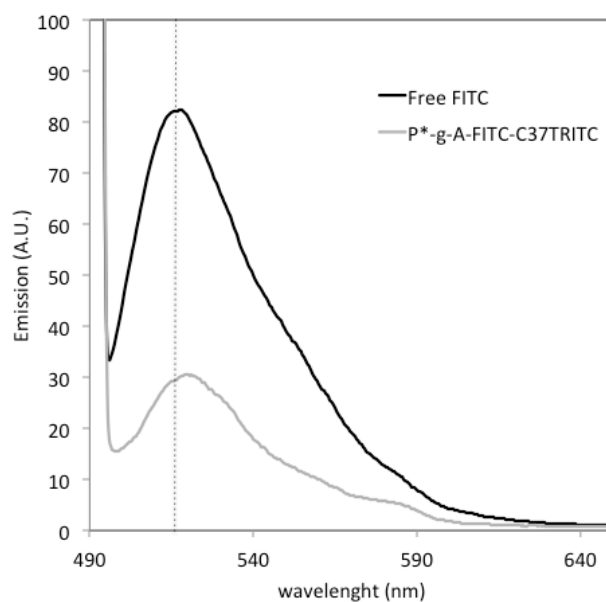


Figure 8.21: Emission spectra of free FITC and P*-g-A^{FITC}C37^{TRITC} in solution ($\lambda_{\text{exc}}=490\text{nm}$).

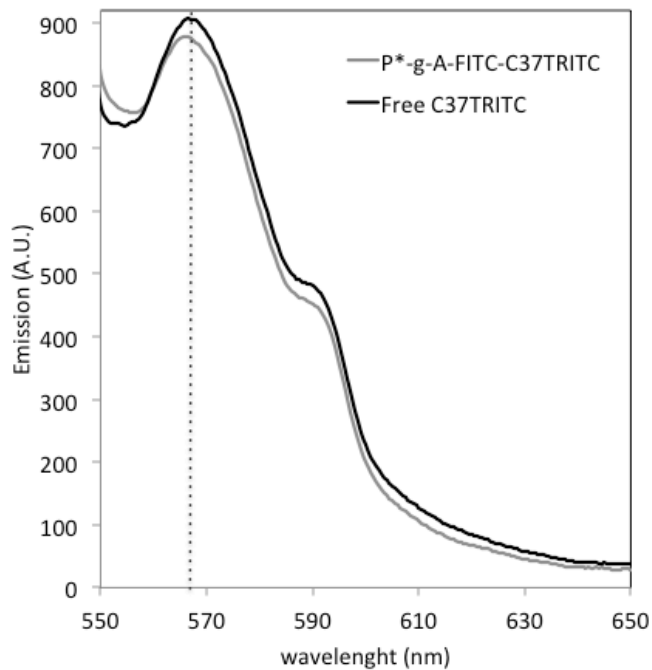


Figure 8.22: Emission spectra of free C37^{TRITC} and P*-g-A^{FITC}C37^{TRITC} in solution ($\lambda_{exc}=550\text{nm}$).

A co-localization study has been performed in the collaboration with Prof. Ghersi's group. In Figure 8.23 the images from fluorescence microscopy carried out on P*-g-A^{FITC}C37^{TRITC} NGs are shown. ECV304 cells nuclei have been dyed with DAPI (blu), the red color refers to TRITC labeled C 37 with and the green color refers to FITC labeled NGs. Since the green and the red color are localized in the same position with respect to the cells nuclei, it can be argued that the antibody moves solidary with nanogels and their bond is stable in the cells culture.

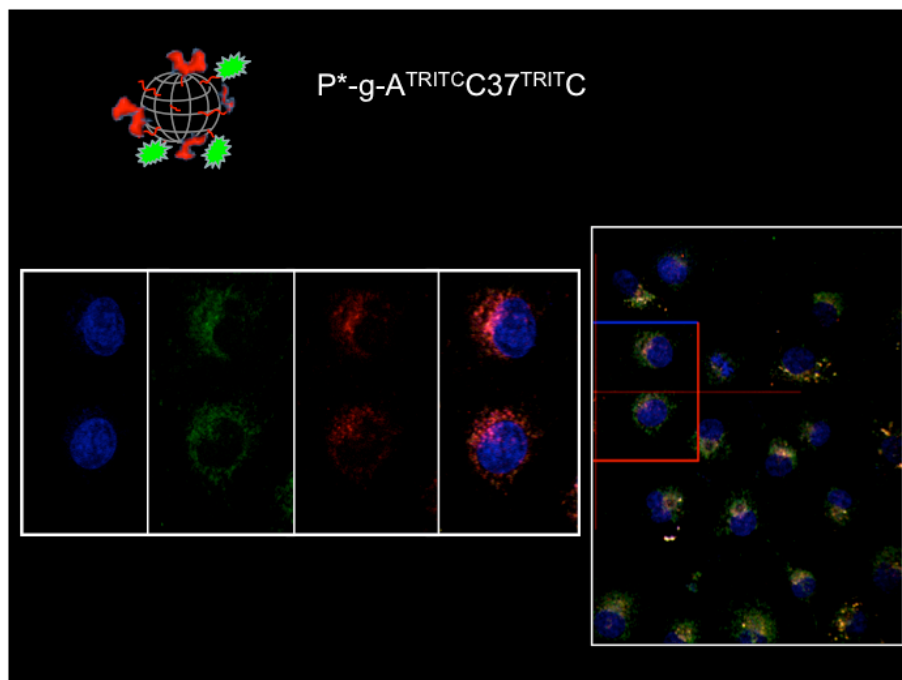


Figure 8.23: Localization study in ECV304 cells. The blue colors refer to cells nuclei. The red color refers to C37^{TRITC} conjugated on NGs and the green refers to FITC conjugated on the same NGs.

The results obtained using C37 clearly show the potentials of these nanogels as base building blocks for the generation of biohybrid composite nanosystems.

All the information gathered on the conjugation of C37 has been transferred to the conjugation of the anti- $\alpha_v\beta_3$ integrin. In particular, anti- $\alpha_v\beta_3$ integrin has been successfully conjugated to P*-g-A NGs. The biological activity of this antibody after the conjugation with NGs has been tested. This antibody showed a strong targeting ability towards tumor angiogenic targets. These results have not been reported here since they do not fall within the scope of this thesis work and will be the subject of a future publication.

8.3.3 FAM-FW-N as a model oligonucleotide

A selected carboxyl functionalized nanogel system (P*0.25AA50) has been efficiently decorated with a single strand oligonucleotide, namely FAM-FW-N. In particular, the FAM-FW-N oligonucleotide has been built with a C3-aminolink at the 3'-end, capable of reacting with the carboxyl groups present on nanogels, and with FAM fluorochrome at the 5'-end, in order to make the oligonucleotide fluorescent.

Purposely designed experiments proved that, after the conjugation, the oligonucleotide still shows its pairing ability toward the complementary strand. All the results gathered so far strongly point out toward a possible application of these nanogels as nanocarriers for gene-therapy applications. For a detailed description of the approach and relative results, see Paper VII.

8.4 Conjugation of Doxorubicin to carboxyl-functionalized PVP nanogels.

8.4.1 Drug loading experiments

Redox-responsive NGs have been generated via conjugation of P*0.5AA50 system with aminoethyldithiopropionic acid (AEDP) and doxorubicin (DOX).

The conjugation procedure in two steps, already described for the conjugation of folic acid (see paragraph 8.2), has been also used for the conjugation of DOX.

In particular, the possibility of achieving intracellular drug release in response to a stimulus has been investigated. If the drug is conjugated through a disulphide bridge (S-S) to the nanogels, this bridge may be cleaved under the stimulus of a reducing agent, such as glutathione (GSH). The release trigger is based on the existence of a large difference in the redox potential between the mildly oxidizing extracellular milieu and the reducing intracellular fluids. Indeed, the blood plasma of humans contains micromolar concentrations of GSH, whereas the concentration of GSH in the cells cytosol is around 10 mM. Furthermore, cells with an enhanced level of oxidative stress, such as tumor cells, show GSH cytosolic concentrations several times higher than those of normal cells.¹²³ Therefore, by exploiting this mechanism,

DOX may be released intracellularly and effectively reach the cells nucleus , thus inducing cell death. Reduced, if not inhibited, drug toxicity should be demonstrated if the drug is attached to the NP.

The conjugation degree between Doxorubicin and nanogels has been estimated through UV-vis absorbance measurements. Figure 8.24 shows the UV-vis spectra of a carboxyl-functionalized nanogel suspension in water, before and after conjugation with DOX and the spectrum of free DOX in water, as reference. It can be observed that the NGs do not show any absorption band in the wavelength range where Doxorubicin strongly absorbs. Conversely, the Dox-loaded system shows the characteristic absorption band of Dox, but clearly red-shifted. This shift suggests a modification of the environment for the chromophore. The free DOX and the DOX linked may have different absorption and emission properties. If that is the case the molar extinction coefficient or the quantum yield of the free Dox cannot be used, in principle, for quantifying the amount of conjugated probe.

In a pilot experiment, the amount of DOX conjugated to the NGs has been quantified in two different ways: (1) assuming that the extinction coefficient of the free and bound DOX are the same, and (2) determining the amount of DOX linked to the NGs from the difference in absorbance of the free probe in the uptake solution, prior and after the uptake. In more detail, in the first case the amount of DOX conjugated has been estimated by using the absorption peak at $\lambda_{\text{max}}=486$ nm of the conjugate and the molar extinction coefficient determined for the free DOX. In the second case, the conjugated NGs have been first purified from the not-conjugated DOX by multiple washings and the amount of non-conjugated DOX in the washings has been quantified. The cumulative amount has been subtracted to the total amount of DOX in the uptake solution to estimate the portion that has reacted. Since the two methods yield the same amount of linked DOX, the molar extinction coefficient of the free drug has been used in the followings for quantification purposes.

The concentration of DOX in the conjugated estimated is about 11 $\mu\text{g/ml}$ and the number of molecules of DOX molecules linked to each nanogel particle is around 200.

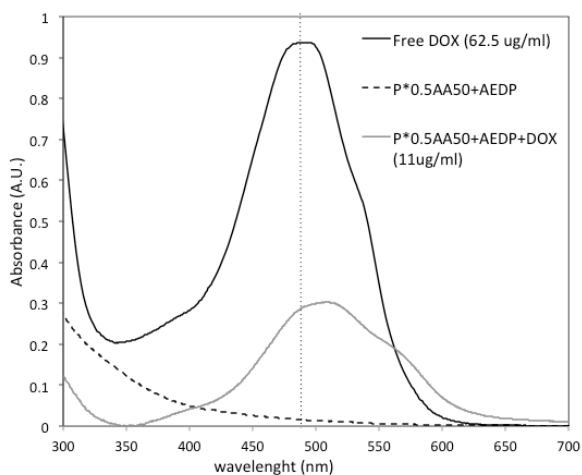


Figure 8.24. UV-vis spectra of a carboxyl-functionalized NG in water before and after conjugation with DOX and of free DOX in water.

8.4.2 *In vitro* drug release experiments

In vitro drug release studies have been performed on DOX-loaded NGs suspensions at 37°C in pH 7.4 PBS with 10 mM of GSH, as well as in the same buffer but with no GSH, as control. The amount of DOX released has been quantified through fluorescence measurements ($\lambda_{em}=550$ nm and $\lambda_{exc}=480$ nm) of samples taken from the receiving phase (for further details see paragraph 3.2.3). The release profiles for both systems as function of the time are shown in Figure 8.25. The amount of DOX released is reported as the molar ratio between the DOX released at the time t and the DOX linked to nanoparticles. It can be observed that both systems release DOX, but in the presence of GSH the amount of DOX released is substantially higher, about 70% vs. 34%, and the release is faster. No burst effects are evident in any case. It can be speculated that the DOX that is released in the absence of GSH is the portion that has been physically bound to the nanogels. In fact, due to its hydrophobicity, DOX can be likely hosted in the nanogels' hydrophobic domains, especially if the chemically bound DOX is making them even

more hydrophobic. Indeed, even after prolonged release time a significant percentage of this drug is not released. The absence of a burst release seems to indicate that there are not “surface” adsorbed molecules. This is quite in line with the idea of nanogels as an “open” structure, which surely offer easy access to small molecules, such as DOX.

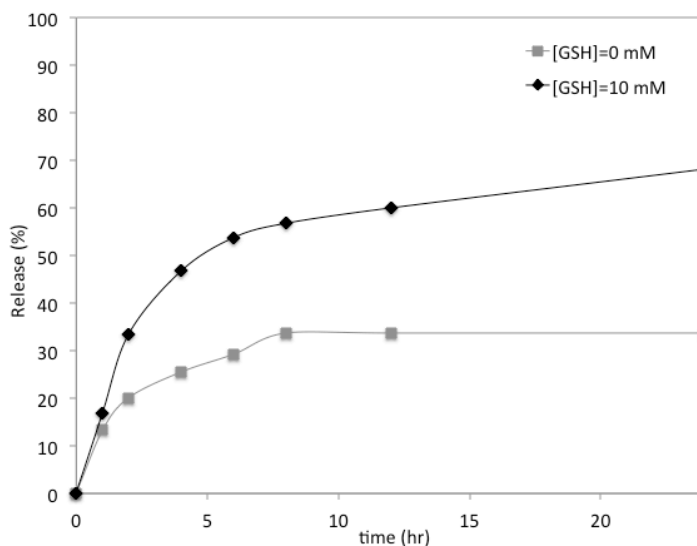


Figure 8.25 : In vitro release of DOX from P*0.5AA50-AEDP-DOX NGs in PBS (pH 7.4) at 37 °C with or without GSH.

In vitro drug release tests have demonstrated that the disulphide bridge can be broken under the stimulus of a reductive molecule, such as GSH. The following experiments will try to assess if this responsive release behavior can be transferred into a cell environment.

8.4.3 Intracellular drug release experiments

Glutathione-mediated intracellular drug delivery has been also investigated against a MC3T3-E cell line by pretreating these cells with glutathione monoester (GSH-OEt), which increases the concentration of GSH in the cytoplasm. This study has

been performed in collaboration with Prof. Gherzi's group. In particular, MC3T3-E1 has been pretreated with 10 mM GSH-OEt and incubated with P*0.5AA50-AEDP-DOX and free Dox for 3 hr. In Figure 8.26 cell viability of both MC3T3-E1 cells treated or non-treated with GSH-OEt, evaluated after 48 and 72 h, is reported. Both after 48 and 72 h, cells that have not been pretreated with GSH-OEt and incubated with P*0.5AA50-AEDP-Dox show a high cell viability, close to 100%. Conversely, cells that have not been pretreated with GSH-OEt and incubated with free Dox, as well as cells treated with GSH-OEt and incubated with either P*0.5AA50-AEDP-Dox or free Dox, all show a reduced cell viability. These results suggest that redox-responsive nanogels are able to delivery DOX into cells nuclei, thus inducing cell death, and quite importantly that when the drug is attached to the NGs has a very much reduced cito-toxicity, also after 72 h.

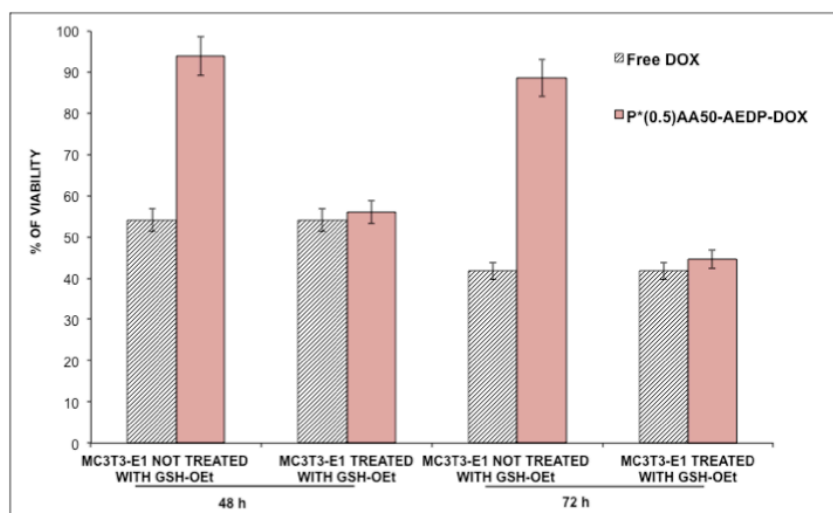


Figure 8.26: Viability of MC3T3-E1 cells cultured with free-DOX or P*0.5AA50-AEDP-DOX for 48 and 72 hr. The cells have been pretreated or not with 10mM of GSH-OEt.

8.5 Gadolinium as model imaging agent

P*0.5AA50 NGs have been used as building blocks for the assembly of an imaging device. This system has been selected among all the others (both carboxyl

and amino-functionalized PVP-based NGs) since it showed the best combination between physico-chemical properties (i.e. size and surface properties) and availability of reactive functional groups.

The conjugation that leads to NGs-mod-DTPA is the multi-step reaction shown in Figure 8.27. In detail, the carboxyl groups of P*0.5AA50 NGs have been first converted into amino groups, able to react with the chelating agent. The conversion of nanogel's functionality has been achieved with 1,5 diaminopentane-BOC, following the usual EDC/Sulfo-NHS protocol. The amino-modified-P*05AA50 variants have been then deprotected and conjugated to DTPA-tBut ester, a modified form of DTPA. DTPA is a chelating agent widely used for Gd^{3+} complexation for its well-known propensity to form stable complexes with metal-ions. In particular, the modified DTPA has five carboxyl groups protected in the form of t-But ester and one "free" carboxyl group, available for the conjugation with the nanogel. Finally, the carboxyl groups of NGs-mod-DTPAt-But ester have been deprotected in order to form NGs-mod-DTPA- Gd^{3+} . For further details, see paragraph 3.2.2.

After the complexation, the amount of Gd^{3+} complexed by NGs-mod-DTPA has been estimated through a complexometric titration using Arsenazo III. In particular, Arsenazo III binds to free metal ions forming an Arsenazo-metal ion complex, which can be quantified through UV-vis absorption measurements. The quantification method is based on the differences in the visible spectra of free and complexed Arsenazo III. The free Arsenazo III shows two absorption maxima in the visible region, respectively at 550 and 652 nm. When the ion Gd^{3+} is added to the solution, the relative intensities of the two absorption bands change, the bands at 652 nm increases whereas the band at 550 nm decreases. In Figure 8.28, the UV-vis spectra of the titrated uptake solutions before and after mixing with NGs are reported.

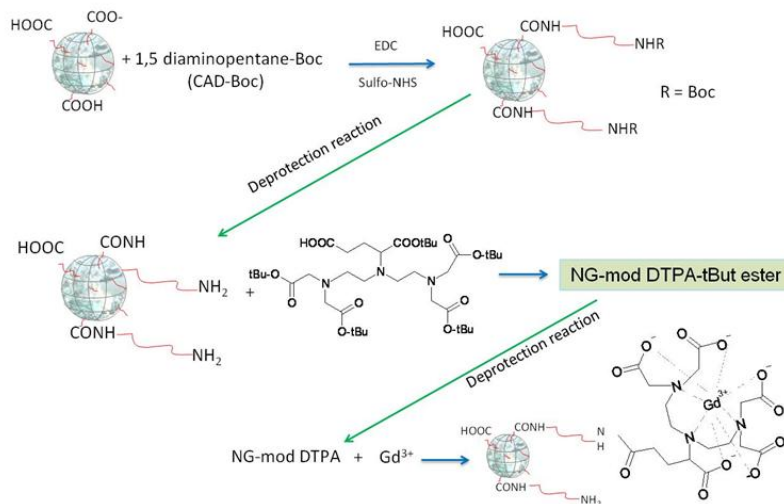


Figure 8.27: Reaction scheme for the formation of NGs-mod DTPA-Gd³⁺ complexes. Step 1. Formation of amino-mod NGs; Step 2. Deprotection of amino groups; Step 3. Formation of NGs-mod DTPA tBut ester; Step 4. Deprotection of carboxyl groups; Step 5. Formation of NGs-mod DTPA-Gd³⁺ complexes.

In the inset the spectra of Gd³⁺-Arsenazo III complexes at different concentration used for calibration are reported. It can be noticed that in the presence of NGs the peak at 550 nm of the uptake solution is higher than the same peak in the absence of NGs. From the difference between these two intensities, the amount of Gd³⁺ complexed by NGs-mod-DTPA has been determined. It has been estimated that the number of Gd³⁺ ions complexed by each nanogels is about 30. These NGs-mod DTPA-Gd³⁺ complexes may be used as contrast agent in magnetic resonance. Some preliminary evaluation studies are ongoing.

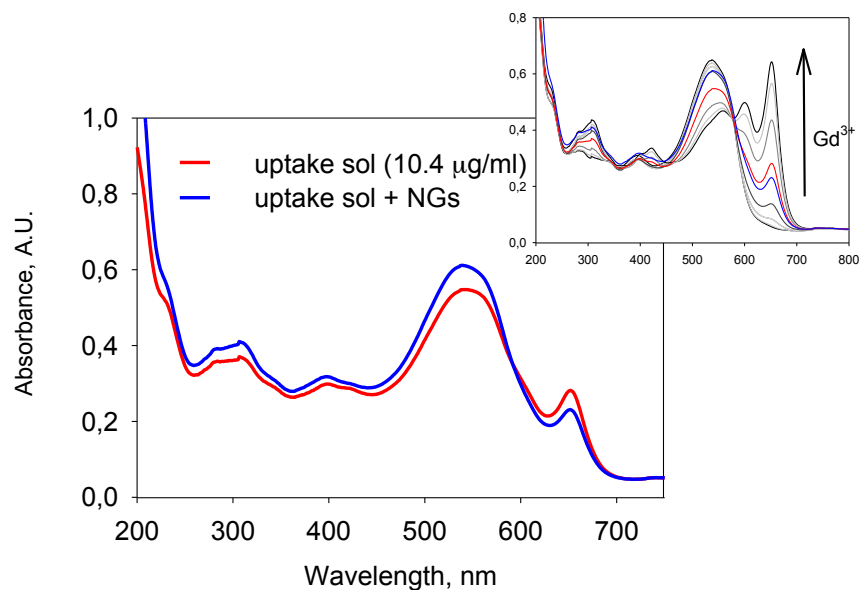


Figure 8.28. UV-vis spectra for “free” Gd^{3+} in the uptake solution before (red) and after (blue) mixing with NGs. The spectra refer to the UV-vis detectable complex formed with Arsenazo III and Gd^{3+} . In the inset: Gd^{3+} -Arsenazo III complexes at different concentration used for calibration.

8.6 Conclusions

Functional groups grafted on PVP NGs have been exploited for conjugation reactions with molecules that have various functional reactive groups (isothiocyanate, amino and carboxyl groups), different hydrophobicity and steric hindrance. In particular, the conjugation reaction protocols established for small molecules have been successfully transferred to bio-macromolecules, such as antibodies and proteins. This implies that NGs reactive functional groups are accessible also to large molecules. Furthermore, two different ligands have been efficiently conjugated on the same nanogel, proving that “multifunctional” nanodevices can be assembled. Finally, it has been proved that all the “model” ligands have preserved their biological activity upon conjugation. More in detail, folate-NG variants have shown the ability of being preferentially taken up by tumor

cells and that their uptake is faster than for bare NGs. Folate-NGs' internalization appears to occur mainly through a specific receptor-mediated endocytosis process. Further studies are needed to better support this hypothesis.

Responsive NGs have been generated by attaching a model drug through a linker with a redox-cleavable bond. In-vitro release studies have shown that these modified NGs quantitatively release the drug when the release is triggered by the presence of a reducing molecule. Moreover, in vitro intracellular release studies have demonstrated that the drug is not active when linked to the nanoparticle, while it exerts its action (cell-death) when it is released.

Nanodevices for bio-imaging purposes have been also successfully designed. In particular, a carboxyl-functionalized NG has been first chemically modified to display primary amino groups and then covalently linked to a chelating agent, which has a terminal carboxyl group-bearing arm for binding purposes. The modified conjugated system has shown the ability to complex Gd^{3+} , a paramagnetic metal-ion widely used as contrast agent in MRI. Studies devoted to the assessment of the applicability of Gd^{3+} -NGs complexes as contrast agents in magnetic resonance are ongoing. This last conjugation approach provides also evidence that nanogels functional groups can be easily modified from carboxyl to e.g. amino groups, when required.

9 Final Remarks

Base and functionalized PVP NGs have been produced either *via* chemical radical polymerization in inverse microemulsion and *via* pulsed e-beam irradiation. All the PVP-based NGs have shown to be biocompatible and able to be internalized by cells owing to: (i) their chemical structure, that closely resembles that of PVP; (ii) the physico-chemical properties imposed by the synthetic approach, i.e. their controlled size at the nanoscale and favorable surface properties. Furthermore, the many functional groups that have been grafted on PVP NGs are available for coupling reactions with bioactive molecules, such as targeting moieties, drugs and metal-ions chelating agents.

This collective evidence validates the generated nanostructures for the intent they have been designed for, i.e. as nanocarriers in the biomedical field. Moreover, due to their great versatility they can be regarded as a “base material platform”. The research is now progressing in the direction of evaluating the nanocarriers in relevant animal models, to study their biodistribution in complex organisms as well as the pharmacodynamics and pharmacokinetics of the loaded drugs.

E-beam irradiation using industrial type accelerators has demonstrated to be a viable manufacturing process since it grants high yields in terms of recovered product and high throughputs. Through a proper selection of the experimental parameters, this approach has allowed to obtain NGs with tailored properties, in terms of size, surface charge density, degree of crosslinking and functionality. A kinetic study, that can be carried out only using research-type electron accelerators - that are more flexible in the set up of their operation parameters than those used in industry - finds in the information collected so far a strong justification and its boundary conditions. I strongly believe that a more fundamental study must now be approached, as it can offer the opportunity of mastering the relationship between process and product properties and, in turn, a powerful tool to optimize both product design and manufacturing process conditions.

10 References

1. Allen, T.M., Cullis, P.R., Drug Delivery Systems: Entering the Mainstream. *Science*, 2004. 303: p. 1818-1822.
2. Kostarelos, K., Rational design and engineering of delivery systems for therapeutics: biomedical exercises in colloid and surface science. *Adv. Colloid Interface Sci.*, 2003. 106: p.147-168.
3. Langer, R., Perspectives: Drug delivery – drugs on target. *Science*, 2001. 293: p. 58-59.
4. Pisal, D.S., Kosloski, M.S., Balu-Iyer, S.V., Delivery of therapeutic proteins. *J Pharm Sci.*, 2010. 99(6): p. 2557–2575.
5. Ferrari, M., Cancer nanotechnology: opportunities and challenges. *Nat. Rev. Cancer*, 2005. 5: p. 161-171.
6. Park, Y., Kim, H.M., Kim, J.H., Moon, K.C., Yoo, B., Lee, K. T., Lee, N., Choi, Y., Park, W., Ling, D., Na, K., Moon, W.K., Choi, S.H., Park, H.,S., Yoon, S.Y., Suh, Y.D., Lee, S.H., Hyeon, T., Theranostic Probe Based on Lanthanide-Doped Nanoparticles for Simultaneous In Vivo Dual-Modal Imaging and Photodynamic Therapy. *Adv. Mater.* 2012. 24: p. 5755–5761.
7. Li Y, Beija M, Laurent S, vander Elst L, Muller RN, Duong HTT, Lowe AB, Davis TP, Boyer C, Macromolecular Ligands for Gadolinium MRI Contrast Agents. *Macromolecules* 2012; 45: 4196–4204.
8. Tandonand, P., Farahani, K., NCI image-guided drug delivery summit. *Cancer Res.*, 2011. 71: p. 314–7.
9. Hynynen, K., MRIGHIFU: a tool for image-guided therapeutics. *J Magn Reson Imaging*, 2011. 34: p. 482–93.
10. Motornov, M., Roiter, Y., Tokarev, I., Minko, S., Stimuli-responsive nanoparticles, nanogels and capsules for integrated multifunctional intelligent systems. *Progress in Polymer Science*, 2010. 35(1-2): p.174–211.

11. Albanese, P.S., Tang, W.C., Chan, W., The Effect of Nanoparticle Size, Shape, and Surface Chemistry on Biological Systems. *Annu. Rev. Biomed. Eng.*, 2012. 14: p. 1–16.
12. Chacko R.T., Ventura, J., Zhuang, J., Thayumanavan, S., Polymer nanogels: A versatile nanoscopic drug delivery platform. *Advanced Drug Delivery Reviews*, 2012. 64: p. 836–851.
13. Traitel, T., Goldbart, R., Kost, J., Smart polymers for responsive drug-delivery systems. *Journal of Biomaterials Science, Polymer Edition*, 2008. 19: p. 755–767.
14. Qiu, Y., Park, K., Environment-sensitive hydrogels for drug delivery. *Advanced Drug Delivery Reviews*, 2012. 64: p. 49–60.
15. Torchilin, V., Multifunctional and stimuli-sensitive pharmaceutical nanocarriers. *European Journal of Pharmaceutics and Biopharmaceutics*, 2009. 79: p. 431–444.
16. Qiu, Y., Liu, Y., Wang, L.M., Xu, L.G., Bai, R., et al., Surface chemistry and aspect ratio mediated cellular uptake of Au nanorods. *Biomaterials*, 2010. 31: p. 7606–19.
17. Chithrani, B.D., Ghazani, A.A., Chan, W.C., Determining the size and shape dependence of gold nanoparticle uptake into mammalian cells. *Nano Lett.* 2006. 6: p. 662–68.
18. Gratton, S.E., Ropp, P.A., Pohlhaus, P.D., Luft, J.C., Madden, V.J., et al., The effect of particle design on cellular internalization pathways. *Proc. Natl. Acad. Sci. USA*, 2008. 105: p. 11613–18.
19. Chithrani, B.D., Chan, W.C., Elucidating the mechanism of cellular uptake and removal of protein-coated gold nanoparticles of different sizes and shapes. *Nano Lett*, 2007. 7: p. 1542–50.
20. Champion, J. A., Katare, Y. K., Mitragotri, S., Particle shape: a new design parameter for micro- and nanoscale drug delivery carriers. *J. Control. Release*, 2007. 121: p. 3–9.
21. Wong, J., Brugger, A., Khare, A., Chaubal, M., Papadopoulos, P., Rabinow, B., Kipp, J., Ning, J., Suspensions for intravenous (IV) injection: a review of development, preclinical and clinical aspects. *Adv. Drug Deliv. Rev.*, 2008. 60: p. 939–954.

22. Alexis, F., Pridgen, E., Molnar, L. K., Farokhzad, O.C., Factors affecting the clearance and biodistribution of polymeric nanoparticles. *Mol. Pharm.*, 2008. 5: p. 505–515.
23. Vinogradov, S. V., Bronich, T. K., Kabanov, A. V., Nanosized cationic hydrogels for drug delivery: preparation, properties and interactions with cells. *Adv. Drug Deliv. Rev.*, 2002. 54: p. 135–147.
24. Soo Choi, H., Liu, W., Misra, P., Tanaka, E., Zimmer, J.P., Ipe, B.I., Bawendi, M.G., Frangion, J.V. Renal clearance of quantum dots. *Nature Biotech.*, 2007. 25: 1165–1170.
25. Owens III, D. E., Peppas, N. A., Opsonization, biodistribution, and pharmacokinetics of polymeric nanoparticles. *Int. J. Pharm.*, 2006. 307: p. 93–102.
26. Illum, L., Davis, S.S., Wilson, C.G., Thomas, N.W., Frier, M., Hardy, J.G., Blood clearance and organ deposition of intravenously administered colloidal particles. The effects of particle size, nature and shape. *Int. J. Pharm.*, 1982. 12: p. 135–146.
27. Moghimi, S. M., Hedeman, H., Muir, I. S., Illum, L., Davis, S. S., An investigation of the filtration capacity and the fate of large filtered sterically-stabilized microspheres in rat spleen. *Biochim. Biophys. Acta*, 1993. 1157: p. 233–240.
28. Porter, C. J., Moghimi, S. M., Illum, L. & Davis, S. S., The polyoxyethylene/polyoxypropylene block copolymer poloxamer-407 selectively redirects intravenously injected microspheres to sinusoidal endothelial-cells of rabbit bone-marrow. *FEBS Lett.*, 1992. 305: p. 62–66.
29. Maeda, H., Greish, K. , Fang, J., The EPR effect and polymeric drugs: a paradigm shift for cancer chemotherapy in the 21st century. *Adv. Polym. Sci.*, 2006. 193: p. 103–121.
30. Matsumura, Y., Maeda, H., A new concept for macromolecular therapeutics in cancer-chemotherapy — mechanism of tumoritropic accumulation of proteins and the antitumor agent Smancs. *Cancer Res.*, 1986. 46: p. 6387–6392.

31. Ishida, O., Maruyama, K., Sasaki, K., and Iwatsuru, M., Size-dependent extravasation and interstitial localization of polyethyleneglycol liposomes in solid tumor-bearing mice. *International Journal of Pharmaceutics*, 1999. 190(1): p. 49-56.
32. Conner, S. D., Schmid, S. L., Regulated portals of entry into the cell. *Nature*, 2003. 422: p. 37–44.
33. Rejman, J., Oberle, V., Zuhorn, I. S. & Hoekstra, D., Size-dependent internalization of particles via the pathways of clathrin- and caveolae-mediated endocytosis. *Biochem. J.*, 2004. 377: p. 159–169.
34. Hillaireau, H., Couvreur, P., Nanocarriers' entry into the cell: relevance to drug delivery. *Cell. Mol. Life Sci.*, 2009. 66: p. 2873–2896.
35. Brandhonneur, N., Chevanne, F., Vie, V., Frisch, B., Primault, R., Le Potier, M.F., Le Corre, P., Specific and non-specific phagocytosis of ligand-grafted PLGA microspheres by macrophages. *Eur. J. Pharm. Sci.*, 2009. 36: p. 474–485.
36. Pathak, Y., Thassu, D., *Drug Delivery Nanoparticles Formulation and Characterization*, 2009. New York: ed Informa Healthcare USA.
37. Segal, E.I., Low, P.S., Tumor detection using folate receptor-targeted imaging agents. *Cancer Metastasis Rev*, 2008. 27: p. 655–664.
38. Zhong, X., Neumann, P., Corbo, M., Loh, E., *Recent Advances in Biotherapeutics Drug Discovery and Development, Drug Discovery and Development - Present and Future*, ed. Dr. Izet Kapetanović, ISBN: 978-953-307-615-7 InTech, 2011. Available from: <http://www.intechopen.com/books/drug-discovery-and-development-present-and-future/recent-advances-in-biotherapeutics-drug-discovery-and-development>.
39. Byrne, J.D., Betancourt, T., Brannon-Peppas, L., Active targeting schemes for nanoparticle systems in cancer therapeutics. *Adv. Drug Delivery Rev.*, 2008. 60: p. 1615–1626.
40. Longmire, M., Choyke P.L., Kobayashi. H., Clearance properties of nano-sized particles and molecules as imaging agents: considerations and caveats. *Nanomedicine*, 2008. 3(5): p. 703–717.

41. Lu, Z.R., Parker, D.L., Goodrich, K.C., Wang, X., Dalle, J.G., Buswell, H.R., Extracellular biodegradable macromolecular gadolinium(III) complexes for MRI. *Magn. Reson. Med.*, 2004. 51: p. 27–34.
42. Wacker, M., Nanocarriers for intravenous injection-the long hard road to the market. *International Journal of Pharmaceutics*, 2013. 457: p. 50-62.
43. Bangham, A., Standish, H.M., Watkins, J., Diffusion of univalent ions across the lamellae of swollen phospholipids. *J. Mol. Biol.*, 1965. 13: p. 238–252.
44. Soppimatha, K.S., Aminabhavia, T.M., Kulkarnia, A.R., Rudzinski, W.E., Biodegradable polymeric nanoparticles as drug delivery devices. *Journal of Controlled Release*, 2001. 70: p. 1–20.
45. Morachis, J.M., Mahmoud, E.A., Almutairi, A., Physical and Chemical Strategies for Therapeutic Delivery by Using Polymeric Nanoparticles. *Pharmacological Reviews*, 2012. 64(3): p. 505-519.
46. Mintzer, M.A., Simanek, E.E., Nonviral Vectors for Gene Delivery. *Chem. Rev.*, 2009. 109: p. 259–302.
47. Agrawal, U., Gupta, M., Jadon, R.S. Sharma, R., Vyas, S.P., Multifunctional nanomedicines: potentials and prospects. *Drug Delivery and Translational Research*, 2013. 3(5): p. 479-497.
48. Malik, A., Chaudhary, S., Garg, G., Tomar, A., Dendrimers: A Tool for Drug Delivery. *Advances in Biological Research*, 2012. 6 (4): p. 165-169.
49. Walter, M.V., Malkoch, M., Simplifying the synthesis of dendrimers: accelerated approaches *Chem. Soc. Rev.*, 2012. 41: p. 4593-4609.
50. Fischer, M., Vögtle, F., Dendrimers: From Design to Application—A Progress Report. *Angewandte Chemie International Edition*, 1999. 38(7): p. 884–905.
51. Thostenson, E.T., Ren, Z., Chou, T.W., Advances in the science and technology of carbon nanotubes and their composites: a review. *Composites Science and Technology*, 2001. 61: p. 1899–1912.
52. Menon, J.U., Nanomaterials for Photo-Based Diagnostic and Therapeutic Applications. *Theranostics*, 2013. 3(3): p. 152-166.
53. Lacerda, L., Bianco, A., Prato, M., Kostarelos, K., Carbon nanotubes as nanomedicines: From toxicology to pharmacology. *Advanced Drug Delivery*

- Reviews, 2006. 58(14): p. 1460–1470.
54. Liu, Z., Tabakman, S., Welsher, K., Dai, H., Carbon nanotubes in biology and medicine: in vitro and in vivo detection, imaging and drug delivery. *Nano Research*, 2009. 2: p. 85–120.
55. Sun, C., Lee, J.S.H., Zhang, M. Magnetic nanoparticles in MR imaging and drug delivery. *Advanced Drug Delivery Reviews*. 2008. 60: p. 1252–1265.
56. Arruebo, M., Fernández-Pacheco, R., Ibarra, M.R., Santamaría, J., Magnetic nanoparticles for drug delivery. *NanoToday*, 2007. 3: p. 22–32.
57. Lasagna-Reeves, C., Gonzalez-Romero, D., Barria, M.A., Olmedo, I., Clos, A., Sadagopa Ramanujam, V.M., Urayama, A., Vergara, L., Kogan' M.J., Soto, C., Bioaccumulation and toxicity of gold nanoparticles after repeated administration in mice. *Biochemical and Biophysical Research Communications*, 2010. 393(4): p. 649–655.
58. Mastrobattista, E., van der Aa, M.A., Hennink, W.E., Crommelin, D.J.A., Artificial viruses: a nanotechnological approach to gene delivery. *Nat. Rev. Drug Discov.*, 2006. 5: p. 115–121.
59. Peer, D., Nanocarriers as an emerging platform for cancer therapy. *Nature Nanotechnology*, 2007. 2: p. 751-760.
60. Yallapu, M.M., Jaggi, M., Chauhan, S.C., Design and engineering of nanogels for cancer treatment. *Drug Discovery Today*, 2001. 16: p. 457-463.
61. Kabov, A.V., Vinogradov S.V., Nanogels as Pharmaceutical Carriers: Finite Networks of Infinite Capabilities. *Angew Chem Int Ed Engl.*, 2009. 48(30): p. 5418–5429.
62. Vermonden, T., Censi, R., Hennink, W.E., Hydrogels for Protein Delivery. *Chem. Rev.*, 2012.112: p. 2853–2888.
63. Oh, J. K., Drumright, R., Siegwart, D. J., Matyjaszewski, K., The development of microgels/nanogels for drug delivery applications. *Prog. Polym. Sci.* 2008. 33: p. 448-477.
64. Gonçalves, C., Pereira, P., Gama, M., Self-Assembled Hydrogel Nanoparticles for Drug Delivery Applications. *Materials*, 2010. 3: p. 1420-1460.

65. Ulanski, P., Rosiak, J. M., Polymeric Micro/Nanogels. In Encyclopedia of Nanoscience and Nanotechnology, 2004. Valencia: Nalwa, American Scientific Publishers.
66. Robinson, B.V., Sullivan, F.M., Borzelleca, J.F., Schwartz, S.L.. PVP, A critical review of kinetics and toxicology of polyvinylpyrrolidone (Povidone). 1990. MI, USA: Lewis Publishers, Inc.
67. Saxena, S.M., Johri, A.K., Ultra-low sized cross-linked polyvinylpyrrolidone nanoparticles as non-viral vectors in vivo for gene delivery, Biomaterials, 2006. 27: p. 5596-5602.
68. Login, R.B., Shih, J.S., Chuang, J.C. , Methods of crosslinking PVP. 1993. US005219950A
69. Antonietti, M., Landfester, K., Polyreactions in miniemulsions. Prog. Polym. Sci., 2002. 27: p. 689-757.
70. Bharali, D.J., Sahoo, S.K., Mozumdar, S., Maitra, A., Cross-linked polyvinylpyrrolidone nanoparticles: a potential carrier for hydrophilic drugs. J. Colloid Interface Sci., 2003. 258(2): p. 415-423.
71. Elaissari, A., Colloidal Polymers: Synthesis and Characterization. 2003: CRC Press.
72. Holmberg, K., Jonsson, B., Kronberg, B., Lindman, B., Chemical Reactions in microheterogeneous systems, in: Surfactants and Polymers in Aqueous Solution. ed. John Wiley & Sons, 2002: West Sussex, p. 507-511.
73. Woods, R. J., Pikaev, A.K., Applied Radiation Chemistry, Radiation Processing. 1994, New York: John Wiley and Sons, Inc.
74. Farahataziz and Rodgers, M.A., Radiation Chemistry, Principles and Applications. 1987, New York: VCH Publishers, Inc.
75. Spinks J. W., Woods R. J. , An Introduction to Radiation Chemistry. third ed. 1990, New York: John Wiley and Sons, Inc.
76. Buxton, G. V., Radiation chemistry of the liquid state: (1) water and homogeneous aqueous solutions, in Radiation Chemistry Principles and Applications, ed. Rogers, Farhataziz and M A J. 1987, New York: VCH. 321-349.
77. Janata, E., Schuler, R. H., Rate constant for scavenging e_{aq}^- in N_2O -saturated

- solutions. *Journal of Physical Chemistry*, 1982. **86**: p. 2078-2084.
78. Steenken, S., O'Neill, P., Selectivity of addition of the hydroxyl radical to ring positions of pyridine and pyridine mono- and dicarboxylic acids, An electron spin resonance investigation. *Journal of Physical Chemistry*, 1978. **82**: p. 372-374.
79. Anbar, M., Meyerste.D and Neta, P., Reactivity of Aromatic Compounds toward Hydroxyl Radicals. *Journal of Physical Chemistry*, 1966. **70**(8): p. 2660-2667.
80. Rosiak, J. M., Ulanski, P., Pajewski, L.A., Yoshii, F., Makuuchi, K., Radiation formation of hydrogels. Some remarks and comments. *Radiat. Phys. Chem.*1995. **46**: p. 161-165.
81. An, J.C., Weaver, A., Kim, B., Barkatt, A., Poster, D., Vreeland, W. N., Silverman, J., Al-Sheikhly, M., Radiation-induced synthesis of poly(vinylpyrrolidone) nanogel. *Polymer* , 2011. **52**: p. 5746–5755.
82. Ulanski, P., Rosiak, J. M., The use of radiation technique in the synthesis of polymeric nanogels. *Nuclear Instruments & Methods in Physics Research Section B-Beam Interactions with Materials and Atoms*, 1999. **151**(1-4): p. 356-360.
83. Behzadi, A., Borgwardt, U., Schnabel, W., Investigations on the Chain Length Dependence of Radical Reactivity. *Ber Bunsenges phys Chemie*, 1970. **74**: p. 649–653.
84. Bartoszek, N., Ulanski, P., Rosiak, J.M., Reaction of a Low-Molecular-Weight Free Radical with a Flexible Polymer Chain: Kinetic Studies on the OH + Poly(N - Vinylpyrrolidone) Model. *International Journal of Chemical Kinetics*, 2011. **43**: p. 474–481.
85. Ulanski, P., Zainuddin and Rosiak, J. M., Pulse-Radiolysis of Poly(Ethylene Oxide) in Aqueous-Solution .2. Decay of Macroradicals. *Radiation Physics and Chemistry*, 1995. **46**(4-6): p. 917-920.
86. Plonka, A., Developments in dispersive kinetics. *Prog. Reaction Kinetics*, 1991. **16**: p. 157.
87. Ulanski, P., Kadlubowski, S., Rosiak, J.M. Synthesis of poly(acrylic acid) nanogels by preparative pulse radiolysis. *Radiation Physics and Chemistry*, 2002. **63**: p. 533–53.

88. von Sonntag, C., Free-radical-induced chain scission and cross-linking of polymers in aqueous solution—an overview. *Radiation Physics and Chemistry*, 2003. 67: p. 353–359.
89. Rosiak, J., Olejniczak, J., Pekala, W., Fast Reaction of irradiated polymers-I. Crosslinking and degradation of polyvinylpyrrolidone. *Radiat.Phys. Chem.* 190. 36: p. 747-754.
90. Dorfman, L.M., Matheson, M.S., Pulse Radiolysis. *Progress in Reaction Kinetics*. Vol. 3. 1965. New York: Pergamon Press.
91. Charlesby, A., Alexander, P., Reticulation of polymers in aqueous solution by γ -rays. *J Chem Phys.* 1955. 52: p. 699-702.
92. Chapiro, A., Radiation grafting of hydrogels to improve the thrombo-resistance of polymers. *Europ. Polym J*, 1983. 19: p. 859.
93. Rosiak, J.M., Olejniczak, J., Medical application of radiation formed hydrogels. *Rad Phys ann Chem*, 1993. 42: p. 903-906.
94. Ajji, Z., Othman, I., Rosiak, J.M., Production of hydrogel wound dressings using gamma radiation. *Nucl. Instrum. Methods Phys. Res., Sect. B.* 2005. 229(3-4): p. 375-380.
95. Lopèrgolo, L.C., Lugao, A.B., Catalani, L.H., Direct UV photocrosslinking of poly(N-vinyl-2-pyrrolidone) (PVP) to produce hydrogel. *Polymer*, 2003. 44: p. 6217–6222.
96. Fechine, G.J.M., Barros, J.A.G., Catalani, L.H., Poly(N-vinyl-2-pyrrolidone) hydrogel production by ultraviolet radiation: new methodologies to accelerate crosslinking. *Polymer*, 2004. 45: p. 4705–4709.
97. Zhu, X., Lu, P., Chen, W., Dong, J., Studies of UV crosslinked poly(N-vinylpyrrolidone) hydrogels by FTIR, Raman and solid-state NMR spectroscopies. *Polymer*, 2010. 51: p. 3054–3063.
98. Xu, D., Hong, J., Sheng, K., Dong, L., Yao, S., Preparation of polyethyleneimine nanogels via photo-Fenton reaction. *Radiation Physics and Chemistry*, 2007. 76: p. 1606–1611.

99. Wang, B., Mukataka, S., Kodama, M., Kokufuta, E., Viscometric and Light Scattering Studies on Microgel Formation by γ -Ray Irradiation to Aqueous Oxygen-free Solutions of Poly(vinyl alcohol). *Langmuir*, 1997. 13: p. 6108-6114.
100. Ulański, P., Janik, I., Rosiak, J.M., Radiation formation of polymeric nanogels. *Rad. Phys. Chem.*, 1998. 52: p. 289–294.
101. Rembaum, A., Yen, S.P.S., Volksen, W., Labeled cells. *Chemtech*, 1978. 3(78): p. 182-190.
102. Kadłubowski, S., Ulanski, P., Rosiak, J. M., Synthesis of tailored nanogels by means of two-stage irradiation. *Polymer*, 2012. 53: p. 1985-1991.
103. Henke, A., Kadłubowski, S., Ulański, P., Rosiak, J. M., Arndt, K.-F, Radiation-induced cross-linking of polyvinylpyrrolidone-poly(acrylic acid) complexes. *Nuclear Instruments and Methods in Physics Research B*, 2005. 236: p. 391–398.
104. Abd El-Rehim, H.A., Swilem, A.E., Klingner, A., Hegazy, E.S.A., Hamed, A.A., Developing the Potential Ophthalmic Applications of Pilocarpine Entrapped Into Polyvinylpyrrolidone–Poly(acrylic acid) Nanogel Dispersions Prepared By γ Radiation. *Biomacromolecules*, 2013.14 (3): p. 688–698.
105. Abd El-Rehim, H.A., Hegazy, E.S.A., Hamed, A.A., Swilem, A.E., Controlling the size and swellability of stimuli-responsive polyvinylpyrrolidone–poly(acrylic acid) nanogels synthesized by gamma radiation-induced template polymerization. *European Polymer Journal*, 2013. 49: p. 601–612.
106. Kaczmarek, H., Szalla, A., Kaminska, A., Study of poly(acrylic acid)-poly(vinylpyrrolidone) complexes and their photostability. *Polymer*. 2001. 42: p. 6057-6059.
107. Chun, M.K., Cho, C.S., Choi, H.K., Mucoadhesive drug carrier based on interpolymer complex of poly(vinyl pyrrolidone) and poly(acrylic acid) prepared by template polymerization. *J Control Release*, 2002. 81(3): p. 327-34.
108. Hermanson, G. T., *Bioconjugate Techniques*, 2nd ed. 2008, New York: Academic Press.
109. Liu, Y., Kai Li, K., Pan, J., Liu, B., Feng, S.S., Folic acid conjugated nanoparticles of mixed lipid monolayer shell and biodegradable polymer core for targeted delivery of Docetaxel. *Biomaterials*, 2010. 31: p. 330–338.

110. Salazar, M. D., Ratnam, M., The folate receptor: what does it promise in tissue-targeted therapeutics? *Cancer Metastasis Rev.*, 2007. 26: p. 141–152.
111. Low, P. S., Henne, W. A., Doorneweerd, D. D., Discovery and development of folic-acid-based receptor targeting for imaging and therapy of cancer and inflammatory diseases. *Acc. Chem. Res.*, 2008. 41: p. 120–129.
112. Gabizon, A., Shmeeda, H., Horowitz, A. T., Zalipsky, S., Tumor cell targeting of liposome-entrapped drugs with phospholipid-anchored folic acid-PEG conjugates. *Adv. Drug Deliv. Rev.*, 2004. 56: p. 1177–1192.
113. Singh, S., Moller, M., Pich, A., Biohybrid Nanogels. *Polymer Chemistry*, 2013. 51: p. 3044–3057.
114. Arruebo, M., Valladares, M., Gonzalez-Fernandez, A., Antibody-Conjugated Nanoparticles for Biomedical Applications. *Journal of Nanomaterials*, 2009. doi:10.1155/2009/439389
115. Nisato, R.E., Tille, J.C., Jonczyk, A., Goodman, S.L., Pepper, M.S., Alpha_vbeta₃ and alpha_vbeta₅ integrin antagonists inhibit angiogenesis in vitro. *Angiogenesis*. 2003. 6 (2): p. 105–119.
116. Minotti, G., Menna, P., Salvatorelli, E., Cairo, G., Gianni, L., Anthracyclines: Molecular Advances and Pharmacologic Developments in Antitumor Activity and Cardiotoxicity. *Pharmacol. Rev.* 2004, 56: p.185–229.
117. Huang, C.K., Lo, C.L., Chen, H.H., Hsiue, G.H., Multifunctional Micelles for Cancer Cell Targeting, Distribution Imaging, and Anticancer Drug Delivery *Adv. Funct. Mater.*, 2007. 17: p. 2291–2297.
118. Nasongkla, N., Shuai, X., Ai, H., Weinberg, B.D., Pink, J., Boothman, D.A., Gao, J., cRGD-functionalized polymer micelles for targeted doxorubicin delivery. *Angew. Chem.*, 2004. 116: p. 6483–6487.
119. Sirova, M., Strohalm, J., Subr, V., Plocova, D., Rossmann, P., Mrkvan, T., Ulbrich, K., Rihova, B., Treatment with HPMA copolymer-based doxorubicin conjugate containing human immunoglobulin induces long-lasting systemic anti-tumour immunity in mice. *Cancer Immunol. Immunother.*, 2007. 56: p. 35–47.

120. Vicent, M.J., Greco, F., Nicholson, R.I., Paul, A., Griffiths, P.C., Duncan, R., Polymer Therapeutics Designed for a Combination Therapy of Hormone-Dependent Cancer. *Angew. Chem.*, 2005. 117: 4129–4134.
121. Gillies, E.R., Fréchet, J.M.J., pH-Responsive copolymer assemblies for controlled release of doxorubicin. *Bioconjugate Chem.*, 2005. 16: p. 361–368.
122. Liu, S.Q., Tong, Y.W., Yang, Y.Y., Incorporation and in vitro release of doxorubicin in thermally sensitive micelles made from poly(N-isopropylacrylamide-co-N,N-dimethylacrylamide)-b-poly(D,L-lactide-co-glycolide) with varying compositions. *Biomaterials*, 2005. 26: p. 5064–5074.
123. West, K. R., Otto, S., Reversible covalent chemistry in drug delivery. *Curr Drug Discov Technol.* 2005. 2(3): p. 123-60.
124. Saito, G., Swanson, J.A., Lee, K.D., Drug delivery strategy utilizing conjugation via reversible disulfide linkages: role and site of cellular reducing activities. *Advanced Drug Delivery Reviews*, 2003. 55(2): p. 199–215.
125. Liu, J., Pang, Y., Huang, W., Huang, X., Meng, L., Zhu, X., Zhou, Y., Yan, D., Bioreducible Micelles Self-Assembled from Amphiphilic Hyperbranched Multiarm Copolymer for Glutathione-Mediated Intracellular Drug Delivery. *Biomacromolecules*, 2011. 12: p. 1567–1577.
126. Caravan, P., Ellison, J.J., McMurry, T.J., Lauffer, R.B., Gadolinium(III) chelates as MRI contrast agents: structure, dynamics, and applications. *Chem Rev* 1999. 99: p. 2293-352.
127. Chun-Yan Cao, C.Y., Shen, Y.Y., Wang, J.D., Li, L., Liang, G.Y., Controlled intracellular self-assembly of gadolinium nanoparticles as smart molecular MR contrast agents. *SCIENTIFIC REPORTS*. 2013. 3: p. 1024-1033.
128. Lehner R, et al, Intelligent nanomaterials for medicine: Carrier platforms and targeting strategies in the context of clinical application. *Nanomedicine: NBM*, 2013: 9: p. 742-757.
129. Li, Y, Beija, M, Laurent, S, vander Elst, L, Muller, RN, Duong, HTT, Lowe, AB, Davis, TP, Boyer, C, Macromolecular Ligands for Gadolinium MRI Contrast Agents. *Macromolecules*, 2012. 45: p. 4196–4204.

130. Xu, S, Luo, Y, Graeser, R, Warnecke, A, Kratz, F, Hauff, P, et al. Development of pH-responsive core-shell nanocarriers for delivery of therapeutic and diagnostic agents. *Bioorg Med Chem Lett*, 2009. 19: p. 1030-1034.
131. Dispenza, C., Ricca, M., LoPresti, C., Battaglia, G., La Valle, M., Giacomazza, D., Bulone, D., E-beam irradiation and UV photocrosslinking of microemulsion-laden poly(N-vinyl-2-pyrrolidone hydrogels for “in-situ” encapsulation of volatile hydrophobic compounds. *Polymer Chemistry*, 2011. 2: p. 192-202.
132. Ghersi, G., Dong, H., Goldstein, L.A., Yeh, Y., Hakkinen, L., Larjava, H.S., Chen, W.T., Regulation of Fibroblast Migration on Collagenous Matrix by a Cell Surface Peptidase Complex. *The Journal of Biological Chemistry*, 2002. 277: p. 29231-29241.
133. Clogston, J.D., Patri, A.K., Detecting and Measuring Free Gadolinium in Nanoparticles for MRI Imaging, In *Characterization of Nanoparticles Intended for Drug Delivery*, *Methods in Molecular Biology*, vol. 697. 2011. Springer Science+Business Media.
134. Lyubchenko, Y.L., Atomic force microscopy imaging of double stranded DNA and RNA. *J Biomol Struct Dyn.*, 1992. 10(3): p. 589-606.
135. Stepanek, P., Data analysis in dynamic light scattering, in: *Dynamic Light Scattering. The Method and Some Applications*. 1993, ed. Brown, W. Oxford: Oxford University Press. 177–240.
136. Frisken, B. J., Revisiting the method of cumulants for the analysis of dynamic light-scattering data. *Appl. Optics*, 2001. 40: p. 4087-4091.
137. Carlfors, J., Rymden, R., Partial specific volume and refractive index increment of polyvinylpyrrolidone in aqueous solutions: Temperature, concentration and wavelength dependence. *Eur. Polym. J.*, 1982. 18: p. 933-937.
138. Pretsch, E., Buhlmann, P., Badertscher, M., ¹³C-Nuclear Magnetic Resonance Spectroscopies, in: *Spectral data for Structure determination of Organic Compounds. Tables of spectral data*. 2009. Springer. 69-156.
139. Conte, P., Spaccini, R., Piccolo, A., State of the art of CPMAS ¹³C-NMR spectroscopy applied to natural organic matter. *Progress in Nuclear Magnetic Resonance Spectroscopy*, 2004. 44: p. 215–223.

140. Lau, C., Mi, Y., A study of blending and complexation of poly(acrylic acid)/poly(vinyl pyrrolidone). *Polymer*, 2002. 43: p.823-829.
141. Sherwood, P.M.A., Practical Surface Analysis. Ed. Briggs, D., Seah , M.P. 1990. New York: Wiley.
142. Wagner, C.D., Davis, L.E.,Riggs, W.M., The energy dependence of the electron mean free path. *Surf. Interface Anal.* 1986. 2: p. 5-8.
143. Touchal, S., Jonquières, A., Clément, R., Lochon, P., Copolymerization of 1-vinylpyrrolidone with N-substituted methacrylamides: monomer reactivity ratios and copolymer sequence distribution, *Polymer*, 2004. 45: p. 8311–8322.
144. Musyanovych, A., Adler, H.J.P., Grafting of Amino Functional Monomer onto Initiator-Modified Polystyrene Particles, *Langmuir*, 2005. 21: p. 2209–2217.
145. Maruthamuthu, M., Subramanian E., Binding of Evans Blue onto Poly (NVinyl-2-Pyrrolidone). *Polym Bull.* 1985. 14: p. 207-212.
146. Luan, Y., Song, A., Xu, G., Location of probe molecule in double-chain surfactant aggregates in absence and presence of water-soluble polymer by NMR, *Soft Matter*, 2009. 5(13): p. 2587-2595.
147. Szàraz, I., Forsling, W., A spectroscopic study of the solvation of 1-vinyl-2-pyrrolidone and poly(1-vinyl-2-pyrrolidone), *Polymer*, 2000. 41: p. 4831–4839.
148. Anseth, K.S., Bowman, C.N., Brennon-Peppas L., Mechanical properties of hydrogels and their experimental determination. *Biomaterials*, 1996. 17: p. 1647-1657.
149. Rubinstein, M., Colby, R., *Polymer Physics*, 2003. New York: Oxford University Press.
150. Flory, P.J., *Principles of Polymer Chemistry*,1953. New York: Cornell University Press.
151. LoPresti C., Vetri V., Ricca M., Foderà V., Tripodo G., Spadaro G., Dispenza C. Pulsatile protein release and protection using radiation-crosslinked polypeptide hydrogel delivery devices. *Reactive and Functional Polymers*, 2011. 71: p. 155–167.
152. Peppas, N. A., Hilt, J. Z., Khademhosseini, A., Langer, R., *Hydrogels in Biology and Medicine: From Molecular Principles to Bionanotechnology*. *Adv. Mater.*, 2006. 18: p. 1345–1360.

153. Ricca, M., Foderà, V., Giacomazza, D., Leone, M., Spadaro, G., Dispenza, C., Probing the internal environment of PVP networks generated by irradiation with different sources. *Colloid Polym Sci*, 2010. 288: p. 969–980.
154. Nakanishi, K., *Infrared Absorption Spectroscopy*. 1962. San Francisco: Holden-Dy.
155. Silverstein, R.M., Bassler, G.C., Morrill, T.C., *Spectrometric Identification of Organic Compounds*, 3rd ed. 1974. New York: John Wiley & Sons, Inc.
156. Guilbaud, J.B., Cummings, L., Khimyak, Y.Z., Encapsulation of Indomethacin in PVP: Solid-State NMR Studies. *Macromol. Symp.*, 2007. 251: p. 41–46.
157. Boyer, R.F., Dependence of mechanical properties on molecular motions in polymers. *Polym. Eng. Sci*, 1968. 8: p. 161–185.
158. Fawcett, A. H., *Polymer Spectroscopy*, 1st ed., 1996. John Wiley & Sons.
159. Moulder, J.F., Stickle, W.F., Sobol, P.E., Bomben, K.D., *Handbook of X-Ray Photoelectron Spectroscopy*, in Physical Electronics Inc.: Eden Prairie. Eds. Chastain, J., Jr King, R.C., 1995. MN, USA.
160. Sionkowska, A., Wisniewski, M., Kaczmarek, H., Skopinska, J., Chevallier, P., Mantovani, D., Lazare, S., Tokarev, V., The influence of UV irradiation on surface composition of collagen/PVP blended films. *Appl.Surf.Sci.*, 2006. 253: p. 1970-1977.
161. Thissen, H., Johnson, G., Hartley, P.G., Kingshott, P., Griesser, H.J. , Two-dimensional patterning of thin coatings for the control of tissue outgrowth. *Biomaterials*, 2006. 27: p. 35-43.
162. Kratochvil, P., *Classical Light Scattering from Polymer Solutions*. 1987. Amsterdam: Elsevier.
163. Lanz, E., Gregor, M., Slavik, J., Kotyk, A., Use of FITC as a Fluorescent Probe for Intracellular pH Measurement. *J. Fluoresc.*, 1997. 4: p. 317-319.
164. Martin, M.M., Lindqvist, L., PH-dependence of fluorescein fluorescence. *J. Lumin.*, 1975. 10: p. 381-390.
165. H. Diehl, H., R. Markuszewski, R., Studies on fluorescein - VII. The fluorescence of fluorescein as a function. *Talanta*, 1989. 36(3): p. 416-8
166. Klonis, N., Clayton, A.H.A., Voss Jr., E.W., Sawyer, W.H., Spectral properties

of fluorescein in solvent-water mixtures: applications as a probe of hydrogen bonding environments in biological systems. *Photochem. Photobiol.*, 1998. 67: p. 500-510.

167. Martin, M.M., Hydrogen bond effects on radiationless electronic transitions in xanthene dyes., *Chem. Phys. Lett.*, 1975. 35: 105-111.

168. Zeng, H.H., Wang, K.M., Yang, X.H., Yu, R.Q., Fibre-optic sensor for the determination of carboxylic acids based on fluorescence enhancement of lipophilized fluorescein isologues. *Anal. Chim. Acta*, 1994. 287: p. 267-272.

Studies of network organization and dynamics of e-beam crosslinked PVPs:

From macro to nano.

C. Dispenza, N. Grimaldi*, M.A. Sabatino, S. Todaro, D. Bulone,

D. Giacomazza, G. Przybytniak, S. Alessi, G. Spadaro.

2012. Rad. Phys. Chem. 81(9), 1349–1353.



ELSEVIER

Contents lists available at [SciVerse ScienceDirect](http://www.sciencedirect.com)

Radiation Physics and Chemistry

journal homepage: www.elsevier.com/locate/radphyschem

Studies of network organization and dynamics of e-beam crosslinked PVPs: From macro to nano

C. Dispenza^{a,b}, N. Grimaldi^{a,*}, M.-A. Sabatino^a, S. Todaro^a, D. Bulone^b, D. Giacomazza^b, G. Przybytniak^c, S. Alessi^a, G. Spadaro^a

^a Dipartimento di Ingegneria Chimica, Gestionale, Informatica, Meccanica, Università degli Studi di Palermo, Viale delle Scienze Ed. 6, 90128 Palermo, Italy

^b CNR – Istituto di Biofisica (Palermo unit), Via U. La Malfa 153, 90146 Palermo, Italy

^c Centre for Radiation Research and Technology, Institute of Nuclear Chemistry and Technology, Dorodna 16, 03-195 Warsaw, Poland

ARTICLE INFO

Article history:

Received 21 September 2011

Accepted 24 November 2011

Available online 3 December 2011

Keywords:

e-Beam irradiation

PVP aqueous solutions

Nanogels

Dynamic mechanical spectroscopy

NMR spin–lattice relaxation

ABSTRACT

In this work the influence of poly(N-vinyl pyrrolidone) (PVP) concentration in water on the organization and dynamics of the corresponding macro-/nanogel networks has been systematically investigated. Irradiation has been performed at the same irradiation dose (within the sterilization dose range) and dose rate. In the selected irradiation conditions, the transition between macroscopic gelation and micro-/nanogels formation is observed just below the critical overlap concentration (~ 1 wt%), whereas the net prevalence of intra-molecular over inter-molecular crosslinking occurs at a lower polymer concentration (below 0.25 wt%). Dynamic–mechanical spectroscopy has been applied as a classical methodology to estimate the network mesh size for macrogels in their swollen state, while ^{13}C NMR spin–lattice relaxation spectroscopy has been applied on both the macrogel and nanogel freeze dried residues to withdraw interesting information of the network spatial organization in the passage of scale from macro to nano.

© 2011 Elsevier Ltd. All rights reserved.

1. Introduction

Among the different synthetic methodologies for the production of hydrogels much interest has been paid to the use of e-beam radiation processing, as it generally yields highly pure materials through environmentally friendly and economically viable processes (Rosiak and Olejniczak, 1993; Rosiak et al., 1995; Rosiak and Yoshii, 1999; Lugao and Malmonge, 2001; Chmielewski et al., 2005; Peppas et al., 2006). It is also well known that one of the most appealing features of radiation processing is the possibility of tuning structure and properties of networks obtained from the same feedstock materials through an apt choice of processing parameters (Ulanski and Rosiak, 1999; Henke et al., 2005; An, 2009). As a consequence, convincing structure–process–properties relationships have to be set in place. When gelation is macroscopic, thereby occurring mainly in virtue of inter-molecular crosslinking, the crosslink density is often estimated by means of macroscopic swelling, mechanical or dynamic–mechanical data (Anseth et al., 1996; Kofonas and Cohen, 1997). These methodologies lead to average values of network mesh size that are a convincing description of the network organization only for homogeneous

network structures. This is not often the case of radiation cross-linked networks (D'Errico et al., 2008; Ricca et al., 2010). Furthermore, these conventional characterization methodologies are not suitable for nanogels.

In this work, information on the network organization and dynamics at different length-scales for hydrogels produced by e-beam irradiation from aqueous solutions of a commercial grade poly(N-vinyl-pyrrolidone) (PVP) has been sought. In particular, an irradiation dose of 40 kGy, therefore within the sterilization dose range, at controlled low temperature and average dose rate of 30 Gy/s has been applied. Different polymer concentrations, from above to below the critical chain overlap concentration for the chosen polymer (~ 1 wt%), have been investigated yielding macrogels and micro-/nanogels. The yield of crosslinking reactions has been estimated gravimetrically and the morphology of the macro/nanogel dry residues has been characterized through scanning electron microscopy (SEM). Conventional swelling and rheological characterizations have been applied to the macrogels, while nanogels' particle size distribution has been determined by dynamic light scattering measurements. A unifying description in terms of network crosslinking density has been attempted through evaluation of spin–lattice relaxation times in the rotating frame ($T_{1\rho}$) from ^{13}C Cross Polarization-Magic Angle Spinning Nuclear Magnetic Resonance ($^{13}\text{C}\{^1\text{H}\}$ CP-MAS NMR) spectroscopy.

* Corresponding author. Tel.: +39 9123863738; fax: +39 9123860841.
E-mail address: nataschia.grimaldi@unipa.it (N. Grimaldi).

2. Experimental

PVP k60 (Aldrich, $M_n = 1.60 \times 10^5$ g/mol, $M_w = 4.1 \times 10^5$ g/mol and radius of gyration, $R_g = 27$ nm the last two from static light scattering measurements), was supplied as 45 wt% aqueous solution. PVP critical chain overlapping concentration in water, ~ 1 wt%, was determined by intrinsic viscosity measurements and confirmed by laser light scattering measurements (Dispenza et al., 2011).

All solutions were carefully deoxygenated by gaseous nitrogen and bottled in hermetically closed 15 ml glass vials. Solutions at 0.5, 0.25, 0.1 and 0.05 wt% were also saturated by N_2O prior to irradiation in order to increase the concentration of hydroxyl radicals formed from water radiolysis during irradiation. Electron beam irradiation was performed using LAE 13/9, a 10 MeV linear accelerator of the ICHTJ of Warsaw (Poland) at 0–4 °C. Irradiation conditions were set to have an average current of 0.08 μ A, pulse duration and frequency of 10–12 μ s and 37.5 Hz, respectively. Total absorbed dose and homogeneous dose distribution along the samples were measured by film polyvinyl chloride dosimeters on a basis of UV–vis absorbance at 396 nm. Macroscopically gelled systems were separated from their soluble portions by immersion for 72 h in excess double-distilled water at 40 °C and successively freeze-dried.

After irradiation, samples at 0.5, 0.25, 0.1 and 0.05 wt% were dialyzed against distilled water for 48 h using dialysis tubes of 100 kDa cut-off (Aldrich). For these systems the yield of the process was determined gravimetrically by comparing the dry weight of the polymer in the sample before and after irradiation followed by dialysis. For PVP solutions at higher concentrations, 10–2 wt%, the gel fractions were determined by Soxhlet extraction for 24 h, using water as solvent. The gel fraction was determined as ratio of the water-insoluble part with respect to the total amount of the dry sample before extraction. The reported results are the average of minimum three independent measurements and the experimental error was $\pm 2\%$.

The morphology of both macro and nanogels' dried residues has been investigated by a field emission scanning electron microscopy (FESEM) system (JEOL) at an accelerating voltage of 10 kV. Swelling measurements were carried out according to an established methodology (Dispenza et al., 2011). Rehydration ratio is defined as $RR = w_s/w_d$, where w_s and w_d are the measured weights of the hydrogel in the swollen and dry states, respectively. Dynamic–mechanical properties of the hydrogels were assessed by small-amplitude shear experiments. Tests were performed using a Stress-controlled Rheometer Ar 1000TA Instruments with an aluminum plate geometry (diam. 20 mm), gap of 1000 μ m and temperature of 25 ± 1 °C. The mechanical response of the material is expressed in terms of shear storage or elastic modulus, G' , and shear loss modulus, G'' , as a function of the frequency. Frequency sweep tests were performed in the LVR at frequency values ranging from 0.01 to 200 rad/s at the controlled stress of 10 Pa, as determined by preliminary strain sweep tests over the range 1–1000 Pa.

The hydrodynamic radius, R_h , of the irradiated PVP samples were measured by dynamic light scattering (DLS) techniques, using a Brookhaven Instruments BI200-SM goniometer. Samples were kept at constant temperature of 20 ± 0.1 °C. The light scattered intensity and time autocorrelation function were measured using a Brookhaven BI-9000 correlator and a 100 mW Ar laser (Melles Griot) tuned at $\lambda = 632.8$ nm. Measurements were taken at different scattering vectors $q = 4\pi n \lambda / \sin(\theta/2)$, where n is the refraction index of the solution, λ is the wavelength of the incident light and θ is the scattering angle. Samples were placed in the quartz cell used for the measurement, as produced, after dilution with bidistilled water and/or syringe filtration (0.8, 0.45

and 0.22 μ m pore size—Millipore). Because samples showed low polydispersity, dynamic light scattering data were analyzed by the method of cumulants. According to this method the logarithm of the field-correlation function can be written in terms of a polynomial of the delay time τ . This function can be then easily fitted by application of linear least-squares technique. Mean hydrodynamic radius of nanoparticles and standard deviation (the amplitude of size distribution curve) can be calculated accordingly (Stepanek, 1993).

^{13}C Cross Polarization–Magic Angle Spinning Nuclear Magnetic Resonance (^{13}C { 1H } CP-MAS NMR) spectra were obtained at room temperature through a Bruker Avance II 400 MHz (9.4T) spectrometer operating at 100.63 MHz for the ^{13}C nucleus with a MAS rate of 13 kHz, 1024 scans, a contact time of 1.5 ms and a repetition delay of 4 s. All samples were placed in 4 mm zirconia rotors with KEL-F caps. The proton spin–lattice relaxation time in the rotating frame $T_{1\rho}H$ was determined with the variable spin lock (VSL) pulse sequence using delay times ranging from 0.1 to 7.5 ms and a contact time of 1.5 ms.

3. Results and discussion

At a preliminary visual inspection, the irradiated samples from solutions at 10, 8 and 6 wt% appear completely macroscopically gelled, while at 4, 2 and 0.5 wt% present both macrogel islands and a separated aqueous phase. At lower concentrations, all irradiated systems appear optically transparent liquids and would be “traditionally” classified as “sols”.

“Gel fraction” values for macroscopic gels are reported in Table 1. Systems from 10 to 2 wt% have similar high gel fraction values (above 85%), while the “0.5 wt%” system has a lower but still significant gel fraction (about 55 wt%) and the sol fraction shows the presence of nanoparticles, as it will be discussed in the following. Mass recovery from dialysis and freeze drying of systems with PVP concentration below 0.5 wt% was always higher than 90%. SEM morphology of PVP macro and nanogels can be observed in Fig. 1. The dry nanogel particles of the “0.25 wt%” system form a thin layer of sub-micron globular aggregates (Fig. 1a). Freeze-dried residues of macrogels obtained at 2, 4 and 8 wt% are shown in Fig. 1b–d. While at 2 wt% the freeze dried gels does not present porosity, increasing polymer concentration, up to 6 wt%, a fairly regular porous structure is evidenced. Above this value, porosity is reduced in size with evident heterogeneity in size distribution.

The dynamic storage, G' , and loss moduli, G'' , as function of frequency are shown in Fig. 2. G' and G'' values at 1 Hz are also reported in Table 1. It can be observed that, in the investigated angular frequency range, G' values are almost constant and higher than the corresponding G'' values. This indicates that gels formed by irradiation in these conditions are typical “strong gel”, i.e. with prevalent elastic behavior (Anseth et al., 1996). Looking closer at the influence of the polymer concentration, from 2 to 6 wt%, G' increases, while G'' is almost constant. At higher concentration

Table 1

Gel fraction, shear storage modulus (G'), shear loss modulus (G'') at 1 rad/s, molecular weight of the polymer chain between two neighboring crosslinking points (M_c), and network mesh size (ξ), and rehydration ratio at plateau (RR_{plateau}).

Pol. conc. (wt%)	GF (%)	G' (Pa)	G'' (Pa)	M_c (Da)	ξ (nm)	RR_{plateau}
10	91.2	1974	21	48848	11.5	25.3
8	92.8	2811	33.5	37468	11.4	27.5
6	94	3385	70	28343	11.4	21.3
4	93.5	2260	76.	33007	12.6	20.4
2	86	1740	75	32900	14.0	16.5

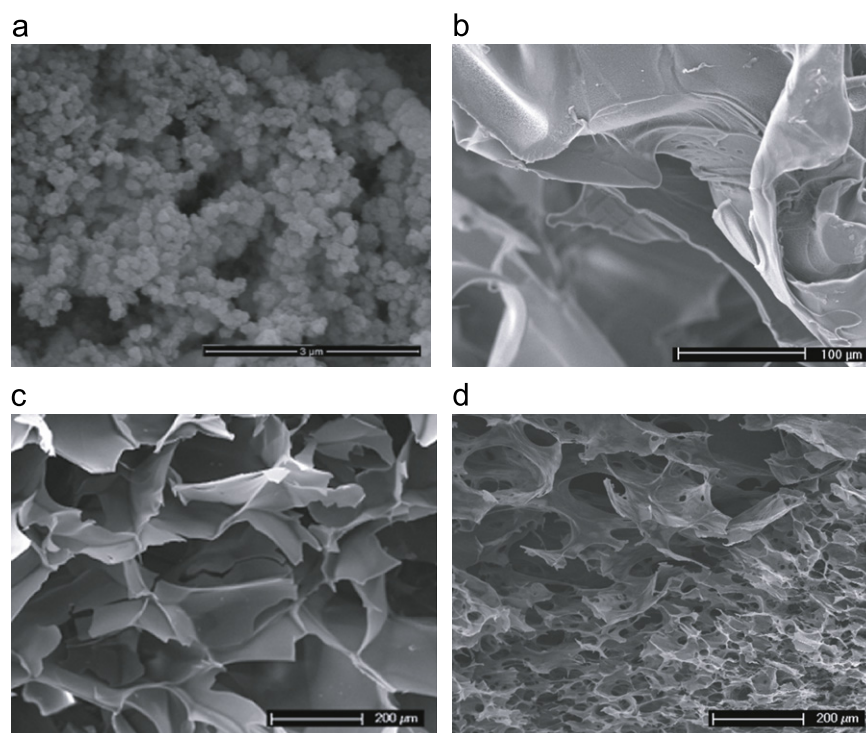


Fig. 1. SEM images of dried residues of hydrogels obtained at the variance of polymer concentration in water: (a) 0.25 wt%; (b) 2 wt%; (c) 4 wt%; (d) 8 wt%.

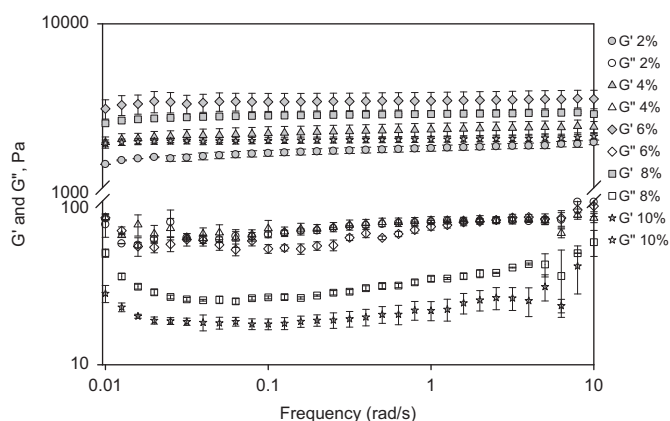


Fig. 2. Storage modulus, G' , (a) and loss modulus, G'' , (b), as function of the frequency of macrogels obtained at the variance of polymer concentration in water.

(8 and 10 wt%) a decrease of both G' and G'' occurs. The G' increase for systems ranging from 2 to 6 wt% can be attributed to the increase of crosslinking density. Above 6 wt% the crosslinking density may further increase locally, but at the expense of the spatial network homogeneity yielding very compact but weakly interconnected clusters. Accordingly, G'' decreases: the reduction of dissipative phenomena, evidenced by the decrease of G'' , can be explained with the relative easiness of mutual slipping of neighboring densely crosslinked clusters. The average molecular weight between two adjacent crosslinks, M_c , and the average distance between crosslinks or mesh size, ζ , were calculated from well known equations derived from the general theory of rubber elasticity (Rubinstein and Colby, 2003; Flory, 1953; LoPresti et al., 2011) and reported in Table 1. The lowest M_c pertains to the macrogel at 6 wt%. Increases in M_c , as well as of network mesh size, for concentrations below this value may reflect a looser networked structure. Conversely, hydrogels at 8 and 10 wt% combine lower ζ values with higher average molecular weight

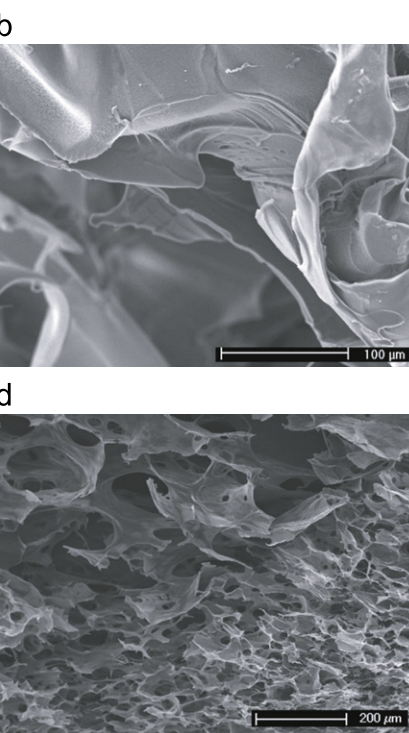


Table 2

Mean hydrodynamic radius and standard deviation of nanogels obtained at different polymer concentrations.

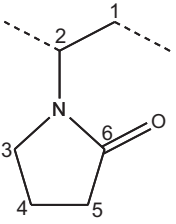
	Av. R_h , nm (Std. Dev.)			
	0.5 (Sol fract.)	0.25	0.1	0.05
Not irradiated	22 (3)	22 (8)	20 (10)	20 (9)
Irradiated	36 (8)	60 (14)	15 (4)	13 (4)

between adjacent crosslinks. In the aforementioned hypothesis of spatial heterogeneity of the networks for these two systems, the two average molecular parameters calculated from a bulk macro-mechanical behavior found the limit of their usefulness.

The RR plateau values are in well agreement with the above discussed hypothesis on the network organization of macrogels. The poorly developed network of the 2 wt% system, upon freeze-drying, collapses into a non-porous solid (see Fig. 2b) that cannot be fully rehydrated. The yet limited number of crosslinking points, in fact, reduces the polymer chains mobility, thus preventing full hydration of PVP polar groups and activation of the typical hydrogel swelling driving forces, such as capillary and osmotic forces (Peppas et al., 2006). The 4 and 6 wt% systems can be considered proper “wall to wall” macrogels that optimally combine chain elasticity and network permeability, thus ensuring “reversibility” of the freeze-drying/rehydration processes. Finally, 8 and 10 wt% systems show high RR values at plateau. For the postulated inhomogeneity in the distribution of crosslink points, the RR measured see the modest contribution of the highly cross-linked regions and a most conspicuous contribution of the looser tie zones.

The soluble part of the 0.5 wt% system and all the other systems produced at lower polymer concentration have been investigated through dynamic light scattering. In Table 2 the calculated average hydrodynamic radii and relative standard deviations for the scattering angle $\theta=90^\circ$ are reported. Values refer to systems that were subjected to filtration with 0.22 mm pore size filters and to four times dilution with distilled water. It

Table 3
 ^{13}C (^1H) CP-MAS NMR—proton spin lattice relaxation time in the rotating frame of hydrogels.

	$T_{1\rho}\text{H}$ (ms)	Not irradiated	0.25	2	4	6	8
	C_6	21.4 ± 0.2	4.6 ± 0.3	8.4 ± 0.3	8.9 ± 0.3	10.5 ± 0.3	17.6 ± 0.3
	$\text{C}_2\text{--}\text{C}_3$	14.3 ± 0.3	9.8 ± 0.4	8.6 ± 0.4	8.3 ± 0.2	12.3 ± 0.3	12.6 ± 0.3
	C_1	13.9 ± 0.3	11.3 ± 0.5	8.7 ± 0.5	12.3 ± 0.3	11.9 ± 0.3	18.7 ± 0.2
	C_5	15.5 ± 0.5	13.0 ± 0.3	8.5 ± 0.3	14.4 ± 0.3	10.6 ± 0.3	11.7 ± 0.3
	C_4	35.3 ± 0.7	6.0 ± 0.3	8.7 ± 0.3	11.2 ± 0.5	13.3 ± 0.5	21.4 ± 0.4

is worth noting that decay curves, here not shown for the sake of brevity, were the same for systems at different dilution ratios and before and after successive filtration with filters of 5, 1.2, 0.8 and 0.45 μm , thus indicating that all the systems are fairly stable colloids. Further filtration with 0.22 μm leaves unaffected the decay curves of the 0.5 and 0.25 wt% formulations but causes a slight reduction in scattering light intensity for 0.1 and 0.05 wt% systems. Finally, measurements carried out at the variance of the scattering angle, in the range of 30–150°, lead always to the same average hydrodynamic diameters. Standard deviations are only slightly higher at the lowest value in the range. The 0.5 and 0.25 wt% systems present nanoparticles with average hydrodynamic radii of 32 and 50 nm, respectively, that are higher than those of the unirradiated PVP coils. This can be due to the occurrence of both intermolecular and intramolecular crosslinking. On the contrary, nanogels obtained from 0.1 and 0.05 wt% solutions have hydrodynamic radii lower than that of the corresponding unirradiated systems. In this case, intramolecular crosslinking may be the prevailing phenomenon, according to the already reported effect of polymer concentration on the nanogels size (Ulanski and Rosiak, 1999). No reduction of average weight molecular weight has been observed in these irradiation conditions, as determined by static light scattering.

In Table 3 the proton spin lattice relaxation times in the rotating frame ($T_{1\rho}\text{H}$) are reported, both for linear PVP and the lyophilized irradiated systems. It is known that $T_{1\rho}\text{H}$ values are sensitive to the molecular motions, which occur in the kHz regions and are associated with cooperative polymer backbone rearrangements, which envelop the collective motions of a large number of monomer units (Boyer, 1968).

As a general consideration, the $T_{1\rho}\text{H}$ values are higher for linear PVP than the corresponding values for the irradiated ones. This indicates that the local motions of the linear polymer are more hindered, probably due to the higher packaging density attained in the solid state from the flexible linear PVP chains and establishment of extensive inter and intra-molecular interactions, such as water molecules mediated hydrogen bonding as well as electrostatic interactions between the negatively charged carbonyl groups and positively charged amino groups of different pyrrolidone rings formed by keto–enol tautomerization. Upon crosslinking, the reduced mobility of macromolecular segments makes the establishment of inter/intramolecular interactions in the solid state less efficient and $T_{1\rho}\text{H}$ values are comparatively lower. A comparison among the different irradiated macrogels shows that increasing the polymer concentration, the $T_{1\rho}\text{H}$ values steadily increase, thus suggesting a monotonic increase of crosslinking density. These results support the interpretation of the rheological data, which showed for the 8 wt% system, a decrease of both G' and G'' values, with respect to the systems with lower polymer concentration. Finally, the data for the lyophilized nanogel (0.25 wt% system) indicates the formation of a faster

relaxing structure with respect to the linear PVP with $T_{1\rho}\text{H}$ values close to the corresponding values for the 4 and 6 wt% macrogels. The very low relaxation times for C_6 and C_4 reflect a partial modification of chemical structure of PVP in these two positions, observed for the nanogels only, that will be the subject of a further dedicated paper.

4. Conclusions

It is well known that high dose-rate pulsed electron irradiation leads to either macrogels or nanogels depending on the polymer concentration in water. Here we have irradiated aqueous solutions of a commercial PVP at concentrations ranging from above (10 wt%) to below (0.05 wt%) its critical chain overlap concentration ($C^* \cong 1$ wt%) with an integrated dose that is within the sterilization dose range (40 kGy). When gelation is macroscopic, thereby occurring mainly in virtue of inter-molecular crosslinking, the average crosslink density can be estimated by dynamic-mechanical data. When the network crosslinking density is not homogeneous or when the network is nanoscalar in size this conventional approach is not applicable. Solid-state ^{13}C NMR has been applied to calculate the spin–lattice relaxation times in the rotating frame ($T_{1\rho}\text{H}$) for the different carbon atoms of the PVP repetitive unit, to observe that crosslinking is associated to a general reduction of relaxation times of the dry gels with respect to the solid linear polymer, due to the reduced stacking ability of macromolecules upon crosslinking. The spin–lattice relaxation times, that are associated to the mobility of molecular segments in the scale of nanometers, gradually increase with the increase of polymer concentration in water for macrogels, thus confirming more and more densely crosslinked networks. Conversely, at the higher concentrations in the range the average elastic moduli from rheological data decrease, as G' is mainly affected by the loss of spatial homogeneity at the scale of tens of nanometers, leading to highly unrealistic estimated average mesh size values. The same technique can be applied to the formed nanoscalar networks, or nanogels, generated at concentrations lower than C^* , although particular care has to be paid to any eventual structural modification of the polymer. This aspect of high energy irradiation induced modification of the polymer will be specifically addressed in a dedicated paper owing to its fundamental and application-related importance.

Acknowledgments

Solid-state ^{13}C NMR experimental data were provided by Centro Grandi Apparecchiature – UniNetLab – Università di Palermo funded by P.O.R. Sicilia 2000–2006, Misura 3.15 Quota Regionale.

This work was partially supported by the IAEA CRP: “Nanoscale radiation engineering of advanced materials for potential biomedical applications” and FW7 COST Action MP0701.

References

- An, J.-C., 2009. Synthesis of poly(vinyl pyrrolidone) nanohydrogels by the template-assisted ionizing radiation. *J. Ind. Eng. Chem.* 15, 148–152.
- Anseth, K.S., Bowman, C.N., Brennon-Peppas, L., 1996. Mechanical properties of hydrogels and their experimental determination. *Biomaterials* 17, 1647–1657.
- Boyer, R.F., 1968. Dependence of mechanical properties on molecular motion in polymers. *Polym. Eng. Sci.*, 161–185 (Society of Plastics Engineers, Inc.).
- Chmielewski, A.G., Haji-Saeid, M., Ahmed, S., 2005. Progress in radiation processing of polymers. *Nucl. Instrum. Methods Phys. Res. Sect. B* 236, 44–54.
- D'Errico, G., De Lellis, M., Mangiapia, G., Tedeschi, A., Ortona, O., Fusco, S., Borzacchiello, A., Ambrosio, L., 2008. Structural and mechanical properties of UV-photocrosslinked poly(vinyl-2-pyrrolidone) hydrogels. *Biomacromolecules* 9, 231–240.
- Dispenza, C., Ricca, M., LoPresti, C., Battaglia, G., La Valle, M., Giacomazza, D., Bulone, D., 2011. E-beam irradiation and UV photocrosslinking of microemulsion-laden poly(N-vinyl-2-pyrrolidone) hydrogels for “in-situ” encapsulation of volatile hydrophobic compounds. *Polym. Chem.* 2, 192–202.
- Flory, P.J., 1953. *Principles of Polymer Chemistry*. Cornell University Press, New York.
- Henke, A., Kadlubowski, S., Rosiak, J.M., Arndt, K.F., 2005. Radiation-induced cross-linking of polyvinylpyrrolidone-poly(acrylic acid) complexes. *Nucl. Instrum. Methods Phys. Res. Sect. B* 263, 391–398.
- Kofonas, P., Cohen, R., 1997. Development of methods for quantitative characterization of network morphology in pharmaceutical hydrogels. *Biomaterials* 18, 1361–1369.
- LoPresti, C., Vetri, V., Ricca, M., Foderà, V., Tripodo, G., Spadaro, G., Dispenza, C., 2011. Pulsatile protein release and protection using radiation-crosslinked polypeptide hydrogel delivery devices. *React. Funct. Polym.* 71, 155–167.
- Lugao, A.B., Malmonge, S.M., 2001. Use of radiation in the production of hydrogels. *Nucl. Instrum. Methods Phys. Res. Sect. B* 185, 37–42.
- Peppas, N.A., Hilt, J.Z., Khademhosseini, A., Langer, R., 2006. Hydrogels in biology and medicine: from molecular principles to bionanotechnology. *Adv. Mater.* 18, 1345–1360.
- Ricca, M., Foderà, V., Giacomazza, D., Leone, M., Spadaro, G., Dispenza, C., 2010. Probing the internal environment of PVP networks generated by irradiation with different sources. *Colloid Polym. Sci.* 288, 969–980.
- Rosiak, J.M., Olejniczak, J., 1993. Medical applications of radiation formed hydrogels. *Radiat. Phys. Chem.* 42, 903–906.
- Rosiak, J.M., Ulanski, P., Pajewski, L.A., Yoshii, F., Makuuchi, K., 1995. Radiation formation of hydrogels for biomedical purposes. Some remarks and comments. *Radiat. Phys. Chem.* 46, 161–168.
- Rosiak, J.M., Yoshii, F., 1999. Hydrogels and their medical applications. *Nucl. Instrum. Methods Phys. Res. Sect. B* 151, 56–64.
- Rubinstein, M., Colby, R., 2003. *Polymer Physics*. Oxford University Press, New York.
- Stepanek, P., 1993. Data analysis in dynamic light scattering. In: Brown, W. (Ed.), *Dynamic Light Scattering*. Oxford University, Oxford, UK, pp. 177–240.
- Ulanski, P., Rosiak, J.M., 1999. The use of radiation technique in the synthesis of polymeric nanogels. *Nucl. Instrum. Methods Phys. Res. Sect. B* 151, 356–360.



Minimalism in Radiation Synthesis of Biomedical Functional Nanogels..

C. Dispenza*, M.A. Sabatino, N. Grimaldi, D. Bulone, M. L. Bondì,

M. P. Casaletto, S. Rigogliuso, G. Adamo, G. Gherzi.

2012. *Biomacromolecules*.13(6), 1805–1817.

Minimalism in Radiation Synthesis of Biomedical Functional Nanogels

Clelia Dispenza,^{*,†,‡} Maria Antonietta Sabatino,[†] Natascia Grimaldi,[†] Donatella Bulone,[‡] Maria Luisa Bondi,[§] Maria Pia Casaletto,[§] Salvatrice Rigogliuso,^{||} Giorgia Adamo,^{||} and Giulio Gherisi^{||}

[†]Dipartimento di Ingegneria Chimica, Gestionale, Informatica, Meccanica, Università degli Studi di Palermo, Viale delle Scienze Ed. 6, 90128 Palermo, Italy

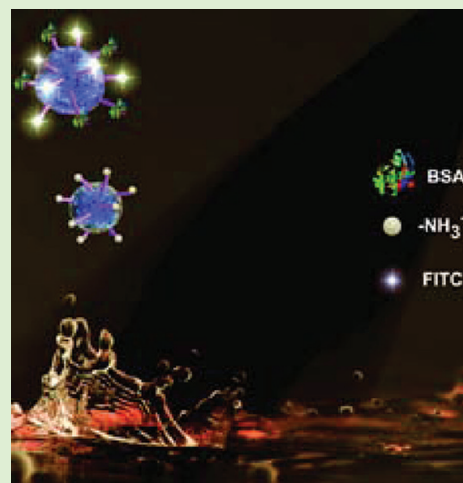
[‡]CNR - Istituto di Biofisica (IBF) UOS Palermo, via Ugo La Malfa 153, 90146 Palermo, Italy

[§]CNR - Istituto per lo Studio dei Materiali Nanostrutturati (ISMN) UOS Palermo, via Ugo La Malfa, 153, 90146 Palermo, Italy

^{||}Dipartimento di Scienze e Tecnologie Molecolari e Biomolecolari, Università degli Studi di Palermo, Viale delle Scienze, Ed. 16, 90128 Palermo, Italy

S Supporting Information

ABSTRACT: A scalable, single-step, synthetic approach for the manufacture of biocompatible, functionalized micro- and nanogels is presented. In particular, poly(*N*-vinyl pyrrolidone)-grafted-(aminopropyl)methacrylamide microgels and nanogels were generated through e-beam irradiation of PVP aqueous solutions in the presence of a primary amino-group-carrying monomer. Particles with different hydrodynamic diameters and surface charge densities were obtained at the variance of the irradiation conditions. Chemical structure was investigated by different spectroscopic techniques. Fluorescent variants were generated through fluorescein isothiocyanate attachment to the primary amino groups grafted to PVP, to both quantify the available functional groups for bioconjugation and follow nanogels localization in cell cultures. Finally, a model protein, bovine serum albumin, was conjugated to the nanogels to demonstrate the attachment of biologically relevant molecules for targeting purposes in drug delivery. The described approach provides a novel strategy to fabricate biohybrid nanogels with a very promising potential in nanomedicine.



INTRODUCTION

Hydrogels have been often proposed as matrices for incorporation and controlled release of drugs, owing to their benign toxicological profile, soft and rubbery consistency, tailored chemical and physical properties.^{1–4} Further opportunities are offered by the control of size and shape of hydrogels down to the micro and the nanoscale. Differently from “gels”, that is, macroscopic networks, their nanometric/micrometric analogues, that is, “nanogels” (NGs) or “microgels” (MGs), may “dissolve” in solvents, just as linear macromolecules do, yet preserving an almost fixed molecular conformation. They may swell in aqueous environments and respond to stimuli, such as temperature, pH, redox potentials, and other modifications of the environmental conditions.^{5,6}

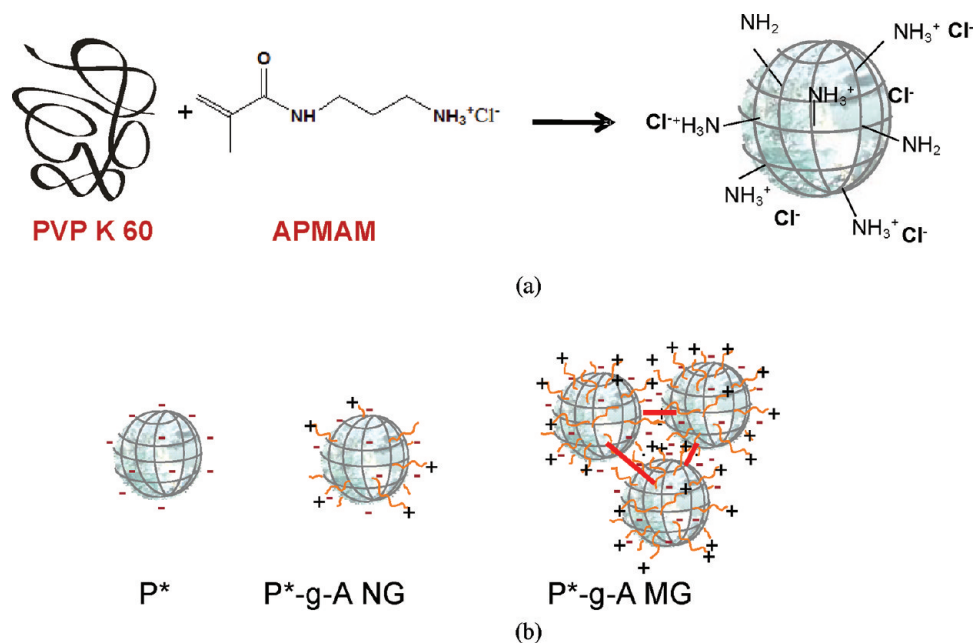
Pharmaceutical NGs bearing reactive groups can represent a convenient alternative to the classical pharmacological treatment for several diseases, particularly in cancer chemotherapy, owing to a more specific and efficient particle surface functionalization, drug uptake, and release features.⁷ One of the main problems associated with the administration of pharmaceutical drugs, in fact, depends on the nonspecificity in recognition of the target sites and consequent homogeneous

distribution of the drug in the body.^{8,9} Functionalized NGs, unlike other biomaterials, offer the unique advantages stemming from spacious aqueous interiors, high surface areas, and tunable, and thereby highly specific, chemical and physical characteristics. The high surface area enables us to bind the carrier with appropriate ligands, creating a system that can improve the localization of the drug near or at the target site. Localization in specific sites can be realized either through “passive targeting”, when it is entrusted only to the best match between morphological, chemical, and physical properties of the carrier and the anatomical and physiological characteristics of the target site, or through “active targeting”, that is realized by binding to the carrier rather appropriate moieties or entire molecules able to interact with membrane receptors on cells of the target site. The availability of inexpensive and robust preparation methodologies of such nanocarriers is at the basis of the development of effective NG-based theragnostic devices, and it has been the main limitation to their development.¹⁰

Received: February 27, 2012

Revised: May 2, 2012

Published: May 10, 2012

Scheme 1^a

^a(a) One-step synthesis of amino-functionalized PVP nanogel via e-beam irradiation. Both PVP and APMAM are present in the irradiated aqueous solution. PVP cross-linking and APMAM monomer grafting occur simultaneously. (b) Schematics of a typical base PVP nanogels (P^*): the polymer network and negative surface charge density are evidenced; amino-grafted PVP (P^* -g-A) nanogels (NG) and microgels (MG). The curly orange lines represent grafted APMAM carrying a primary amino group. Bold red lines represent APMAM monomers or oligomers bridging cross-linked PVP coils.

Our radiation-engineered NGs are conceived to be produced with a process that ensures, simultaneously, polymer cross-linking, particles size control, chemical functionalization, and sterilization of the produced materials. They are characterized by a remarkable chemical and colloidal stability¹¹ and amenability of subsequent decoration with a variety of specific ligands, thus combining the absence of toxicity with the specificity of effects only on selected targets. The structural integrity of the designed NGs will avoid interference between the incorporated therapeutics and polymeric carrier degradation products. It has already been established that NGs can be produced under high-dose pulse irradiation of dilute aqueous solutions of water-soluble polymers.¹² Under these conditions polymer macroradicals form and recombine mainly within the same polymer coil, that is, intramolecularly. As a result, internally cross-linked single macromolecules are formed. Analogies and differences in cross-linking reaction mechanisms and kinetics underlying NGs formation have been discussed,^{13,14} but no adequate efforts have been paid so far in developing formulations based on these findings to generate multifunctional particles with the required properties for application as nanocarriers. With the present work, we have assessed the possibility of generating biocompatible, functionalized MGs and NGs using existing industrial-type electron accelerators and setups, that is, with a robust, economically viable and thereby industrially implementable process. Poly(*N*-vinyl-pyrrolidone) has been chosen as the base material for its known propensity to cross-link under irradiation in water and because it is widely used in pharmaceutical and cosmetic formulations. Water-soluble functional monomers can be added to the polymer aqueous solution before irradiation. Here we are presenting the results obtained with (3-*N*-aminopropyl) methacrylamide hydrochloride, at different concentrations

(see Scheme 1a), chosen to insert primary amino groups amenable to subsequent conjugation with either fluorescent or biological source molecules, for localization and active targeting purposes, respectively. The influence of process parameters on the control of particle size and the feasibility of derivatization reactions with fluorescein isothiocyanate (FITC) and BSA, as a model protein, were investigated.

MATERIALS

Chemicals. PVP K60 (Aldrich, $M_n = 1.60 \times 10^5$ g/mol), (3-*N*-aminopropyl) methacrylamide hydrochloride (APMAM, Polyscience), and FITC (Research Organics) were used without further purification. PVP's molecular weight, $M_w = 4.1 \times 10^5$ g/mol, and radius of gyration, $R_g = 27$ nm, were estimated from the usual Zimm plot analysis¹⁵ of static light scattering measurements, carried out at 25 °C. Dialysis tubes of 12.000 and 100.000 Da cutoff (Membrane Spectra/Por Biotech RC and CE, respectively, Spectrum Laboratories), 0.22 μ m pore size syringe filter (Millipore), and centrifuge filter device 10 kDa cutoff (Centricon 10, Millipore) were used.

Cell Culture Reagents. The osteoblastic cell line MC3T3-E1 from a C57BL/6 mouse calvaria was grown in Dulbecco's modified Eagle's medium (DMEM) supplemented with 10 wt % fetal calf serum (FCS; Euroclone, Celbio), 1 wt % antibiotic, and 1 wt % glutamine (Euroclone, Celbio).

METHODS

Poly(*N*-vinyl pyrrolidone)-grafted-(aminopropyl) Methacrylamide Micro/Nanogels Synthesis. PVP aqueous solutions at 0.1 wt % (equivalent to $\sim 0.9 \times 10^{-2}$ mol of repetitive unit (RU) per liter, respectively) with APMAM (0.045, 0.09, 0.18, and 0.36 mM, corresponding 1:200, 1:100, 1:50, and 1:25 APMAM/PVP's RU molar ratios, respectively) and without APMAM (base PVP NGs) were prepared by overnight stirring, filtered with 0.22 μ m pore size syringe filters, carefully deoxygenated with gaseous nitrogen, and bottled in

glass vials sealed with rubber septa and aluminum caps. Samples were individually saturated with N_2O ($N_2O \geq 99.99\%$) prior to irradiation to increase the concentration of hydroxyl radicals formed from water radiolysis during irradiation.¹⁶

Electron beam irradiation was performed using two 10 MeV linear accelerators at the ICHTJ of Warsaw (Poland), LAE 13/9, and Elektronika 10/10. For irradiation runs with LAE 13/9, parameters were set to have an average beam current of 0.40 μA , pulse length of 10–12 μs , and pulse repetition rate of 75 Hz. The dose per pulse was ~ 1.8 Gy, corresponding to ~ 500 kGy/h. Samples irradiated under these conditions were named after “LX-500”, where X is a number indicating the total absorbed dose in kGy. The homogeneous dose distribution and the integrated absorbed dose by the sample were measured using cellulose triacetate film dosimeters on the basis of absorbance at 298 nm. Sample vials were placed horizontally in front of the electron emission port in a suitable container filled with ice. Temperature during irradiation was measured to be maintained between 5 and 10 $^{\circ}C$.

Irradiation with Elektronika 10/10 was carried out at an average beam current of 0.45 mA, pulse length of 4.5 μs , and pulse repetition rate of 300 Hz. In this case, dosimetry was performed using a graphite calorimeter; the measuring error was $\pm 4\%$. Samples were horizontally placed in a box filled with ice and conveyed under the beam via a transporting belt at a speed of 0.3 m/min. An integrated dose of 40 kGy was supplied with a single pass, whereas the higher dose investigated here (80 kGy) was obtained with a double-pass exposure. The total absorbed dose results from a combination of e-beam accelerator's setup parameters and speed of the conveyer's belt. From a measurement of the residence time of the vials under the beam (~ 10 s) we can estimate an approximate absorbed dose per pulse of ~ 13 Gy. Samples irradiated under these conditions were named after “EX”, where X is the total absorbed dose in kGy.

After irradiation, samples were dialyzed against distilled water for 48 h. Dialysis was initially performed with two different membranes: 12k MWCO and 100k MWCO. Samples recovered from dialysis were subjected to light scattering measurements to compare the intensity of scattered light. Results are reported as Figure S1 of the SI. pH of the systems was measured before and after irradiation and after dialysis at the controlled temperature of 25 ± 1 $^{\circ}C$ with CRISON GLP 22 pH and ion meter. All formulations had a pH of 6.0 to 7.0 prior to irradiation, which turned out to be in the range 3.1 to 4.5 after irradiation and between 4.5 to 5.8 after dialysis.

Product Yield Determination. The yield of the micro/nanogels production process was determined gravimetrically as the weight ratio of recovered product after irradiation, dialysis (MWCO 12k), and freeze-drying and the corresponding initial weight of the polymer and the monomer loaded to the vial. Measurements were always carried out in triplicate from independent irradiation runs.

By dialysis, we expect to remove eventual low-molecular-weight fragments eventually deriving from PVP degradation and APMAM monomer not grafted to the polymer. Homopolymerization of APMAM should be minimal under the selected irradiation conditions, owing to (i) the low concentration of monomer (4.5×10^{-5} to 3.6×10^{-4} M vs 0.9×10^{-2} M of PVP RU) and (ii) the low pH (always lower than APMAM's $pK_a = 8.5$).¹⁷ Repulsive forces acting between charged monomers should effectively prevent them coming into proximity and react. This hypothesis is supported by light

scattering and 1H NMR data collected on irradiated APMAM solutions. (For details, see Figure S2 of the SI.)

Spectroscopic Characterizations. FTIR analysis was carried out with Perkin-Elmer-Spectrum 400 apparatus by dispersing the dry product in potassium bromide and compressing into pellets. Spectra were recorded at 30 scans per spectrum and 1 cm^{-1} resolution in the $4000\text{--}400\text{ cm}^{-1}$ range.

^{13}C $\{^1H\}$ CP-MAS NMR analysis was performed on solid samples with a Bruker Avance II 400 MHz (9.4 T) spectrometer operating at 400.15 MHz for the 1H nucleus and 100.63 MHz for the ^{13}C nucleus with a MAS rate of 13 kHz, 1024 scans, a contact time of 1.5 ms and a repetition delay of 2 s. The optimization of the Hartmann–Hahn condition was obtained using an adamantane standard. All samples were placed in 4 mm zirconia rotors with KEL-F caps. Silica powder was mixed with the samples to obtain a more compact filling of the rotor's volume.

Surface chemical composition of the samples was investigated by XPS in an ultrahigh vacuum (UHV) chamber with a base pressure in the range of 10^{-8} Torr during data collection. Photoemission spectra were collected by a VG Microtech ESCA 3000 Multilab spectrometer, equipped with a standard Al K_{α} excitation source ($h\nu = 1486.6$ eV) and a nine-channeltrons detection system. The hemispherical analyzer operated in the CAE mode, at a constant pass energy of 20 eV. The binding energy (BE) scale was calibrated by measuring C 1s peak (BE = 285.1 eV) from the surface contamination, and the accuracy of the measure was ± 0.1 eV. Photoemission data were collected and processed by using the VGX900 software. Data analysis was performed by a nonlinear least-squares curve-fitting program using a properly weighted sum of Lorentzian and Gaussian component curves, after background subtraction according to Shirley and Sherwood.¹⁸ Surface relative atomic concentrations were calculated by a standard quantification routine, including Wagner's energy dependence of attenuation length¹⁹ and a standard set of VG Escalab sensitivity factors. The uncertainty on the atomic concentration is of the order of 10%.

Light Scattering Measurements. The hydrodynamic radius (R_h) of particles dispersion was measured by dynamic light scattering (DLS) using a Brookhaven Instruments BI200-SM goniometer. Samples, placed in the quartz cell after dilution (0.025 mg/mL) with bidistilled water, were put in the thermostatted cell compartment of the instrument at 20 ± 0.1 $^{\circ}C$. Intensity autocorrelation function at the scattering angle of 90° and time autocorrelation function were measured by using a Brookhaven BI-9000 correlator and a 50 mW He–Ne laser (MellesGriot) tuned at $\lambda = 632.8$ nm. The correlator was operated in the multi- τ mode; the experimental duration was set to have at least 2000 counting on the last channel of the correlation function. All irradiated samples were analyzed as produced, without filtration, to minimize artifacts. Particular care was paid in treating the samples in a clean environment to reduce contamination. No influence of pH on the decay curves when varying from 4 to 6 was observed by the different systems (data here not reported for brevity). In consideration of the fact that the samples showed a monomodal distribution, DLS data were analyzed by the method of cumulants. According to this method, the logarithm of the field-correlation function is expressed in terms of a polynomial in the delay time τ , with the first and second cumulant providing information on the mean value and standard deviation of the distribution of nanoparticles

hydrodynamic size.^{15,20} Measurements were carried out on a minimum two samples from three independent runs. For each formulation and irradiation condition analyzed, very similar results were obtained in terms of particle size distribution. The weight-average molecular weight (M_w) and radius of gyration of PVP in aqueous solution at 25 °C were estimated from Zimm plot of static light scattering measurements at different scattering angles and polymer concentration. The refractive index increment (dn/dc) of PVP in aqueous solution was measured by using a Brookhaven Instruments differential refractometer at $\lambda = 620$ nm. We obtained the value of 0.18 ± 0.004 mL/g in good agreement with a literature value.²¹ When attempting to draw a Zimm plot with scattered light data collected on NGs samples, a strong downward curvature in the scattering angle dependence was observed, probably due to polydispersity and interparticles interactions. This occurrence prevented a reliable determination of extrapolated light scattered values at zero scattering angle. However, a rough estimate of the molecular weight in the case of particular interest was obtained by averaging the values obtained through Debye's plots for each different scattering angle. To determine the relative gyration radius, each data set at different concentration was analyzed in terms of the Guinier's expression: $1/P(q) = 1 + (qR_g)^2/3 + \Theta(q)$, where $P(q) = I(q)/I(q = 0)$ and $q = 4\pi n/\sin(\theta/2)$. Taking q^2 as an independent variable, a polynomial fit of $1/P(q)$ was applied by considering only the points at low q value, and R_g was derived by the first-order coefficient.

ζ -Potential Measurements. The surface charge of the NGs in water was measured according to the principles of laser Doppler velocitometry and phase analysis light scattering (M3-PALS technique) and expressed as ζ potential. It was measured on diluted dispersions (0.025 mg/mL) at 25 °C using a ZetaSizerNano ZS (Malvern Instruments, Malvern, U.K.) equipped with a He–Ne laser at a power of 4.0 mW. As for particle size distribution, also ζ potential measurements were carried out on minimum two samples from three independent runs. Error bars reported in the ζ potential plot refer to the width of the ζ potential distribution for each sample, which was fairly high for some formulations.

Preparation and Characterization of Fluorescent Micro/Nanogels Variants. A given volume (0.6 mL) of MG or NG dispersion was mixed with 0.05 M Borax (pH 9.3) and 0.4 M NaCl aqueous solution (1.4 mL) and with 14 μ g/mL methanol/water solution (0.1 vol % MeOH) of FITC (2 mL). The solution was kept at 37 °C while stirring for 2 h. The FITC conjugated MGs or NGs were then thoroughly dialyzed against pH 7.4 PBS, using a dialysis tubing (MWCO 12–14 kDa), refreshing the solutions twice a day. Different dialysis times were investigated to ascertain that unbound FITC was effectively removed. In general, after 72 h of dialysis, unreacted FITC was removed. With the aim of quantitatively estimating the concentration of reacted amino groups for selected conjugated systems, FITC detachment from P*-g-A NGs was performed by changing the pH of the conjugated NGs' dispersions from 7.4 to 12, adding a small quantity of NaOH (1M). Dispersions were kept stirred at pH 12 and room temperature for 2 h. Afterward, the pH was brought back to 7.4, and the detached FITC was separated from the NGs using a centrifuge filter device (cut off 10 kDa) at a speed of 4000g. The solution of FITC collected under the filter and the NGs retained by the filter and dispersed in a note volume of pH 7.4 PBS was analyzed. In particular, UV–visible absorption and

fluorescence spectroscopy were carried out on (i) the conjugated amino-functionalized MG or NG dispersions (P*-g-A^{FITC}); (ii) the nonconjugated analogues as negative controls (P*-g-A); (iii) free probe solutions as positive controls or solutions separated from NGs after detachment (FITC sol); and (iv) base PVP systems subjected to the same protocols applied for reacting FITC with P*-g-A variants (P*^{FITC}).

UV–visible absorption measurements were carried out with a Shimadzu 2401-PC spectrofluorimeter (scan speed 40 nm/min, integration time 2 s, bandwidth 1 nm) at room temperature. Fluorescence spectra were acquired with a JASCO FP-6500 spectrofluorimeter, equipped with a Xenon lamp (150 W). Emission spectra, at the required excitation wavelength, were obtained with emission and excitation bandwidth of 1 and 3 nm, respectively. Samples were excited at the maximum absorption wavelength for FITC ($\lambda_{ex} \cong 490$ nm). Emission spectra were normalized with respect to the absorption at the excitation wavelength.

Preparation of BSA Conjugated Variants. P*-g-A(100) NGs dispersion (1.2 mL) was incubated with an equal volume of Borax solution (0.05 M - pH 9.3) with NaCl (0.4 M) for 10 min at room temperature. An aqueous solution (600 μ L) containing 1 mg of ultrapure bovine serum albumin (BSA; Sigma-Aldrich) was added. The control system was also prepared as described above, but BSA was not added. The mixtures were then incubated at 37 °C for 2 h, while shaking. Afterward, both BSA conjugated systems (P*-g-A^{BSA}) and relative control were thoroughly dialyzed against PBS using 100 kDa membranes, to allow the release of nonconjugated BSA. To confirm the occurrence of conjugation, samples were tested by a DU 730 Life Science spectrophotometer (Beckman Coulter) in a range between 200 and 500 nm. To quantify the amount of conjugated BSA to the nanoparticles, we built up a calibration curve using solutions with increasing concentrations of the protein. Nanogel-BSA conjugates were stored up to 4 weeks at 4 °C and subjected to UV–vis analysis after double washings with PBS, showing no appreciable changes in the spectra.

Caspase 3 Enzymatic Assay on Synthetic Fluorescent Substrate. MC3T3-E1 cells were seeded at high density on a six-well plate for 24 h in complete medium; then, they were grown for another 24 h after incubation with P*-g-A (100) NGs. Cells were enzymatically detached from culture plate using a solution of Trypsin-EDTA 1X (Sigma) and centrifuged at 1000 rpm for 5 min. Pelleted cells were then resumed in 70 μ L of Triton X 100 (1%) in PBS and incubated 10 min at room temperature; the extract cell proteins suspension was centrifuged at 10,000 rpm for 10 min; then, the pellet containing the cellular bodies and nonextracted portion was removed, while the amount of extracted proteins present in the supernatant was quantified by Bradford microassay method (Bio-Rad, Segrate, Milan, Italy) employing BSA (Sigma-Aldrich) as standard.

MC3T3-E1 cells extracts (20 μ g), obtained as previously described, were used to detect the presence of activated caspases 3/7/8. In the assay, both untreated MC3T3-E1 cells (negative control) and 10 μ M Doxorubicin (DXR, known as apoptotic inducer)-treated cells for 4 h (positive control) were also used. The Ac-Asp-Glu-Val-Asp-MCA peptide (Pepta Nova, Peptide Institute), a specific substrate for activated caspase 3/7/8 (typical apoptosis marker)^{22,23} was used. It ties a fluorophore in its cutting site, which emits fluorescence when activated by enzymes. In these experiments, the previously

described extracts were added to 75 μL (8 μM) of the substrate in a 96-well plate. By spectrofluorimetric reading, it was possible to quantify the degree of caspase activation. The spectrofluorimetric analysis was performed using Spectra Max Gemini EM-500 (Molecular Devices) and elaborated by Soft Max Pro 5.2 software.

MC3T3-E1 Cell Viability by MTT Assay. The MC3T3-E1 cells were seeded in a 96-well plate at density of 1×10^4 cell/well. After 24 h of growth in the presence of the previously described dispersion, cells were washed with PBS and then incubated with 200 μL /well of complete medium containing 0.25 mg/mL of MTT solution for 2 h at 37 C. After solubilization of the resulting formazan product with 100 μL /well of DMSO solution, the absorbance of intense purple staining at 490 nm wavelength was read on a DU-730 Life Science spectrophotometer (Beckman Coulter). MC3T3-E1 cells treated with DXR (5 μM) for 24 h were used as positive control. Each experiment was repeated eight times.

Cellular Internalization Studies: Confocal Analysis. The MC3T3-E1 was grown at a density of 5×10^3 cells/well in 12-well plates containing sterile coverslips in complete DMEM for 24 h. Next, the cells were incubated with a given amount of P*-g-A(100)^{FITC} NGs dispersion (20 μg /well), which emits green fluorescence by FITC conjugation.

After different incubation times, respectively, 30 min, 1, 3, 6, 8, 24, and 48 h, the cells were washed twice with PBS to remove nanoparticles that were not taken up by the cells or were only loosely bound to the cellular membrane, fixed with 3.7 wt % formaldehyde for 15 min, and washed again twice with PBS. Afterward, cells were stained with ethidium bromide (EtBr 1:1000, an intercalating agent commonly used as a fluorescent red tag to label the cell nucleus) for 1 min at room temperature. The nanoparticle position was monitored by confocal microscopy analysis (Olympus 1×70 with MellesGriot laser system); a 1 μm thickness optical section was taken, and about 15 sections were taken for each sample.

Spectrofluorimetric Analysis of Fluorescent Nanoparticles Uptaken by Cells. The MC3T3-E1 cells were seeded in a 96-well tissue plate at a density of 7×10^3 cells/well, grown for 24 h in DMEM complete medium, and incubated in the presence of P*-g-A(100)^{FITC} (4 μg /well) NGs for different times (0, 30 min, 1, 3, 6, 24, and 48 h). For each time, three wells were subjected to spectrofluorimetric readings (excitation at 485 nm and emission at 538 nm) to measure the total fluorescence on the well; then, the cells were separated from the medium and washed twice with PBS. Fluorescence from the nanoparticles present inside the cells, in the separated medium, and in the washings was singularly evaluated using Spectra Max Gemini EM-500 (Molecular Devices, using the Soft Max Pro 5.2 software).

RESULTS AND DISCUSSION

Synthesis and Dimensional Characterization of Micro and Nanogels. It has been already demonstrated that electron beam irradiation applied to semidilute PVP aqueous solutions, at relatively high doses per pulse, can fix a specific polymer conformation in water through only a few intramolecular covalent bonds, thus leading to the formation of micro and nanogels. In N_2O -saturated aqueous solutions of PVP, carbon-centered PVP radicals are promptly formed by the rapid H-abstraction reaction by $\cdot\text{OH}$ and $\cdot\text{H}$, which are the predominant radical species formed in such solutions, with radical yields of approximately 0.58 and 0.06 $\mu\text{mol J}^{-1}$.¹⁶ The decay of PVP

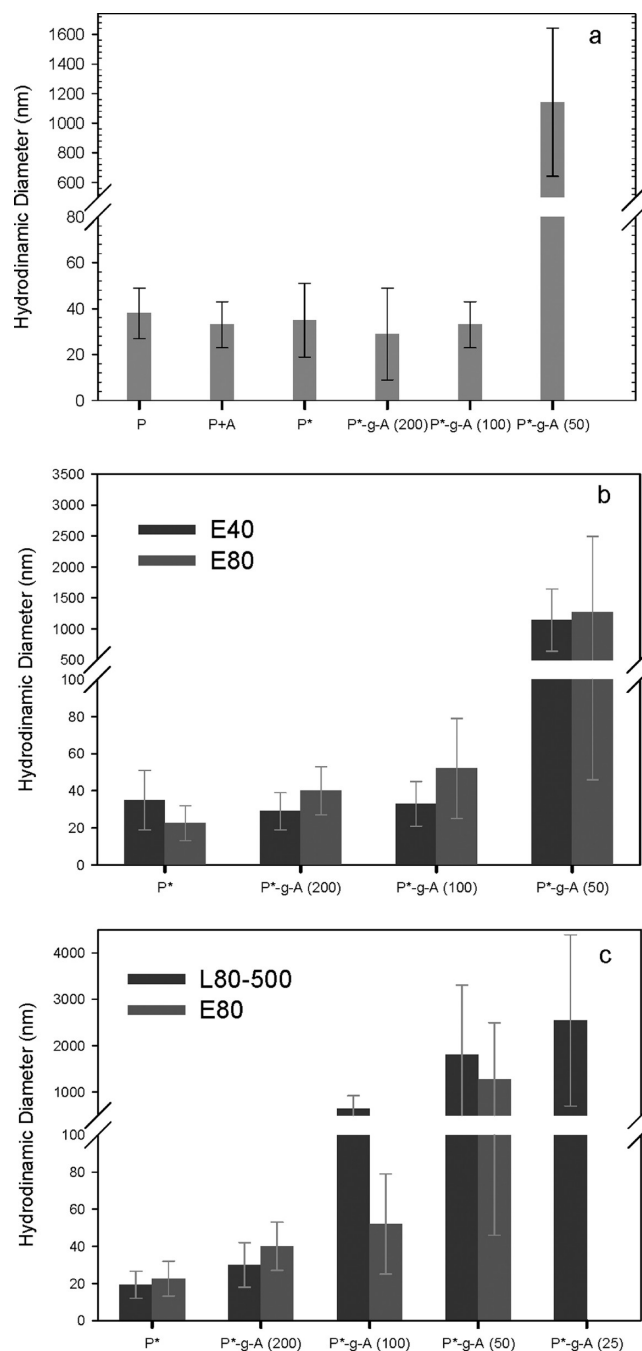


Figure 1. MGs and NGs hydrodynamic diameters from DLS analysis at 20 °C in water. (a) Systems irradiated with low dose-rate and the lower dose (E40). Nonirradiated aqueous PVP both in the presence and in the absence of APMAM is reported for comparison. (b) Influence of irradiation dose for the different formulations. (c) Influence of dose-rate for the different formulations. Error bars represent the variance of the particle size distribution.

radicals after a single pulse imparted to the linear polymer is generally faster than the time between two successive pulses. When the average number of radicals generated on each polymer chain upon a pulse significantly exceeds one, polymer radicals prevalently recombine intramolecularly. NGs can thus be obtained in correspondence of relatively low irradiation doses (5–10 kGy).^{11,12,14,24}

If sterility has to be granted, as it would be desirable for biomedical application of such NGs, then higher irradiation

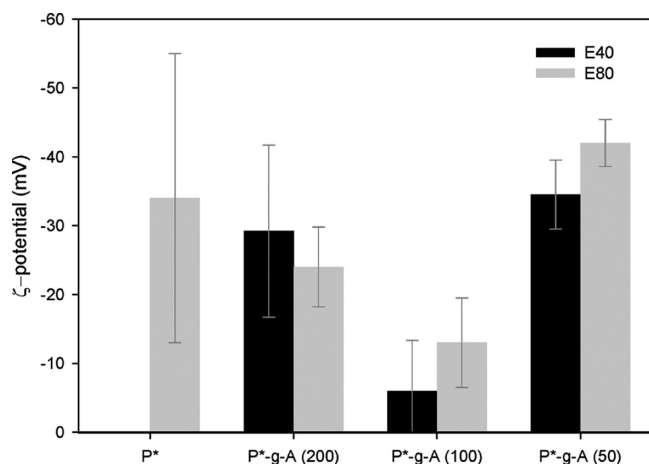


Figure 2. Surface charge density for the micro and nanogels produced at the different PVP RU/APMAM molar ratios and at the two doses of 40 and 80 kGy. Error bars represent the width of the surface charge distribution.

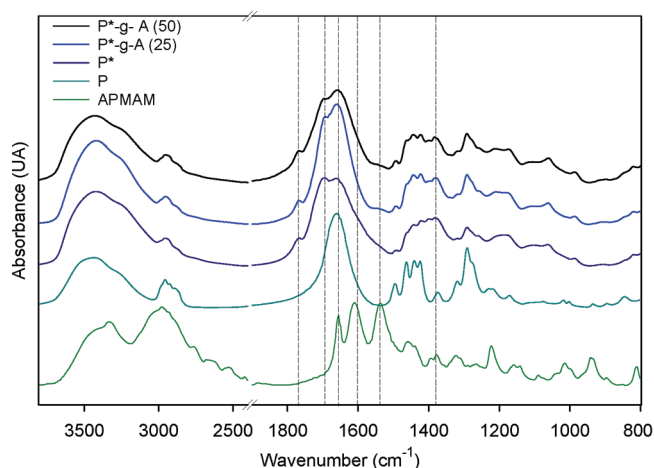


Figure 3. Comparison of FT-IR spectra of the nonirradiated PVP, base PVP nanogels (P*) and amino-functionalized variants irradiated with LAE 13/9 at 80 kGy. All spectra, with the exception of that of APMAM, were normalized with respect to the peak at 2956 cm⁻¹. Vertical dashed lines correspond to the following peaks: 1661, 1695, 1765, 1600, 1537, and 1388 cm⁻¹.

doses would be required (20–40 kGy) and, for a more conservative approach, materials should also be tested at twice the anticipated maximum dose. The possibility of generating as-borne sterile functional micro- or nanoparticles was investigated here by irradiating PVP/APMAM dilute aqueous solutions at total absorbed doses of 40 and 80 kGy, with the purpose of inducing simultaneously polymer cross-linking, monomer grafting to the cross-linked particles, and sterility, in a single step.

Two different irradiation conditions, that is, electron beam pulse frequency and dose per pulse, were selected: 300 Hz with 13 Gy/pulse and 75 Hz with 1.8 Gy/pulse, corresponding to two significantly different dose rates. Under the first set of conditions, irradiation of a 0.1 wt % of PVP leads to an approximate average number of radical centers for macromolecule equal to four, whereas under the latter conditions it is one every two chains. Under none of these conditions do we expect polymer radicals' intramolecular recombination to be the predominant reaction. The macromolecular constructs formed

will be the result of the competition of several possible reactions: recombination of polymeric macroradicals, both intra- and intermolecularly, recombination of macroradicals with other radicals, disproportionation, chain scission, radical transfer through H-abstraction, and so on.²⁵ As we are moving in an unexplored territory of possible simultaneous acts of macromolecular structure disruption and reconstruction, the final product will be the result of an evolutionary process that will affect more the loosely cross-linked portions of the material and less the more densely networked ones.^{26,27} Micro/nanoparticle structure and functionality will be controlled by the irradiation conditions and the gradual modification of the materials that is being irradiated.

In the presence of the acrylic monomer, we would expect that reactions of polymeric macroradicals can also involve APMAM, leading to monomer grafting (Scheme 1a). To confirm whether the overall approach can be successful, there are two possibilities: one is to attempt an identification of the radicals formed during the process and a kinetic analysis of their decay, the other is to perform an accurate product analysis. None of these two approaches is fast or simple. It has been preferred to collect first information about the usefulness of these micro- and nanostructures, which can then provide motivation to a deeper fundamental understanding of the reaction mechanisms.

The yield of the process, in terms of recovered dry product after dialysis, which may include both cross-linked and un-cross-linked PVP and PVP-g-APMAM, was investigated gravimetrically after extensive dialysis and freeze-drying. For all irradiation conditions and formulations, the yield was always above 98 wt %.

In Figure 1a, the average hydrodynamic diameter and relative standard deviations from DLS measurements carried out on the linear PVP, coded as “P”, and the corresponding NG dispersions (P*), as obtained after e-beam irradiation at the integrated dose of 40 kGy and the highest dose rate (E40), are shown. No appreciable differences in the two average hydrodynamic diameters are observed. From a more careful examination of the scattered light decay curves (see Figure S3 of the SI), some differences can be appreciated: P* is characterized by a larger proportion of smaller objects and few larger objects. This suggests that irradiation is causing a slight contraction of the great majority of polymer coils and simultaneously the formation of few bigger particles. The addition of APMAM to PVP (at the molar ratio 1:50 with respect to PVP RU) is causing a slight reduction of D_h (P–A system) already prior to irradiation. PVP presents ionic and/or polar negative charges owing to keto–enolic tautomerism of pyrrolidone carbonyls. Accordingly, the surface charge distribution for nonirradiated PVP macromolecules in double-distilled water shows a main broad peak centered around neutrality and a second peak at about –20 mV. (See Figure S4 of the SI.) Therefore, shrinkage of PVP coils is likely due to the shielding effect exerted by the protonated amino groups of APMAM toward the anionic charges of PVP. The average hydrodynamic diameters (D_h) of the particles obtained upon irradiation, at the variance of APMAM content, are also reported in Figure 1a. Poly(*N*-vinylpyrrolidone)-grafted-(aminopropyl) methacrylamide MGs or NGs are coded P*-g-A(*X*), where *X* = 200, 100, 50, or 25 depending on the APMAM/PVP's RU molar ratio.

Increasing APMAM content from 1:200 to 1:100, D_h only slightly increases, always leading to NGs of comparable size to

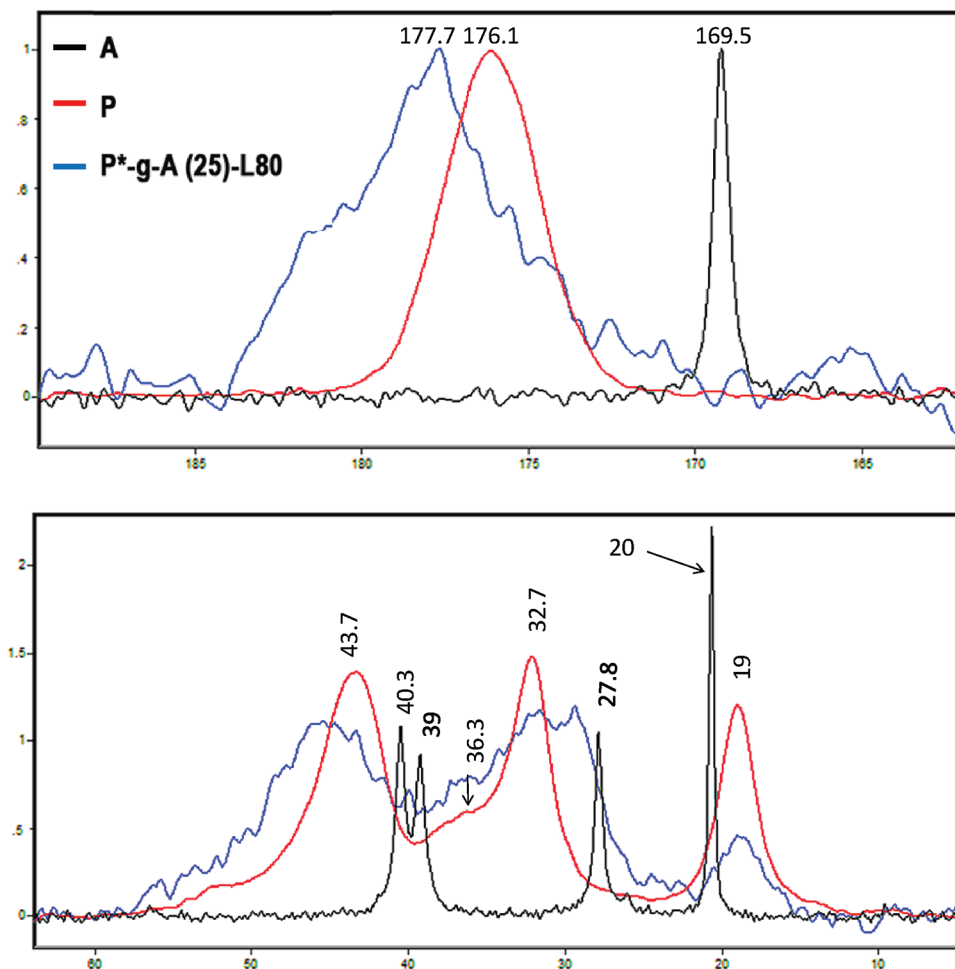


Figure 4. Overlaid ^{13}C $\{^1\text{H}\}$ CP MAS NMR spectra of nonirradiated PVP (P), APMAM monomer (A), and amino-functionalized nanogels ($\text{P}^*\text{-g-A}$ (25)-L80) on an expanded scale. Spectra are normalized with respect to the carbonyl peak.

the P^* values. At 1:50 ratio, particle size suddenly increases to few micrometers. This sudden increase in D_h is likely to be associated with a step change in the main type of cross-linking reactions upon irradiation. When e-beam irradiation of the aqueous solutions of PVP with APMAM is carried out with both components present at low concentration, it induces grafting of APMAM to individual PVP nanoparticles, whereas at the increase in APMAM content interparticle bridging may concur (Scheme 1b). As a consequence, the stepwise increase in particles size is observed and microparticles are formed.

Figure 1b compares the dimensions of particles obtained for the same pulse repetition rate and dose per pulse at two integrated doses: namely, 40 and 80 kGy. The effect of increasing the dose, from 40 to 80 kGy, for the base PVP systems is in the direction of reducing the NGs' particle size and narrowing the particle size distribution. In principle, this effect could be caused by either a high degree of intramolecular cross-linking, inducing of polymer coil shrinkage, or chain scission, that is, molecular degradation. To rule out any significant influence of radiation-induced molecular degradation at this fairly high irradiation dose, we carried out static light scattering measurements on this system at the variance of the scattering angle and sample concentration to determine the weight-average molecular weight. A marked downward curvature in the scattering angle dependence was observed in the case of P^* , thus making unreliable the extrapolation

procedure. The molecular weight and gyration radius were therefore estimated following the procedure described in the Materials and Methods sections. In the light of these measurements, one can observe that M_w varies from $4.20 \times 10^5 (\pm 0.1)$ for the nonirradiated PVP to $9.62 \times 10^5 (\pm 0.4)$ for P^* and the radius of gyration changes from 27 to 19 nm. The observed increase in average molecular weight, accompanied by a reduction of R_g is the result of a densification of the material upon prolonged irradiation. Furthermore, irradiation at this dose induces a marked anionic character to the NGs, as it will be further discussed.

When it comes to comparing hydrodynamic diameters of systems obtained by irradiation of PVP in the presence of APMAM, higher doses generally lead to bigger particles that are still in the nanoscale range for the lower molar ratios (1:200 and 1:100), whereas they become micrometer-sized for the 1:50 ratio, with concomitant particle size distribution broadening. Under this last condition, prolonged irradiation acts as both an axe and a cement for the already formed microparticles, thus suggesting chain scission, macromolecular segments grafting, and cross-linking as concurrent phenomena. When the dose is imparted at the lower dose rate (L80) (Figure 1c), the influence on D_h of the diminished pulse repetition rate and dose per pulse is not very significant for the base PVP systems or for $\text{P}^*\text{-g-A}$ (200) because of the high dilution of potentially reactive species. It becomes quite important at the higher

Table 1. Attribution of Main ^{13}C NMR Chemical Shifts of Nonirradiated (Linear) PVP, APMAM Monomer, and P*-g-A(50) L80 MG

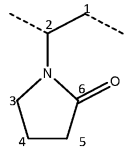
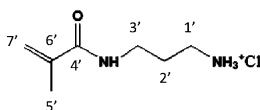
PVP	Carbon	Chemical shift
	C ₆	176,1
	C ₂ - C ₃	43,7
	C ₁	36,3
	C ₅	32,7
	C ₄	19
APMAM		
	C _{1'}	39
	C _{2'}	27,8
	C _{3'}	40,3
	C _{4'}	169,45
	C _{5'}	20,4
	C _{6'}	122,5
	C _{7'}	138,8
P*-g-A (25) L80		
	C ₆ as in PVP	177,1
	C ₂ - C ₃ as in PVP	45,4
	C ₂ as in APMAM	29,5

Table 2. XPS Surface Quantitative Analysis of the Investigated Samples^a

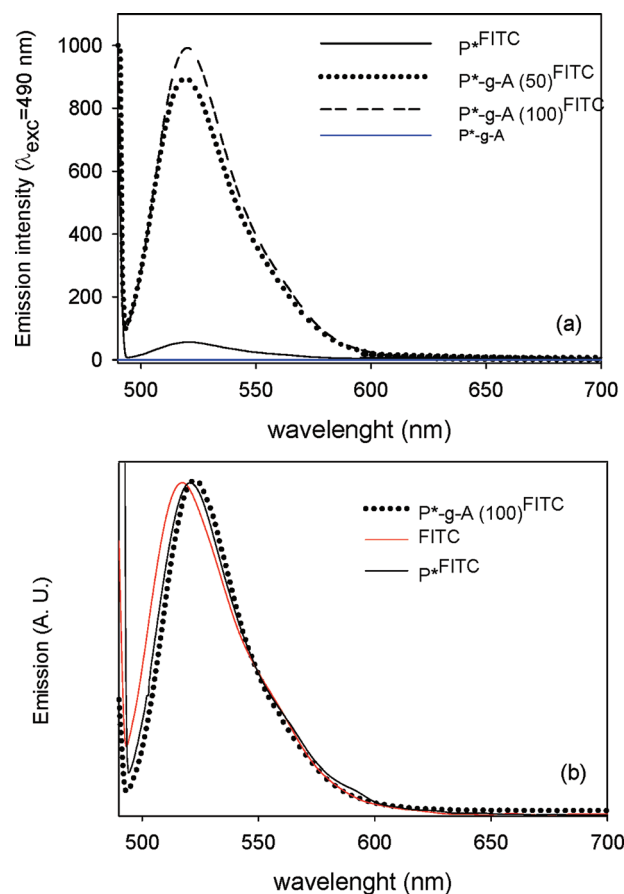
system	C 1s	O 1s	N 1s	O/C	N/C
PVP	76.1	12.9	11.0	0.169	0.144
P* L80	70.4	23.0	6.6	0.327	0.094
P*-g-A (50) L80	68.7	22.9	8.4	0.333	0.122
P* E80	70.7	22.0	7.3	0.311	0.103
P*-g-A (50) E80	72.9	20.1	7.0	0.276	0.096
P*-g-A (100) E80	61.2	31.4	7.4	0.513	0.121

^aElemental concentration is expressed as atomic percentage (at %).**Table 3.** XPS Surface Distribution of Carbon Species Resulting from the Curve-Fitting of C 1s Photoelectron Peak^a

system	C 1sBE (eV)		
	285.1	286.5	288
PVP	69.8	20.5	9.7
P* L80	67.8	12.9	19.4
P*-g-A (50) L80	64.6	16.9	18.5
P* E80	66.1	16.3	17.6
P*-g-A (50) E80	72.4	10.6	17.0
P*-g-A (100) E80	67.5	15.0	17.5

^aCarbon species are expressed as peak area percentage.

APMAM concentrations, where the switch from mainly intramolecular modification to interparticle bridging leading to microparticle formation occurs already for the 1:100 PVP RU/APMAM molar ratio. Reducing the dose rate (i.e., frequency) makes the time lag between two successive pulses

**Figure 5.** UV-vis emission spectroscopy of: (a) Nonconjugated amino-functionalized nanogels, two FITC-conjugated variants, and corresponding FITC-incubated base PVP nanogel (irradiation condition: E80). (b) Normalized emissions of a typical FITC-conjugated amino-grafted nanogel/microgel ($\text{P}^*\text{-g-A}^{\text{FITC}}$), FITC-incubated base PVP nanogels ($\text{P}^{*\text{FITC}}$), and free FITC aqueous solution (FITC).**Table 4.** Emission Intensity at λ_{peak} for the FITC Conjugated Systems

system	emission intensity at peak (A.U.)
P* E40	55
P*-g-A (100) E40	450
P*-g-A(50) E40	202
P* E80	50
P*-g-A (100) E80	990
P*-g-A(50) E80	890
P* L80	60
P*-g-A (100) L80	446
P*-g-A(50) L80	105

comparable to the time scale of encounters of potentially reactive species, thus favoring particle size buildup.

Surface Charge Density of Base and Amino Grafted PVP Micro/Nanogels. Micro- and nanogels in suspension exhibited electrostatic charges on their surfaces that can be expressed as ζ -potential and can be used to predict mutual interactions and thereby the long-term stability. In fact, particle flocculation and aggregation is less likely to occur in suspensions with higher ζ -potential. Furthermore, a role is played by nanoparticles' surface charge in their entry through the cells membrane, their intracellular pathway, and fate.²⁸ In

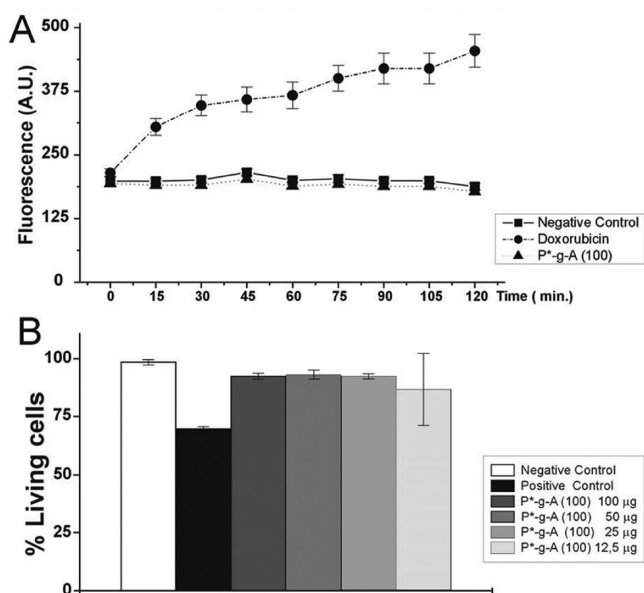


Figure 6. Cell viability by Caspase 3-7-8 enzymatic activation and MTT evaluation. (A) Activated caspases profiles obtained by spectrofluorimetric evaluation of Ac-Asp-Glu-Val-Asp-MCA peptide digestion at different times (from 0 to 120 min). In the Figure (—■—) represents untreated MC 3T3-E (negative control); (—●—) represents the MC 3T3-E1 DXR-treated cells (positive control); and (—▲—) represents MC 3T3-E1 cells in the presence of P*-g-A (100) NG dispersion. In ordinate, the fluorochrome emission is reported as arbitrary units. (B) MC 3T3-E1 cell viability as metabolic respiration. In ordinate, the amount of living cells in % with respect to nontreated cells.

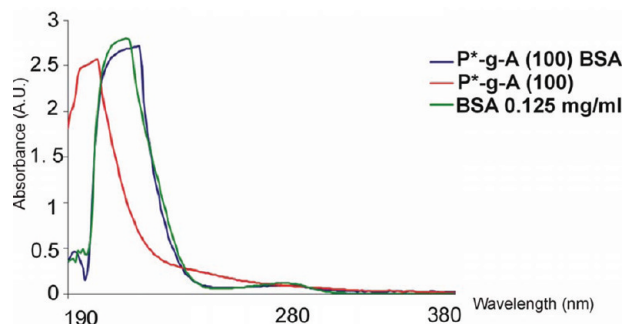


Figure 7. UV-vis absorption spectra of BSA-conjugated P*-g-A(100) system; nonconjugated P*-g-A(100) system as control; free BSA as reference.

Figure 2, ζ -potentials of E40 and E80 systems are shown. It has been pointed out that the nonirradiated PVP at the same concentration (0.1 wt %) shows a slightly anionic character. Conversely, the irradiated base systems present a marked anionic behavior, more pronounced at the higher dose. (See Figures S4 and S5 for the entire ζ -potential curves in the SI.) The average surface charge density is above -30 mV, with a wide distribution of values that span from -15 to -55 mV. (See Figure S6 in the SI.) It is worth pointing out that this distribution reflects the inherent heterogeneity of charge density for the MGs or NGs constituting the sample. The anionic character is likely to be induced by a change in the chemical structure and functionality of PVP upon irradiation under these conditions. This important aspect will be the subject of a dedicated paper, and some spectroscopic evidence

of the irradiated base “L80” system will be anticipated in the next paragraph. NGs obtained from PVP in the presence of increasing amounts of APMAM show a progressively reduced anionic character, likely due to the already proposed screening effect of the negative charges of PVP by the protonated amino groups of APMAM. At the highest concentration of APMAM, when MGs are formed from aggregation of several PVP chains, this monomer or its oligomers are expectedly no longer preferentially located at the particles surface but in their interiors; therefore, ζ -potential values become comparable to that of the base PVP systems.

Structural Characterization of Amino-Functionalized PVP Micro/Nanogels. Spectroscopic confirmation of the chemical attachment of APMAM to PVP has been sought by a combination of different spectroscopic techniques. In particular, in Figure 3, FTIR spectra of nonirradiated PVP, P*, P*-g-A(50), and P*-g-A(25) are presented. The spectrum of APMAM is also reported for comparison. All of the irradiated systems present: (i) higher absorptions in the high wavenumber range of the spectrum (3700 – 3000 cm^{-1}), where stretching vibration modes of hydroxyls ($\nu\text{O-H}$) and amidic ($\nu\text{N-H}$) groups and their associations are evident and (ii) an important modification of the amide I band ($\nu\text{C=O}$), generally at 1661 cm^{-1} and related to carbonyl stretching of pyrrolidone groups, with two new bands appearing at 1695 and 1765 cm^{-1} . These bands possibly refer to the formation of an imide and precisely refer to the symmetric and asymmetric stretching of five-membered cyclic imide.^{29,30} Furthermore, the enlargement of the amide I band toward lower wavenumbers and a new band at 1388 cm^{-1} strongly suggests the formation of carboxylate anions (asymmetric and symmetric carboxylate anion stretch at 1600 and 1385 cm^{-1} , respectively),³¹ which may explain both the low pH measured and the anionic surface charges for these nanoparticles’ dispersions. (See also Figure S8 of the SI.) A possible reaction pathway for the proposed structural modifications of irradiated PVP is provided as Figure S9 in the SI. When irradiation is carried out in the presence of APMAM, differences with respect to the base P* system are subtle. A relative increase of the absorption related to the amide I band of PVP and a shoulder at 1537 cm^{-1} can be noticed, probably due to the contribution of amide/amine bands of APMAM.³⁰ The strong peak at 1610 cm^{-1} present in the free monomer and mainly related to double-bond stretching vibration is not present in any of the irradiated systems or any of the corresponding characteristic bands at 1013 , 940 , and 811 cm^{-1} . This last evidence suggests a radical addition reaction of APMAM to PVP.

Solid-state ^{13}C NMR has been carried out on the 1.5P*-g-A(25) L80 and on the linear PVP and monomeric APMAM, as reference. (See Figure 4 and Table 1.) Chemical shifts with reference to those of both pure PVP and APMAM were assigned according to literature data^{29,32} and are reported in Table 1, where major peaks for MG are also reported. Modification of the spectral features of the MG with respect to the linear PVP is evident in all of the different carbon sites. Although the obtained spectrum is not suitable for an exact identification and quantification of the different species, the evident shift of the carbonyl band toward the higher chemical shifts is in good agreement with the proposed structural modifications of PVP.

The influence of the electron beam irradiation on the surface chemical composition of the produced MGs and NGS was also investigated by X-ray photoelectron spectroscopy (XPS) due to

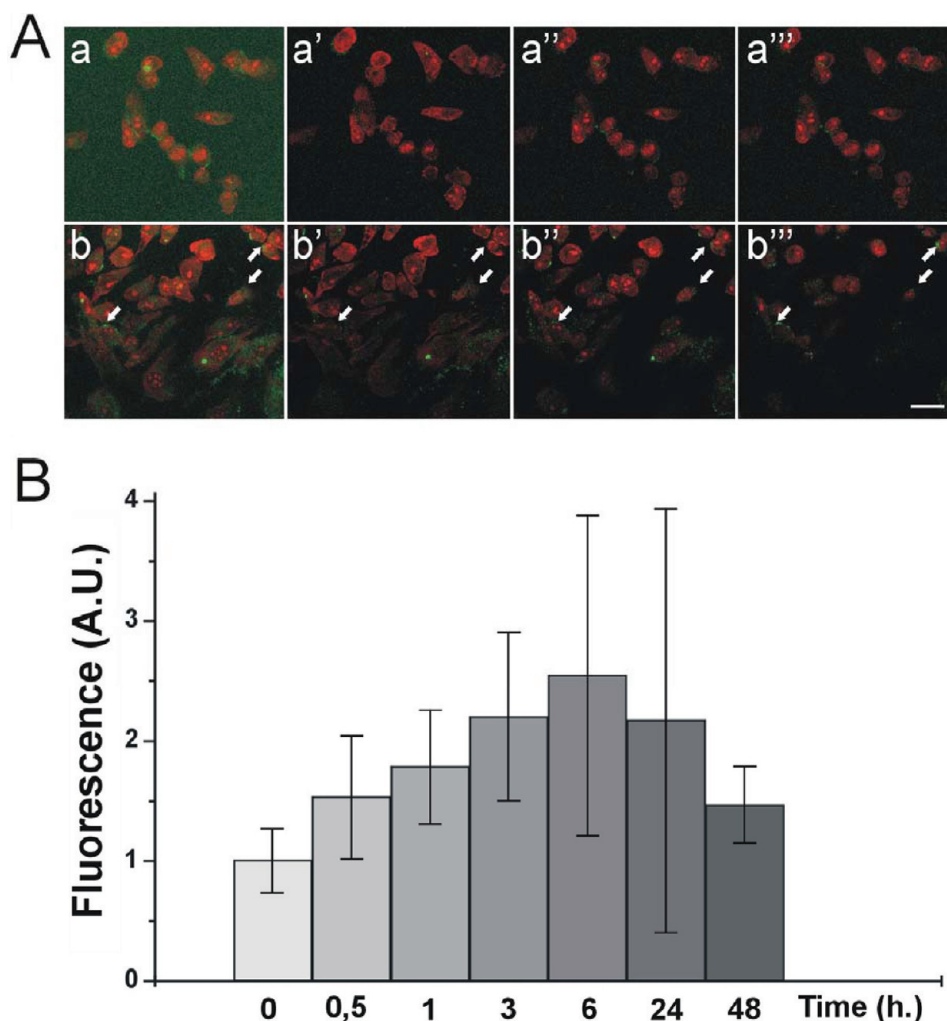


Figure 8. Localization of P*-g-A (100)^{FITC}NGs in MC3T3-E1 cells. (A) Confocal analysis of MC3T3-E1 cells stained with EtBr (red) in the presence of P*-g-A(100)^{FITC} NGs (green) at 30 min (a–a'') and 6 h (b–b''). Panels (a,b) show the images obtained by resumption of all sections, with an overall thickness of ~15 μm; in the panels (a'–b'), (a''–b''), and (a'''–b''') sections were at a depth of 3, 6, and 10 μm, respectively. Arrows in (b–b'') indicate the positions of P*-g-A (100)^{FITC} NGs inside the cells. Scale bar is 20 μm. (B) Histogram represents the amount of fluorescent nanoparticles present inside the MC3T3-E1 cells at different times (from 0 to 48 h). In ordinate, the fluorescence emission is reported as arbitrary units.

its ability to provide surface quantitative elemental and chemical state information. The surface chemical composition of the investigated samples is reported in Table 2, and quantitative results are expressed as atomic percentage (at %). A sample of nonirradiated PVP was taken as reference. Differences in atomic percentage are detected before and after irradiation of aqueous PVP. A noticeable increase in the oxygen concentration and a slight decrease in the carbon and nitrogen amounts are evidenced on the surface of the irradiated PVP samples (P*). The value of the O/C ratio increases from 0.169 to 0.327 after irradiation with LAE at 80 kGy, and the N/C decreases from 0.144 to 0.094, as reported in Table 2. These results confirm an increased level of PVP oxidation upon irradiation, which is consistent with the findings of the other spectroscopic techniques applied. No significant differences were observed in surface quantitative analysis among the samples subjected to irradiation at different dose rates or in the presence of APMAM, with the only exception of P*-g-A (100) E80. This sample shows the highest O/C ratio and a slightly higher N/C with respect to P*-g-A (50) E80 despite the fact that it comes from a halved amount of APMAM in the feed.

A nonlinear least-squares curve fitting routine was used for the analysis of XPS spectra, separating elemental species in different oxidation states. In all of the investigated samples the N 1s photoelectron peak consists of a single component located at BE = 400.1 eV that can be attributed to nitrogen species in the amide group $\text{N}-\text{C}=\text{O}$.³³ In all O 1s spectra, the component of the photoelectron peak corresponding to the BE of the carbonyl group is located at BE = 531.5 eV, which is assigned to oxygen species in $\text{N}-\text{C}=\text{O}$.^{33,34} The curve-fitting of the C 1s photoelectron peak revealed the presence of three components at BE = 285.1, 286.5, and 288.1 eV, which can be assigned to carbon atoms in C–C, C–O, and C=O bonds, respectively.^{34,35} Results of the curve-fitting procedure of C 1s peak are reported in Table 3. The relative amount of C–O and C=O species in nonirradiated PVP well describes the tautomerism of the pyrrolidone group in the linear polymer. A different content of $\text{N}-\text{C}=\text{O}$ carbon species, corresponding to C 1s component at BE = 288.1 eV, is detected in the base PVP samples before and after irradiation. Electron beam irradiation induces a significant increase in the concentration of carbon species in the amide group, coherently with the

proposed formation of a cyclic imide. The increase of these species are confirmed by the already discussed increase of the $N-C=O$ species in the O 1s spectra.

Conjugation of FITC to Amino-Functionalized PVP Micro/Nanogels. Chemical conjugation of FITC to the amino-functionalized MGs and NGs has been attempted to determine whether the primary amines are available for chemoligation and also to generate fluorescent variants for biological evaluation *in vitro*. UV–visible absorption and emission spectroscopies have been used to assess the success of conjugation and to quantify the amount of bound FITC. In particular, in Figure 5a the emission spectra of fluorescent E80 MGs and NGs are reported (1:50 and 1:100, respectively). A nonconjugated system and the FITC-incubated base P^* are also shown. Both the base (P^*) and amino-graft nonconjugated systems (P^*-g-A) do not present any significant emission band when excited at 490 nm, whereas P^{*FTIC} systems show a modest emission. Figure 5b reports the normalized emissions of FITC-conjugated P^*-g-A , FITC-incubate P^* , and free probe. Normalization allows easier identification of shifts in the λ_{peak} . It is evident that the emission band of a FITC-conjugated amino-grafted MG or NG is similar to that of the free probe with a significant red shift (+5 nm), which confirms the formation of thioureic bond.³⁶ The P^{*FTIC} systems show a modest emission band, with a peak at an intermediate position between that of the free and the bound probe. This emission is likely caused by FITC physically entrapped in the cross-linked particles. A previous work of some of the authors has established that PVP macrogels produced through e-beam irradiation have hydrophobic pockets that favorably, and in some circumstances also irreversibly, house fewer polar molecules present in aqueous systems.⁴

Absorption spectra for conjugated systems and free FITC solutions are reported as Figures S10 and S11 of the SI. Like in the emission spectra, the maximum absorption peak of the conjugated micro/nanogels is shifted with respect to the free FITC solution. Furthermore, ζ -potential measurements carried out on all conjugated systems show narrower charge distributions, centered around neutrality, thus suggesting a modification of the surface charge distribution. (See Figure S7 in the SI.) All this evidence confirms the success of conjugation.

Emission intensities at the peak for 1:100 and 1:50 P^*-g-A systems and the corresponding base P^{*FTIC} NGs under the different irradiation conditions are reported in Table 4. The emission intensity of the $P^*-g-A^{FTIC}(100)$ systems is higher than that of $P^*-g-A^{FTIC}(50)$, despite the two-fold increase in APMAM moles in the formulation for the latter. $P^*-g-A(100)$ systems are genuinely NGs, whereas $P^*-g-A(50)$ systems are MGs under all investigated irradiation conditions. If the formation of bigger particles is involving APMAM as a coupling agent, then a relevant amount of the amino groups may not be accessible to FITC or may have been depleted by the establishment of strong interactions with PVP.

FITC detachment was performed for $P^*-g-A(100)^{FTIC}$ and $P^*-g-A(50)^{FTIC}$ E80 to attempt a quantitative estimate of the content of primary amino groups available for chemoligation. A molar extinction coefficient for “bound FITC” was experimentally determined (see the SI for details), and the moles of available amino groups (4.4×10^{-4} and 1.3×10^{-4} mM) represent about 0.5 and 0.3% of the moles of APMAM charged in the feed for $P^*-g-A(100)$ and $P^*-g-A(50)$, respectively. Despite the fact that only a low proportion of the theoretical

amino groups present are available, the FITC-conjugated variants enabled NG visualization *in vitro* cells studies.

Biological Evaluation. PVP is a FDA approved, biocompatible polymer widely used in pharmaceutical applications. In particular, cross-linked PVP nanoparticles have already been evaluated for drug and gene delivery.^{37,38} It has also been shown that these particles can be administered intravenously and can remain in circulation for a considerable period of time evading the immune system.³⁹ Biological assays were here performed on cells treated with NGs to verify their biocompatibility. In particular, we report in detail the results obtained with $P^*-g-A(100)$ E80. To exclude apoptotic events, we performed an enzymatic assay on caspases activation. (See Materials and Methods sections.) As shown in Figure 6A, MC3T3-E1 cells treated or not (negative control) with the NGs at different times were compared with the ones treated with DXR (positive control). NG-treated cells did not show any activation of enzymes, whereas time-dependent fluorochrome release was observed in DXR-treated cells. A morphological evaluation, by confocal microscopy, was also carried out on MC3T3-E1 cells incubated in the presence of NGs for 24 h and stained with acridine orange/EtBr solution (data not shown); the staining allows us to discriminate among alive, damaged, and dead cells. This observation is in agreement with the enzymatic assay; in fact, cells treated with NGs do not show any apoptotic signs, equally to untreated cells used as negative control. Differently, the typical signs of apoptosis were observed in the positive control in which cells were treated with DXR, known to be an apoptosis inducer.

Once the absence of cytotoxicity of NGs was established, a cell viability assay was performed to assess if these nanoparticles influence cellular metabolism. As it is possible to observe in Figure 6B, MC3T3-E1 cells treated with different concentrations of NG aqueous dispersion have a similar profile to untreated cells; differently, DXR-treated cells (positive control) show a mortality of $\sim 30\%$.

As all gathered data suggest a good degree of biocompatibility of the produced NGs, experiments of biological molecules conjugation were performed to assess NGs' potential as smart drug delivery systems. In particular, aiming to bind stably biological molecules, such as proteins or antibodies, for active targeting, we performed conjugation experiments using BSA as a model. Absorption spectra reported in Figure 7 show that the BSA-conjugated NG spectrum has a peak at 280 nm that coincides with the one of free BSA, used as reference, whereas no absorption peak was observed in the nonconjugated system. The interaction between BSA and nanoparticles is fairly strong as it survives upon extensive dialysis and repeated washings. It was estimated that the weight percentage of retained BSA per polymer is ~ 30 , and, in consideration of the dimensions of BSA, we expect the protein to be located at the nanoparticles' surface.

To test nanoparticles viability thought cell compartments, we used the fluorescent $P^*-g-A(100)^{FTIC}$ variant. MC3T3-E1 cells were treated with the NGs for different incubation periods to follow their localization inside and through the cells. Figure 8A (a–a'') shows that after 30 min of incubation NGs were present in the media and on the cells' surface, whereas after 6 h of incubation (Figure 8A (b–b'')), NG distribution in cytoplasm compartment was mostly evident; similarly, in samples incubated for 24 and 48 h, cytoplasmic distribution was still evident (data not shown), although in lower amount. NGs' secretion as waste products or their digestion by the

lysosomal cell system could be hypothesized. In vivo and ex vivo tests will be performed to elucidate this aspect. Spectrofluorimetric measurements on the incubated cells after extraction and purification from the culture medium confirm the results of confocal microscopy. Figure 8B relates the amount of P*-g-A^{FITC}NGs inside or attached to MC3T3-E1 cells to the incubation time. A maximum of fluorescence has been found after 6 h of incubation, corresponding to 6% of the loaded amount, which decreases in 24 h and further in 48 h. Measurements of fluorescence from the culture medium and washings nicely balance the changes in emissivity from the cells, as shown in Figure S12 of the SI.

CONCLUSIONS

We believe that the work presented here can strongly encourage us to pursue using e-beam radiation processing as a viable and effective synthetic methodology to manufacture functional nanocarriers in a single step and with high yields. After irradiation, no expensive or time-consuming purification procedures are required, as no recourse to catalysts, initiators, or surfactants is made. Simultaneous sterilization can also be achieved by a proper selection of the irradiation doses. In particular, cross-linked PVP grafted with APMAM, a monomer bearing primary amino groups, has been chosen to demonstrate the potential of the approach. The analyzed P*-g-A(100) NGs are biocompatible and able to bind biological molecules stably. Cellular internalization experiments showed a significantly enhanced cellular accumulation of NGs, probably by an endocytic pathway: a direct translocation process without observable cytotoxic processes. This study offers a very exciting prospect in the use of the generated nanoparticles as potential drug delivery carriers.

ASSOCIATED CONTENT

Supporting Information

The following figures are provided: DLS autocorrelation function curves for a representative NGs dispersion after dialysis with different MWCO membranes (Figure S1); ¹H NMR spectra of nonirradiated and irradiated aqueous APMAM with LAE at 80 kGy (Figure S2); DLS autocorrelation function curves for nonirradiated PVP (P), irradiated PVP E40 (P*), and irradiated PVP E40 (P*) after 0.22 μm filtration (Figure S3); ζ-potential curves for nonirradiated PVP in water (Figure S4) and for base PVP NGs (P* E80) in water (Figure S5), a typical amino-functionalized NG/MG and a FITC conjugated amino-functionalized system, (P*-g-A(50)^{FITC}) (Figures S6 and S7); Overlaid FTIR spectra of nonirradiated and irradiated PVP (Figure S8); reaction pathway to for the proposed structural modifications of irradiated PVP (Figure S9); normalized absorption spectra for a typical conjugated NG system and a free FITC solution (Figure S10); and experimental details and calculations for the quantitative determination of available amino groups through FTIC detachment experiments. Absorption spectra of a typical FTIC-conjugated NG (P*-g-A(100)^{FITC}), FITC solution collected under the filter after detachment, and conjugated NG recovered from the top of the filter (redispersed in PBS) after detachment (Figure S11); histogram representing the total fluorescence in the wells containing MC3T3-E1 cells incubated with fluorescent NGs in their culture medium, and fluorescence signals from extracted cells, culture medium, and washings collected in cells extraction process, at different times (from 0 to 48 h), as obtained from independent measurements. In ordinate, the fluorescence

emission is reported as arbitrary units. Emission derives from the fluorescent NGs as they partition in the different locations as function of the time (Figure S12). This material is available free of charge via the Internet at <http://pubs.acs.org>.

AUTHOR INFORMATION

Corresponding Author

*Tel: +39 091 23863710. Fax: +39 091 23863738. E-mail: Clelia.dispenza@unipa.it.

Notes

The authors declare no competing financial interest.

ACKNOWLEDGMENTS

This work was partially supported by the IAEA CRP: "Nanoscale radiation engineering of advanced materials for potential biomedical applications" and FW7-COST Action MP0701.

We acknowledge the assistance of the Centre for Radiation Research and Technology, Institute of Nuclear Chemistry and Technology, (Warsaw) for e-beam irradiation. In particular, we gratefully thank Prof. A. Chmielewski, Prof. G. Przybytniak, and Prof. I. Kaluska for their support and advice.

Solid-state ¹³C NMR experimental data were provided by Centro Grandi Apparecchiature UniNetLab—Università di Palermo, funded by P.O.R.Sicilia2000–2006, Misura 3.15 Quota Regionale.

REFERENCES

- (1) Hoffman, A. S. *Adv. Drug Delivery Rev.* **2002**, *43*, 3–12.
- (2) Kopecek, J. *Biomaterials* **2007**, *28*, 5185–5192.
- (3) Peppas, N. A.; Bures, P.; Leobandung, W.; Ichikawa, H. *Eur. J. Pharm. Biopharm.* **2000**, *50*, 27–46.
- (4) Ricca, M.; Foderà, V.; Giacomazza, D.; Leone, M.; Spadaro, G.; Dispenza, C. *Colloid Polym. Sci.* **2010**, *288*, 969–980.
- (5) Oishi, M.; Nagasaki, Y. *Nanomedicine* **2010**, *5*, 451–468.
- (6) Vinogradov, S. V. *Nanomedicine* **2010**, *5*, 165–168.
- (7) Liu, Y.; Miyoshi, H.; Nakamura, M. *Int. J. Cancer.* **2007**, *120*, 2527–2537.
- (8) Moghimi, S. M.; Hunter, A.-C.; Murray, J.-C. *Pharmacol. Rev.* **2001**, *53*, 283–318.
- (9) Ganta, S.; Devalapally, H.; Shahiwala, A.; Amiji, M. *J. Controlled Release* **2008**, *126*, 187–204.
- (10) Jung Kwon, O.; Drumright, R.; Siegwart, D. J.; Matyjaszewski, K. *Prog. Polym. Sci.* **2008**, *33*, 448–477.
- (11) Dispenza, C.; Grimaldi, N.; Sabatino, M.-A.; Todaro, S.; Bulone, D.; Giacomazza, D.; Przybytniak, G.; Alessi, S.; Spadaro, G. *Radiat. Phys. Chem.* **2011**, DOI: 10.1016/j.radphyschem.2011.11.057.
- (12) Ulanski, P.; Janik, I.; Rosiak, J. M. *Radiat. Phys. Chem.* **1998**, *52*, 289–294.
- (13) Kadlubowski, S.; Grobelny, J.; Olejniczak, W.; Cichomski, M.; Ulanski, P. *Macromolecules* **2003**, *36*, 2484–2492.
- (14) Jeszka, J. K.; Kadlubowski, S.; Ulanski, P. *Macromolecules* **2006**, *39*, 857–870.
- (15) Stepanek, P. Data Analysis in Dynamic Light Scattering. In *Dynamic Light Scattering: The Method and Some Applications*; Brown, W., Ed.; Oxford University Press: Oxford, U.K., 1993; pp 177–240.
- (16) Woods, R. J.; Pikaev, A. K. *Applied Radiation Chemistry: Radiation Processing*; John Wiley and Sons, Inc.: New York, 1994; Chapter 6.
- (17) Musyanovych, A.; Adler, H.-J. P. *Langmuir* **2005**, *21*, 2209–2217.
- (18) Sherwood, P. M. A. In *Practical Surface Analysis*; Briggs, D., Seah, M. P., Eds; Wiley: New York, 1990; p 181.
- (19) Wagner, C. D.; Davis, L. E.; Riggs, W. M. *Surf. Interface Anal.* **1986**, *2*, 5.
- (20) Frisken, B. J. *Appl. Opt.* **2001**, *40*, 4087–4091.

- (21) Carlfors, J.; Rymden, R. *Eur. Polym. J.* **1982**, *18*, 933–937.
- (22) Nicholson, D. W.; Ali, A.; Thornberry, N. A.; Vaillancourt, J. P.; Ding, C. K.; Gallant, M.; Gareau, Y.; Griffin, P. R.; Labelle, M.; Lazebnik, Y. A. *Nature* **1995**, *6*, 37–43.
- (23) Thornberry, N. A.; Rano, T. A.; Peterson, E. P.; Rasper, D. M.; Timkey, T.; Garcia-Calvo, M.; Nordstrom, P. A.; Roy, S.; Vaillancourt, J. P.; Chapman, K. T.; Nicholson, D. W. *J. Biol. Chem.* **1997**, *18*, 17907–11.
- (24) An, J.-C.; Weaver, A.; Kim, B.; Barkatt, A.; Poster, D.; Vreeland, W. N.; Silverman, J.; Al-Sheikhly, M. *Polymer* **2011**, *52*, 5746–5755.
- (25) Chapiro, A. *Radiation Chemistry of Polymeric Systems*; Wiley-Interscience: New York, 1962.
- (26) Al-Assaf, S.; Phillips, G. O.; Deeble, D. J.; Parsons, B.; Starnes, H.; von Sonntag, C. *Radiat. Phys. Chem.* **1995**, *46*, 207–217.
- (27) Ulanski, P.; Kadlubowski, S.; Rosiak, J. M. *Radiat. Phys. Chem.* **2002**, *63*, 533–537.
- (28) Verma, A.; Stellacci, F. *Small* **2010**, *6*, 12–21 and references herein..
- (29) Zhu, X.; Lu, P.; Chen, W.; Dong, J. *Polymer* **2010**, *51*, 3054–3063.
- (30) Nakanishi, K. *Infrared Absorption Spectroscopy*; Holden-Dy: San Francisco, 1962.
- (31) Silverstein, R. M.; Bassler, G. C.; Morrill, T. C. *Spectrometric Identification of Organic Compounds*, 3rd ed.; John Wiley & Sons, Inc.: New York, 1974.
- (32) Pretsch, E.; Buhlmann, P.; Badertscher, M. ¹³C-Nuclear Magnetic Resonance Spectroscopies. In *Spectral Data for Structure Determination of Organic Compounds. Tables of Spectral Data*; Springer: New York, 2009; pp 69–156.
- (33) Moulder, J. F.; Stickle, W. F.; Sobol, P. E.; Bomben, K. D. *Handbook of X-Ray Photoelectron Spectroscopy: A Reference Book of Standard Spectra for Identification and Interpretation of XPS Data*; Chastain, J., King, R. C., Jr., Eds.; Physical Electronics, Inc.: Eden Prairie, MN, 1995.
- (34) Sionkowska, A.; Wisniewski, M.; Kaczmarek, H.; Skopinska, J.; Chevallier, P.; Mantovani, D.; Lazare, S.; Tokarev, V. *Appl. Surf. Sci.* **2006**, *253*, 1970–1977.
- (35) Thissen, H.; Johnson, G.; Hartley, P. G.; Kingshott, P.; Griesser, H. J. *Biomaterials* **2006**, *27*, 35–43.
- (36) Lanz, E.; Gregor, M.; Slavik, J.; Kotyk, A. *J. Fluoresc.* **1997**, *4*, 317–319.
- (37) Hamidi, M.; Azadi, A.; Rafiei, P. *Adv. Drug Delivery Rev.* **2008**, *60*, 1638–1649.
- (38) Saxena, A.; Mozumdar, S.; Johri, A. K. *Biomaterials* **2006**, *27*, 5596–5602.
- (39) Bharali, D. J.; Sahoo, S. K.; Mozumdar, S.; Maitra, A. *J. Colloid Interface Sci.* **2003**, *258*, 415–23.



Large Scale Radiation Manufacturing of Hierarchically Assembled Nanogels..

C. Dispenza*, M.A. Sabatino, N. Grimaldi, G. Spadaro, D. Bulone,

M. L. Bondi, G. Adamo, S. Rigogliuso.

2012. Chem. Eng. Trans. 27, 229-232.

Large-scale Radiation Manufacturing of Hierarchically Assembled Nanogels

Clelia Dispenza^{*a,b}, Maria Antonietta Sabatino^a, Natascia Grimaldi^a,
Giuseppe Spadaro^a, Donatella Bulone^b, Maria Luisa Bondi^c,
Giorgia Adamo^d, Salvatrice Rigogliuso^d

^aDipartimento di Ingegneria Chimica, Gestionale, Informatica, Meccanica, Università degli Studi di Palermo, Edificio 6, Viale delle Scienze 90128 Palermo, Italy

^bCNR-Istituto di Biofisica U.O.S. di Palermo, via Ugo La Malfa 153 90146 Palermo, Italy

^cCNR-Istituto per lo Studio dei Materiali Nanostrutturati (ISMN), via Ugo La Malfa, 153 90146 Palermo, Italy

^dDipartimento di Scienze e Tecnologie Molecolari e Biomolecolari, Università degli studi di Palermo, Viale delle Scienze, Edificio 16, 90128 Palermo, Italy
clelia.dispenza@unipa.it

Nanogels (NGs), or small particles formed by physically or chemically crosslinked polymer networks, represent a niche in the development of "smart" nanoparticles for drug delivery and diagnostics. They offer unique advantages over other systems, including a large and flexible surface for multivalent bio-conjugation; an internal 3D aqueous environment for incorporation and protection of (bio)molecular drugs; the possibility to entrap active metal or mineral cores for imaging or phototherapeutic purposes; stimuli-responsiveness to achieve temporal and/or site control of the release function and biocompatibility. The availability of inexpensive and robust preparation methodologies is at the basis of the development of effective nanogel-based theragnostic devices. The design rules for mass fabrication of nanoscale hydrogel particles with the recourse to industrial-type accelerators is here discussed.

1. Introduction

Nanogels are particles formed by physically or chemically crosslinked polymer networks of nanoscale size. They are very promising carriers for drug delivery and have some favorable properties, such as high biocompatibility, a large surface area for bioconjugation and an internal 3D aqueous network for the incorporation of bioactive molecules, inorganic nanocrystals or magnetic nanoparticles useful as contrast agents for optical and magnetic imaging. The smooth and elastic outlayers make these nanoparticles able to penetrate through small pores and channels and generate extremely low friction with various biological surfaces. Their tunable size and chemical functionalities enable NGs responsiveness to environmental factors and biodegradability, when required. The design of functional nanoparticles must include a high degree of control of product properties through both process and material chemistry.

Major synthetic strategies for the preparation of nanogels belong to either micro-fabrication methodologies (photolithography, microfluidic, micromoulding) or to self-assembly approaches that exploit ionic, hydrophobic or covalent interactions (Oh et al., 2008, Morimoto et al., 2005, Gonçalves et al., 2010 and reference herein). For the latter, in particular, dimensional control

has been often achieved by the recourse to surfactants. Therefore, while micro-fabrication methods are limited by the need of costly equipments, the recourse to surfactants as well as organic solvents, initiators and catalysts may detrimentally affect the toxicological profile of the nanogels produced in colloidal systems. The availability of inexpensive and robust preparation methodologies is at the basis of the development of effective nanogel-based theragnostic devices. Radiation induced cross-linking is a versatile and “clean” process, it generally yields highly pure materials through environmentally friendly and economically viable processes (Rosiak and Olejniczak, 1993; Rosiak et al., 1995; Rosiak and Yoshii, 1999; Lugao and Malmonge, 2001; Peppas et al., 2006). High energy radiation processing demonstrated its potential for the production of nanogels already in the late '90s, owing to the pioneeristic work of Rosiak and collaborators, but since then no adequate efforts have been spent in developing a viable technology based on these findings to generate multi-functional nanoparticles with the required properties (Ulanski, et al., 1998). This paper documents the potential of e-beam irradiation to generate consistently and quantitatively biocompatible base and amino-functionalised poly(N-vinyl-pyrrolidone) (PVP) nanogel variants, as for dimensions and chemical structure, and thereby functionality, from the aqueous solutions of their polymer and monomer precursors.

2. Experimental

PVP k60 (Aldrich, $M_n=1.60 \times 10^5$ g/mol, $M_w = 4.1 \times 10^5$ g/mol, $R_g = 27$ nm (Dispenza et al., 2011)) and (3-aminopropyl)methacrylamide hydrochloride (APMAM, Polyscience) were used as received. PVP aqueous solutions at different polymer concentration (from 10 % to 0.05 %wt) were carefully deoxygenated with gaseous nitrogen. PVP aqueous solutions at 0.1 %wt were added with APMAM, the primary amino groups carrying monomer, at different concentrations (1:200, 1:100 and 1:50 molar ratios with respect to PVP RU). Electron beam irradiation was performed using two 10 MeV linear accelerators at the ICHTJ of Warsaw (Poland): LAE 13/9, which allowed to select two different average dose-rates, by tuning pulse repetition rate and duration time (100 kGy/h, 500 kGy/h), and many different doses by varying the irradiation time; Elektronika, that is equipped with a conveyor belt that allows many vials in a tray to pass under the beam at a given speed, which was set to supply 40 kGy per pass. In this last condition a much higher average dose-rate was achieved. Temperature was always maintained between 4-10 °C. Macroscopically gelled systems obtained at the higher polymer concentrations in the investigated range were separated from their soluble portions and successively freeze-dried. Nanogel dispersions obtained at 0.5, 0.25, 0.1 and 0.05 %wt were dialyzed against distilled water for 48 h using dialysis tubes of 12-100 kDa cut-off (Aldrich). The yield of the process was determined gravimetrically. Molecular structure of the macro/nanogels produced was confirmed through FT-IR and solid-state ^{13}C -NMR. FTIR analysis was carried out with Perkin Elmer-Spectrum 400 apparatus by dispersing the freeze-dried residues in potassium bromide and compressing into pellets. Spectra were recorded at 30 scans per spectrum and 1 cm^{-1} resolution in the $4000\text{-}400\text{ cm}^{-1}$ range. The average hydrodynamic diameter, D_h , and the relative standard deviation (giving information on the width of the particle size distribution) were measured by dynamic light scattering (DLS), using a Brookhaven Instruments BI200-SM goniometer. Samples were kept at constant temperature of 20 ± 0.1 °C. The light scattered intensity and time autocorrelation function were measured by using a Brookhaven BI-9000 correlator and a 100 mW Ar laser (Melles Griot) tuned at $\lambda = 632.8$ nm. The presence of grafted primary amino groups was confirmed by reaction with fluorescein isothiocyanate (FITC, Research Organics) yielding a highly fluorescent product, accordingly to an in-house developed protocol. Fluorescence spectra of the different conjugated amino-functionalised microgel or nanogel were acquired with a JASCO FP-6500 spectrofluorimeter, equipped with a Xenon lamp (150 W). Caspase 3 enzymatic assay on synthetic fluorescent substrate. MC3T3-E1 cells were seeded at high density on 6 well plate for 24 h in complete medium and grown for another 24 h after incubation with NGs. Cells were enzymatically detached from culture plate and extracted using a solution of Triton X 100 (1 %) in PBS. The amount of extracted proteins present in the

supernatant were quantified by Bradford micro assay method (Bio-Rad, Segrate, Milan, Italy) employing BSA (Sigma-Aldrich) as standard. MC3T3-E1 cells extracts (20 μ g), obtained as previously described, were used to detect the presence of activated caspases 3/7/8, typical apoptosis' marker. The Ac-Asp-Glu-Val-Asp-MCA peptide (Pepta Nova, Peptide Institute, inc), a specific substrate for activated caspase 3/7/8 was used. It ties a fluorophore in its cutting site, which emits fluorescence when cut by activated enzymes. In these experiments, the previously described extracts were added to 75 μ L (8 μ M) of the substrate in a 96 well plates. By spectrofluorimetric reading, it was possible quantify the degree of caspases activation. Spectrofluorimetric analysis were performed using Spectra Max Gemini EM-500 (Molecular Devices) and elaborated by Soft Max Pro 5.2 software.

MC3T3-E1 cell viability by MTT assay. The MC3T3-E1 cells were seeded in 96-well plate at density of 1x10⁴ cell/well. After 24 h of growth in presences of NGs, cells were washed with PBS and then incubated with 200 μ L/well of complete medium containing 0.25 mg/mL of MTT solution for 2 h at 37 $^{\circ}$ C. After solubilisation of the resulting formazan product with 100 μ L/well of DMSO solution, the absorbance of intense purple staining at 490 nm wavelength was read on DU-730 Life Science Spectrophotometer (Beckman Coulter). MC3T3-E1 cells treated with DXR (5 μ M) for 24 h were used as positive control.

3. Results and discussion

It is well known that high dose-rate pulsed electron irradiation leads to either macrogels or nanogels depending on the polymer concentration in water. Irradiated aqueous solutions of a commercial PVP at concentrations ranging from above (from 10 %wt) to below (up to 0.05 %wt) its critical chain overlap concentration ($C^* \cong 1$ %wt (Dispenza et al., 2011)) were irradiated at a constant integrated dose (40 KGy) and dose rate (100 KGy/h). At a preliminary visual inspection, the irradiated samples from solutions at 10, 8 and 6 %wt appear completely macroscopically gelled, while at 4, 2 and 0.5 %wt present both macrogel islands and a separated aqueous phase. At lower concentrations, all irradiated systems appear optically transparent liquids, and they would "traditionally" classify as "sols", but DLS analysis revealed that liquids are actually NGs dispersions, as it will be discussed in the following. The yield of PVP crosslinking, either in the form of "infinite" networks or of "finite" nanoparticles, was always high (Dispenza et al., 2012). FTIR spectra of the dry networks have been compared to the linear, commercial PVP spectrum for macro-systems and NGs (spectra not presented here for sake of brevity). All the characteristic peaks of the linear PVP are also present in the macrogels spectra with no evident shifts, while spectra of nanogels show two new and well resolved peaks at 1769 and 1698 cm^{-1} near to the amide I band of the pyrrolidone ring: these peaks are generally associated to C=O (symmetric and asymmetric, respectively) stretching vibrations of 5-members cyclic imides. The appearance of the new band at 820 cm^{-1} , attributable to the ring CH_2 twisting of succinimide, further supports the aforementioned hypothesis that this new specie is formed. The crosslinked structures were also studied by CP/MAS solid state ¹³C-NMR spectroscopy that confirms the formation of the abovementioned specie.

Information about the effect of the polymer concentration on the particles size, the soluble part of the 0.5 %wt system and all the other systems produced at lower polymer concentration has been sought through DLS. Polymer concentration significantly influences the size of gel nanoparticles produced. In figure 1-A the calculated average D_h and relative standard deviations at the variance of polymer concentration are reported. The 0.5 and 0.25 %wt systems present nanoparticles with average D_h of 64 and 100 nm, respectively, that are higher than those of the not irradiated PVP coils. This can be due to the occurrence of both intermolecular and intramolecular crosslinking. On the contrary, NGs obtained from 0.1 and 0.05 %wt solutions have D_h lower than that of the corresponding not irradiated systems. In this case, intramolecular crosslinking may be the prevailing phenomenon. In order to completely rule out that chain-scission and molecular degradation phenomena are responsible for the reduction of D_h , a concomitant increase of light scattering intensity was observed with respect to the not-irradiated PVP aqueous solutions at the same concentration, that suggests an increment of

nanoparticles density. Dh changes also varying the average dose rate or the integrated dose when the polymer concentration in water is kept constant. In figure 1-B the effects of the average irradiation dose rate at the same integrated dose (40 kGy) for different polymer concentrations is shown, while in figure 1-C the influence of the integrated dose (from 0 to 80 kGy) for two polymer concentrations (0.1 %wt and 0.25 %wt) is reported. The effect of increasing the average dose rate or the integrated dose on Dh goes in the same direction: when polymer aqueous solutions were irradiated under higher average dose rates or higher integrated doses, Dh increases and this effect is more pronounced for systems at higher polymer concentration. Average hydrodynamic diameters of amino-functionalised particles obtained by adding the functionalized monomer (APMAM) to the feedstock are reported in figure 1-D. Increasing APMAM content from 1:200 to 1:100 ratio, Dh only slightly increases, while at 50:1 ratio particle size step-wise rises to few microns, probably due to APMAM and/or APMAM oligomers bridging together many PVP chains. In order to understand this behavior it is necessary to emphasize that PVP can present both ionic and/or polar negative charges owing to keto-enolic tautomerisation of pyrrolidone carbonyls. Therefore, an APMAM molecule which is grafted to PVP, owing to the homolytic rupture of its unsaturated acrylic moiety, can also electrostatically interact with another PVP chain (or segment) with its terminal protonated amino group ($pK_a = 8.5$).

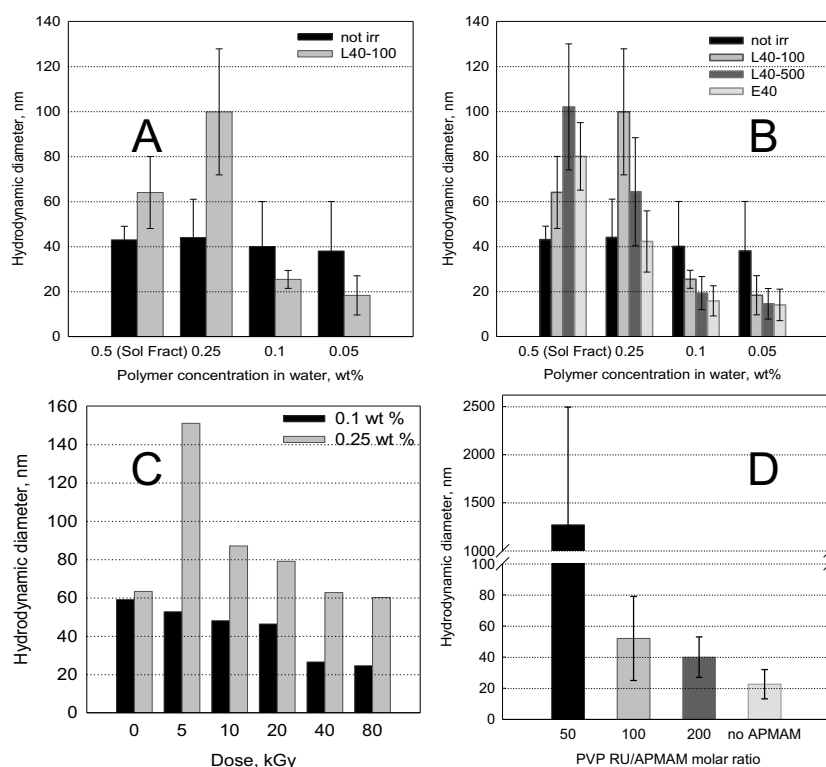


Figure 1: Average hydrodynamic diameters and relative standard deviation of solution of commercial PVP (K60) and irradiated PVP at the variance of the polymer concentrations (A); average dose rate for different polymer concentration (B); integrated dose for two polymer concentrations (C); APMAM molar ratio with respect to PVP RUs (D)

Chemical conjugation of fluorescein isothiocyanate (FITC) to the amino functionalized microgels and nanogels was attempted to explore whether the primary amines introduced with APMAM are available for chemoligation. Emission spectroscopy was used to assess the success of conjugation. In particular, Figure 3 shows the normalized emissions spectra of a typical PVP-

grafted-APMAM system conjugated with FITC (P*-g-A-FITC) in comparison with a buffered aqueous solution of the free probe at the same pH, a not-conjugated PVP-g-APMAM system (P*-g-A) and a base PVP nanogel dispersion, P*, that has been incubated with FITC according to the same protocol as for the amino-functionalized variants. Normalization allows easier identification of shifts in the maximum wavelength of emission. From the examination of this figure it is evident that the typical emission of a FITC-conjugated amino-grafted PVP micro/nanogel system is similar to that of the free probe but red shifted (+5 nm), which confirms the formation of thiourea bond. The base PVP nanogels incubated with FITC show a modest emission band, with a peak at an intermediate position between that of the free and the bound probe. This emission is likely caused by FITC physically entrapped in the gel particles. Conversely, all the conjugated P*-g-A systems show a distinct emission band at 520 nm, that suggest chemical attachment of FITC.

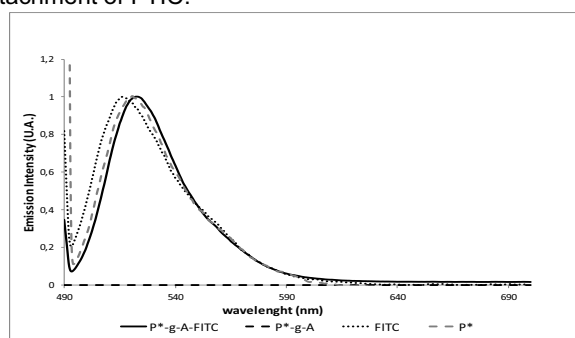


Figure 2: Normalized emissions of a typical FITC conjugated amino-grafted nanogel (microgel) formulation ($\lambda_{\text{peak}}=520$ nm), of a FITC incubated base PVP formulation ($\lambda_{\text{peak}}=517$ nm) and free FITC aqueous solution ($\lambda_{\text{peak}}=515$ nm) all at the same pH (7.4 PBS).

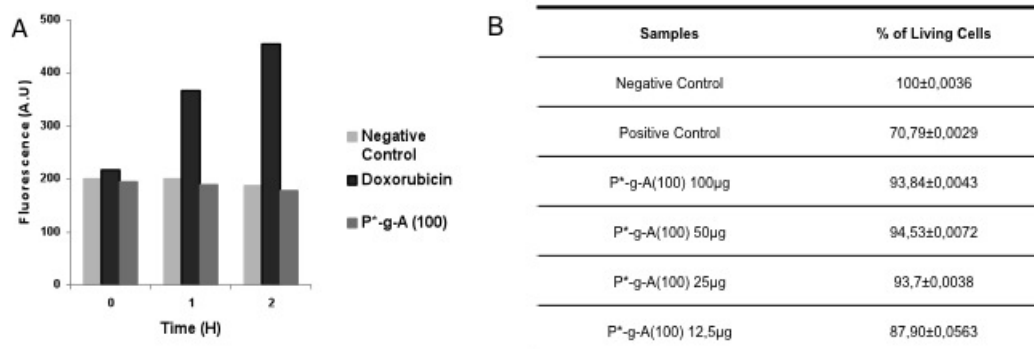


Figure 3: Biological evaluation of a typical amino-functionalized NG dispersion. A) Caspase 3 enzymatic assay on synthetic fluorescent substrate. B) MC3T3-E1 cell viability by MTT assay.

Biological evaluations in vitro were also performed to prove biocompatibility of NGs. MC3T3-E1 cells were incubated with P*-g-A (100) system and absence of cytotoxicity and cell viability were performed in order to assess if these nanoparticles influence cellular metabolism. Figure 3A shows MC3T3-E1 cells treated or not (negative control) with NGs at different times, compared to the ones treated with DXR (positive control). NG-treated cells did not show any activation of enzymes, while time-dependent fluorochrome release was observed in DXR-treated cells. In Figure 3B, MC3T3-E1 cells treated with different concentrations of NGs have similar profile to untreated cells; differently, DXR-treated cells (positive control) show a mortality of about 30 %. All gathered data suggest a good degree of biocompatibility of the produced NGs, they can be

considered suitable as nanocarriers in drug delivery applications or as building blocks for tissue-engineering scaffolds.

4. Conclusions

High energy radiation processing allows the production of biocompatible both base and amino-functionalised PVP NGs with high yields, no need of initiators, crosslinkers or recourse to toxic solvents and surfactants, therefore of complex purification procedures. Appropriate tuning of process parameters of industrial-type accelerators enables the control of the chemical structure and the size of the NGs produced, with adequate accuracy. Simultaneous sterilization can also be achieved, thus demonstrating the suitability of this technology for large scale production of NGs. Current developments are aimed at decorating these radiation-engineered nanogels with different biological moieties, such as complementary peptides, complementary antibody and enzyme fragments, to form bio-hybrid micro/nanoparticles with site-recognition functions or programmable hierarchical assembly.

References

- Dispenza C., Ricca M., Lopresti C., Battaglia G., La Valle M., Giacomazza D., Bulone D., 2011, E-beam irradiation and UV photocrosslinking of microemulsion-laden poly(N-vinyl-2-pyrrolidone) hydrogels for "in-situ" encapsulation of volatile hydrophobic compounds, *Polym. Chem.*, 2 192-202.
- Dispenza C., Grimaldi N., Sabatino M.A., Todaro S., Bulone D., Giacomazza D., Przybytniak G., Alessi S., Spadaro G., 2012. Studies of network organisation and dynamics of e-beam crosslinked PVPs: from macro to nano, *Rad. Phys. Chem.*, DOI: 10.1016/j.radphyschem.2011.11.057.
- Gonçalves C., Pereira P., Gama M., 2010, Self-Assembled Hydrogel Nanoparticles for Drug Delivery Applications, *Materials*, 3 1420-1460.
- Lugao A.B., Malmonge S.M., 2001, Use of radiation in the production of hydrogels, *Nucl. Instrum. Methods Phys. Res., Sect. B*, 185, 37-42.
- Morimoto N., Endo T., Iwasaki Y., Akiyoshi K., 2005, Design of hybrid hydrogels with self-assembled nanogels as cross-linkers: Interaction with proteins and chaperone-like activity, *Biomacromolecules*, 6, 1829-1834.
- Muthu M.S., Feng S.S., 2010, Nanopharmacology of liposomes developed for cancer therapy, *Nanomedicine*, 5 (7) 1025.
- Nishiyama N., 2007, Nanomedicine: Nanocarriers shape up for long life, *Nature Nanotechnology*, 2, 203.
- Oh J.K., Drumright R., Siegwart D.J., Matyjaszewski K., 2008, The development of microgels/nanogels for drug delivery applications, *Prog. Polym. Sci.*, 33, 448-477.
- Peppas N.A., Hilt J.Z., Khademhosseini A., Langer R., 2006, Hydrogels in Biology and Medicine: From Molecular Principles to Bionanotechnology, *Adv. Mater.*, 18, 1345-1360.
- Rosiak J. M., Olejniczak J., 1993, Medical applications of radiation formed hydrogels, *Rad. Phys. Chem.*, 42, 903-906.
- Rosiak J.M., Ulanski P., Pajewski L.A., Yoshii F., Makuuchi K., 1995, Radiation formation of hydrogels for biomedical purposes. Some remarks and comments, *Radiat. Phys. Chem.*, 46 161-168.
- Rosiak J.M., Yoshii F., 1999, Hydrogels and their medical applications, *Nucl. Instrum. Methods Phys. Res., Sect. B*, 151, 56-64.
- Sekhon B.S., Kamboj S.R., 2010, Inorganic nanomedicine—Part 2, *Nanomedicine: Nanotechnology, Biology, And Medicine*, 6, 612-618.
- Shen M., Shi X., 2010, Dendrimer-based organic/inorganic hybrid nanoparticles in biomedical applications. *Nanoscale*, 2, 1596-1610.
- Steinmetz N.F., 2010, Viral nanoparticles as platforms for next-generation therapeutics and imaging devices, *Nanomedicine: Nanotechnology, Biology, And Medicine* 6 634-641.
- Ulanski P., Janik I., Rosiak J.M., 1998. Radiation formation of polymeric nanogels, *Radiat. Phys. Chem.*, 52, 289-294.

Polymeric Nanogels: nanocarriers for Drug Delivery Application.

S. Rigogliuso*, M.A. Sabatino, G. Adamo, N. Grimaldi, C. Dispenza, G. Gherzi.

2012. Chem. Eng. Trans. 27, 247-250.



Polymeric Nanogels:

Nanocarriers For Drug Delivery Application.

Salvatrice Rigogliuso^a, Maria A. Sabatino^b, Giorgia Adamo^a, Natascia Grimaldi^b, Clelia Dispenza^{b,c} and Giulio Ghersi^{a*}

^aDipartimento di Scienze e Tecnologie Molecolari e Biomolecolari, Università degli Studi di Palermo, Viale delle Scienze, 16, Palermo-Italy.

^bDipartimento di Ingegneria Chimica, Gestionale, Informatica, Meccanica, Università degli Studi di Palermo, viale delle Scienze ed. 6, Palermo - Italia.

^c CNR-Istituto di Biofisica U.O.S. di Palermo, via Ugo La Malfa 153 90146 Palermo
giulio.ghersi@unipa.it

The application of nanotechnology to medicine has enabled the development of functionalised nanoparticles that, acting as carriers, can be loaded with drugs or genetic material to be released with a controlled mechanism in specific districts of the organism. Even though nanomedicine is a relative new branch of science, many type of nanocarriers for drug delivery have been developed over the past 30 years, such as liposomes, dendrimers, quantum dots, solid lipid nanoparticles, viruses and virus-like nanoparticles as well as a wide variety of polymeric nanoparticles. Among these last, in our opinion, nanogels deserve a special attention.

Nanogels are nanoscalar polymer networks, with a tendency to imbibe water when placed in an aqueous environment. Their affinity to aqueous solutions, superior colloidal stability, inertness in the blood stream and the internal aqueous environment, suitable for bulky drugs incorporation, make them ideal candidates for uptake and delivery of proteins, peptides, and other biological compounds. We have synthesised different variants of poly(N-vinyl-pyrrolidone)-based nanogels and demonstrated the absence of cell toxicity, which encourage further development of these materials as smart delivery systems.

In particular, in this work we demonstrate the capability of these nanogels to bypass the cell plasma membrane by following their localization in cell cultures as function of the time. We have analyzed this process by both confocal microscopy and a spectrofluorimetric approach. Results show nanoparticles preferential localization on cell surface, inside the cell and again back in the cell culture medium at different times. Ongoing experimentation is now aimed to the loading of nanocarriers with biomolecules involved in a specific substrate recognition function. This approach, if proved successful, may have a real impact in nanomedicine.

1. Introduction

The development of nanoparticles for delivery of therapeutic agents has introduced new opportunities for the improvement of medical care and, even though nanomedicine is a relative new branch of science, many type of nanocarriers for drug delivery have been proposed over the past 30 years, such as: liposomes, dendrimers, quantum dots, solid lipid nanoparticles, viruses and virus-like nanoparticles, as well as a wide variety of polymeric nanoparticles.

The motivation of the growing interest for these systems is to find alternative and more effective procedures than conventional therapies in the pharmacological treatment of various diseases.

Among the many micellar aggregates and their mediated systems, polymeric nanoparticles have been designed to successfully encapsulate drugs in order to target cells and avoid drug degradation and toxicity as well as to improve drug efficacy (Allermann et al., 1993; Couvreur et al., 2002).

Functionalized nanoparticles can be very useful for various diseases like cancer, a leading cause of morbidity and mortality worldwide, or in diseases of the central nervous system, whose treatment is very difficult because the brain is not directly accessible to intravenously (i.v.) administered drugs owing to the presence of the blood–brain barrier (BBB) (Patel et al., 2009). The development of drug delivery systems able to diffuse into the central nervous system (CNS) or to localize preferentially, if not exclusively, at the tumor site represents one of the main fields of interest in modern pharmaceutical research.

In our opinion, in the realm of polymeric nanocarriers, nanogels deserve a special consideration. Several investigations have shown that nanogels can be used efficiently as colloidal supramolecular devices for the delivery of oligonucleotides into the brain (Vinogradov S.V. et al., 2004), because of their favorable physicochemical properties, such as their narrow size distribution (Soni S. et al., 2006).. The goal of this strategy resides in the absence of adverse toxic effects from these devices after *in vivo* administration (Vinogradov et al., 2004).

Nanogels are nanoscale polymer networks, with a tendency to imbibe water when placed in an aqueous environment. Their affinity to aqueous solutions, superior colloidal stability, inertness in the blood stream and the internal aqueous environment, suitable for bulky drugs incorporation, make them ideal candidates for uptake and delivery of proteins, peptides, and other biological compounds.

A typical advantage of these hydrogel nanoparticles, respect to the classic nanoparticles, is the possibility of obtaining an elevated degree of encapsulation and offering an ideal tridimensional microenvironment for many macromolecule types. Due to their molecular size, ranging between 100-700 nm, nanogels can escape renal clearance and have prolonged serum half-life period (Wilk et al., 2009). Often they cannot penetrate the endothelial junctions of normal blood vessels. But vascular endothelium in pathological sites (solid tumors, inflammation tissues and infarcted areas) is discontinuous with large fenestrations of 200-780 nm, which allow the nanoparticle passage (Gaumet et al., 2008).

Nanoparticles-based controlled-release systems can follow two distinct approaches: a "passive targeting", where the nanoparticles loaded with biological molecules show a preferential release in the specific district where they were inoculated or where they accumulate in relation of their size and/or surface charge or other physico-chemical properties. In this case, a non-specific uptake of the nanoparticles in circulation is still present in healthy organs.

The second strategy is the "active targeting": in this case the nanoparticles are functionalized with molecules able to recognize and bind specific receptors over-expressed in target cells, such as cancer cells in which the site-specific accumulation becomes maximum. This mechanism is able to improve the therapeutic strategy, limiting toxicity around to the addressed site, differently from e.g. traditional chemotherapy where there is an aspecific drug distribution.

Controlled release of drugs encapsulated into the functionalized-nanoparticles can also be induced by external stimuli, for example by application of ultrasounds or an increase of temperature, etc. With an active targeting in mind, we have synthesised and characterised different variants of amino-functionalised poly(N-vinyl-pyrrolidone)-based nanogels.

The amino groups are amenable of bioderivation with biologically relevant molecules for targeting purposes. We have demonstrated the absence of cell toxicity, which has encouraged further development of these materials toward the application for which they have been designed. In particular, in this work we show the capability of these nanogels to bypass the cell plasma membrane, following their localisation in the cells as function of the time.

2. Experimental

2.1 Materials

Nanogels of poly(N-vinyl-pyrrolidone)-co-aminopropylacrylamide(PVP-APMAM) were produced by pulsed electron irradiation of PVP-APMAM aqueous solutions with a Linac 10MeV accelerator. Irradiation was performed with Electronika, a 10 MeV linear accelerator at the ICHTJ of Warsaw (Poland), equipped with a conveyor belt that allows many vials in a tray to pass under the beam at a given speed, which was set to supply 40 kGy per pass. An integrated dose of 80 kGy was supplied with two passes under the beam. Temperature was always maintained between 4-10 °C. After synthesis, nanogels were conjugated with fluorescein isothiocyanate (FITC) and extensively dialyzed prior to the use in cell cultures. Nanogel concentration in the aqueous dispersion is approximately 1 mg/ml.

The osteoblastic cell line MC3T3-E1 were obtained from a C57BL/6 mouse calvaria (Health Protection Agency) and were grown in Dulbecco's modified Eagle's medium (DMEM) supplemented with 10 % fetal calf serum (FCS; Euroclone, Celbar), 1 % antibiotic and 1 % glutamine (Euroclone, Celbar).

2.2 Cellular internalization studies: Confocal Analysis

The MC3T3-E1 were grown at a density of 5×10^3 cells/well into 12-well plates containing sterile glass coverslips in complete DMEM, for 24 h. Next, the cells were incubated with FITC -labeled PVP-APMAM nanogels, which emit green fluorescence by FITC conjugation.

After different incubation times, respectively, 1 h, 3 h, 6 h, 8 h and 24 h, the cells were washed twice with PBS to remove nanoparticles not taken up by the cells, fixed with 3.7 % formaldehyde for 15 min, and again washed twice with PBS.

Afterwards, the cells were stained with ethidium bromide (1:1000) for 1 min at room temperature. The monitoring was carried out observing the green fluorescence within the cells by confocal microscopy (Olympus 1x70 with Melles Griot laser system).

2.3 Cellular internalization studies: Spectrofluorimetric Analysis

The MC3T3-E1 cells were seeded in a 96 well tissue plate at a density of 7×10^3 cells/well and grown for 24 h in DMEM complete medium. Then, the cells were incubated with PVP-APMAM-FITC (4ug/well) nanogels and the nanoparticles percent into the cells after several incubation periods (0; 30', 1 h, 3 h, 6 h, 24 h and 48 h) was calculated by spectrofluorimetric readings (excitation at 485 nm and emission at 538 nm) using Spectra Max Gemini EM-500 (Molecular Devices) developed by Soft Max Pro 5.2 software.

In particular, for each incubation period and each sample (represented by 12 wells), the total fluorescence, as obtained by the fluorescence reading from cells incubated in a complete medium added with the nanoparticles, was read. Also, the cell's conditional medium was moved in a new 96 well culture plate and the fluorescence present only in the medium was read.

After removing the medium from the cells, they were washed twice with PBS to remove the excess of nanoparticles that hadn't internalized yet. The washes were collected in another 96 well culture plate and the residual fluorescence was also read. The fluorescence intensity from the culture medium, the cells and washings was checked to be equal to the initial total fluorescence.

3. Results and Discussion

3.1 Image Analysis Of Nanogels-Cells Interaction

In order to investigate nanogels interaction with cells, we tested PVP-APMAM-FITC nanoparticles in presence of MC3T3-E1 cells for different incubation periods and we followed their movement inside and through the cells.

As shown in Figure 1, after 1 h of incubation, nanogels are distributed around the cells' surface. Whereas, after 3 h of incubation, it was noted their penetration into the cytoplasm compartment. A similar distribution can be observed also in samples incubated for 6h., and then the nanogels concentration begins to decrease over time.

Probably, the nanogels are excreted as waste products in the extracellular environment, although a degradation by the lysosomal cell system of the PVP-based nanoparticle itself or of the link with the fluorescent label cannot be excluded.

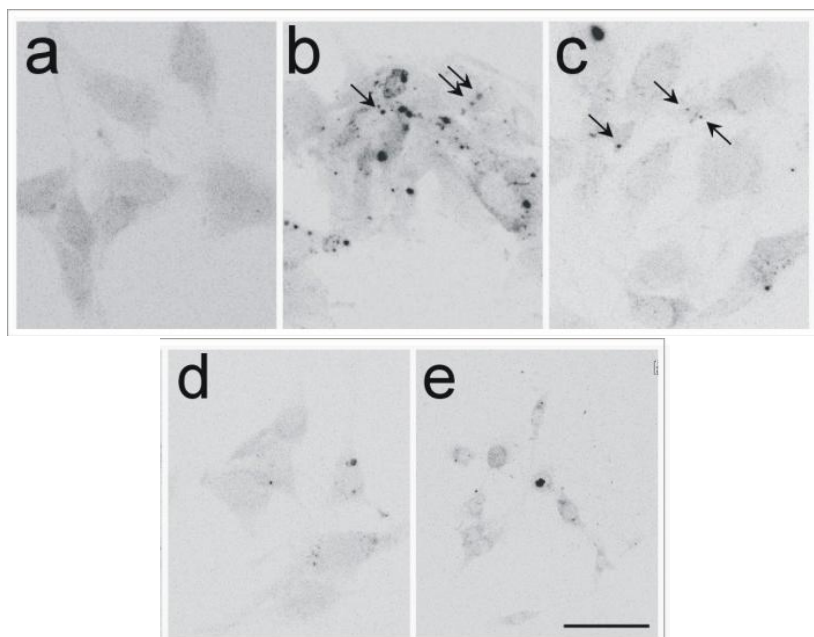


Figure 1: Nanogels-cell interaction : PVP-APMAM-FITC was incubated with MC3T3-E1 cells for different time. The localization was valued after 1 (a); 3(b); 6 (c); 8 (d) and 24 (e) hours respectively. Images, obtained by confocal microscopy observations, show the fluorescent nanoparticles. Arrows indicate the nanoparticles into the cells. Bar= 10 μ m

3.2 Path of nanoparticles inside the cells

Nanoparticles distribution was quantitatively estimated, by spectrofluorimetric measurements, at different time. For this purpose, FITC-conjugated PVP-APMAM nanoparticles were incubated with MC3T3-E1 cells.

Through spectrofluorimetric readings, for each sample, the total fluorescence (in the cells and in the medium), the amount of fluorescence inside the cells and of the fluorescence present in the waste wash were measured.

As shown in the Figure 2, at 0 time a high percent of fluorescence was present in the culture medium (86 %) and in the wash (14 %), indicating that the nanoparticles hadn't interacted with the cells yet. After 30 min of incubation, the fluorescence present inside the cells was about 3 % of the total, indicating the onset of uptake. We can suppose that this could be due to the addressing of nanoparticles in direction of cell endocytotic pathway, that could be associated to the typical clathrin-coated vesicles transport system.

On the other hand, a decrease of the medium fluorescence about 72 % was detected and an increase in the wash (25 %) is present. These data suggest that the excess of nanoparticles that are not internalized, are then removed through the wash, just as in the early times.

After 3 h, the cells-fluorescence was increased up to 5 %, while decreasing both in the wash and culture medium.

At 6 h fluorescence inside to the cell reached the maximum value (7 %) and decreased until to 3 % in 48 h. The rest of fluorescence was mainly concentrated into the culture medium (about 80 %), and to a lesser extent, in the wash (17 %); suggesting a nanoparticles extrusion mechanism through the exocytotic path.

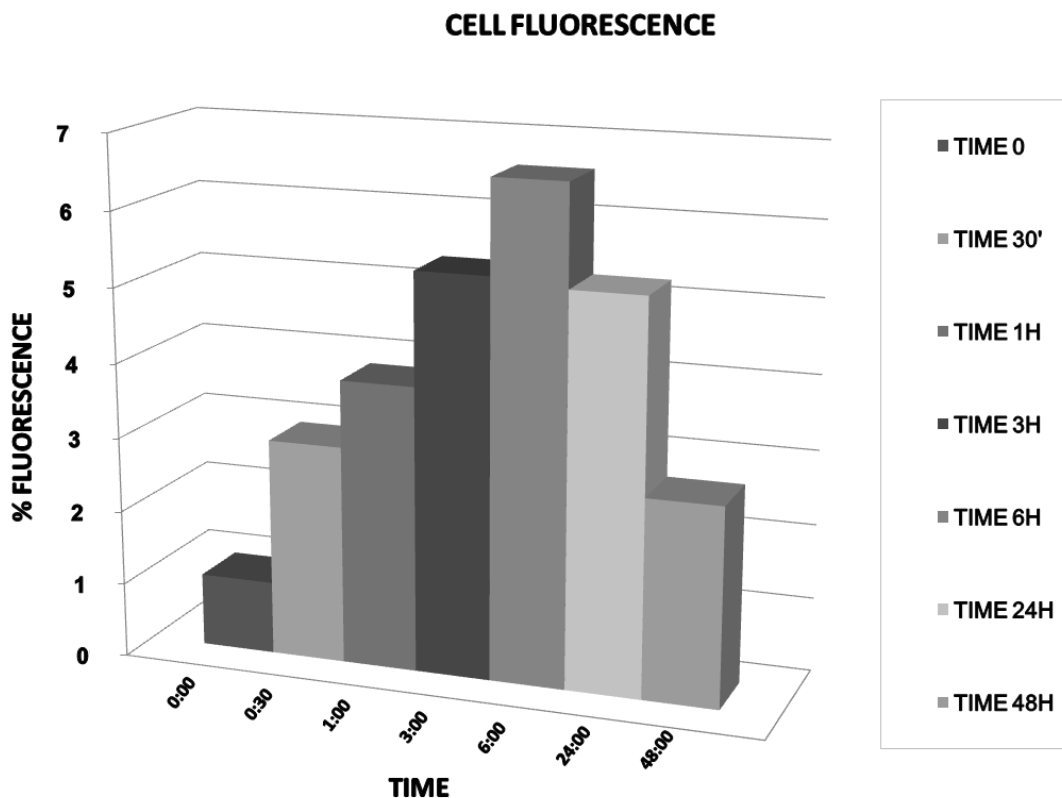


Figure 2: Path of nanoparticles through the cell compartments. PVP-FITC was incubated with MC3T3-E1 cells for different time. The nanoparticles localization was valued by spettrorfluorimetric analysis. The graph shows the percentage of cells fluorecence. Standard deviation was about 2% in each samples.

4. Conclusions

Cellular-internalization experiments showed that our nanoparticles exhibited a significantly enhanced cellular accumulation, without causing observable cytotoxic processes; according to previous results obtained in cytocompatibility and toxicity test (data not shown).

This study, although preliminary, offers an exciting prospect in use the generated nanoparticles as potential drug delivery carriers thanks to their capability of using a physiological pathway to come through the cell compartments. Therefore, it encourages to further progress in the design, manufacture and evaluation of advanced nanogels with embeded cell-target specific recognition functions.

References

- Allermann E., Gury R., Doelker E., 1993. Drug-loaded nanoparticles-preparation methods and drugs targeting issues, *Eur. J. Pharm. Biopharm.*, 39, 173-191.
- Gaumet M., Vargas A., Gurny R., Delie F., 2008. Nanoparticles for drug delivery: The need for precision in reporting particle size parameters, *Eur. J. Pharm. Biopharm.*, 69,1-9.
- Wilk K.A., Zielińska K., Pietkiewicz J., Saczko J., 2009. Loaded nanoparticles with cyanine-tipe photosensizers:preparation, characterization and encapsulation. *Chemical Engineering Transactions*, 17, 987-992, DOI:10.3303/CET0917165.
- Patel M.M., Goyal B.R., Bhadada S.V., Bhatt J.S., Amin A.F., 2009. Getting into the brain: approaches to enhance brain drug delivery. *CNS Drugs*, 23, 35–58.

- Vinogradov S.V., Batrakova E.V., Kabanov A.V., 2004. Nanogels for oligonucleotide delivery to the brain. *Bioconjug. Chem.*, 15, 50–60.
- Soni S., Babbar A.K., Sharma R.K., Maitra A., 2006. Delivery of hydrophobised 5-fluorouracil derivative to brain tissue through intravenous route using surface modified nanogels. *J. Drug Target.*, 14, 87–95.

*High-energy radiation processing, a smart approach
to obtain PVP-graft-AA nanogels..*

N. Grimaldi*, M.A. Sabatino, G. Przybytniak, I. Kaluska, M.L. Bondi,
D. Bulone, S. Alessi, G. Spadaro, C. Dispenza.

2014. Radiat. Phys. Chem. 94, 76-79



ELSEVIER

Contents lists available at ScienceDirect

Radiation Physics and Chemistry

journal homepage: www.elsevier.com/locate/radphyschem

High-energy radiation processing, a smart approach to obtain PVP-graft-AA nanogels

N. Grimaldi^{a,*}, M.A. Sabatino^a, G. Przybytniak^b, I. Kaluska^b, M.L. Bondì^c, D. Bulone^d, S. Alessi^a, G. Spadaro^a, C. Dispenza^{a,d}^a Dipartimento di Ingegneria Chimica, Gestionale, Informatica, Meccanica, Università degli Studi di Palermo, Viale delle Scienze Ed. 6, 90128 Palermo, Italy^b Centre for Radiation Research and Technology, Institute of Nuclear Chemistry and Technology, Dorodna 16, 03-195 Warsaw, Poland^c CNR—Istituto per lo Studio dei Materiali Nanostrutturati (ISMN), UOS Palermo, via Ugo La Malfa 153, 90146 Palermo, Italy^d CNR—Istituto di Biofisica (IBF), UOS Palermo, via Ugo La Malfa 153, 90146 Palermo, Italy

H I G H L I G H T S

- Aqueous solutions of PVP and AA were irradiated by industrial electron accelerator.
- NGs with different physico-chemical and molecular properties can be obtained.
- Carboxyl-functionalized NGs produced are promising building blocks for bio-devices.

A R T I C L E I N F O

Article history:

Received 16 November 2012

Accepted 3 April 2013

Available online 19 April 2013

Keywords:

Poly(N-vinylpyrrolidone)

Acrylic acid grafting

Nanogels

E-beam irradiation

A B S T R A C T

Poly(N-vinylpyrrolidone)-grafted-acrylic acid biocompatible nanogels (NGs) were prepared using an exiting industrial-type electron accelerator and setups, starting from semi-dilute aqueous solutions of a commercial PVP and the acrylic acid monomer. As a result, NGs with tunable size and structure can be obtained quantitatively. Sterility was also imparted at the integrated dose absorbed. The chemical structure of the NGs produced was confirmed through Fourier Transformer Infrared Spectroscopy (FT-IR). The molecular and physico-chemical properties of NGs, such as the hydrodynamic dimensions and surface charge densities, for various polymer and monomer concentrations in the irradiated solutions, are discussed here.

© 2013 Elsevier Ltd. All rights reserved.

1. Introduction

Nanogels are particles formed by physically or chemically crosslinked polymer networks of nanoscale size. They are very promising carriers for drug delivery owing to their favorable properties, such as high biocompatibility, tunable size and chemical functionalities, a large surface area for bioconjugation and an internal 3D aqueous network for the incorporation of bioactive molecules (Kabanov and Vinogradov, 2009). Specific chemical functionality must be present on NGs, such as –COOH, –OH, –SH or –NH₂ groups, to achieve effective conjugation with biomolecules to improve their affinity toward the target biological system, e.g. an organ or a tissue or a cell type (Pathak and Thassu, 2009). The development of effective NG-based therapeutic devices is limited by the availability of inexpensive and robust synthesis methodologies. In the last decade, different synthetic approaches

have been proposed to produce nanogels either starting from monomers solutions or polymers solutions. Each of these has advantages and disadvantages and leads to similar, yet not identical, nanostructures (Dispenza et al., 2012a; Dispenza et al., in press; Oh et al., 2008; Ulanski and Rosiak, 2004). Radiation-induced cross-linking is a well-established, robust and economically viable synthetic strategy to produce NGs (Charlesby, 1960; Ulanski and Rosiak, 1999; Dispenza et al., 2012b), that simultaneously ensures polymer cross-linking, particles size control, chemical functionalization and sterilization of the produced materials. We have recently demonstrated that amino-graft PVP nanogels of different particle sizes and degrees of functionality can be generated, using an exiting industrial-type electron accelerator and setups, with high yields from aqueous solutions containing linear PVP and APMAM (N-(3-aminopropyl)methacrylamide) (Dispenza et al., 2012a). The available primary amino groups have been subsequently used for nanogels labeling with fluorescence probes and for protein attachment. In this work, we present the results related to a new family of functionalized PVP NGs, generated in the presence of acrylic acid. Grafted carboxyl groups

* Corresponding author. Tel.: +39 091 23863738. fax: +39 091 23860841.
E-mail address: nataschia.grimaldi@unipa.it (N. Grimaldi).

on the nanoparticles will enable conjugation reactions with short peptides and amino terminated nucleic acids. In our approach semi-dilute aqueous solutions of the polymer, at two different concentrations, in the presence of the acrylic monomer were subjected to pulsed electron beam irradiation at relatively low dose per pulse, high frequency and 40 kGy of integrated dose. The influence of feed composition on particles size, surface charge properties, molecular weight and chemical structure was investigated.

2. Experimental

2.1. Materials

PVP K60 and acrylic acid (AA) were supplied by Aldrich and used without further purification. The weight average molecular weight ($M_w = 4.1 \times 10^5$ g/mol) and radius of gyration ($R_g = 27$ nm) for PVP K60 were estimated using static light scattering measurements (Dispenza et al., 2011).

2.2. Poly(*N*-vinylpyrrolidone) based nanogels synthesis

PVP/AA aqueous solutions with two concentrations of PVP, 0.1 and 0.25 wt% (equivalent to ~9.0 and 22.5 mM of repetitive unit (RU), respectively) and the same molar ratio of PVP's RU to AA, precisely 50, were prepared by overnight stirring, filtered with 0.22 μm pore size syringe filters, carefully deoxygenated with gaseous nitrogen and individually saturated with N_2O ($\text{N}_2\text{O} \geq 99.99\%$) prior to irradiation. Base PVP systems were prepared in the same conditions as above. Electron beam irradiation was performed using the linear accelerator at the ICHTJ of Warsaw (Poland), Electronika 10/10. Irradiation was carried out at an average beam current of 0.45 mA, pulse length of 4.5 μs and pulse repetition rate of 400 Hz (Dispenza et al., 2012a). Samples were horizontally placed in a box filled with ice and conveyed under the beam via a transporting belt at a speed of 0.3 m/min. From a measurement of the residence time of the vials under the beam (~10 s) we can estimate an approximate absorbed dose per pulse of ~13 Gy. The integrated dose of 40 kGy was supplied in a single pass. After irradiation, samples were dialyzed (MWCO 100 kDa) against distilled water for 48 h to remove eventual unreacted monomers, oligomers and low MW polymer and re-equilibrate pH (Dispenza et al., 2012a). In fact, all formulations had a pH of about 6.0 prior to irradiation, which turned to be in the range 4–4.5 after irradiation and between 5 and 5.8 after dialysis. The yield of recovered nanogels after dialysis was determined gravimetrically (Dispenza et al., 2012c). Samples were coded after as $P^*(0.1)$ and $P^*(0.25)$, when referring to the two base irradiated PVP solutions, and as $P^*(0.1)\text{AA}(50)$ and $P^*(0.25)\text{AA}(50)$, when referring to the two corresponding PVP/AA systems.

2.3. Characterizations

FT-IR analysis was carried out with a Perkin-Elmer Spectrum 400 apparatus by dispersing the dry product in potassium bromide and compressing into pellets. Spectra were recorded at 30 scans per spectrum and 1 cm^{-1} resolution in the 4000–400 cm^{-1} range.

The hydrodynamic diameters (D_h) of NGs in dispersions were measured by dynamic light scattering (DLS; Dispenza et al., 2012c). Weight average molecular weight (M_w) of nanogels was estimated from multi-angle static light scattering measurements at 25 ± 0.1 °C in aqueous solution. Light scattering measurements were carried out using a Brookhaven BI-9000 correlator and a 50 mW He–Ne laser (Melles Griot) tuned at $\lambda = 632.8$ nm. A refractive index increment (dn/dc) value of 0.185 was determined using a Brookhaven Instruments differential refractometer

at $\lambda = 620$ nm for PVP in aqueous solution. Static light scattering data were analyzed according to the Zimm plot method, using for all nanogels the dn/dc value of linear PVP (Ulanski and Rosiak, 1999). Surface charge density of nanogels in water was measured at 25 °C using a ZetaSizerNano ZS (Malvern Instruments Ltd, Malvern, UK) equipped with a He–Ne laser at a power of 4.0 mW. For systems characterized by a monomodal ζ -potential distribution, the mean ζ -potential and the relative distribution width are reported. Conversely, for systems that show a more heterogeneous surface charge density, i.e. multimodal ζ -potential distribution, mean ζ -potential values, relative widths and relative abundance (% areas) of the different modes are reported.

3. Results and discussion

EB-irradiation of semi-diluted aqueous solutions of PVP, i.e. at concentration lower than the critical chain overlap concentration (1 wt%; Dispenza et al., 2011), in the presence of acrylic acid was performed at relatively high frequency, low dose per pulse and in an oxygen-free, N_2O saturated atmosphere. The integrated dose of 40 kGy has been selected in order to provide sterility (Lambert and Hansen, 1998), and supplied at 13 Gy per pulse, to ensure that a minimum of one radical per PVP chain per pulse is formed. In principle, in these conditions we do not expect intramolecular recombination as the dominant process, since intermolecular crosslinking, as well as grafting of monomer molecules may also occur. Homopolymerization of acrylic acid is not favored either, due to the mutual repulsion between the unprotonated acrylic acid molecules at the pH of the irradiated solutions (pH=6), which is above the pKa of acrylic acid (pKa=4.75). Furthermore, any poly (acrylic acid) eventually formed during irradiation would undergo chain scission (Henke et al., 2005). Therefore, it is essentially the monomeric form of acrylic acid that may graft onto PVP, while it simultaneously crosslinks. For all systems nanogels were recovered, after synthesis and purification, with yields always higher than 95%.

3.1. Structural properties

Spectra of base and functionalized NGs with respect to non-irradiated PVP are shown in Fig. 1a and b. For all NGs, the characteristic carbonyl peak of PVP becomes a multi-band envelope, which stretches both toward the higher and lower wavenumbers. With the only exception of $P^*(0.25)$, the height of the carbonyl band at 1661 cm^{-1} , as well as the broad hydroxyl band peaking at 3400 cm^{-1} , increases. These spectral features point out to an increased level of oxidation of the nanoscalar networks, mainly resulting from radiation-induced modification of PVP. For $P^*(0.25)$ the carbonyl band enlarges mainly toward the lower wavenumbers at the expenses of its height, suggesting partial ring opening reactions and formation of pendant carboxylate anions (Sabatino et al., 2013). $P^*(0.25)\text{AA}(50)$ spectrum is essentially different from that of $P^*(0.25)$ with a substantial increase of hydroxyl and carbonyl bands intensity, due to AA grafting. For the 0.1 wt% systems two new peaks, at 1769 and 1698 cm^{-1} , are clearly evident, attributable to the formation of 5-member cyclic imides (Silverstein et al., 1974). At lower polymer concentration, intramolecular termination reactions (including crosslinking and disproportionation) prevail over bimolecular, diffusion-controlled, terminations. Polymer coils stiffen and owing to the formation of double bonds through intramolecular disproportionation, they become also more vulnerable to irradiation-induced oxidation (An et al., 2011). These conditions are at the basis of the overwhelming imide character shown by both $P^*(0.1)$ and $P^*(0.1)\text{AA}(50)$ nanogels (Sabatino et al., 2013).

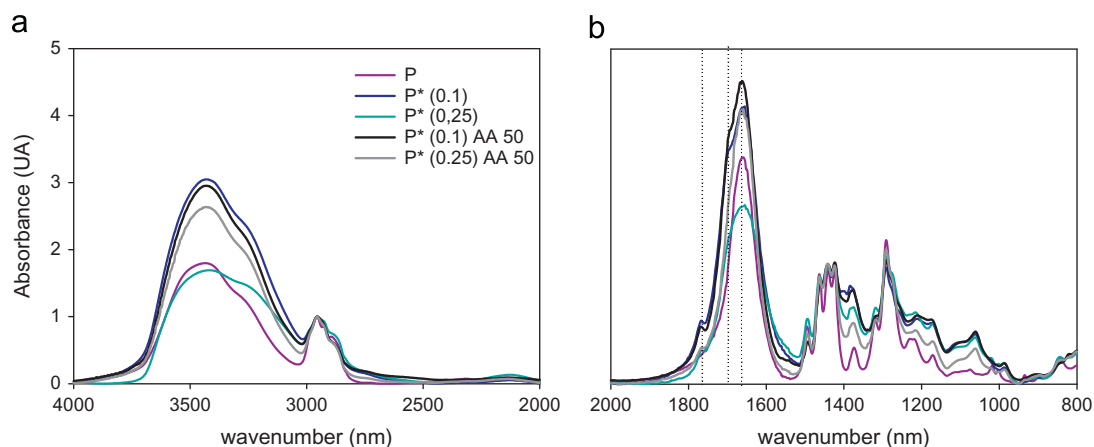


Fig. 1. a and b: FT-IR spectra of nonirradiated PVP and nanogels. All spectra were normalized with respect to the peak at 2956 cm^{-1} . Vertical dashed lines correspond to the following peaks: 1769 , 1698 and 1662 cm^{-1} .

Table 1

Hydrodynamic diameter (D_h), average ζ -potential value and weight average molecular weight of the polymer (MW) for linear PVP and NGs.

System	D_h (nm)		ζ -potential (mV)			MW (MDa)	
	Mean	Width	Mean	Width	Area (%)	Mean	Width
Linear PVP	40	16	-6.1	5.45	83	0.41	0.015
$P^*(0.1)$ NGs	34	10	-23.6	4.29	17	0.99	0.11
			-24.9	7.82	45		
$P^*(0.1)$ AA50 NGs	14	5	-21.9	8.4	100	0.65	0.07
$P^*(0.25)$ NGs	50	14	-30.2	9.45	100	1.96	0.024
$P^*(0.25)$ AA50 NGs	26	10	-40	9.26	100	1.3	0.025

3.2. Physico-chemical and molecular properties

In Table 1 the weight average molecular weight (MW) and the mean hydrodynamic diameter for nonirradiated PVP, base and functionalized PVP NGs are reported. In general, changes in the molecular weight of irradiated polymers result from the competition between chain scission and intermolecular recombination of macroradicals, while the intramolecular recombination causes only a reduction of the polymer hydrodynamic diameter, without affecting the molecular weight (Ulanski and Rosiak, 1999). Both base and carboxyl-functionalized NGs show an increase of the MW with respect to the linear PVP. This increase is more pronounced for the systems with the higher PVP concentration (0.25 wt%), which suggests intermolecular crosslinking occurring to a higher extent. Base NGs show higher MW than corresponding functionalized NGs, suggesting a competition between intermolecular crosslinking and monomer grafting to PVP. $P^*(0.25)$ shows a hydrodynamic diameter higher than that of nonirradiated PVP, while $P^*(0.1)$ system is characterized by smaller particles, despite the observed increase of MW. This indicates a prevalence of intramolecular crosslinking, yielding to a denser network. All carboxyl-functionalized PVP NGs have hydrodynamic diameters smaller than those of the corresponding base NGs, for the above postulated competition between grafting and intermolecular crosslinking and/or AA mediated further intramolecular crosslinking. Particle size distributions are monomodal for all systems and variability of size is always below 30%.

Surface charge density can be expressed as ζ -potential, used to predict the colloidal stability of NGs and gives insight on their chemical structure. The bimodal distribution of ζ -potential values of semi-diluted linear PVP (0.1 wt%), with a main peak close to neutrality and a second peak at about -20 mV, can be explained in

the light of the keto–enol tautomerism and possible partial ring opening of pyrrolidone, respectively (Kaczmarek et al., 2001; Maruthamuthu and Subramanian, 1985; Sabatino et al., 2013). In general, all irradiated nanogels present a distinct anionic character, owing to the chemical modifications of PVP induced by irradiation. In particular, for $P^*(0.1)$ the surface charge distribution is still bimodal and the proportion of slightly charged over uncharged particles increases with respect to PVP. $P^*(0.25)$ and both the AA functionalized variants show monomodal distributions of charge densities. The increase of the anionic character of $P^*(0.25)$ is likely due to the already discussed contribution from radiation-induced pyrrolidone ring opening reactions, while for $P^*(0.25)$ AA(50) NGs and $P^*(0.1)$ AA(50) NGs it seems like the contribution of also carboxyl groups from the grafted acrylic acid.

4. Conclusions

E-beam irradiation of PVP semi-dilute aqueous solutions in the presence of acrylic acid allows producing, in a single step and with high yields, as-born sterile nanogels with controlled particle size and functionality. Recourse to surfactants to control particle size is not required, as the PVP itself acts as a soft template; therefore complex purification procedures are unnecessary. A favorable combination of both manufacturing process and product properties makes the generated carboxyl functionalized nanogels very promising candidates as nanocarriers in drug delivery or diagnostic applications.

References

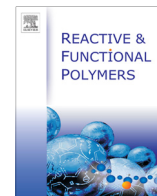
- An, J.-C., Weaver, A., Kim, B., Barkatt, A., Poster, D., Vreeland, W.N., Silverman, J., Al-Sheikhly, M., 2011. Radiation-induced synthesis of poly(vinylpyrrolidone) nanogel. *Polymer* 52, 5746–5755.
- Charlesby, A. (Ed.), Pergamon Press, New York.
- Dispenza, C., Grimaldi, N., Sabatino, M.-A., Todaro, S., Bulone, D., Giacomazza, D., Przybytniak, G., Alessi, S., Spadaro, G., 2012c. Studies of network organization and dynamics of e-beam crosslinked PVPs: from macro to nano. *Radiat. Phys. Chem.* 81 (9), 1349–1353.
- Dispenza, C., Ricca, M., Lopresti, C., Battaglia, G., La Valle, M., Giacomazza, D., Bulone, D., 2011. E-beam irradiation and UV photocrosslinking of microemulsion-laden poly(N-vinyl-2-pyrrolidone) hydrogels for “in-situ” encapsulation of volatile hydrophobic compounds. *Polym. Chem.* 2, 192–202.
- Dispenza, C., Rigogliuso, S., Grimaldi, N., Sabatino, M.-A., Bulone, D., Bondi, M. L., Gheri, G., Structure and biological evaluation of amino-functionalized PVP nanogels for fast cellular internalization. *React. Funct. Polym.*, in press.
- Dispenza, C., Sabatino, M.-A., Grimaldi, N., Bulone, D., Bondi, M.L., Casaletto, M.P., Rigogliuso, S., Adamo, G., Gheri, G., 2012a. Minimalism in radiation synthesis of biomedical functional nanogels. *Biomacromolecules* 13 (6), 1805–1817.

- Dispenza, C., Sabatino, M.-A., Grimaldi, N., Spadaro, G., Bulone, D., Bondi, M.L., Adamo, G., Rigogliuso, S., 2012b. Large scale radiation manufacturing of hierarchically assembled nanogels. *Chem. Eng. Trans.* 27, 229–232.
- Henke, A., Kadlubowski, S., Ulanski, P., Rosiak, J.M., Arndt, K.F., 2005. Radiation-induced cross-linking of polyvinylpyrrolidone–poly(acrylic acid) complexes. *Nucl. Instrum. Methods Phys. Res. B* 236, 391–398.
- Kabanov, A.V., Vinogradov, S.V., 2009. Nanogels as pharmaceutical carriers: finite networks of infinite capabilities. *Angew Chem. Int. Ed. Engl.* 48 (30), 5418–5429.
- Kaczmarek, H., Szalla, A., Kaminska, A., 2001. Study of poly(acrylic acid)–poly(vinylpyrrolidone) complexes and their photostability. *Polymer* 42, 6057–6059.
- Lambert, B.J., Hansen, J.M., 1998. ISO radiation sterilization standards. *Radiat. Phys. Chem.* 52, 11–14.
- Maruthamuthu, M., Subramanian, E., 1985. Binding of Evans Blue onto poly(N-vinyl-2-pyrrolidone). *Polym. Bull.* 14, 207–212.
- Oh, J.K., Drumright, R., Siegwart, D.J., Matyjaszewski, K., 2008. The development of microgels/nanogels for drug delivery applications. *Prog. Polym. Sci.* 33, 448–477.
- Pathak, Y., Thassu, D. (Eds.), 2009. Informa Healthcare USA, New York.
- Sabatino, M.A., Bulone, D., Veres, M., Spinella, A., Spadaro, G., Dispenza, C., 2013. Structure of e-beam sculptured poly(N-vinylpyrrolidone) networks across different length-scales, from macro to nano. *Polymer* 54, 54–64.
- Silverstein, R.M., Bassler, G.C., Morrill, T.C., 1974. *Spectrometric Identification of Organic Compounds*, 3rd ed. John Wiley & Sons, New York.
- Ulanski, P., Rosiak, J.M., 1999. The use of radiation technique in the synthesis of polymeric nanogels. *Nucl. Instr. Methods Phys. Res. B* 151, 356–360.
- Ulanski, P., Rosiak, J.M., 2004. *Encyclopedia of Nanoscience and Nanotechnology*. In: Nalwa, H.S. (Ed.), *Polymeric micro/nanogels*. American Scientific Publishers, Stevenson Ranch, CA.

*Structure and biological evaluation of amino-functionalized PVP nanogels
for fast cellular internalization..*

C. Dispenza*, S. Rigogliuso, N. Grimaldi, M.A. Sabatino, D. Bulone,
M. L. Bondi, G. Gherzi.

2014. React. Funct. Polymer, 73, 1103- 1113.



Structure and biological evaluation of amino-functionalized PVP nanogels for fast cellular internalization



C. Dispenza^{a,c,*}, S. Rigogliuso^{b,*}, N. Grimaldi^a, M.A. Sabatino^a, D. Bulone^c, M.L. Bondì^d, G. Gherzi^b

^a Dipartimento di Ingegneria Chimica, Gestionale, Informatica, Meccanica, Università degli Studi di Palermo, Viale delle Scienze, Ed. 6, 90128 Palermo, Italy

^b Dipartimento di Scienze e Tecnologie Biologiche, Chimiche e Farmaceutiche, Università degli Studi di Palermo, Viale delle Scienze, Ed. 16, 90128 Palermo, Italy

^c CNR – Istituto di Biofisica (IBF) UOS Palermo, via Ugo La Malfa, 153, 90146 Palermo, Italy

^d CNR – Istituto per lo Studio dei Materiali Nanostrutturati (ISMN) UOS Palermo, via Ugo La Malfa, 153, 90146 Palermo, Italy

ARTICLE INFO

Article history:

Received 14 February 2013

Received in revised form 17 April 2013

Accepted 24 April 2013

Available online 30 April 2013

Keywords:

Nanogels

Poly(N-vinyl pyrrolidone)

Microemulsion polymerization

Proton spin–lattice relaxation time

Cellular internalization

ABSTRACT

Aminopropyl methacrylamide chloride-graft-poly(N-vinyl pyrrolidone) nanogels (NGs) were designed to exploit the favorable properties of poly(N-vinyl pyrrolidone) (PVP), such as its high affinity to water and complexation ability of ions, molecules and macromolecules, with the availability of primary amino groups for bioconjugation reactions. A thorough structural characterization of the nanoscalar networks was performed via ¹H NMR and solid state ¹³C NMR spectroscopies, while solid state NMR relaxation time measurements completed the NGs description in terms of polymer network density. Information on the hydrodynamic size and surface charge densities were sought via dynamic light scattering (DLS) and ζ-potential measurements. These measurements, carried out both in water and in buffer and at the variance of pH, temperature and time, support the excellent colloidal stability of the amino-graft PVP nanogels and their redispersability from the dry physical form. The total absence of *in vitro* toxicity and immunogenicity was ascertained first, and then cell localization studies in cell cultures of fluorescent variants were performed. Furthermore, the possibility of decorating the nanogels with bovine serum albumin (BSA) to obtain a stable bio-hybrid colloidal nanoconstruct was established. All the gathered evidences qualify these materials as potential candidates to be used as nanocarriers for intra-cellular delivery of protein and other biomolecular drugs.

© 2013 Elsevier Ltd. All rights reserved.

1. Introduction

Nanoscalar particles formed by chemical networks of cross-linked poly(N-vinyl pyrrolidone) and functional monomers are promising candidates for the purpose of generating multifunctional “smart” nanocarriers in drug delivery and diagnostics. Poly(N-vinyl pyrrolidone) is a well-known polymer, recognized by FDA as GRAS and widely used in pharmaceutical formulations. Both linear and crosslinked PVP show *in vivo* biocompatibility and escape ability from the body by natural pathways and processes, depending on molecular weight or particle size [1]. PVP is also characterized by excellent complexing properties for ionic or π-electron system containing substances, such as multivalent cations, acids or aromatic compounds. For this reason it is often used as polymeric stabilizer in aqueous dispersions of quantum dots, noble,

superparamagnetic or other polymer's nanoparticles [2–4]. Furthermore, it can be converted into a biocompatible macrogel by gamma, electron beam or UV-irradiation [5–13]. Nanoscale PVP networks couple the advantages of the PVP structure with the opportunities arising from the controlled size at the nanoscale. Crosslinked PVP nanoparticles have already been proposed for gene delivery [14]. They have been used to encapsulate and protect DNA from intracellular degradation, facilitating internalization into vesicular structures. It has been shown that these particles can be administered intravenously and remain in circulation for a considerable period of time evading the immune system [15]. In the design of a multifunctional nanocarrier, the presence of reactive functional groups, typically primary amino groups, terminal carboxyl groups or thiol groups are highly desirable, e.g. for the immobilization, protection and release of proteins [16,17] or to conjugate critical genetic markers associated with certain disease states for diagnostic and/or active targeting purposes [18,19]. We have already established the possibility of generating amino-functionalized PVP nanogels through a robust and economically viable process, consisting of e-beam induced crosslinking of PVP aqueous solutions in the presence of a primary amino group carrying monomer namely (3-aminopropyl) methacrylamide hydrochloride (APMAM) [20]. In the

* Corresponding authors. Address: Dipartimento di Ingegneria Chimica, Gestionale, Informatica, Meccanica, Università degli Studi di Palermo, Viale delle Scienze, Ed. 6, 90128 Palermo, Italy. Tel.: +39 091 23863710; fax: +39 091 23860840 (C. Dispenza), tel.: +39 091 238 97409; fax: +39 091 6577210 (S. Rigogliuso).

E-mail addresses: clelia.dispenza@unipa.it (C. Dispenza), salvatrice.rigogliuso@unipa.it (S. Rigogliuso).

chosen irradiation conditions, a significant chemical modification of PVP is observed and nanogels develop a distinct anionic character [20,21]. Although APMAM was successfully copolymerized, increasing the APMAM content led to uncontrolled particle size due to opposite charges interaction and reduced availability of primary amino groups at the surface. The possibility of obtaining variants of amino-functionalised PVP nanogels with different size or a higher APMAM content, through a conventional free-radical heterogeneous polymerization of VP, is here explored for the first time. Polymerization and simultaneous crosslinking of N-vinyl pyrrolidone, APMAM and/or other water soluble functional monomers, was carried out inside the aqueous pods of a w/o microemulsion, using N,N'-methylene-bisacrylamide as crosslinker and ammonium persulfate as initiator [22,23]. In the chosen reaction conditions it is expected that VP and the other functional monomers, as well as the water soluble initiator, will favorably partition toward the inner aqueous phase of the microemulsion, as obtained with the assistance of a surfactant. Polymerization will start simultaneously in all APS visited micelles and particle growth occurs as a result of radical transfer to monomer molecules coming from other micelles, either by diffusion of monomer through the continuous phase or by contact of neighbor micelles as a result of their center mass Brownian motion [24]. When reaction is completed, an accurate purification process from unreacted monomers, organic solvent and surfactant must follow. This work demonstrates how the success of this synthetic approach, both in terms of yield of recovered product and control of particle size, is very much dependent on the optimal combination of both synthetic and purification procedures. The obtained functionalized nanogels were characterized in terms of particle size and size distribution, surface charge density, stability upon storage in the form of aqueous dispersions, as function of pH and time and redispersability from the dry form. The NGs chemical structure was confirmed by both ^1H NMR and ^{13}C NMR analyses, while for a selected formulation the NG network density was characterized through determination of proton spin-lattice relaxation times in the rotating frame ($T_{1\rho\text{H}}$) from solid-state NMR, using linear PVP and an "equivalent macrogel" system as reference materials. The characterization was completed by a thorough biocompatibility evaluation and NGs localization studies in cell cultures. Finally, a bio-hybrid stable nanoconstruct was generated by binding BSA on the NG's surface, with the aim of demonstrating the potential of the amino functionalized nanogels to be used as protein drug nanocarriers for intra-cellular delivery.

2. Experimental

2.1. Materials

The 1-vinyl-2-pyrrolidone (VP, Aldrich) monomer was freshly distilled before polymerization, N,N'-methylene-bisacrylamide (MBA, Aldrich), fluorescein diacrylate (FDA, Aldrich), (3-aminopropyl) methacrylamide hydrochloride (APMAM, Polyscience), ammonium persulfate (APS, Aldrich), N,N,N',N'-tetramethyl ethylenediamine (TEMED, Aldrich), N-hexane (Aldrich), docusate sodium salt (AOT, Aldrich), Brij 30 (Aldrich), linear PVP (k60) (Aldrich) were all used as received, without further purification.

2.2. Cell culture reagents

The osteoblastic cell line MC3T3-E1, from a C57BL/6 mouse calvaria, passage N°:2, was grown in Dulbecco's modified Eagle's medium (DMEM) supplemented with 10% w fetal calf serum (FCS; Euroclone, Celbio), 1% w antibiotic and 1% w glutamine (Euroclone, Celbio). Cell cultures were incubated at 37 °C in a humidified atmosphere at 5% v CO₂ in air, with three times a week

medium changes. Cells were used between the N°:3 and the N°:6 passages.

2.3. Preparation of cross-linked VP base nanogels and fluorescein functionalized variants

Reverse micelles were prepared by dissolving the surfactant in a given volume of *n*-hexane at room temperature. The reaction of VP and FDA, when present, was conducted in the presence of APS and MBA. Different formulations were investigated, whose composition is summarized in Table 1. In a typical preparation for non ionic nanogels (VP-MBA; VP-MBA-FDA), 120 ml of 0.03 M AOT solution in hexane was carefully deoxygenated with gaseous nitrogen (99.99%) and sequentially added of a solution (2.52 ml) containing freshly distilled VP and MBA (2.7 mg/ml), FDA (2.3 mg/ml) when present, and TEMED (45 μl). The mixture was homogenized (Ultra-Turrax T25 basic) resulting optically transparent. Then, 120 μl of aqueous APS (20% w/v) was added drop-wise at 0–4 °C while stirring. Polymerization was carried out at 37 °C under gaseous nitrogen with continuous stirring for 48 h. Hexane was evaporated in a rotary evaporator and the dry mass was resuspended in 10 ml of water. Purification from surfactant was carried out as follows (method 1): 1 ml aliquots of 30% w/v calcium chloride solution were added drop-wise while continuous stirring to precipitate the water-insoluble surfactant, AOT, as calcium salt by centrifugation [15]. Two distinct phases were obtained upon centrifuging: an aqueous solution containing most of the cross-linked nanoparticles and an AOT salt cake, which may contain some of the nanoparticles. The precipitate was dissolved in 15 ml of hexane and residual nanoparticles were extracted using water. The phase-separated aqueous layers were drained out and added to the previously centrifuged aqueous supernatant solution. The surfactant-free nanogel dispersions were subjected to dialysis (12 K MWCO) against water to remove any eventual low molecular weight hydrophilic residues. The total aqueous dispersions of nanoparticles were then sub-divided in aliquots and either reduced in volume to produce nanoparticles concentrates or to a completely dry powder by freeze-drying. The yield of recovered dry product was determined as the ratio of the dry product after the purification and the total weight of monomers present in the reaction mixture and it was measured in triplicate.

2.4. Preparation of amino-functionalized crosslinked VP nanogels

The application of both synthetic and purification conditions described above for the non-ionic nanogels led to a considerable decrease of yield in terms of recovered dry product when APMAM was present in the feed, possibly due to the strong interaction between the cationic monomer (APMAM) and the anionic surfactant (AOT). Both the reaction conditions and the purification procedure were modified to improve recovery. Briefly, the recourse to a non-ionic co-surfactant (Brij 30) was made to increase the ease of emulsification and the inverse microemulsion stability [24], and the initiator concentration was decreased to reduce the overall system reactivity. As a result a noticeable increase of product yield was observed. The reduction of reaction time to 24 h from 48 h was proved to have no significant effects on the yield. A different purification procedure was developed (method 2). In this case, after hexane evaporation, the mass of dry product was resuspended in ethanol and subjected to extensive dialysis (12,000 MWCO) against water/ethanol solution (20% v of water). At the end of the dialysis, ethanol was evaporated and the dry product was resuspended in a note volume of water.

Table 1
Feed composition of base, fluorescent and amino functionalized PVP nanogels.

System	Description	VP/MBA	VP/APMAM	VP/APS	Vhex/Vwat	AOT (M)	Brij 30 (M)	React time (h)
#1	VP-MBA	64	–	150	235	0.03	–	48
#2	VP-MBA-FDA	64	200	150	235	0.03	–	48
#3	VP-MBA-APMAM(200)	64	200	150	235	0.03	–	48
#4	VP-MBA-APMAM(200)	64	200	25	34.5	0.09	0.2	24
#5	VP-MBA-APMAM(50)	64	50	25	34.5	0.09	0.2	24
#6	VP-MBA-APMAM(10)	64	10	25	34.5	0.09	0.2	24

2.5. FITC and BSA conjugation to amino-functionalized nanogels

The conjugation was performed accordingly to an already in-house established protocol [20]. Briefly, a given volume (0.6 ml) of NG dispersion was mixed with 0.05 M Borax (pH 9.3) and 0.4 M NaCl aqueous solution (1.4 ml) and with 14 µg/ml methanol/water solution (0.1% v MeOH) of FITC (2 ml). The solution was kept at 37 °C while stirring for 2 h. FITC conjugated nanogels (VP-MBA-APMAM^{FITC}) were then dialyzed against pH 7.4 PBS for 120 h at room temperature. Both reaction and dialysis were carried out in dark conditions.

The above described conjugation protocol was also applied to decorate nanogels with BSA. After conjugation, the adduct was thoroughly dialyzed against PBS using 100 kDa MWCO membranes. Purified product was analysed both by UV-Vis spectrometry on DU 730 Life Science Spectrophotometer (Beckman Coulter) and by cellulose acetate electrophoresis. The membrane was preliminarily wetted with the running buffer (Tris Ippurate at pH 8.8) and loaded with 25 µl of each sample. Electrophoresis was carried out for 30 min at 200 V. Then, the membrane was stained with Ponceau red, washed with 5% v acetic acid solution then put into a bleach solution. Migration patterns of nanogels were compared to that of free BSA [4 mg/ml] as control.

2.6. Physico-chemical characterization

The hydrodynamic radius (R_h) of particles dispersion was measured by dynamic light scattering (DLS) using a Brookhaven Instruments BI200-SM goniometer equipped with a 50 mW He-Ne laser (Melles Griot) tuned at $\lambda = 632.8$ nm. Samples, placed in the quartz cell after dilution with bidistilled water or PBS buffers at different pH, were put in the thermostated cell compartment of the instrument at 25 ± 0.1 °C or 37 ± 0.1 °C. The intensity autocorrelation function at 90° scattering angle and the time autocorrelation function were measured by using a Brookhaven BI-9000 correlator operating in the multi- τ mode. The experimental duration was set to have at least 2000 countings on the last channel of the correlation function. All irradiated samples were analyzed as produced, without filtration, to minimize artifacts. Particular care was paid in treating the samples in a clean environment to reduce dust contamination. Since the samples showed a monomodal distribution, DLS data were analyzed by the method of cumulants [20]. Results here reported were obtained from three independent measurements, and the error is always below 10%.

The surface charge of nanogels at 25 °C and 37 °C was measured using a ZetaSizerNano ZS (Malvern Instruments Ltd, Malvern, UK) equipped with a He-Ne laser at a power of 4.0 mW. As for particle size distribution, also ζ potential measurements were carried out on minimum three samples from independent preparations, and the error is always below 6%.

2.7. Spectroscopic characterisation

¹H NMR spectra were recorded in D₂O solution by using a Bruker Advance series 300 MHz spectrometer. ¹³C {¹H} CP-MAS NMR

Table 2Average hydrodynamic radius and ζ -potential of nanogel systems in water at 25 °C.

System; Purif. method	R_h (nm)	PDI	ζ -potential (mV)	Width (mV)
#1; 1	96	0.30	–19.5	5.94
#2; 1	367	0.88	–30	10.7
#3; 1	237	0.73	–26	9.6
#4; 2	131	0.99	–29	8.2
#5; 2	111	0.43	–40.6	6.55
#6; 2	92	0.20	15.8	7.8

analysis was performed on solid samples with a Bruker Avance II 400 MHz (9.4 T) spectrometer operating at 400.15 MHz for the ¹H nucleus and 100.63 MHz for the ¹³C nucleus with a MAS rate of 13 kHz, 1024 scans, a contact time of 1.5 ms and a repetition delay of 2 s. The optimization of the Hartmann–Hahn condition was obtained using an adamantane standard. All samples were placed in 4 mm zirconia rotors with KEL-F caps. Silica powder was mixed with the samples to obtain a more compact filling of the rotor's volume. The proton spin-lattice relaxation time in the rotating frame, $T_{1\rho H}$, was determined with the variable spin lock (VSL) pulse sequence, using delay times ranging from 0.1 to 7.5 ms and a contact time of 1.5 ms.

2.8. Surface morphology

Surface morphology was imaged by a field emission scanning electron microscopy (FESEM) system (JEOL) at an accelerating voltage of 10 kV. Nanogel dispersions were deposited on aluminum stubs and air dried before being gold sputtered with a JFC-1300 gold coater (JEOL) for 30 s at 30 mA.

2.9. Biological evaluation

To evaluate presence of apoptosis, MC3T3-E1 cells were plated on coverslips of 6-well plates, incubated for 24 h in DMEM complete medium, whether or not in presence of nanoparticles. Samples were stained with Acridine Orange/Ethidium Bromide solution (AO/EtBr, Sigma) (100 µg/ml). Doxorubicin hydrochloride (DXR) (5 µM) (Ebewe Pharma) was used as apoptotic inducer (positive control). Cells were observed by confocal microscopy (Olympus 1 × 70 with Melles Griot laser system).

MC3T3-E1 cell extracts for Caspase 3 enzymatic assay were prepared by seeding the cells at high density on 6 well plate for 24 h in DMEM complete medium and growing them for further 24 h after incubation with nanogels. Cells were enzymatically detached from culture plate using Trypsin-EDTA 1X solution (Sigma) and centrifuged at 1000 rpm for 5 min. Pelleted cells were then resumed in 70 µl of Triton X 100 (1%) on PBS and incubated for 10 min at room temperature. Suspensions were centrifuged at 10,000 rpm for 10 min to extract cell proteins. The pellets were removed, while the amount of extracted proteins contained in the supernatant was quantified using Bradford micro assay method (Bio-Rad, Segrate, Milan, Italy) employing Bovine Serum Albumin (Sigma) as standard. MC3T3-E1 cells extracts (20 µg), obtained as

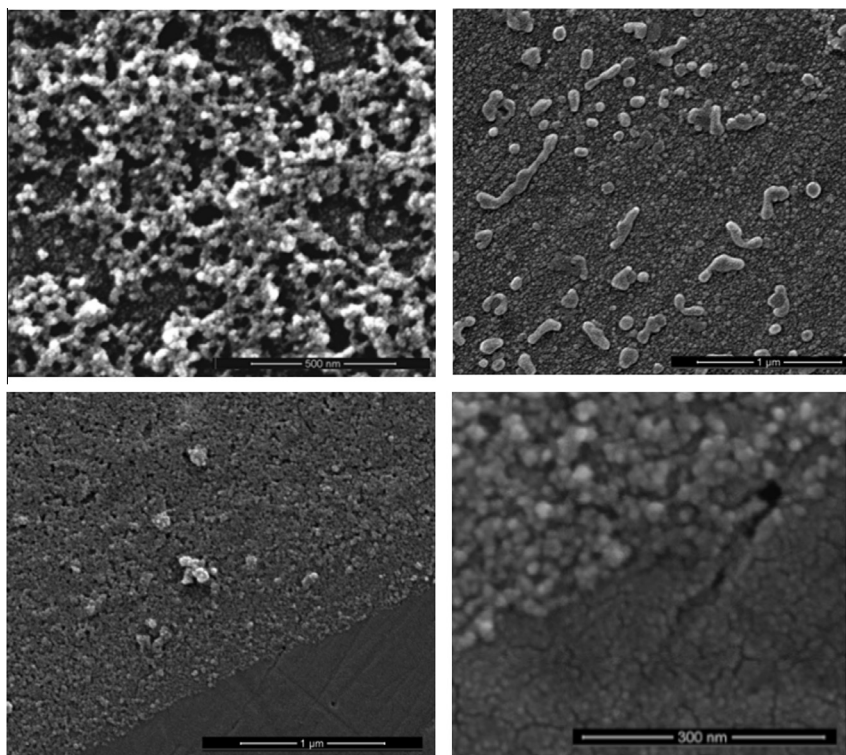


Fig. 1. SEM micrographs of an air-dried deposit of (top left) VP-MBA (formulation #1 – purification method 1); (top right) VP-MBA-APMAM(200) (formulation #3 – purification method 1); (bottom left) VP-MBA-APMAM(50) (formulation #5 – purification method 2); (bottom right) detail of (bottom left) at higher magnification. Both in (bottom left and bottom right) dry nanogels particles cover only part of the stub to evidence the difference in morphology with the gold sputtered substrate.

previously described, were used to detect the presence of activated Caspases 3/7/8. In the assay, both untreated MC3T3-E1 cells (negative control) and 10 μM DXR treated cells for 4 h (positive control) were used. The AspAc-Glu-Val-Asp-MCA peptide (Pepta Nova, Peptide Institute, Inc.), a specific substrate for activated Caspase 3/7/8 (typical apoptosis' marker) was used [25,26]. The substrate ties a fluorophore in its cutting site, which emits fluorescence when activated by the enzyme. In these experiments, the previously described extracts were added to 75 μl (8 μM) of the substrate in 96 well plates. The degree of Caspases activation was quantified by spectrofluorimetric reading using Spectra Max Gemini EM-500 (Molecular Devices) and Soft Max Pro 5.2 software for data elaboration.

For MTT assay, MC3T3-E1 cells were seeded on 96-well plate at density of 1×10^4 cell/well. After 24 h incubation with nanoparticles, the cells were washed with PBS and then incubated with 200 μl /well of complete medium containing 0.25 mg/ml of MTT solution for 2 h at 37 $^{\circ}\text{C}$. After dissolving the produced formazan salt, using 100 μl /well of DMSO solution, the absorbance of the intense purple staining ($\lambda = 490$ nm) was read on DU 730 Life Science Spectrophotometer (Beckman Coulter). Incubation with DXR (5 μM) for 24 h was used as a positive control. Each experiment was performed eight times.

For an immune localization assay, the MC3T3-E1 osteoblastic cell line was seeded on coverslips and grown in DMEM for 24 h, then incubated with different nanoparticles, or with 5 μM DXR for further 24 h. At different incubation times cells were fixed with 3.7% w formaldehyde for 15 min, washed three times in PBS, then labeled as follows: biotinylated Annexin V (Sigma) (1:1000) for 90 min at 37 $^{\circ}\text{C}$ and, then, Dapi (Sigma) (1:1000) for 90 min at 37 $^{\circ}\text{C}$. At the end of each different incubation time, slides were thoroughly washed in PBS and observed by confocal microscopy (Olympus 1 \times 70 with Melles Griot laser system).

Comet Assay was performed to assess nanogels for genotoxicity. MC3T3-E1 cells were seeded on 24-well plate; after 24 h of

incubation in presence of nanoparticles, cells were washed with PBS and about 10^4 single cells or nuclei present in 10 μl were mixed with 120 μl of Low Melting Agarose (LMA 0.5%) and added to an iced microscope slide, precoated with 1% w agarose. After the preparation of slides, the cells were lysed in an alkaline solution (1 M NaCl, 0.03 M NaOH, 0.5% w N-lauroyl-sarcosine and 2 mM EDTA) for 1 h in dark conditions, then rinsed in 0.03 M NaOH, 2 mM EDTA for 1 h to remove salt and detergent and electrophoresed in 0.03 M NaOH, 2 mM EDTA for 25 min at 0.6 V/cm, 250 mA. Comets were stained with 2.5 $\mu\text{g}/\text{ml}$ of Propidium Iodide (PI) for 15 min and analyzed using a fluorescence microscope and image analysis (Comet Assay IV, Perceptive Instruments). Fifty cells per slide were evaluated and the mean of the Tail Moment was used as an indicator of DNA damage [27].

2.10. Movement of nanogels across cell membranes

MC3T3-E1 osteoblastic cells were seeded on coverslips and grown in complete DMEM for 24 h, then incubated with nanogels dispersion (VP-MBA-FDA or VP-MBA-APMAM(50)^{FTIC}) which emit green fluorescence. After different incubation times, cells were fixed with 3.7% w formaldehyde for 15 min, washed three times in PBS, then stained with EtBr (1:1000) for 1 min at room temperature. Samples were characterized by Confocal Microscopy (Olympus 1 \times 70 with Melles Griot laser system).

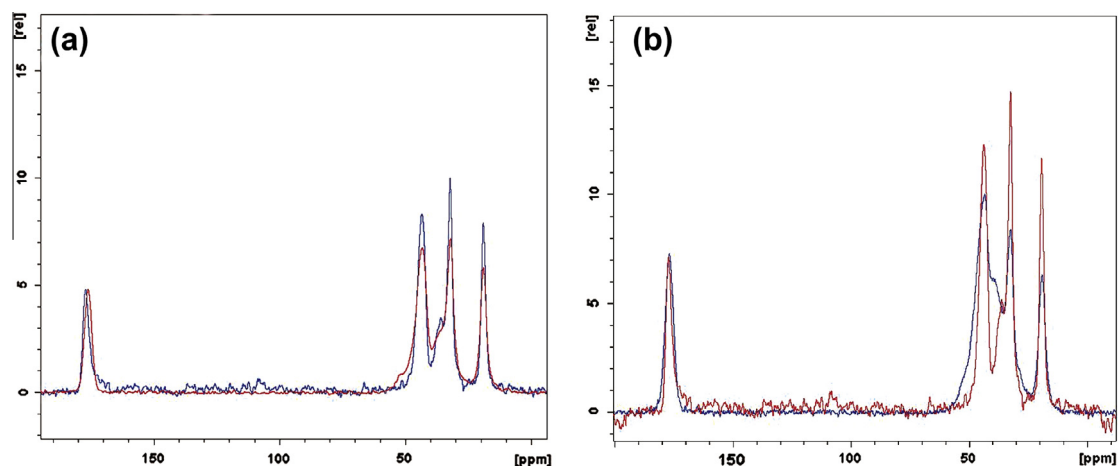
3. Results and discussion

3.1. Preparation of base and amino-graft-PVP nanogels

Base and functionalized nanogels were synthesized in inverse microemulsion conditions, using AOT as surfactant. The gravimetric yield in terms of recovered product, for the base (VP-MBA)

Table 3Average hydrodynamic radius and ζ -potential for an amino-graft crosslinked VP nanogels redispersed in PBS, as function of pH and temperature.

pH	VP/MBA/APMAM (50)							
	25 °C		37 °C		25 °C		37 °C	
	R_h (nm)	PDI	R_h (nm)	PDI	ζ -potential (mV)	Width (mV)	ζ -potential (mV)	Width (mV)
2.5	115	0.51	150	1	−5.2	3.2	−5.0	6.4
4.5	99	0.57	97	0.76	−13.6	5.8	−14.3	9.1
6.8	93	0.38	125	0.66	−21.8	6.7	−23.8	4.2
7.4	110	0.35	130	0.50	−25.2	5.4	−26.3	7.5
8	120	0.46	91	0.49	−13.8	8.4	−16.1	10.4

**Fig. 2.** (a and b) ^{13}C $\{^1\text{H}\}$ CPMAS NMR overlaid spectra of (left) linear PVP (red) and VP-MBA-APMAM(50) nanogels (blue); (right) VP-MBA-APMAM(50) nanogels (blue) and VP-MBA-APMAM(10) macrogel (red). (For interpretation of the references to colour in this figure legend, the reader is referred to the web version of this article.)

systems, was about 25 wt%. When polymerization was carried out in the presence of APMAM, the cationic monomer localizes preferentially at the water/surfactant interface due to the electrostatic interaction with the anionic surfactant. In this case, the yield of recovered product after purification was significantly lower. Considering that initiation and propagation rate constants of APMAM are significantly higher than VP's [28], the loss in recovered product cannot be attributed to a reduced reactivity of the reaction feed. Furthermore, homopolymerization of APMAM and formation of linear chains is not favored at the synthesis pH (5.5), owing to the electrostatic mutual repulsion between positively charged APMAM molecules (APMAM pK_a is 8.5 [29]). On the other hand, it is very likely that the ionic interactions between the cationic monomers present at the nanogels surface and the anionic surfactant complicated the separation of the nanogels from AOT. By the introduction of a non-ionic surfactant, Brij 30, and the contextual reduction of both APS and monomer contents in the aqueous phase, the recovery of VP-MBA-AMPAM(50) increased and separation of nanogels from AOT/Brij was quantitative, although not excellent. A product recovery of $\sim 20\%$ w was consistently reached for VP-MBA-APMAM(50), this value being somewhat lower for VP-MBA-APMAM(10).

3.2. Particle size and surface charge of base and amino-graft-PVP nanogels

The efficiency of surfactant in controlling the particle size of nanogels was studied through DLS measurements at fixed angle (90°) and temperature (25°C) in water. Table 2 shows the results in terms of average hydrodynamic radius and PDI. Surface charge density of nanogels is also reported as ζ -potential values. Base VP-MBA nanogels show the target value of 96 nm for the radius,

which is an optimal starting value for what it may constitute the core of e.g. an antibody-decorated bio-hybrid nanogel. In fact, nanocarriers with an average diameter of 200 nm are suitable for intravenous administration and cellular uptake. Smaller nanocarriers may not reside in the cytoplasm enough to accomplish their function and they may not provide adequate surface or internal volume for the cargo or for the targeting moieties to be attached [30].

When the reaction feed is modified, e.g. by introduction of FDA or APMAM, the average particle size increases and the particle size distribution widens. An inefficient surfactant separation procedure contributes to this result, as it is confirmed by SEM analysis on the air-dried nanoparticles. Fig. 1 (top left and top right) shows the comparison between VP-MBA (#1) and VP-MBA-APMAM(200) (#3) systems. Dry VP-MBA nanoparticles have a diameter of about 10 nm (Fig. 1 top left), which is approximately twenty times smaller than the hydrodynamic diameter when the nanogels are swollen in the aqueous media and move with their hydration water shell. Big lumps of aggregated nanoparticles are clearly visible for dry VP-MBA-APMAM(200) at the micron scale (Fig. 1 top right). The presence of nanogel-surfactant aggregates likely affects the measured R_h values too. By modification of both the reactor feed and the purification procedure, improvements in particle size control, particularly for the formulations containing the higher amount of APMAM, such as VP-MBA-APMAM(50) and VP-MBA-APMAM(10), and higher yields of recovered product were achieved. SEM analysis shows for VP-MBA-APMAM(50) a deposit of dry nanoparticles characterized by a fairly uniform particle size, similarly to the base VP-MBA system (Fig. 1 bottom left and bottom right).

Z-potential measurements show that the surface charge of VP-MBA nanogels in water is slightly negative, similarly to linear PVP. The partially anionic character of PVP is attributed to the

Table 4

¹H NMR proton chemical shifts (ppm) of protons bound to different carbon atoms for linear PVP and a representative amino-graft-PVP nanogel system.

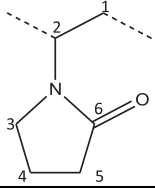
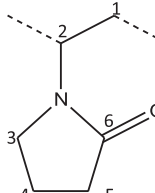
	Linear PVP	VP-MBA-APMAM(50)
	3.5112	3.6702
	3.5674	3.7097
C3	3.0301	3.1784
	3.0616	3.2249
C5	2.1793	2.1450
	2.3161	2.2290
	2.1658	2.3660
C4	1.8931	1.9392
C1	1.6139	1.6493

Table 5

¹³C {¹H} CP-MAS NMR-proton spin-lattice relaxation time in the rotating frame ($T_{1\rho H}$).

	$T_{1\rho H}$ (ms)	
	Macrogel	Nanogel
	7.4	8.8
	13.3	8.4
C1	16.4	6.8
C5	13.3	6.0
C4	12.2	5

keto-enolic tautomerism of pyrrolidone, which is at the basis of its zwitterionic form [20]. For VP-MBA-APMAM(50) the anionic charge increases, probably due to the shielding of grafted APMAM positive charges by chlorine counter ions, since APMAM is grafted in its chlorine salt form. When the content of APMAM is further increased, as for the VP-MBA-APMAM(10) system, the average ζ -potential becomes slightly positive. The proximity of many amino propylene grafts on the NG surface may render the charge shielding by the counter ions less effective and the overall charge density becomes more affected by the fixed positive charges from the protonated amino groups.

3.3. Influence of temperature and pH on dimensions and surface charge density

Freeze-dried amino-graft-PVP nanogels were redispersed in PBS buffers with similar ionic strength (0.2 M) and different pH, and characterized for their particle size and surface charge distributions, both at room temperature (25 °C) and at body temperature (37 °C). The NGs hydrodynamic size, measured at room temperature and in PBS at pH around neutrality, were very similar to those of the *as prepared* NG dispersions in water, thus proving their excellent redispersibility from the dry form. It is worth pointing out that the VP-MBA nanogels always showed irreversible aggregation upon freeze-drying, with an increase of particle size (data not shown), therefore the surface chemical modification of networks

through grafting of APMAM contributed to this important applicative property.

Colloidal stability of the VP-MBA-APMAM NGs dispersions in PBS buffer was fairly good in the pH range from 4.5 to 8, as demonstrated by the invariance of both the DLS scattered light intensity and hydrodynamic size of these NGs as function of the time, when stored at 5 °C for 2–3 weeks (data not reported). No evident influence of pH on particle size was also observed between 4.5 and 7.4, while at pH 8 NGs are slightly bigger (see Table 3) and yet stable colloids upon storage. Conversely, at pH = 2.5 and lower, aggregation and precipitation occurred in a temporal window of few hours. The hydrodynamic radius reported for pH 2.5 in Table 3 refers to freshly prepared dispersions, but this value increases with time at 25 °C up to the onset of precipitation, when the scattered light intensity drops to very low values.

The increase of temperature from 25 °C to 37 °C did not affect hydrodynamic size in a systematic way, but it generally increased the PDI, for the pH values within the NGs colloidal stability range (4.5–8). It can be speculated that the increase of temperature enhances the inherent variety of chemical structures of the system, in terms of distribution of functional groups, their protonation states and/or extent of interactions with the solvent (i.e. swelling degree). A contribution coming from nanoparticles aggregation cannot be ruled out in consideration of the relatively low absolute ζ -potential values of these nanoparticles. Indeed, faster aggregation kinetics are responsible for the significant higher R_h value at 37 °C for pH 2.5.

Z-potential values for the various pHs and $T = 25$ °C (Table 3) show that the anionic character is attenuated when NGs are in buffer at pH 7.4 with respect to water (−26.3 mV vs. −40.6 mV), probably due to ions exchange between nanogels and medium, with substitution of the chlorine ions of APMAM with loosely bound phosphate anions. This evidence indirectly confirms the role that chlorine counter ions have in determining the fairly strong negative surface charge of the original nanogels dispersions in water.

A change of pH, in the range 2.5–8, essentially affects the contribution of pyrrolidone rings to NGs charge density, being the pH always below the pK_a of APMAM. At pH 2.5 NGs become almost non ionic, with a maximum in anionic character at pH 7.4 and slight decrease at pH 8. This behavior is at all similar to that observed for linear PVP (unpublished results). No appreciable effects on NGs surface charge density are observed at the increase of temperature.

3.4. Internal structure of amino-graft-PVP nanogels

3.4.1. Proton and solid state ¹³C NMR spectroscopy

Fig. 2a shows solid state ¹³C {¹H} CP-MAS NMR spectra of VP-MBA-APMAM(50) nanogels after purification and freeze-drying, compared with the spectra of linear PVP. Peaks attribution for linear PVP is reported in a previous work [20]. It is evident that the chemical structure of the nanogel closely resembles that of the linear PVP. No evidence of residual surfactant or unreacted monomers is present, thus confirming the effectiveness of the purification procedure. The bands for the nanogels are narrower than those of the linear polymer, for the higher level of rigidity of macromolecular segments in the nanoscale network. The carbonyl carbon chemical shift is positioned at higher values and the band shows a shoulder stretching to lower fields. This behavior can be associated to a variety of carbonyls, attributable to PVP's pyrrolidone and secondary amides of MBA and APMAM. The spectrum of VP-MBA-APMAM(50) did not allow to obtain a spectroscopic evidence of the presence of the APMAM, for the low concentration of the monomer and the small quantities of materials produced at the laboratory scale. An indirect confirmation of the occurrence of copolymerization between VP, MBA and APMAM in the selected reaction conditions was obtained by preparing the “equivalent” macrogel of the 10:1

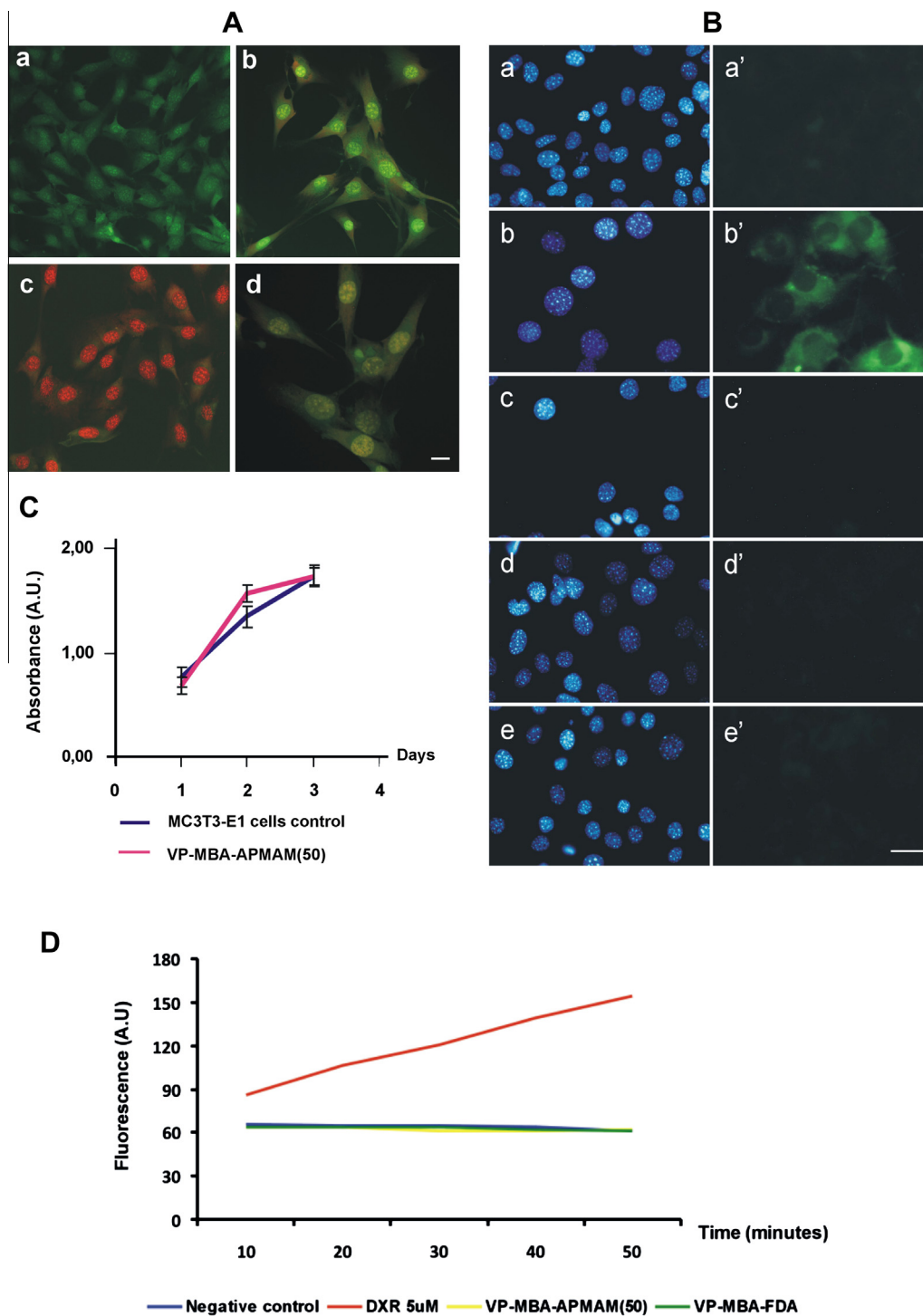


Fig. 3. (A) Apoptotic evaluation by AO/EtBr (a) untreated MC3T3-E1 cells, MC3T3-E1 cells in the presence of (b) VP-MBA NGs, (c) DXR (d) VP-MBA-FDA NGs. Bar = 10 μ m. Red: nucleus of apoptotic cells; green: cell cytoplasm. (B) Apoptotic evaluation by Annexin V. (a–a') untreated MC3T3-E1 cells, MC3T3-E1 cells in the presence of (b–b') DXR, (c–c') 25 μ l, (d–d') 50 μ l, (e–e') 100 μ l of VP-MBA NGs for 18 h. Blue: cell nucleus (DAPI staining); Green: Annexin V, bound to apoptotic cells membrane. Bar = 10 μ m. (C) MTT assay. (D) Enzymatic Caspase 3 substrate activation. (For interpretation of the references to colour in this figure legend, the reader is referred to the web version of this article.)

formulation, named after “VP-MBA-APMAM(10) macro”. For this macrogel, polymerization and crosslinking was carried out starting from the same composition of the aqueous phase as the corresponding microemulsion. Purification from unreacted monomers was performed by extensive washings with water and the insoluble fraction was freeze dried and analyzed. Fig. 2b shows the overlaid spectra of macrogel and linear PVP. A new band appears at 39 ppm, that can be attributed to APMAM [20]. ^1H NMR spectrum

of VP-MBA-APMAM(50) nanogels confirms the above discussed findings. Attribution of proton chemical shifts for the nanogel and linear PVP [31,32] is reported in Table 4.

3.4.2. Proton spin lattice relaxation times in the rotating frame ($T_{1\rho H}$)

In Table 5 the proton spin lattice relaxation times in the rotating frame ($T_{1\rho H}$) are reported, for the VP-MBA-APMAM(10)

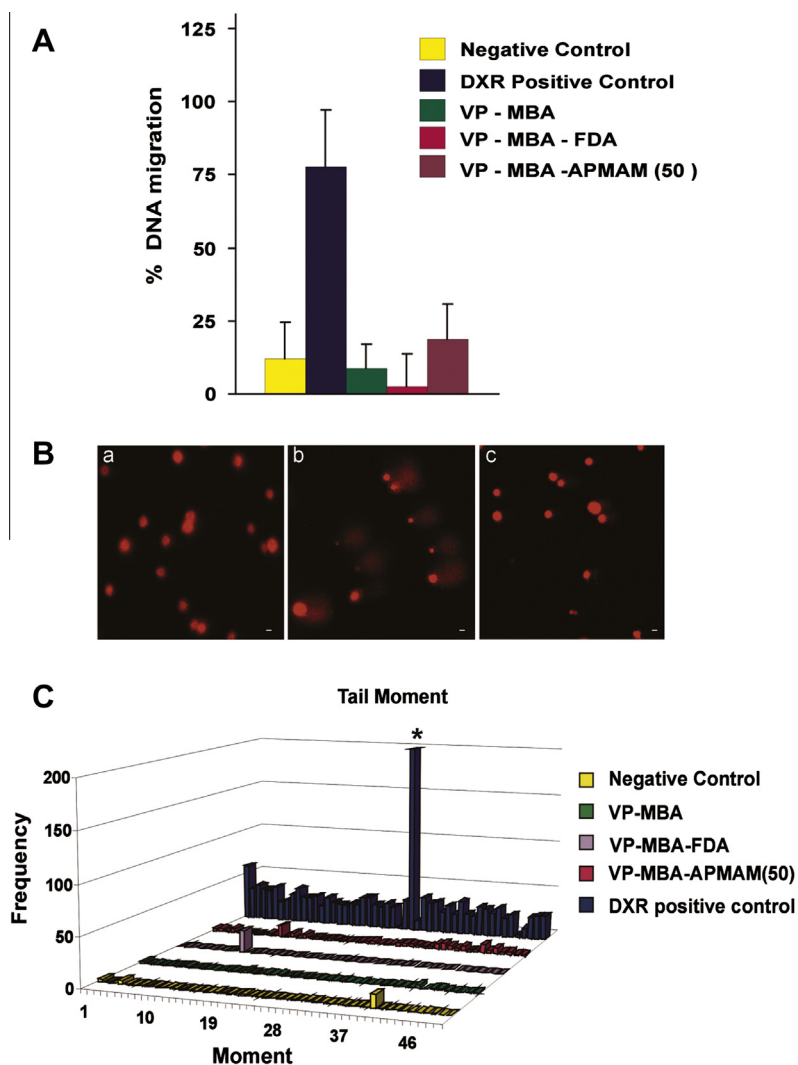


Fig. 4. Comet assay. (A) Evaluation of % DNA migration; (B) typical morphology in comet analysis for MC3T3E1 cells: (a) untreated, (b) cells treated with a genotoxic inductor, (c) cells treated with NGs; (C) genotoxicity evaluation of nanogels expressed by the Tail Moment parameter (the bar marked with *) is out of the represented range, the corresponding value being 325.73).

formulation both in the form of macrogel and nanogel and with specific reference to the characteristic chemical shifts of the PVP repeat unit in the network. It is known that $T_{1\rho}H$ values are sensitive to the molecular motions which occur in the kHz regions, associated with cooperative polymer backbone rearrangements, thus enveloping the collective motions of a large number of monomer units. As a general consideration, $T_{1\rho}H$ values are much higher for the macrogel than for the corresponding nanogels, with the only exception of the carbonyl carbon. This indicates that the local motions are more hindered in the 3D-extended macroscopic network, especially at the C1 position, which is the most affected by the proximity to T- and X-type crosslinks formed by MBA. For the nanogels, we would be inclined to think that the overall average crosslinking density is lower. In consideration of the fact that the size of the domains where spin–lattice relaxation times are averaged is of the same order of magnitude of the size of nanogel dry particles (tens of nanometers), the increase of mobility may reflect a significant contribution of polymer segments at the particle surface, which is the richest in polymer loose loops and flexible chain ends. Carbonyl groups, which are strongly interacting with bound water, show much closer values.

3.5. Cytocompatibility studies

The possible use of nanogels as nanocarriers for controlled release prompted us to check firstly their biocompatibility by *in vitro* assays of cytotoxicity and genotoxicity. The same biological analyses were performed on each variant of the nanoparticles produced. Since the results were in general very similar, a selection of systems for each test was used to represent the behaviour of the entire family. MC3T3-E1 cells were always used as model. In particular, as shown in Fig. 3A, MC3T3-E1 cells were analysed by AO/EtBr staining to value apoptosis induced processes. Nanoparticles treated cells, Fig. 3A_{b, d}, do not show the apoptotic phenotype similarly to non treated cells (negative control – Fig. 3A_a) whereas DXR-treated cells do (Fig. 3A_c).

Another morpho-functional evaluation was performed by Annexin V staining, as presented in Fig. 3B. Only DXR-treated cells show in the cytoplasm the typical staining for Annexin V (Fig. 3B_b); differently, MC3T3-E1 cells cultured in presence of different concentration of nanoparticles (Fig. 3B_{c|c'-e|e'}), similarly to the non treated cells (negative control, Fig. 3B_{a|a'}), do not show any cytoplasm staining or any nuclei malformations. The same result is obtained for the amino-functionalised NG variants.

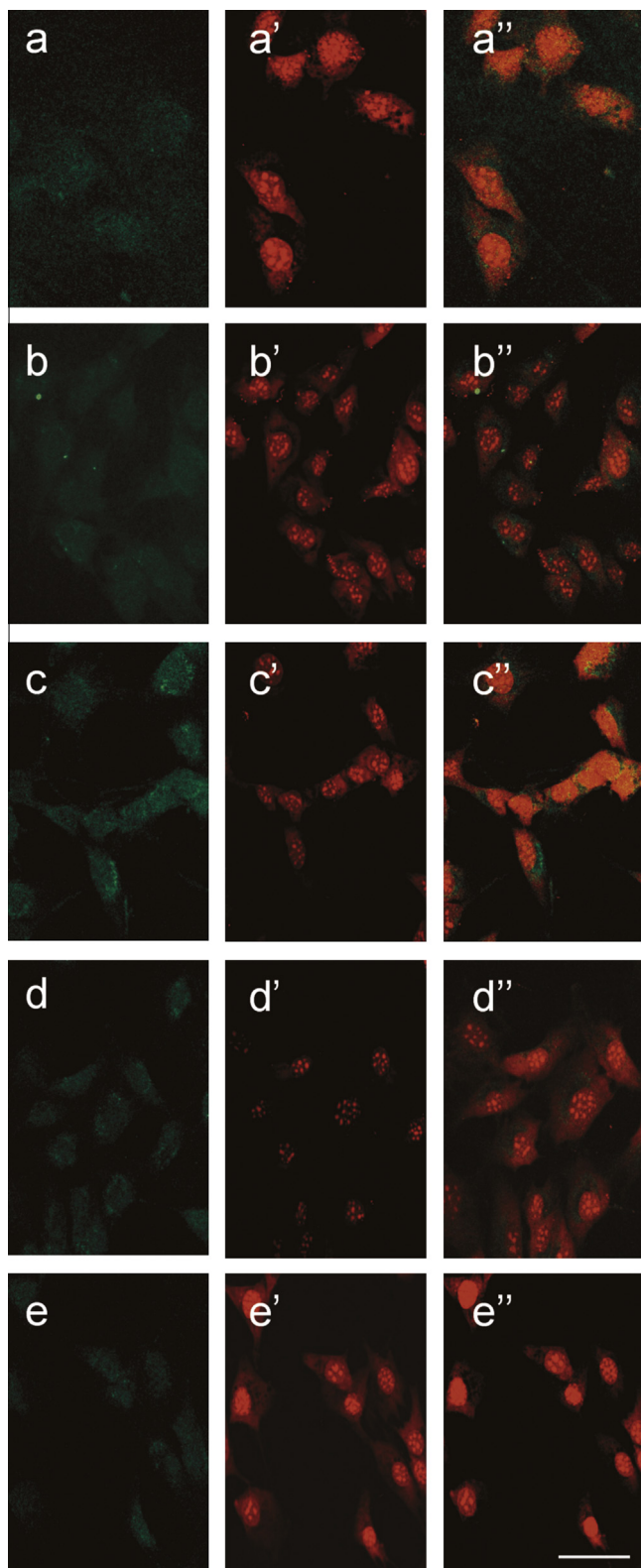


Fig. 5. MC3T3-E1 cells cultured in presence of VP-MBA-FDA nanoparticles fixed and observed by confocal microscopy. Resumption of all sections, with an overall thickness of about 20 μm . Nanogels localization is evaluated after 1 h (a); 3 h (b); 6 h (c); 8 h (d) and 24 h (e). In (a–e) the green fluorescein-labeled nanoparticles, in (a'–e') cells stained using ethidium bromide to visualize nuclei and in (a''–e'') the merger of a,a'–e,e' images. Bar = 30 μm .

Metabolic experiments carried out by MTT assay as function of time (Fig. 3C) prove that there are no evident effects on MC3T3-E1

cells treated with VP-MBA-APMA(50); a similar result was obtained, also, by the use of a halved or doubled amount of the same nanoparticles for the same incubation times and for all the other NGs.

The absence of toxicity was also enzymatically evaluated using a Caspase activation assay. In Fig. 3D, the enzymatic assay performed on VP-MBA-APMAM(50) and VP-MBA-FDA variants of NGs is shown. As it can be observed, only DXR-treated cells show induced Caspases activation with the characteristic dose-dependent digestion of the specific substrate, while both non treated cells (negative control) and nanoparticles treated do not show any effect.

Genotoxic effects induced by the nanogels were also investigated via a Comet Assay [27]. As shown in Fig. 4A, an appreciable % of DNA migration was observed only for DXR treated cells (DXR positive control), while all kind of nanoparticles treated cells as well as non treated (negative control) EC3T3-E1 cells do not show any appreciable variation. Similar results were obtained in tail movement, as shows in Fig. 4C.

3.5.1. Movement of nanogels through the cell compartments

Nanogels movement through cell membrane was investigated using two different fluorescent nanoparticle constructs: VP-MBA-FDA and VP-MDA-APMAM(50)^{FITC}.

VP-MBA-FDA particles had a hydrodynamic diameter of about 370 nm and their surfaces were negative charged. They were analyzed as for cell compartments distribution at different times. As shown by Fig. 5a after 1 h incubation nanoparticles are preferentially located outside and/or on the cell membrane surface, after 3 h (Fig. 5b) their localization is progressively cytoplasmic, polarized in precise intracellular domains after 6 h (Fig. 5c) (possibly Endoplasmic Reticulum (ER) or Golgi), starting to be not specifically localized after 8 h and finally completely not detectable inside the cells after 24 h.

A similar approach was used with VP-MBA-APMAM(50)^{FITC} nanogels that, differently from VP-MBA-FDA, are smaller in hydrodynamic size (110 nm) and do not show a net surface charge density, as a result of conjugation reaction with FITC (average ζ -potential = -1.0 mV, width = 5 mV). As shown by Fig. 6, the pattern of the movement through cell surface and in cell compartments of these nanoparticles was very similar to that previously described (Fig. 5). Moreover, confocal section analyses at diverse depths (4, 10, 12, 14 and 16 μm from the surface) for different times of incubation show that after 30 min of incubation, Fig. 6a–e, the nanoparticles visible for the green label are evident mainly at the extracellular level and only in sections at lower depths. After 3 h (Fig. 6a'–e') their distribution is clearly mainly intracellular, while after 24 h (Fig. 6a''–e'') their localization inside the cells at the lower depths is significantly reduced, whereas their presence at the higher depths, both inside the cells and in the surrounding medium, is clearly evident. This evidence suggests a re-addressing of nanogels outside the cells. Interestingly, similar results were obtained with the radiation synthesized amino-graft-PVP analogues [33]. Similarities among all these nanoconstructs are essentially in their chemical structure, being vinyl pyrrolidone always the main building block, and thus in their surface charge densities, which are always slight negative (-10 to -25 mV), whereas the hydrodynamic size actually varies from about 50 nm for the radiation synthesized NGs [33] to about 370 nm for the chemically crosslinked VP-MBA systems. The mechanism of internalization is currently under investigation through dedicated further *in vitro* experiments.

3.5.2. Surface functionalization of amino-graft-PVP nanogels

Successful conjugation with BSA as a model protein was tested by UV-Vis spectrophotometry. Absorption spectra, reported in

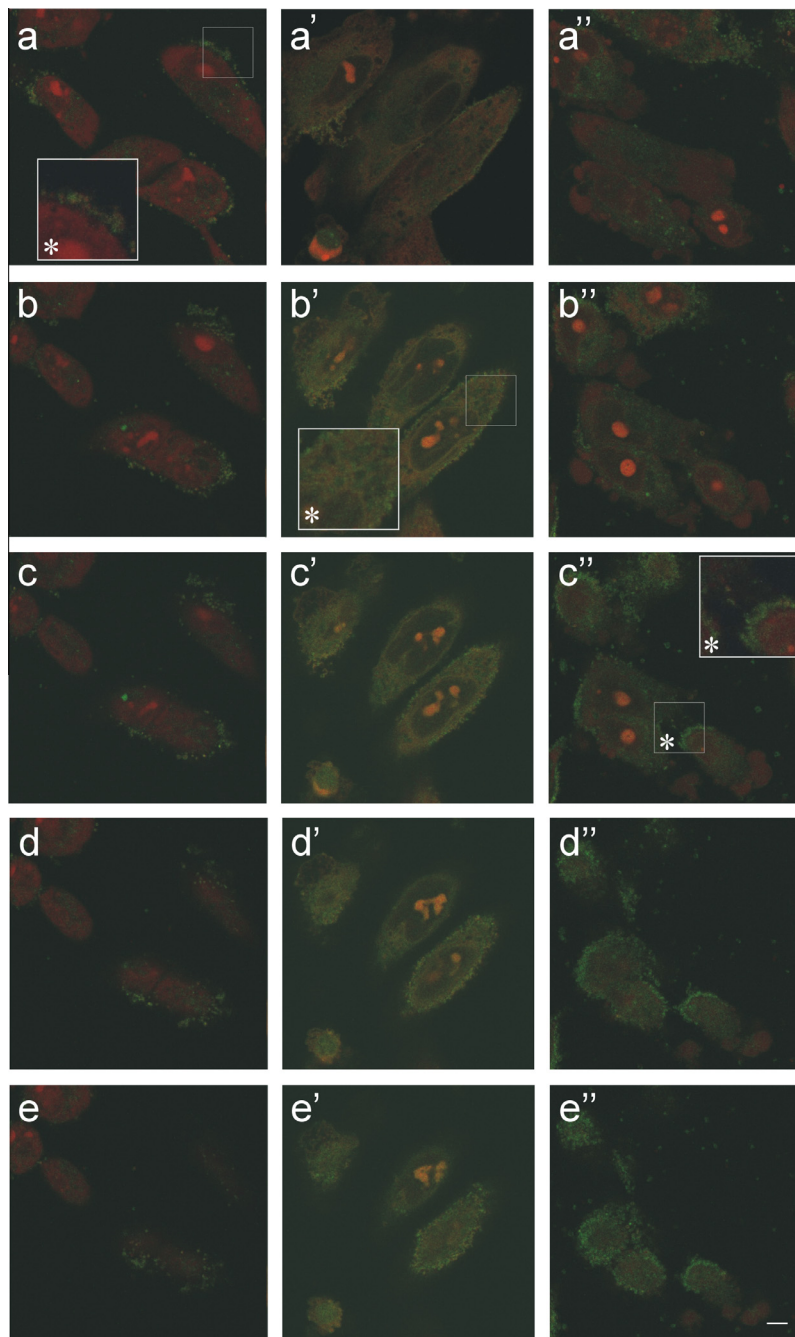


Fig. 6. Confocal microscope laser sections (merged) at 4, 10, 12, 14, 16 μm from the MC3T3-E1 cell surface after 30 min (a–e); at 8, 12, 14, 16, 18 μm from the cell surface after 3 h (a'–e'); and at 4, 10, 14, 18, 20 μm (a''–e'') from the cell surface, after 24 h (a''–e'') of incubation with PVP-MBA-APMAM^{FTIC} nanoparticles. In the figure squared areas marked with * represent 2 \times magnification. Bar = 5 μm .

Fig. 7A, show that the BSA-conjugated NG spectrum has a peak at 280 nm which coincides to the one of free BSA used as reference; while no absorption peaks were observed in the non-conjugated system. To confirm this result electrophoresis on cellulose acetate was also performed, that shows the band of BSA in the conjugated system (Fig. 7B). The interaction between BSA and nanoparticles is fairly strong, as it survives upon extensive dialysis and repeated washings. In consideration of the dimensions of BSA, we expect the protein to be essentially located at the nanoparticles' surface. The same protocol is now being applied to generate monoclonal antibody decorated nanogels.

4. Conclusions

Amino-graft-PVP nanogels were produced via inverse emulsion free radical polymerization of VP and a primary amino group carrying acrylic monomer. In the proper reaction and purification conditions, this synthetic approach allows to obtain functional nanogels with tailored size and surface properties. The nanogels produced have been fully characterized for their structural and physico-chemical properties as well as for their biocompatibility *in vitro*. They resulted fairly stable nanocolloids in aqueous solutions and redispersible from the dry physical form. The comparison

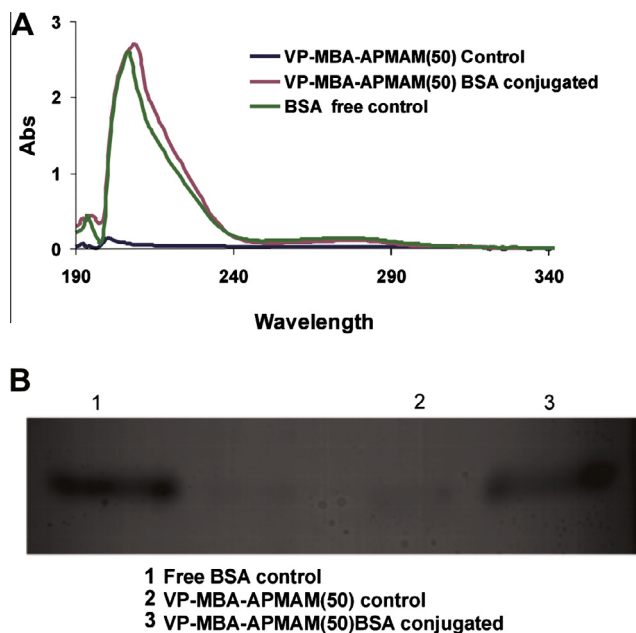


Fig. 7. (A) UV-Vis spectra and (B) mobility on cellulose acetate membrane of VP-MBA-APMAM(50) and VP-MBA-APMAM(50)^{BSA}.

between the proton spin–lattice relaxation times in the rotating frame for one the nanogel variants and the corresponding macrogel “analogue” suggests that the overall average crosslinking density is lower for the nanogels than for the macrogel obtained from the same monomer mixture, likely due to a greater contribution in macromolecular segments mobility from polymer loose loops and flexible chain ends at their surface. This approach will be further applied to other nanogel/macrogel systems to build up structure–property relationships that can be applied for nanoscalar networks, where other approaches, such as rheology, see the limits of their usefulness.

As a result of a wide experimental evidence, we can also conclude that these nanoparticles are not cytotoxic and/or genotoxic at the cellular level. Indeed, they showed a good affinity for cells, as they rapidly and quantitatively bypass the cellular compartments, to accumulate in specific cell portions for the first 4–6 h, then being released from the cells after 24 h. Their final fate will be the subject of future investigation through *in vivo* and *ex vivo* tests with animal models. Furthermore, these novel amino-functionalized PVP nanogels, owing to the available amino groups, are particularly apt for binding therapeutic agents, drugs, biomolecules, and particularly proteins or attaching to their surface ligands for specific receptors to provide addressing to specific substrate target.

Acknowledgments

Solid-state ¹³C NMR experimental data were provided by Centro Grandi Apparecchiature UniNetLab Università di Palermo, funded by P.O.R. Sicilia 2000–2006, Misura 3.15 Quota Regionale.

This research was supported by a grant from the Italian Ministry of University and Scientific Research (PRIN 2010–2011NANOMED).

References

- [1] R.B. Login, J.S. Shih, J.C. Chuang, Method of crosslinking PVP, Patent US005219950A (1993).
- [2] C. Dispenza, M.A. Sabatino, M. Leone, S. Piazza, D. Chmielowska, C. LoPresti, G. Battaglia, *React. Funct. Polym.* 72 (3) (2012) 185–197.
- [3] V. Biju, R. Kanemoto, Y. Matsumoto, S. Ishii, S. Nakanishi, T. Itoh, Y. Baba, M. Ishikawa, *J. Phys. Chem. C* 111 (2007) 7924–7932.
- [4] Y. Zhang, J.Y. Liu, S. Ma, Y.J. Zhang, X. Zhao, X.D. Zhang, Z.D. Zhang, *J. Mater. Sci. Mater. Med.* 21 (2010) 1205–1210.
- [5] Z. Aiji, I. Othman, J.M. Rosiak, *Nucl. Instrum. Methods Phys. Res., Sect. B* 229 (3–4) (2005) 375–380.
- [6] C. Dispenza, M. Ricca, C. LoPresti, G. Battaglia, M. La Valle, D. Giacomazza, D. Bulone, *Polym. Chem.* 2 (2011) 192–202.
- [7] C. Dispenza, N. Grimaldi, M.A. Sabatino, S. Todaro, D. Bulone, D. Giacomazza, G. Przybytniak, S. Alessi, G. Spadaro, *Radiat. Phys. Chem.* 81 (9) (2012) 1349–1353.
- [8] M. Ricca, V. Foderà, D. Giacomazza, M. Leone, G. Spadaro, C. Dispenza, *Colloid. Polym. Sci.* 288 (9) (2010) 969–980.
- [9] C. Dispenza, C. LoPresti, C. Belfiore, G. Spadaro, S. Piazza, *Polymer* 47 (2006) 961–971.
- [10] C. Dispenza, M.A. Sabatino, A. Niconov, D. Chmielowska, G. Spadaro, *Radiat. Phys. Chem.* 81 (9) (2012) 1456–1459.
- [11] X. Zhu, P. Lu, W. Chen, J. Dong, *Polymer* 51 (2010) 3054–3063.
- [12] L.C. Lopègolo, A.B. Lugao, L.H. Catalani, *Polymer* 44 (2003) 6217–6222.
- [13] C. Dispenza, M.A. Sabatino, N. Grimaldi, G. Spadaro, D. Bulone, M.L. Bondi, G. Adamo, S. Rigogliuso, *Chem. Eng. Trans.* 27 (2012) 229–234.
- [14] S.M. Saxena, A.K. Johri, *Biomaterials* 27 (2006) 5596–5602.
- [15] D.J. Bharali, S.K. Sahoo, S. Mozumdar, A. Maitra, *J. Colloid Interface Sci.* 258 (2003) 415–423.
- [16] T. Vermonden, R. Censi, W.E. Hennink, *Chem. Rev.* 112 (2012) 2853–2888.
- [17] C. LoPresti, V. Vetri, M. Ricca, V. Foderà, G. Tripodo, G. Spadaro, C. Dispenza, *React. Funct. Polym.* 71 (2) (2011) 155–167.
- [18] J.D. Byrne, T. Betancourt, L. Brannon-Peppas, *Adv. Drug Delivery Rev.* 60 (2008) 1615–1626.
- [19] N.V. Nukolova, Z. Yang, J.O. Kim, A.V. Kabanov, T.K. Bronich, *React. Funct. Polym.* 71 (3) (2011) 315–323.
- [20] C. Dispenza, M.A. Sabatino, N. Grimaldi, D. Bulone, M.L. Bondi, M.P. Casaletto, S. Rigogliuso, G. Adamo, G. Gherzi, *Biomacromolecules* 13 (6) (2012) 1805–1817.
- [21] M.A. Sabatino, D. Bulone, M. Veres, A. Spinella, G. Spadaro, C. Dispenza, Structure of e-beam sculptured poly(N-vinylpyrrolidone) networks across different length-scales, from macro to nano, *Polymer*, doi 10.1016/j.polymer.2012.11.031.
- [22] J.K. Oh, R. Drumright, D.J. Siegwart, K. Matyjaszewski, *Prog. Polym. Sci.* 33 (2008) 448–477.
- [23] P. Ulanski, J.M. Rosiak, *Polymeric Micro/Nanogels*, in: H.S. Nalwa (Ed.), *Encyclopedia of Nanoscience and Nanotechnology*, American Scientific Publishers, Valencia, CA, USA, 2004, pp. 1–14.
- [24] K. Holmberg, B. Jonsson, B. Kronberg, B. Lindman, *Chemical Reactions in microheterogeneous systems*, in: John Wiley & Sons (Eds.), *Surfactants and Polymers in Aqueous Solution*, West Sussex, 2002, pp. 507–511.
- [25] D.W. Nicholson, A. Ali, N.A. Thornberry, J.P. Vaillancourt, C.K. Ding, M. Gallant, Y. Gareau, P.R. Griffin, M. Labelle, Y.A. Lazebnik, *Nature* 6 (23) (1995) 37–43.
- [26] N.A. Thornberry, T.A. Rano, E.P. Peterson, D.M. Rasper, T. Timkey, M. Garcia-Calvo, P.A. Nordstrom, S. Roy, J.P. Vaillancourt, K.T. Chapman, D.W. Nicholson, *J. Biol. Chem.* 18 (1997) 17907–17911.
- [27] E. Rojas, M.C. Lopez, M. Valverde, *J. Chromatogr., B* 722 (1–2) (1999) 225–254.
- [28] S. Touchal, A. Jonquières, R. Clément, P. Lochon, *Polymer* 45 (2004) 8311–8322.
- [29] A. Musyanovych, H.J.P. Adler, *Langmuir* 21 (2005) 2209–2217.
- [30] A. Albanese, P.S. Tang, W.C.W. Chan, *Annu. Rev. Biomed. Eng.* 14 (2012) 1–16.
- [31] Y. Luan, A. Song, G. Xu, *Soft Matter* 5 (13) (2009) 2587–2595.
- [32] I. Szàraz, W. Forsling, *Polymer* 41 (2000) 4831–4839.
- [33] S. Rigogliuso, M.A. Sabatino, G. Adamo, N. Grimaldi, C. Dispenza, G. Gherzi, *Chem. Eng. Trans.* 27 (2012) 247–252.

Oligonucleotides-decorated-poly (N-vinylpyrrolidone) nanogels for gene therapy.

C. Dispenza*, G. Adamo, M.A. Sabatino, N. Grimaldi,

S. Rigogliuso, G. Ghersi.

2014. J Appl. Polym. Sci. 131(2), 39774-39782.

Oligonucleotides-Decorated-Poly(*N*-vinyl pyrrolidone) Nanogels for Gene Delivery

Clelia Dispenza,^{1,2} Giorgia Adamo,³ Maria Antonietta Sabatino,¹ Natascia Grimaldi,¹
Donatella Bulone,² Maria Luisa Bondi,⁴ Salvatrice Rigogliuso,³ Giulio Gherzi³

¹Dipartimento di Ingegneria Chimica, Gestionale, Informatica, Meccanica, Università degli Studi di Palermo, Viale delle Scienze, Edificio 6, 90128 Palermo, Italy

²CNR - Istituto di Biofisica (IBF) UOS Palermo, Via U. La Malfa, 153, 90146 Palermo, Italy

³Dipartimento di Scienze e Tecnologie Biologiche, Chimiche e Farmaceutiche (STEBICEF), Università degli Studi di Palermo, Viale delle Scienze, Edificio 16, 90128 Palermo, Italy

⁴CNR - Istituto per lo Studio dei Materiali Nanostrutturati (ISMN) UOS Palermo, via Ugo La Malfa, 153, 90146 Palermo, Italy

Correspondence to: C. Dispenza (E-mail: clelia.dispenza@unipa.it)

ABSTRACT: Pulsed electron-beam irradiation of a semi-dilute poly(*N*-vinyl pyrrolidone) (PVP) aqueous solution in the presence of acrylic acid has led to a carboxyl functionalized nanogel system. Nanoparticles hydrodynamic size and surface charge density, in water and as a function of pH, were investigated by dynamic light scattering and laser doppler velocimetry, respectively. Nanogels (NGs) were proved not to be cytotoxic at the cellular level. Indeed, they rapidly bypass the cellular membrane to accumulate in specific cell portions of the cytoplasm, in the perinuclear area. The availability of pendant carboxyl groups on the crosslinked PVP NGs core prompted us to attempt their decoration with a single strand oligonucleotide, which holds a terminal amino group. The recognition ability of the attached single helix of its complementary strand was investigated. © 2013 Wiley Periodicals, Inc. *J. Appl. Polym. Sci.* **2014**, *131*, 39774.

KEYWORDS: biomedical applications; gels; irradiation

Received 8 May 2013; accepted 18 July 2013

DOI: 10.1002/app.39774

INTRODUCTION

A big challenge in nanomedicine is the intracellular delivery of genetic material in conditions that can preserve its structure and ability to mediate biological processes. The most efficient gene vectors proposed up to date are viruses, because of their natural ability to transfect cells. However, viral vectors can produce adverse systemic immune responses, including patient fatalities. Moreover, without further genetic engineering, virus-targeting efficiency is limited to the specificity of the virus.^{1,2} The incorporation or the chemical attachment of an oligonucleotide, siRNA, or DNA, on smart nanoparticles surface can offer the opportunity to efficiently transport genetic material within cells, limiting adverse side effects. Nanoparticles, because of their small size are able to penetrate within even small capillaries, to be taken up by cells. Receptor-mediated, site-specific localization can be also realized by decorating nanoparticles surface with targeting agents.³ However, the development of therapeutic devices based on nanoparticles is still limited by the lack of synthetic strategies, which are simultaneously economically viable and able to grant a good degree of control over the

device properties, especially when produced at a large scale. We have recently developed a single-step synthetic platform to generate either carboxyl or primary amino groups bearing poly(*N*-vinyl pyrrolidone) (PVP) nanogels.^{4–7} The synthetic approach is based on high-energy irradiation of semi-dilute aqueous solutions of PVP in the presence of a functional group carrying acrylic monomer, namely acrylic acid. Polymer crosslinking, monomer grafting and sterilization are simultaneously achieved. The manufacturing process does not require long purification procedures, as it does when recourse to surfactants is made,⁸ it can be easily scaled-up at industrial level with high throughputs and it ensures high control over materials properties, like particles size, surface charge densities, and degree of functionalization.^{4,9} The produced nanogels, in virtue of the abundance of their reactive functional groups, can be decorated in mild reaction conditions with fluorescent probes and biomolecules.⁴ Recently, several studies have demonstrated that nanogels can release active antisense oligonucleotides (ODN), which were shown to be able to produce some desired effects on gene expression in specific cell lines.¹⁰ Furthermore, it has been

demonstrated that nanogels can transport ODN across cellular barriers, such as the blood–brain barrier (BBB) or monolayers of human intestine epithelial cells, thus ensuring ODN protection from enzymatic degradation.¹¹ Generally, nanogel-DNA complexes are prepared in physiological buffers through cooperative systems of salt bonds between the functional groups of a cationic polymer nanoparticle and the phosphate groups of DNA.¹² Recourse to surfactants is often made to improve colloidal stability of the complexes with adverse effects in efficiency, whereas in some cases DNA conformational changes have been observed.¹³

Herein, we describe the properties of a carboxyl functionalized PVP nanogel system, surface decorated with a single strand oligonucleotide. The bioconjugation reaction has been carried out using a terminal amino group present in the ODN to form an amide bond with one of the available carboxyl groups of the nanoparticles. The hydrodynamic size and surface charge density of the system in aqueous solutions and in a wide pH range (2.5–10) have been preliminarily investigated, as well as the absence of induced cytotoxicity and the ability of the nanoparticles to quickly bypass cell membranes. Subsequently, the pairing ability of the conjugated single strand oligonucleotide toward the complementary strand has been proved. In particular, purposely designed experiments where the nanoparticles decorated with a fluorescent variant of the ODN are annealed with the complementary strand, bearing a fluorescence quencher, were carried out. All the results gathered so far, strongly point out toward a possible application of these nanogels as nanocarriers for gene-delivery applications.

EXPERIMENTALS

Synthesis of Carboxyl-Functionalized Crosslinked-PVP Nanogels

An aqueous solution of PVP K60 (Aldrich, $M_w = 4.1 \times 10^5$ g/mol, $R_h = 20 \pm 10$ nm from DLS measurements in water at 25°C)¹⁴ at a concentration of 0.25 wt % in the presence of acrylic acid (AA, Aldrich), at a molar ratio between PVP repetitive unit and AA equal to 50, was prepared. The solution was carefully deoxygenated by gaseous nitrogen, bottled in hermetically closed glass vials and saturated by N₂O (99.99%) prior to irradiation. Electron beam irradiation was performed using the linear accelerator at the ICHTJ of Warsaw (Poland), Elektronika 10/10. Irradiation was carried out at an average beam current of 0.45 mA, pulse length of 4.5 μ s, and pulse repetition rate of 400 Hz.⁴ Samples were horizontally placed in a box filled with ice and conveyed under the beam via a transporting belt at a speed of 0.3 m/min. An integrated dose of 40 kGy, within the sterilization dose range, was supplied with a single pass and at a dose-rate of 13 Gy per pulse.¹⁵ After irradiation, samples were dialyzed (MWCO 100 kDa) against distilled water for 48 h to remove eventual unreacted monomer, oligomers, and low MW polymer and re-equilibrate pH.⁴ The formulation had a pH of about 6.0 prior to irradiation, which turned to be 4.9 after irradiation and 5.8 after dialysis. The yield of recovered nanogels after dialysis was determined gravimetrically and resulted to be always above 95 wt %.¹⁴ The system was coded P*(0.25)AA50.

Light Scattering and ζ Potential Measurements

The hydrodynamic diameters (D_h) of particles dispersed in water and in water solutions of different pH and same ionic strength were measured by dynamic light scattering (DLS).⁴ Intensity autocorrelation function at the scattering angle of 90° and time autocorrelation function were measured by using a Brookhaven BI-9000 correlator and a 50 mW He–Ne laser (MellesGriot) tuned at $\lambda = 632.8$ nm. In consideration of the fact that samples showed a monomodal size distribution, DLS data were analyzed by the method of cumulants. Measurements were carried out on a minimum two samples from three independent runs, with excellent reproducibility.

Weight average molecular weights (M_w) were estimated from multiangle static light scattering measurements at 25°C \pm 0.1°C in aqueous solution. The refractive index increment (dn/dc) of NGs system in aqueous solution was measured by using a Brookhaven Instruments differential refractometer at $\lambda = 620$ nm and resulted to be 0.1866 ± 0.002 . Static light scattering data were analyzed according to the Zimm plot method.¹⁶

Surface charge densities of nanogels in water and in water solutions of different pH and same ionic strength was measured at 25°C using a ZetaSizer Nano ZS (Malvern Instruments, Malvern, UK) equipped with a He–Ne laser at a power of 4.0 mW. As for particle size distribution, also ζ potential measurements were carried out on minimum two samples from three independent runs, always showing consistent results.

Preparation of NGs Fluorescent Variant

The P*(0.25)AA50 NG system was labeled with a fluorescent probe, amino-fluorescein (AF), using a standard protocol based on 1-ethyl-3-[3-dimethylaminopropyl]carbodiimide hydrochloride/N-hydroxysulfosuccinimide (EDC/sulfo-NHS, Aldrich).¹⁷ The reaction was carried out at 25°C in 2-(N-morpholino)ethanesulfonic acid (MES, Aldrich) buffer at pH 5, in the excess of AF (molar ratio between AA in the irradiated solution and AF equal to 10), under continuous stirring. The probe-conjugated NG system was then purified through prolonged dialysis against water. Reaction and purification were both performed in the dark.

Conjugation degree was estimated by UV-Visible absorption measurements with Shimadzu 2401-PC spectrofluorimeter (scan speed 40 nm/min, integration time 2 sec, bandwidth 1 nm) at room temperature. Fluorescence spectra were acquired with a JASCO FP-6500 spectrofluorimeter, equipped with a Xenon lamp (150 W). Emission spectra, at the required excitation wavelength, were obtained with emission and excitation bandwidth of 1 and 3 nm, respectively. Samples were excited at the maximum absorption wavelength for AF ($\lambda_{ex} = 490$ nm, $\lambda_{em} = 520$ nm). The labeled sample is coded as P*(0.25)AA50-AF.

Cell Culture and Biological Studies

Human umbilical vein endothelial cells (ECV304) were grown and maintained using a suitable culture medium (MEM199, Euroclone, Celbar) supplemented with 10% fetal bovine serum (Euroclone, Celbar), 1% L-glutamine (Euroclone, Celbar), and 1% penicillin-streptomycin antibiotic solution (Euroclone, Celbar) at 37°C, in a humidified atmosphere of 5% CO₂.

Acridine-Orange Staining

ECV304 cells were plated on coverslip and grown in MEM199 complete medium for 24 h. Then, cells were incubated, respectively, at 60 and 250 $\mu\text{g}/\text{mL}$ of P*(0.25)AA50 nanogels for 24 h. After the incubation period, the medium was removed and cells were washed with PBS; subsequently, cells were stained with Acridine Orange PBS solution (Sigma) at 100 $\mu\text{g}/\text{mL}$ for 10 min at room temperature and quickly examined by fluorescence microscopy (Leica, DFC450C). Acridine Orange is a cell-permeating nucleic acid binding dye that emits green fluorescence when bound to double-strand DNA and red fluorescence when bound to single-strand DNA or RNA. This staining discriminates between alive (green nuclei) to damaged (red nuclei) cells. As a positive control, cells were treated with Doxorubicin (DXR, Ebewe Pharma) at 5 μM for 24 h.

Apoptosis Evaluation by Enzymatic Assay

ECV304 were seeded at a density of 5×10^5 cells/well in a six-well plate and cultured for 24 h in MEM199 complete medium; afterwards, cells were incubated at 250 $\mu\text{g}/\text{mL}$ of P*(0.25)AA 50 for 24 h. Cells were enzymatically detached using Trypsin-EDTA 1X (Sigma) solution and centrifuged at 1000 rpm for 5 min. Pelleted cells were lysed in 70 μL of 1% Triton X 100 solution in PBS, incubated 10 min at room temperature and successively centrifuged at 10.000 rpm for 10 min. The amount of protein extract in the supernatant medium was quantified using Bradford micro-assay method (Bio-Rad, Segrate, Milan, Italy). A standard curve built with a known amount of BSA (Sigma-Aldrich) was used as a reference. ECV304 cells extracts (20 μg), obtained as previously described, were used to detect the presence of activated Caspases 3/7/8, that is a typical apoptosis marker, using Asp.Ac-Glu-Val-Asp-MCA peptide (Pepta Nova, 380 Peptide Institute).^{18,19} This specific substrate for Caspases has a fluorophore in its cleavage site, which emits fluorescence when cleaved by these enzymes, suggesting that mechanisms of cell death have been activated. The degree of Caspase activation was quantified by spectrofluorimetric readings using Spectra Max Gemini EM-500 (Molecular Devices) and elaborated by SoftMax Pro 5.2 software.

Untreated ECV304 cells were used as negative control and cell treated with DXR at 5 μM for 24 h, as positive control.

Cell Viability Assay

Cellular viability was determined using the MTT assay (Sigma). Cells were seeded in a 96-well plates at a density of 1×10^4 cell/well. After 24 h from seeding, cells were incubated for a further 24 h at different concentrations (30, 60, 120 $\mu\text{g}/\text{mL}$) of P*(0.25)AA50 particle suspension. Nontreated cells were used as negative control and treated cells with of DXR at 5 μM for 24 h were used as positive control. Cell viability was evaluated using MTT reagent. MTT (0.25 mg/mL) solution was added to each well; the plates were incubated for 2 h at 37°C. The insoluble formazan crystals, produced in the mitochondrial compartment of viable cells, were dissolved using dimethyl sulfoxide (DMSO, 100 $\mu\text{L}/\text{well}$). The purple solution, obtained from enzymatic reaction with the mitochondrial dehydrogenase of alive cells, was read at a wavelength of 490 nm using a DU-730 Life Science spectrophotometer (Beckman Coulter). The percentage of

cell viability was calculated as ratio between each sample with respect to the negative control (100% of cell viability).

Cellular Internalization Studies by Confocal Analysis

ECV 304 cells were grown at a density of 5×10^3 cells/well in 12-well plates containing sterile coverslips in complete medium MEM199 for 24 h. Cells were incubated at 120 $\mu\text{g}/\text{mL}$ of P*(0.25)AA50-AF. At different incubation times, and in particular 1, 3, 6, and 24 h, cells were quickly washed with PBS to remove nanoparticles that were loosely bound to the cellular membrane, fixed with 3.7% of formaldehyde for 15 min, and washed again twice with PBS. Afterward, cells were stained for 1 min at room temperature with Ethidium Bromide (EtBr 1:1000). Nanoparticles localization inside cells was monitored by confocal microscopy analysis (Olympus 1 \times 70 with 419 Melles Griot laser system).

Functionalization of Nanogels with ODN

Modified ODN used were FAM-FW-N (FAM-5'-AAA ACT GCA GCC AAT GTA ATC GAA-3'-NH₂), REV-BHQ1 (5'-TTC GAT TAC ATT GGC TGC AGT TTT-3'-BHQ1), G1-REV-N (5'-TTC GAT TAC ATT GGC TGC AGT TTT-3') (Eurofins). P*(0.25)AA50-FAM-FW-N conjugates were prepared using an EDC/SulfoNHS coupling solution. FAM-FW-N has been directly attached to the carboxyl groups of nanogels through the C3-amine modified link at 3' end (see Scheme 1A)

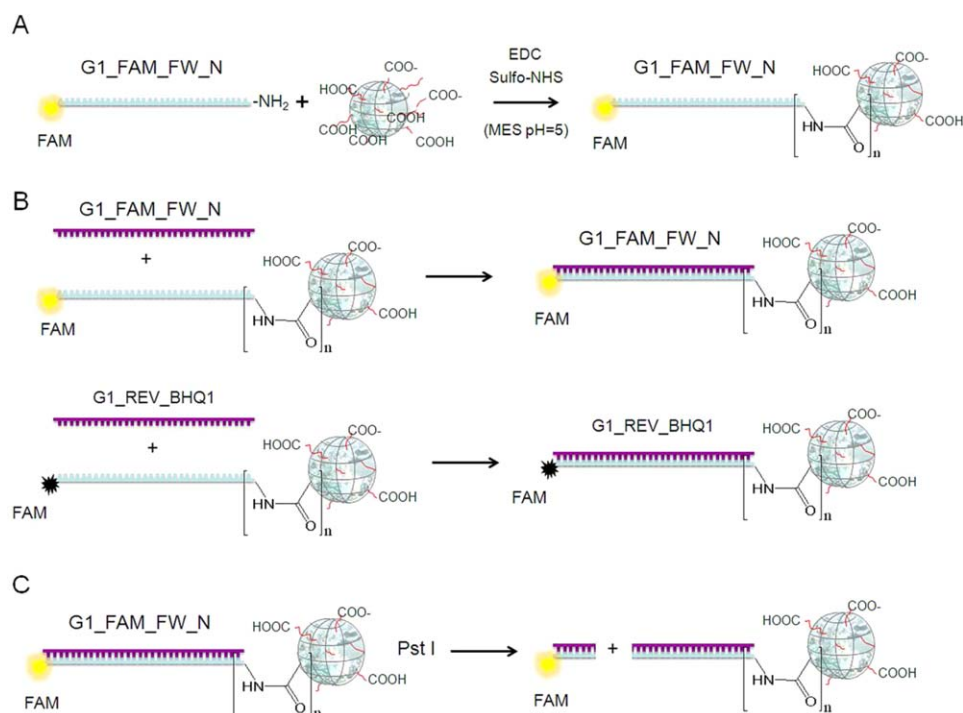
Firstly, 200 μL of P*(0.25)AA50 were incubated with EDC/NHS solution for 30 min at 37°C, while gentle stirring was provided; then, 1.0 μL of FAM-FW-N (2.5×10^{-2} μmol) was added and incubated for 3 h at 37°C, while stirring. The same solution, without FAM-FW-N, was also prepared and used as control. Both oligonucleotide-conjugated systems (P*(0.25)AA50-FAM-FW-N) and the relative control were thoroughly dialyzed (72 h) against milli-Q water using membranes with MWCO 14 kDa, to remove the nonconjugated oligonucleotide. In order to confirm the occurrence of conjugation and quantify the amount of oligonucleotide effectively conjugated, the fluorescence emitted by the FAM fluorophore (excitation 495 nm, emission 520 nm) present on the 5'end of the oligonucleotide FAM-FW-N was estimated using GloMax® Multi System (Promega). A calibration curve was made using solutions with increasing concentrations of FAM-FW-N.

Annealing and Digestion Test using Oligonucleotide-Conjugated Nanogels

In order to verify the accessibility by the complementary semi-helix to the oligonucleotide conjugated to the nanoparticles, an annealing test with was performed (see Scheme 1B).

The annealing reaction was carried out using a thermocycler (Perkin Elmer, GeneAmp PCR system), in which two thermal cycles were carried for the P*(0.25)AA50-FAM-FW-N system in the presence of REV-BHQ1, 50 mM NaCl, TE buffer 1X (10 mM Tris-Cl pH 7.5, 1 mM EDTA), passing through the specific annealing temperature of the two sequences.

After the annealing step, samples were washed many times with an equal volume of milli-Q water to remove the not annealed REV-BHQ1, using 100 kDa spin-dryer filters (Amicon) at 300 rpm. As negative control, the same reaction was carried out



Scheme 1. (A) Conjugation of P*(0.25)AA50 nanogels with a single strand oligonucleotide (FAM-FW-N) bearing a fluorescent label (FAM). (B) Annealing reaction of P*(0.25)AA50-FAM-FW-N with the complementary semi-helix with (REV-BHQ1) and without (G1-REV-N) a fluorescence quencher. (C) Digestion of FAM-FW-N conjugated P*(0.25)AA50 nanogels with the sequence-specific cutting enzyme Pst I. [Color figure can be viewed in the online issue, which is available at wileyonlinelibrary.com.]

using G1-REV-N, the complementary oligonucleotide lacking of the quencher. Finally, the FAM-fluorescence present in both samples was detected by GloMax® Multi System 3.

As the oligonucleotide sequences brought are cognition site for a specific restriction enzyme, the Pst I endonuclease, the double-strand DNA-nanoparticles, obtained after the annealing were incubated with Pst I (75 μM ; BioLabs) in their appropriate buffer, at 37°C for 2 h (see Scheme 1C). After the digestion step, the samples were washed 20 times with an equal volume of milli-Q water, using 100 kDa spin-dryer filters at 300 rpm, to remove the DNA fragments cleaved by Pst I. These washings were lyophilized and suspended again in 100 μL of milli-Q water. Then, the FAM-fluorescence present in the wash was detected by GloMax® Multi System 3.

RESULTS AND DISCUSSION

Nanogels Physicochemical and Molecular Properties

An easy, robust, and scalable at industrial level synthetic approach is at the basis of the development of therapeutic devices based on radiation-engineered carboxyl functionalized PVP nanogels.^{4,14} Here we describe the main physicochemical and molecular properties of a selected acrylic acid-grafted-PVP system used for conjugation with ODN. In particular, in Table I mean hydrodynamic diameter (D_h), ζ -potential in water (pH = 6), and weight average molecular weight (MW) values for the P*(0.25)AA50 NGs system are shown. The average hydrodynamic diameter of the NGs is 26 ± 9 nm. The ζ -potential plot shows a markedly anionic behavior of the nanogels dispersed in water, with a single narrow peak. The small particle size and the

anionic character grant the colloidal stability of the system in water solution. Indeed, we do not have observed precipitation even after prolonged storage. Chemical composition of P*(0.25)AA50 NGs was also characterized through spectroscopic analysis and closely resembles that of PVP.⁶

Hydrodynamic size and surface charge density were also measured in water solutions at different pHs (2.5–10) and controlled ionic strength (1 mM). Data are displayed in Figure 1. Particles size distributions are monomodal for all the pHs and the hydrodynamic size of NGs is almost invariant with pH when above 5. At pH below the pKa of AA (pKa=4.75), a great proportion of carboxyl groups present on nanogels becomes protonated and the corresponding ζ -potential value approaches 0 mV. The fading of the electrostatic charge repulsion as well as the related increase of hydrophobicity lead to NGs aggregation and their precipitation upon storage. At pH above the pKa of AA, ζ -potentials are negative and their absolute values increase with pH because of the progressive dissociation of carboxyl groups. As the protonation state of carboxyl groups does not significantly affect the hydrodynamic size of the nanogels, but only

Table I. Average Hydrodynamic Diameter (D_h), ζ -Potential in Water (pH 6) and Weight Average Molecular Weight of the Polymer (MW) for P*(0.25)AA50 NGs

Sample	D_h (nm)	ζ -potential (mV)	Zeta dev. (mV)	MW (MDa)
P*(0.25)AA50	26 ± 9	-40	9.26	1.02

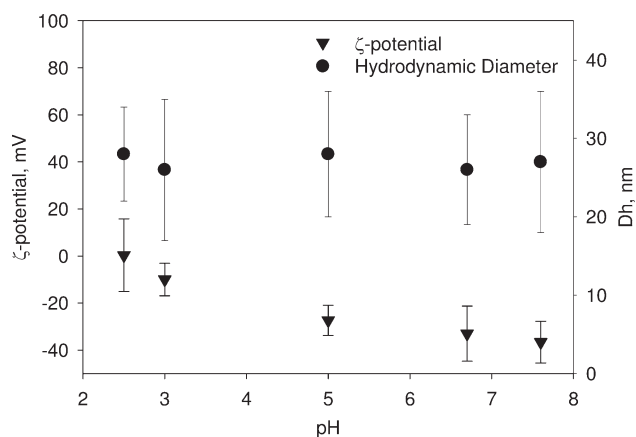


Figure 1. Average hydrodynamic diameters and ζ -potential values of NG dispersions in water at the variance of pH and constant ionic strength (1 mM). Error bars represent the width of particles size or surface charge density distributions.

their surface charge density, we expect these groups to be mainly present as grafted arms on the crosslinked PVP cores.

In order to verify if nanogels are able to bypass the cell plasma-membrane and localize in specific cell districts, localization studies in cell cultures were performed. For the purpose, P*(0.25)AA50 system was labeled with a green emissive fluorescent probe. The conjugation degree, reported as molar ratio between ligand and nanoparticle, estimated through UV-Vis absorption measurements, is equal to 5. The emissivity of probe labeled NGs was also tested through UV-Vis emission spectroscopy. Figure 2 shows the comparison between the non-emissive bare system and its fluorescent variant.

Biological Evaluations

Nanogels biocompatibility was tested by *in vitro* assays. To verify the absence of apoptotic events, a morphological evaluation

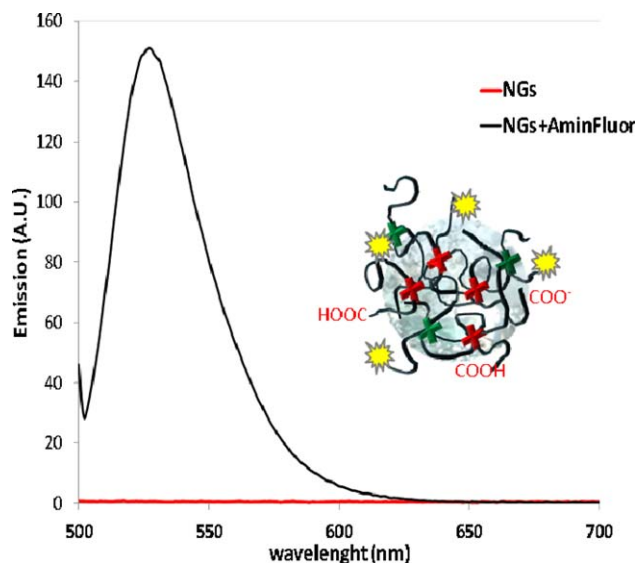


Figure 2. UV-Vis emission spectra of P*(0.25)AA50 and its fluorescent variant. [Color figure can be viewed in the online issue, which is available at wileyonlinelibrary.com.]

by fluorescence microscopy analyses was performed on ECV304 cells incubated with different concentration of NGs and stained with an Acridine Orange solution (Figure 3A). As it can be observed in Figure 3A (panel c-d), cells incubated respectively at 60 and 250 $\mu\text{g}/\text{mL}$ of P*(0.25)AA50 do not show the classical morphological changes associated with apoptotic events. Indeed, cells show mainly uniform bright green nuclei with organized structures, similarly to the negative control (panel a). Conversely, damaged DNA is evident in cells treated with DXR (panel b), which are characterized by red nuclei with condensed or fragmented chromatin.

In order to further support this evidence, an enzymatic assay was carried out using the Ac.Asp-Glu-Val-Asp-MCA substrate, a selective fluorogenic peptide for identification and quantification of Caspases 3,7,8 activity. The fluorogenic MCA residue, released by activated Caspase cleavage, was quantified by spectrofluorimeter readings. ECV304 cells, treated or not (negative control) at 250 $\mu\text{g}/\text{mL}$ of P*(0.25)AA50 nanoparticles for 24 h were compared with the ones treated with DXR (positive control). At different incubation times with the Caspase substrate,

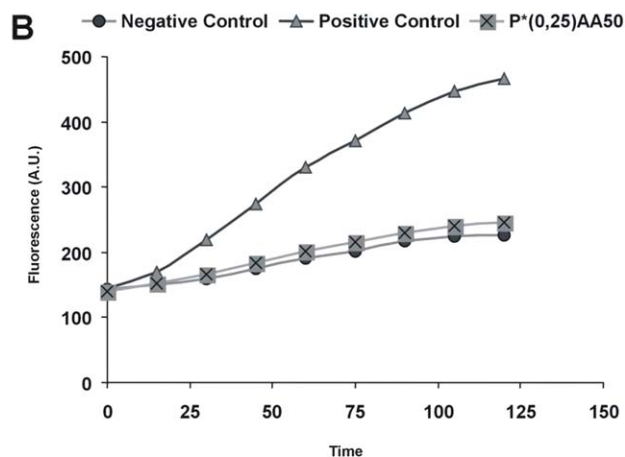
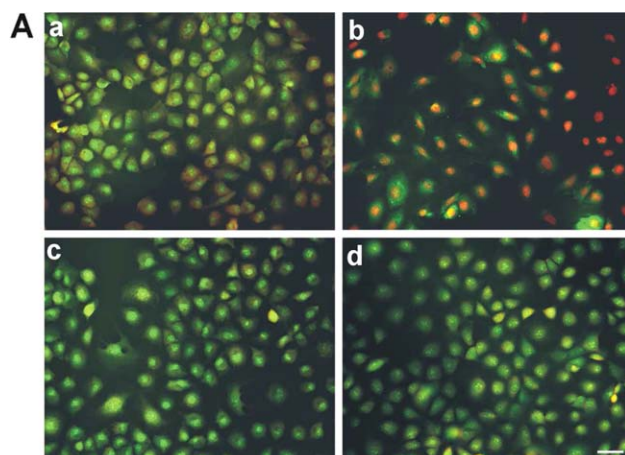


Figure 3. A: Apoptotic evaluation by AO on ECV304 cells: (a) untreated; (b) in the presence of DXR [5 μM]; (c) incubated with nanogels at 60 $\mu\text{g}/\text{mL}$; and (d) at 250 $\mu\text{g}/\text{mL}$ for 24 h. Magnification 20 \times . Bar = 100 μm . B: Enzymatic Caspase 3 substrate activation. [Color figure can be viewed in the online issue, which is available at wileyonlinelibrary.com.]

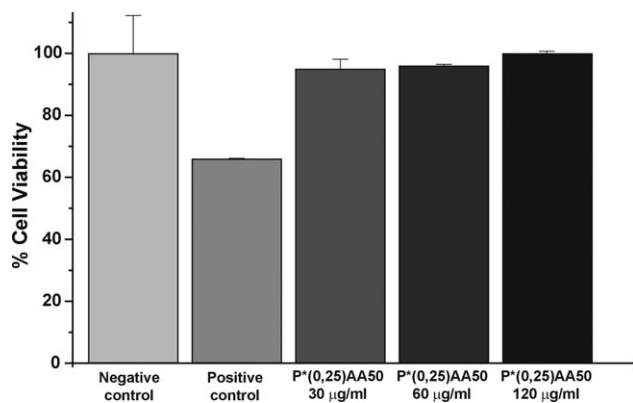


Figure 4. Cytotoxicity evaluations by MTT assay. Percentage of cell viability is expressed with reference to the untreated cells.

ECV304 cells' extracts were analyzed to determine the amount of fluorescence of each sample. As shown in Figure 3B, NGs-treated cells did not show any activation of Caspases, while time-dependent fluorochrome release was observed for the DXR-treated cells (positive control). These results confirm the absence of programmed cell death induced by the presence of P*(0.25)AA50 nanogels.

The absence of cytotoxicity of P*(0.25)AA50 nanogels was also evaluated by the MTT viability assay. Figure 4 shows the relative viability of ECV304 cells after 24 h of incubation in the presence of different amount of nanogels. It is evident that the viability of the cells in the presence of nanogels is similar to that of the negative control (untreated cells), differently from the DXR-treated cells (positive control), which show a mortality increase. As a result of both the morphological evaluation and the MTT assay, we can conclude that the nanogels show very good biocompatibility.

Nanogels Localization in Cell Culture

In order to verify if the nanogels are able to bypass the cell plasma-membrane and to localize in specific cell districts, localization studies in cell cultures were performed. ECV304 cells were treated for different incubation times with the aminofluorescein labeled variant of the NGs; their movement through cell membrane and localization inside cells was followed by confocal microscopy analysis. As shown in Figure 5, the amount of NGs inside the cells slowly increases, after 1 h (A) and further after 3 h (B) of incubation to reach its maximum concentration in the cytoplasm compartments, and particularly in the perinuclear area, after 6 h (C). After 24 h, (D) evidence of cytoplasmic

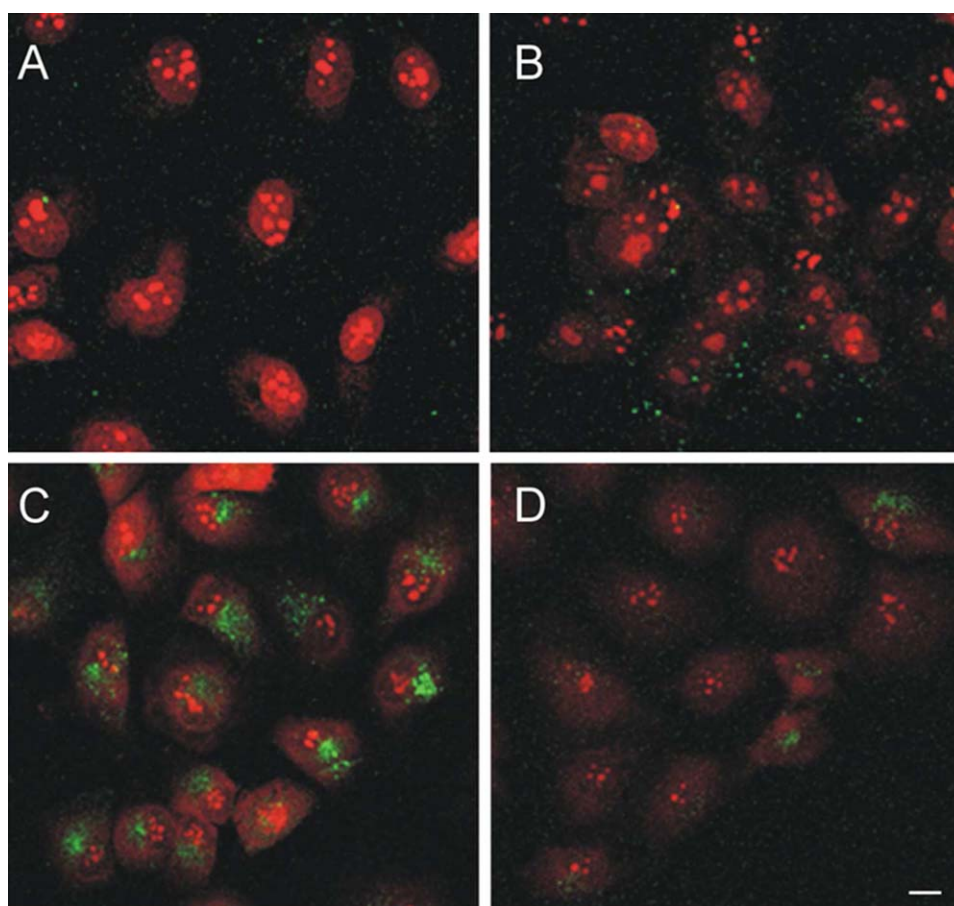


Figure 5. Localization study by confocal microscopy analysis of aminofluorescein conjugated nanogels incubated on ECV304 cells for: (A) 1 h; (B) 3 h; (C) 6 h; and (D) 24 h. Cells were stained with EtBr (Red). Magnification 40 \times . Bar = 10 μ m. [Color figure can be viewed in the online issue, which is available at wileyonlinelibrary.com.]

localization of NGs is still present, although at lower concentration. It is interesting to observe that the pattern of the nanogels localization in cell culture is similar to that observed for the amino-functionalized crosslinked PVP nanogels obtained by either radiation-processing⁴ or by a inverse microemulsion chemical polymerization.⁸ A similar perinuclear localization has been also documented for a number of different nanoparticulate carriers and bio-hybrid conjugates, such as Au NPs conjugated both with antisense ODN and/or synthetic peptides,²⁰ DNA-containing gelatin and PEGylated gelatin NPs²¹ or polyethylenimine/DNA nanocomplexes.²² While the specific mechanism of the internalization process of our NGs is currently under investigation, some general hypotheses can be proposed on the account of the analogies with other systems described in the literature. The endocytic pathway is often proposed as the major cellular uptake mechanism of any biological agent or biomolecular therapeutics-carrying nanoparticle. Particles or biological entities entering the cells through the endocytic pathway become entrapped in the endosomes, where they experience a pH change from ~ 7 to ~ 5 , and eventually end up in the lysosomes, where active enzymatic degradation processes take place. In order to protect the nanocarrier contents from degradation and ensure their cytosolic delivery, strategies for facilitating the “endosomal escape” of the loaded carrier have to be set in place. Several approaches have been attempted for the purpose.²³ For pH-responsive synthetic polymers either proton-sponge effects or membrane-destabilizing activities have been often proposed [Ref. ²³ and references herein]. In particular, the pH-dependent, membrane-destabilizing activity of poly(alkylacrylic acid) polymers has been described by Hoffman and coworkers.^{24,25} Protonation of the carboxyl acid groups placed at the end of relatively short (C2-C4) lateral alkyl chains in the polymer reversibly transform the hydrophilic “stealth-like” polymers at physiologic pH into hydrophobic membrane-destabilizing nanoparticles. With reference to the carboxyl functionalized PVP nanogels here described, we already demonstrated that alongside intra- and inter-molecular crosslinking of poly(N-vinyl pyrrolidone) also significant degradation reactions can occur with possible pyrrolidone ring opening and subsequent formation of butyric acid pendant groups.⁷ These groups may be responsible for the hydrophilic to hydrophobic conversion of nanogels, which is also at the basis of the observed colloidal destabilization of dispersions at pH < 5.

Nanogels Functionalization with Modified ODN

The FAM-FW-N oligonucleotide was built with a C3-aminolink at the 3'-end, capable of reacting with the carboxyl groups present on nanogels, and with FAM fluorochrome at the 5'-end, in order to make the oligonucleotide fluorescent. The amount of oligonucleotide linked to nanoparticles was estimated by fluorimetric analysis. As nanoparticles present a slight self-fluorescence in correspondence of FAM emission peak (520 nm), this contribution was subtracted to the emission intensity of oligonucleotide conjugated-nanogels. The absolute emission intensity of nanogels and oligonucleotide conjugated-nanogels are shown in Figure 6. In order to exclude a non-specific attachment of the ODN to the nanoparticle and to verify that it maintains its ability to form a double-strand DNA, an annealing

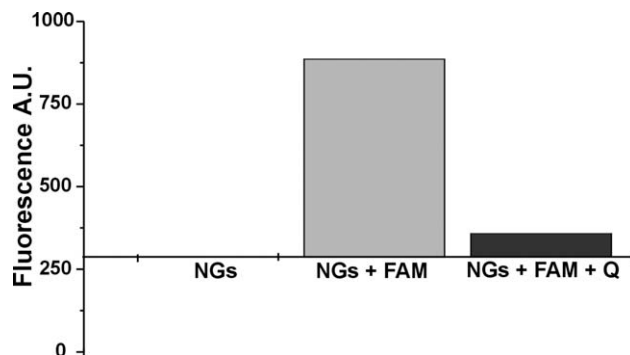


Figure 6. Fluorescence intensity of bare nanogels (NGs), FAM-FW-N conjugated nanogels (NGs + FAM) and FAM-FW-N conjugated nanogels after annealing with REV-BHQ1 (NGs + FAM + Q).

test was performed. For the annealing test, two different types of complementary sequences were used, with and without a FAM-black hole quencher. As shown in Figure 6, after two cycles at the annealing temperature, the FAM fluorescence is quenched (20 times lower) when NGs are annealed in the presence of REV-BHQ1. Conversely, when the annealing test was performed with the complementary sequence without the quencher, the FAM fluorescence is not attenuated. This experimental evidence shows that even if the FAM-FW-N sequence is linked to the nanogels, it takes the correct folding reacting with the correct complementary sequence. To further support this evidence, Pst I restriction enzyme digestion was performed. As a consequence of the enzymatic cut, the double helix of DNA formed upon annealing loses the 5' end that carries the FAM fluorochrome. The digestion products were separated from the NGs and their fluorescence was measured. After the digestion nanogels conjugated and annealed with the complementary sequences (with or without the quencher) show only their initial auto-fluorescence values (data not shown). This result corroborates the previous one, as the sequence-specific cutting operated by the enzyme Pst I works only if the base pairing is specific, i.e. without DNA mismatching.

CONCLUSIONS

Nanogels, formed by radiation-induced crosslinking of PVP and simultaneous grafting of acrylic acid, were obtained quantitatively and reproducibly by electron-beam irradiation of semi-dilute aqueous solutions of the polymer. At the selected irradiation dose of 40 kGy, system sterility is also achieved. As a result, nanogels with a crosslinked PVP core and AA groups bearing arms form. A good control of hydrodynamic size of nanogels at the nanoscale is achieved. Furthermore, nanogels show a net negative surface charge density at physiological pHs, which collaborate to their colloidal stability. The availability of carboxyl groups prompted us to attempt the attachment of a single strand oligonucleotide by its terminal amino group in a way that preserved its pairing ability with the complementary strand. Absence of induced cytotoxicity by these nanoparticles and their ability to bypass cell membranes, to then localize in the perinuclear area of the cytoplasm, encourage a further development of these nanocarriers as intracellular delivery devices of genetic material for therapeutic purposes.

ACKNOWLEDGMENTS

This research was supported by a grant from the Italian Ministry of University and Scientific Research (PRIN 2010-2011 NANOMED). We acknowledge the assistance of the Centre for Radiation Research and Technology, Institute of Nuclear Chemistry and Technology, Warsaw, Poland for e-beam irradiation.

REFERENCES

1. Mintzer, M. A.; Simanek, E. E. *Chem. Rev.* **2009**, *109*, 259.
2. Morille, M.; Passirani, C.; Vonarbourg, A.; Clavreul, A.; Benoit, J. -P. *Biomaterials* **2008**, *29*, 3477.
3. Byrne, J. D.; Betancourt, T.; Brannon-Peppas, L. *Adv. Drug Deliver. Rev.* **2008**, *60*, 1615.
4. Dispenza, C.; Sabatino, M. A.; Grimaldi, N.; Bulone, D.; Bondi, M. L.; Casaletto, M. P.; Rigogliuso, S.; Adamo, G.; Ghersi, G. *Biomacromolecules* **2012**, *13*, 1805.
5. Dispenza, C.; Sabatino, M. A.; Grimaldi, N.; Spadaro, G.; Bulone, D.; Bondi, M. L.; Adamo, G.; Rigogliuso, S. *Chem. Eng. Trans.* **2012**, *27*, 229.
6. Grimaldi, N.; Sabatino, M. A.; Przybytniak, G.; Kaluska, I.; Bondi, M. L.; Bulone, D.; Alessi, S.; Spadaro, G.; Dispenza, C. *Rad. Phys. Chem.* doi:10.1016/j.radphyschem.2013.04.012.
7. Sabatino, M. A.; Bulone, D.; Veres, M.; Spinella, A.; Spadaro, G.; Dispenza, C. *Polymer* **2013**, *54*, 54.
8. Dispenza, C.; Grimaldi, N.; Sabatino, M. A.; Bulone, D.; Bondi, M. L.; Rigogliuso, S.; Ghersi, G. *React. Funct. Polym.* **2013**, *73*, 1103.
9. Ulanski, P.; Rosiak, J.M. In: *Encyclopedia of Nanoscience and Nanotechnology*, Nalwa, H. S., Ed.; American Scientific Publishers: Valencia, CA, USA, **2004**; p 1.
10. Vinogradov, S. V.; Batrakova E. V.; Kabanov A. V. *Colloid Surf. B* **1999**, *16*, 291.
11. Vinogradov, S. V.; Batrakova, E. V.; Kabanov, A. V. *Bioconjug. Chem.* **2004**, *15*, 50.
12. Lemieux, P.; Vinogradov S. V.; Gebhart C. L.; Guérin, N.; Paradis, G.; Nguyen H. K.; Ochietti, B.; Suzdaltseva Y. G.; Bartakova E. V.; Bronich T. K.; St-Pierre, Y.; Alakhov, V. Y.; Kabanov A. V. *J Drug Target.* **2000**, *8*, 91.
13. Mitra, A.; Imae, T. *Biomacromolecules* **2004**, *5*, 69
14. Dispenza, C.; Grimaldi, N.; Sabatino, M. A.; Todaro, S.; Bulone, D.; Giacomazza, D.; Przybytniak, G.; Alessi, S.; Spadaro, G. *Radiat. Phys. Chem.* **2012**, *81*, 1349.
15. Lambert, B. J.; Hansen, J. M. *Radiat. Phys. Chem.* **1998**, *52*, 11.
16. Stepanek, P. Data analysis in dynamic light scattering. In *Dynamic Light Scattering*, Brown, W., Ed.; Oxford University Press: Oxford, **1993**; p 177.
17. Hermanson, G. T. *Bioconjugate Techniques*, 2nd ed.; Academic Press: New York, **2008**.
18. Nicholson, D. W.; Ali, A.; Thornberry, N. A.; Vaillancourt, J. P.; Ding, C. K.; Gallant, M.; Gareau, Y.; Griffin, P. R.; Labelle, M.; Lazebnik, Y. A. *Nature* **1995**, *6*, 37.
19. Thornberry, N. A.; Rano, T. A.; Peterson, E. P.; Rasper, D. M.; Timkey, T.; Garcia-Calvo, M.; Nordstrom, P. A.; Roy, S.; Vaillancourt, J. P.; Chapman, K. T.; Nicholson, D. W. *J. Biol. Chem.* **1997**, *18*, 17907.
20. Patel, P. C.; Giljohann, D. A.; Seferos, D. S.; Mirkin, C. A. *Proc. Natl. Acad. Sci. USA* **2008**, *105*, 17222.
21. Kaul, G.; Amiji, M. *J. Pharma. Sci.* **2005**, *94*, 184.
22. Suh, J.; Wirtz, D.; Hanes, J. *Proc. Natl. Acad. Sci. USA* **2003**, *100*, 3878.
23. Varkouhi, A. K.; Scholte, M.; Storm, G.; Haisma H. J. *J. Control. Release* **2011**, *151*, 220.
24. Cheung, C. Y.; Murthy, N.; Stayton, P. S.; Hoffman, A. S. *Bioconjug. Chem.* **2001**, *12*, 906.
25. Convertine, A. J.; Benoit, D. S. W.; Duvall, C. L.; Hoffman, A. S.; Stayton, P. S. *J. Control. Release* **2009**, *113*, 221.

*Water-borne Polymeric Nanoparticles for Glutathione-Mediated
Intracellular Delivery of Anticancer Drugs.*

N. Grimaldi*, M.A. Sabatino, D. Bulone, G. Adamo,
S. Rigogliuso, G. Gherzi, C. Dispenza.

2013. NSTI-Nanotech 2013, www.nsti.org, ISBN 978-1-4822-0586-2. 3, 155-158.

***Water-borne* Polymeric Nanoparticles for Glutathione-Mediated Intracellular Delivery of Anticancer Drugs**

N. Grimaldi^{*}, M.-A. Sabatino^{*}, D. Bulone^{**}, G. Adamo^{***}, S. Rigogliuso^{***}, G. Ghersi^{***}, C. Dispenza^{***}

^{*} Dipartimento di Ingegneria Chimica, Gestionale, Informatica, Meccanica, Università di Palermo, Viale delle Scienze, Edificio 6, 90128 Palermo, Italy.

^{**} CNR - Istituto di Biofisica (IBF) UOS Palermo, via Ugo La Malfa 153, 90146 Palermo, Italy.

^{***} Dipartimento di Scienze e Tecnologie Molecolari e Biomolecolari, Università di Palermo, Viale delle Scienze, Edificio 16, 90128 Palermo, Italy.

ABSTRACT

A new family of *water-borne*, biocompatible and carboxyl-functionalized nanogels was developed for glutathione-mediated delivery of anticancer drugs. Poly(N-vinylpyrrolidone)-co-acrylic acid nanogels were generated by e-beam irradiation of aqueous solutions of a crosslinkable polymer, using industrial-type linear accelerators and set-ups. Nanogels physico-chemical properties and colloidal stability, in a wide pH range, were investigated. In vitro cell studies proved that the nanogels are fully biocompatible and able to quantitatively bypass cellular membrane. An anticancer drug, doxorubicin (DOX), was linked to the carboxyl groups of NGs through a spacer containing a disulphide cleavable linkage. In vitro release studies showed that glutathione is able to trigger the release of DOX through the reduction of the S-S linkage at a concentration comparable to its levels in the cytosol.

Keywords: nanogels, e-beam radiation, disulphide linkage, doxorubicin.

Introduction

The efficacy of a cancer therapeutic drug is measured by its ability to reduce and eliminate tumors without damaging healthy tissue. However, anticancer drugs suffer some limitations related to their poor solubility in aqueous environment, non-specificity in their distribution through the body compartments and severe adverse side effects. Furthermore, during the prolonged treatment with chemotherapeutic drugs, tumor cells develop multidrug resistance (MDR) and the drugs effectiveness decreases over time [1]. Cancer-fighting therapeutic devices based on nanoparticle systems offer the possibility of overcoming the

problems mentioned above. In fact, nanocarriers are able to increase the solubility of hydrophobic drugs, decrease the toxicity toward healthy cells and escape from multi-drug resistance bypassing the efflux pumps and increase the drug intracellular concentration. Nanoparticles can be formulated with appropriate size, shape, surface properties and specific chemical functionality for covalent coupling of targeting moieties. Because of these tunable physico-chemical properties, nanoparticles may combine active and passive targeting in one single platform. Upon nanoparticle devices reach the target cells, they should be able to release the drug. Stimulus-mediated release is receiving great attention for intracellular drug delivery and various stimuli-responsive nanoparticles have been developed and investigated extensively, including temperature, pH, ultra sound, redox, and enzyme responsive ones [2]. Doxorubicin is one of the most effective chemotherapeutic anticancer drugs and it is crucial for the treatment of a wide range of tumors as breast cancer, acute leukemia and malignant lymphoma [3]. We have developed a new family of *water-borne*, biocompatible and carboxyl-functionalized nanogels (NGs) for glutathione-mediated delivery of Doxorubicin. In our approach, DOX is linked to nanoparticles through a linker containing a cleavable disulphide bridge, aminoethyldithiopropionic acid (AEDP). The release mechanism is based on the existence of a large difference in the redox potential between the mildly oxidizing extracellular milieu and the reducing intracellular fluids. The reducing agent is glutathione (GSH) that is found in the blood plasma of humans with micromolar concentrations, whereas it is around 10 mM in the cytosol. The concentration level of cytosolic GSH in cells with an enhanced level of oxidative stress, as in tumor cells, is several times higher than that in normal cells [2]. In alternative to more conventional synthetic approaches, which often imply several reactive and purification steps, a

robust and economically viable manufacturing process was developed for the production of nanogels. Nanogels were generated by e-beam irradiation of semi-dilute aqueous solutions of a crosslinkable polymer and acrylic acid, using industrial-type linear accelerators and irradiation conditions typically applied for sterilization purposes in industry, by irradiating at relatively low dose per pulse, high frequency and 40 kGy of integrated dose [4-6]. In particular, poly(N-vinyl-pyrrolidone)-co-acrylic acid (PVP-co-AA) variants with controlled size and surface charge density, high colloidal stability in a wide pH range (5 - 10) and multi-arms with terminal functional groups available for further conjugation, were generated quantitatively and reproducibly. Physico-chemical properties and colloidal stability of the generated nanoparticles were investigated through DLS techniques and ζ -potential measurements. In vitro cell studies proved that the nanogels are fully biocompatible and able to quantitatively bypass cellular membrane. In vitro release experiments showed that GSH is able to trigger the release of DOX through reduction of the disulphide linkage at concentrations comparable to its levels in cytosol.

Experimentals

Materials

PVP k60, acrylic acid (AA), amino-fluorescein (AF), 1-ethyl-3-(3 dimethylaminopropyl) carbodiimide (EDC), and 2-(N-morpholino)ethanesulfonic acid (MES), glutathione (GSH), doxorubicin (DOX) were supplied by Aldrich. AEDP was supplied by VWR.

Methods

Preparation of PVP-co-AA NGs: PVP aqueous solutions at a concentration of 0.5 wt% in presence of acrylic acid (molar ratio between PVP repetitive unit and acrylic acid equal to 50) were prepared by overnight stirring, filtered with 0.22 μm pore size syringe filters, carefully deoxygenated with gaseous nitrogen and individually saturated with N_2O ($\text{N}_2\text{O} \geq 99.99\%$) prior to irradiation. Electron beam irradiation was performed using a 10 MeV linear accelerator at the ICHTJ of Warsaw (Poland). An integrated dose of 40 kGy was supplied. After irradiation samples were dialyzed (MWCO 100K Da) against distilled water for 48 h to remove eventual unreacted monomer, oligomers and low MW polymer. The yield of recovered nanogels after dialysis was determined gravimetrically. Hydrodynamic diameters (D_h) of NGs dispersions were measured by dynamic light scattering (DLS) using Brookhaven BI-9000 correlator and a 50 mW He-Ne laser (MellesGriot) tuned at $\lambda = 632.8$ nm. Particles size distributions expressed as volume % and the mean

hydrodynamic diameter and PDI determined by the cumulant method are reported [8]. Surface charge density of NGs in water was measured at 25°C using a ZetaSizerNano ZS (Malvern Instruments Ltd, Malvern, UK) equipped with a He-Ne laser at a power of 4.0 mW. Mean ζ -potential values and the relative width of the distribution were reported for each sample. Both DLS and ζ -potential measurements were carried on 1 mg/ml dispersions at 20°C in water solutions of different pHs and controlled ionic strength (IS=1mM).

Cytotoxicity of nanoparticles on vein endothelial cell (ECV304) was assessed by MTT assay (Sigma). Cells were seeded in a 96-well plates at density of 1×10^4 cell/well, in complete medium MEM199. After 24 hr from seeding, cells were exposed to particle suspension at different concentrations (30 $\mu\text{g}/\text{ml}$, 60 $\mu\text{g}/\text{ml}$, 120 $\mu\text{g}/\text{ml}$), for 24 hr at 37°C. Not treated ECV304 cells were used as negative control and those treated with DOX [5 μM] for 24 hr were used as positive control. The % of cell viability was calculated as ratio between each sample with respect to the negative control (100% of viability).

Localization studies were performed on ECV 304 cells. ECV 304 were grown at a density of 5×10^3 cells/well into 12-well plates containing sterile glass coverslips in complete medium MEM199 for 24 hr. Next, the cells were incubated with 120 $\mu\text{g}/\text{ml}$ of NGs, which emit green fluorescence by aminofluorescein conjugation. After different incubation times, 1 hr, 3 hr, 6 hr and 24 hr respectively, cells were extensively washed with PBS, to remove not reactive nanoparticles, and fixed with 3.7% formaldehyde for 15 minutes; then were again washed with PBS. Subsequently, the cells were stained with EtBr (1:1000) for 1 minute at room temperature. Localization was carried out by confocal microscopy analyzer (Olympus 1x70 with Melles Griot laser system).

Preparation of AEDP-DOX-P(0.5)AA50 NGs:* NGs were conjugated with AEDP and DOX by a two steps process. A standard EDC/Sulfo-NHS based protocol was adapted to our systems [7]. Both steps were carried out at 25°C, in pH 5 MES buffer, in excess of ligands with respect to the carboxyl groups and under continuous stirring. AEDP-DOX-P*(0.5)AA50 NGs were then purified through prolonged dialysis against water.

Reduction-Triggered DOX release: DOX-AEDP-P*(0.5)AA50 NGs were placed into a dialysis tubing (MWCO 12 kDa) with 10 mM of GSH or without, as control, and immersed in 20 ml of PBS (pH 7.4). The systems were kept at 37°C under shaking (200 rpm). At predetermined time intervals (1, 2, 4, 6, 8, 12, 24 hr), 1 ml of external buffer solutions were withdrawn and replaced with 1 ml of fresh PBS.

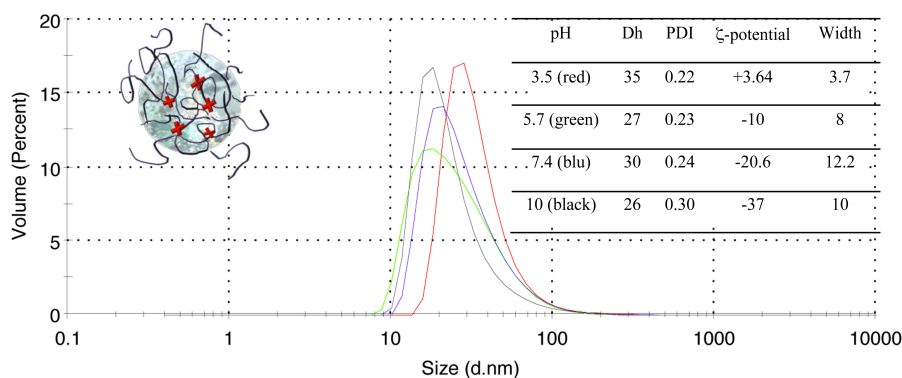


Figure 1. Particles size distributions in water at different pH obtained by DLS measurements. In inset table, the mean hydrodynamic diameter and PDI for each distribution shown and mean ζ -potential and relative width for each system are reported.

The amount of DOX linked to NGs and the amount released were determined by fluorescence measurements (λ_{exc} 480 nm, λ_{em} 550 nm) using a Jasco 6500 spectrofluorimeter.

Results and discussion

Water borne PVP-co-AA NGs were generated through e-beam irradiation, starting from a semi-diluted polymer aqueous solution in presence of acrylic acid. The yield of process was about 90% [9]. Nanogels variants with different particles size, surface properties and degree of functionalization were obtained [9]. In this work only a brief description of the basic physico-chemical properties of the system selected for the conjugation with AEDP and DOX is reported. Size, surface properties and colloidal stability in a wide pH range (5-10) are very important parameters for intracellular delivery of nanoparticles and were investigated through DLS measurements and ζ -potentials determinations. As shown in Figure 1, the particle size distributions of P*(0.5)AA50 NGs in water solution of different pHs and equal ionic strength (IS=1 mM) display a monomodal distributions for all the systems, with an average diameter varying from 35 nm to 26 nm and low PDI values (0.23-0.3). The hydrodynamic diameter is fairly invariant in a wide pH range (5-10), only at pH 3.5, it is slightly bigger due to the onset of aggregation phenomena, which become faster at pH<3.5. At this pH, below the pKa of acrylic acid (pKa=4.75), a great proportion of carboxyl groups present on nanogels multi-arms becomes protonated, thus ζ -potential value is about 0 mV. At pH>3.5, the ζ -potential values become negative and their absolute values increase with the pH due to progressive dissociation of carboxyl groups. Since carboxyl groups are preferentially located on the “multi-branched arms” of NGs, their degree of dissociation does not affect the NGs’ hydrodynamic size. Carboxyl groups located on NGs arms are easily accessible to covalent conjugation with fluorescent probes, small peptides, such as folic acid, and

oligonucleotides. The availability, different positions and accessibility of functional groups on NGs allow performing multiple conjugations on the same nanoparticles (data here not shown for brevity). The chemical structure of the produced NGs was characterized through different spectroscopic techniques and it closely resembles that of the linear PVP [9]. P*(0.5)AA50 NGs were thought as devices for therapeutically purposes, therefore it is necessary to check on their biocompatibility by *in vitro* assays before proposing them for any biomedical application. The biocompatibility of P*(0.5)AA50 NGs was evaluated using MTT viability assay. The Figure 2 shows the relative viability of ECV304 cells after 24 hr of incubation with NGs dispersions at different concentrations. It is evident that, in the presence of NGs, cells viability is similar to that of the negative control (untreated cells). Differently, DOX-treated cells (positive control) show a lower cells viability. P*(0.5)AA50 NGs are not cytotoxic.

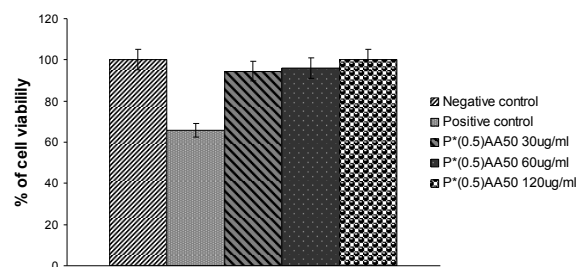


Figure 2. Evaluation of cell viability using MTT analysis.

NGs movements through the cell membrane and their internalization was investigated by confocal microscope analysis using a fluorescent variant of P*(0.5)AA50 NGs. We analyzed nanogels distribution in cell compartments at different times. As shown in Figure 3, after 1 (A) and 3 hr (B) of incubation, the amount of nanoparticles internalized slowly increases; whereas, after 6 hr (C) the nanogels are cytoplasmatic compartmentalized in the perinuclear area.

After 24 hr (D) nanogels concentration inside cells decreases, probably due to excretion as waste products in the extracellular environment. NGs showed a good affinity for cells, as they rapidly and quantitatively bypass the cellular membranes, being then released from the cells. P*(0.5) AA50 NGs were conjugated with AEDP and DOX through a two steps conjugation procedure. The choice to link the drug by a spacer with a cleavable linkage, over the physical encapsulation or the direct bond to NGs, was driven by the need to achieve a great control of drug release at the target site. Upon reaching the target tumor cells, the “drug” conjugated NGs should be internalized by cells and the release triggered by the stimulus. For DOX-AEDP-P*(0.5)AA50 NGs the stimulus is a redox agent, glutathione.

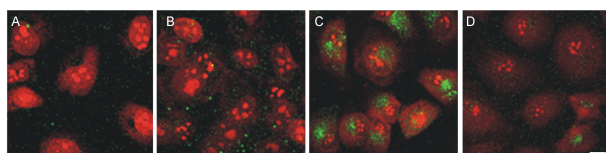


Figure 3. Localization assay by confocal microscopy analysis of a fluorescent variant of P*(0.5)AA50 NGs, incubated on ECV304 cell respectively for: A. 1 hr; B. 3 hr; C. 6 hr and D. 24 hr. Cell were stained with Ethidium Bromide. (Red) Magnification 40X; bar 10 mm.

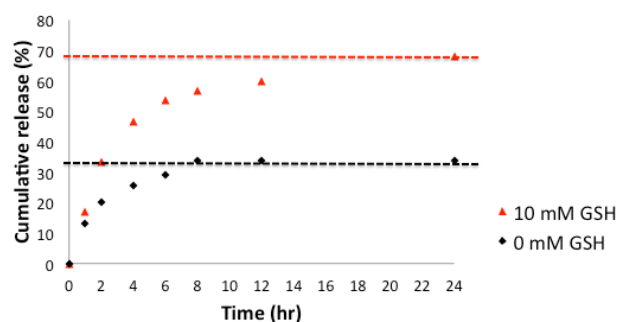


Figure 4. In vitro release of DOX from DOX-AEDP-P*(0.5)AA50 NGs in PBS (pH 7.4) at 37 °C with or without GSH.

The responsiveness of redox-sensitive NGs conjugated with AEDP and Doxo to the GSH stimulus was studied in vitro. The drug release studies were performed with 10 mM of GSH or without, as negative control. The amount of DOX released was quantified through fluorescence measurements. The release profiles for both systems are shown in Figure 4. The % of DOX release is reported as the molar ratio between the DOX released at the time t and the DOX linked to nanoparticles at the time $t=0$ hr. The total amount of DOX linked to the nanogels, after the purification step, was determined through fluorescence measurements. It can be observed that both systems release the DOX, but in the presence of GSH the amount of DOX released is substantially higher, about 70% vs. 34%, and the

release is faster. No burst effects are evident. In absence of GSH, it is likely released the DOX which is not covalent linked to the nanoparticles. In fact, due to its hydrophobicity this molecule can be favorably hosted in the nanogels interiors. In vitro drug release tests demonstrate that the disulphide bridge can be broken under a reductive molecule stimulus, such as the GSH. These results prompted us to evaluate their performance into biological systems.

Conclusions

A new type of redox-responsive NGs was synthesized. The synthetic approach developed ensures the quantitative production of functionalized nanogels with tailored size and surface properties. Nanogels show high colloidal stability, biocompatibility, ability to bypass cell membranes and preferentially accumulate near the nuclei within 6 hr, being then progressively released by cells. The carboxyl groups located on the nanogels multi-branched arms can be used for further conjugation to generate DOX-AEDP-P*(0.5)AA50 redox-responsive NG variants. In vitro release studies showed that glutathione is able to trigger the release of DOX through reduction of the AEDP's S-S linkage at a concentration comparable to its levels in cytosol (10 mM). The combination of a single-step, robust and economically viable manufacturing process with all the favorable properties of the produced NGs make these nanoparticles very interesting candidates as smart nanocarriers of drugs at specific tumor sites. Studies on the GSH mediated intracellular drug release against cells are on going.

References

- [1] M. Creixella, N. A. Peppas, *Nano Today*, 7, 367-379, 2012.
- [2] K. R. West, S. Otto, *Current Drug Discovery Technologies*, 2, 123-160, 2005.
- [3] M. Shi, K. Ho, A. Keating, M. S. Shoichet, *Advanced Functional Materials*, 19, 1689-1696, 2009.
- [4] P. Ulanski, J.M. Rosiak, *Nuclear Instruments and Methods in Physics Research B*, 151, 356-360, 1999.
- [5] C. Dispenza, M.A. Sabatino, N. Grimaldi, G. Spadaro, D. Bulone, M.L. Bondi, G. Adamo, S. Rigogliuso, *Chemical Engineering Transaction* 27, 229-232, 2012.
- [6] C. Dispenza, M.A. Sabatino, N. Grimaldi, D. Bulone, M.L. Bondi, M.P. Casaletto, S. Rigogliuso, G. Adamo, G. Ghersi, *Biomacromolecules*, 13(6), 1805-1817, 2012.
- [7] G.T. Hermanson, “*Bioconjugate Techniques*”, Elsevier, 2008.
- [8] P. Stepanek, “*Dynamic Light Scattering: The Method and Some Applications*”, Oxford University Press: Oxford, U.K., 1993.
- [9] N. Grimaldi, M.A. Sabatino, G. Przybytniak, I. Kaluska, M.L. Bondi, D. Bulone, S. Alessi, G. Spadaro, C. Dispenza, *Radiation Physics and Chemistry*, submitted.

Large-scale manufacturing of radiation sculptured therapeutic nanogels.

C. Dispenza*, N. Grimaldi, M.A. Sabatino, G. Adamo, S. Rigogliuso, G. Gherzi.

2013. NSTI-Nanotech 2013, www.nsti.org, ISBN 978-1-4822-0586-2. 3, 202-205.

Large-scale manufacturing of radiation sculptured therapeutic nanogels

C. Dispenza^{*,**}, N. Grimaldi^{*}, M.-A. Sabatino^{*}, G. Adamo^{***}, S. Rigogliuso^{***}, G. Ghersi^{***}

^{*} Dipartimento di Ingegneria Chimica, Gestionale, Informatica, Meccanica, Università di Palermo, Viale delle Scienze, Edificio 6, 90128 Palermo, Italy.

^{**} CNR - Istituto di Biofisica (IBF) UOS Palermo, via Ugo La Malfa 153, 90146 Palermo, Italy.

^{***} Dipartimento di Scienze e Tecnologie Molecolari e Biomolecolari, Università di Palermo, Viale delle Scienze, Edificio 16, 90128 Palermo, Italy.

ABSTRACT

Pulsed electron-beam irradiation of poly(N-vinyl pyrrolidone) (PVP) aqueous solutions, at relatively low energy per pulse and doses within the sterilization dose range, has led to a variety of PVP nanogels of controlled size, that can be simultaneously grafted with a variety of functional monomers. Their crosslinked cores and multibranched arms with pendant carboxyl or amino groups ensure colloidal stability in a wide range of pHs and amenability to conjugation with fluorescent probes, ligands of specific cell receptors, such as short peptides, antibodies or oligonucleotides, and different type of therapeutics. Nanogels were proved to be not cytotoxic or genotoxic at the cellular level. Indeed, they showed good affinity for cells, as they rapidly and quantitatively bypass the cellular compartments, to accumulate in specific cell portions, then being completely released from the cells within 24 h.

Keywords: e-beam irradiation, PVP, nanogels, antibody, co-localization studies.

Introduction

Nanogels (NGs), or small particles formed by chemically crosslinked polymer networks, are becoming increasingly successful as multifunctional nanocarriers in the development of new therapeutic and diagnostic strategies [1]. They have an internal 3D aqueous environment for incorporation and protection of (bio)molecular drugs and a large and flexible surface for multivalent bio-conjugation. The possibility to entrap molecules, metal or mineral nanoparticles for imaging or phototherapeutic purposes; stimuli-responsiveness to achieve temporal and/or site control of the release function, chemical stability and biocompatibility complete their profile. What has mainly limited their widespread diffusion is that traditionally they have been produced with recourse to surfactants or complex chemistries. The availability of inexpensive, robust and

versatile synthetic methodologies can boost the development of effective nanogel-based theragnostic devices. E-beam irradiation could be a suitable single platform to quantitatively produce engineered nanogels. We have recently established that nanogels can be produced with high yields and through-puts by pulsed e-beam irradiation of semi-dilute aqueous solutions of water-soluble biocompatible polymers and functional groups bearing monomers, e.g. poly(N-vinyl pyrrolidone) (PVP), acrylic acid (AA) or aminopropyl methacrylamide (APMAM), using industrial electron accelerators and set-ups [2-4]. While PVP crosslinks upon irradiation, it acts as a substrate for monomer and oligomers attachment and as nanoscale template. As a result, crosslinked-core PVP nanoparticles with multi-armed surfaces, controlled particles size, crosslinking density, surface electric charge density, number and nature of functional groups and long-term colloidal stability are generated with no recourse to organic solvents, toxic initiators or catalysts and surfactants. Therefore, expensive or time-consuming purification procedures are not required. Simultaneous sterilization can be achieved depending on irradiation doses. Poly(N-vinylpyrrolidone) was chosen as base material because is widely used in pharmaceutical formulations. Both linear and crosslinked PVP have shown *in-vivo* biocompatibility and ability to escape from the body by natural pathways and processes, depending on molecular weight or particle size [5]. All the base and functionalized nanogels proved to be not cytotoxic or genotoxic at the cellular level. Indeed, they showed good affinity for cells, as they rapidly and quantitatively bypass the cellular compartments, to accumulate in specific cell portions after few hours, being then completely released from the cells after 24 h. Functional reactive groups located on NGs arms have been conjugated with either fluorescent molecules to perform localization studies in cell cultures, and/or with biologically relevant model molecules and macromolecules, such as folic acid, oligonucleotides and antibodies. Their physico-chemical properties and interactions with cells will be discussed.

Experimentals

Chemicals.

PVP K60 (Aldrich, Mn=1.60x10⁵ g/mol), acrylic acid (AA, Aldrich), (3-N-aminopropyl) methacrylamide hydrochloride (APMAM, Polyscience), fluorescein isothiocyanate (FITC, Research Organics), were used without further purification.

Synthesis of multifunctional PVP-based nanogels. PVP aqueous solutions at different concentrations in the 0.5-0.1 wt% range were prepared by overnight stirring, filtered with 0.22 μm pore size syringe filters, carefully deoxygenated with N₂ and individually saturated with N₂O. When the functional acrylic monomer was APMAM, it was added to the polymer solution at 1:100 and 1:50 APMAM:PVP's repetitive units (RU) molar ratios. While when AA was added, only 1:50 AA: PVP's RU molar ratio were considered. NGs are named after P*(X)AA(Y) and P*(X)APMAM(Y), where X is the weight percentage of polymer in water and Y is the PVP RU:monomer molar ratio. Electron beam irradiation was performed using a 10 MeV linear accelerators at the ICHTJ of Warsaw (Poland), Electronika 10/10 and the temperature was maintained at 0-4°C. E-beam irradiation was performed at relatively high frequency (400 Hz) and low-dose per pulse (13 Gy). An integrated dose of 40 kGy was supplied. After irradiation samples were dialyzed against distilled water for 48 h with 100k MWCO. The yield of micro/nanogels production process was determined gravimetrically.

Preparation of P(0.1)APMAM100^{FITC} variants.* Conjugation of the amino-graft PVP variants with FITC was carried out at pH 9.3 (Borax) and 37°C for 2 hr, following an already reported protocol [2].

Preparation of Ab-conjugated P(0.1)APMAM100 and Ab-conjugated P*(0.1)APMAM100^{FITC} variants:* Conjugation of the amino-graft PVP variants, with the rat monoclonal Anti-human CD44 Antibody C37 labeled with TRITC (Ab) [6] was performed accordingly to a standard EDC/sulfo-NHS protocol in MES at 25°C [7]. After reaction, nanogels were repeated washed with PBS at pH 7,4 and centrifuged using centrifuge filter devices (cut off 300 kDa) at 500 rpm for 10 min.

Light Scattering Measurements. The hydrodynamic diameter (Dh) of particles dispersion was measured by dynamic light scattering (DLS) using a Brookhaven BI-9000 correlator and a 50 mW He-Ne laser (MellesGriot) tuned at $\lambda = 632.8$ nm. Dynamic light scattering data were analyzed by the method of cumulants [8].

ζ -potential measurements. The surface charge of the nanogels in water was measured on diluted dispersions (1 mg/ml) at 25°C using a ZetaSizerNano ZS (Malvern

Instruments Ltd, Malvern, UK) equipped with a He-Ne laser at a power of 4.0 mW.

Localization studies of Ab-conjugated NGs. The ECV304 endothelial cells were seeded in a 96 well tissue plate at a density of 7x10³ cells/well, grown for 24 hr in DMEM complete medium and incubated in the presence of Ab-conjugated NGs (4 μg /well). After different incubation times, cells were extensively washed with PBS, to remove not reactive nanoparticles, and fixed with 3.7% formaldehyde for 15 minutes; then they were again washed with PBS. Localization was carried out by a confocal microscopy analyzer (Olympus 1x70 with Melles Griot laser system).

Results and discussion

EB-irradiation of semi-diluted aqueous solutions of PVP, i.e. at concentration lower than the critical chain overlap concentration (~1 wt) [9] and in the presence of small concentrations of monomers carrying reactive functional groups was performed at relatively high frequency and low-dose per pulse. The integrated dose of 40 kGy was selected to ensure products sterility [10]. In these conditions, a multiplicity of nanogel variants with different hydrodynamic sizes, surface properties and chemical functionalities were produced varying polymer and monomer concentration as well as solutions pH. The yield of the recovered products after purification was always above 95%. In Table 1, average hydrodynamic diameters and relative particles size distribution widths are reported. All the carboxyl-functionalized NGs (0.1-0.5wt%), have hydrodynamic diameters in the range of 10-50 nm and small particles size distribution widths, while the two amino-functionalized NGs have hydrodynamic sizes which span from the nano to the microscale. A comparison among the carboxyl-functionalized NGs' variants shows that for the same polymer to monomer ratio, increasing the polymer concentration leads only to modest increase in NGs hydrodynamic size. Conversely, in order to obtain amino-functionalized NGs with hydrodynamic diameters comparable to the carboxyl-NGs, both the polymer and APMAM concentrations in the feed had to be maintained fairly low. This suggests that the nature of the functional monomer determines the reaction pathway upon irradiation and it has the most dramatic effect on the physico-chemical properties of the final product. It has been established that in the selected irradiation conditions, hydroxyl radicals form as a result of the interaction of electrons with water. They extract protons from the polymer and form macroradicals that can recombine either inter- or intramolecularly forming crosslinks. In the presence of the acrylic monomer, radical recombination or radical propagation to the monomer reactions may occur forming monomer and/or oligomer grafts.

System	D_h (nm)	Width (nm)	ζ -potential (mV)	Width (mV)
P*(0.1)AA 50	14	5	-22	8
P*(0.25)AA 50	26	10	-40	9
P*(0.5)AA 50	40	16	-32	56
P*(0.1)APMAM 100	33	12	-6	7
P*(0.1)APMAM 50	1140	500	-34	5
P*(0.1)APMAM 50, PBS pH 9.2	200	60	-47	5

Table 1. Mean hydrodynamic diameters and relative particles size distribution widths, ζ -potential and distribution width are reported.

Homopolymerization of both acrylic monomers is not particularly favored at the irradiation pH (pH=6), owing to the electrostatic repulsion between monomer molecules [2,3]. When e-beam irradiation of the aqueous solutions of PVP with APMAM is carried out with both components, the polymer and the monomer, present at relatively high concentrations *inter-particle bridging* occurs. This is because PVP coils are slightly polyanionic due to the keto-enol tautomerism, while APMAM (pKa=8.5) is positively charged at the irradiation pH (5-6) and it shields the negative charges onto PVP, thus promoting bridging between nanogel particles. Conversely, for the carboxyl-functionalised variants, AA and its low molecular weight oligomers essentially graft on PVP chains. When the pH of the polymer-APMAM solution is controlled to be above the pKa of the monomer, as for the system P*(0.1)APMAM 50, PBS pH 9.2, the inter-particle bridging is attenuated and particle size is of about 200 nm. In table 1, ζ -potentials values and the relative width of distributions are shown. All carboxyl-functionalized systems show an anionic character that likely sees the contribution of AA's carboxyl groups. Conversely, when the NGs are obtained in the presence of APMAM they show a reduced anionic character, due to a screening effect of the negative charges of PVP by the protonated amino groups of APMAM. At the higher concentration of APMAM, when aggregation occurs, the monomer is preferentially located inside the microgel particles, therefore ζ -potential values decrease. A thorough structural characterization of the formed nanogels has been carried out by applying complementary spectroscopic techniques as FT-IR, XPS, Raman spectroscopy, liquid and solid state NMR. NGs chemical structure manly resembles

that of PVP, as expected in considerations of the low concentrations of acrylic monomers considered. A clear evidence of carboxyl groups and amino groups, deriving from the grafted monomers was gathered, with XPS and solid-state ^{13}C NMR [2, 3, 11, 12]. Preliminarily to any further development of these nanogels as biomedical nanocarriers, *in-vitro* toxicity was evaluated via MTT assay and caspase 3 enzymatic assay. All the gathered evidences indicate absence of cytotoxicity in vitro [2, 4, 13]. Different conjugation reactions were carried out to attach relevant molecules to the nanogels by converting the functional groups of the multifunctional nanogels. In particular, the carboxyl-functionalized NGs were coupled with a fluorescent probe, aminofluorescein, with a small peptide, like folic acid for targeting purposes, with an anticancer drug, Doxorubicin and oligonucleotides [14]. The amino groups functionalized nanogels were reacted with the isothiocyanate groups of FITC, to generate fluorescein labeled nanogels, with a protein, BSA, and with a TRITC labeled antibody [2, 4]. Localization studies of bare nanogels on cell cultures have been carried out and results are reported elsewhere [13]. Both the carboxyl and amino-functionalized NGs showed good affinity for cells. Nanoparticles start to concentrate inside the cells after 1-h from incubation, reaching a maximum of concentration within 6-7 hours from incubation, being then completely released from the cells after 24 hr [13]. In figure 1a-b localization of P*(0.1)APMAM100 conjugated with Tritc-labeled antibody CV on ECV304 cells after 15 min and 6 h, respectively, are shown. F-actin of cells is marked with green fluorescent phalloidin, while the antibody-conjugated nanoparticles show red fluorescence, owing to the Tritc

label. The pattern of the movement through cell surface and in cell compartments of Ab-conjugated NGs was very similar to that of bare NGs (data reported elsewhere [13]), but Ab-conjugated NGs are internalized faster. After 15 min of incubation they seem to be already preferentially located on the cells (figure 1 a), although a significant proportion is still present in the culture medium. Cells reach their maximum uptake after 6 h, then the red-fluorescence intensity of cells progressively decreases. Fluorescent variants of NGs, namely P*(0.1)APMAM 100^{FITC}, was conjugated with a TRIC- labeled antibody.

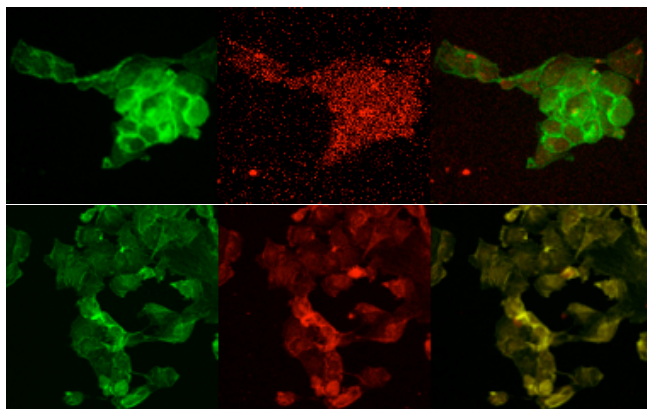


Figure 1. Localization of Ab-conjugated NGs in cell cultures. Confocal microscopy of antibody-conjugated-NGs observed after two different incubation times: (a) 15 min. (b) 6 h. Total sections.

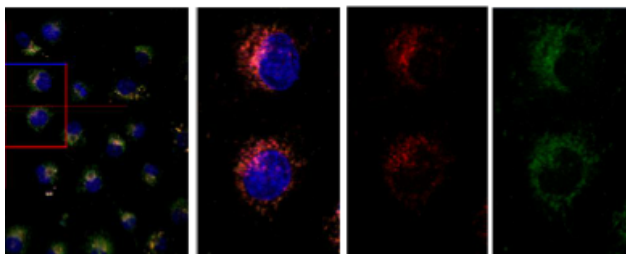


Figure 2. Co-localization of Ab-conjugated P*(0.1)APMAM100^{FITC}NGs. Nuclei were stained with DAPI (blue), nanogels are labeled with FITC (green) and the antibody bound to the nanogels with TRITC (red).

In figure 2, the localization of immuno-nanogels in ECV304 endothelial cell culture after 4 h incubation is shown. Nuclei were stained with DAPI (blue), nanogels are labeled with FITC (green) and the antibody bound to the nanogels with TRITC (red). Co-localization studies prove the stability of the conjugation bond and the localization of the NGs in a specific compartment of the cell, around the nucleus.

CONCLUSIONS

The work here presented shows that e-beam radiation processing is a viable and effective synthetic methodology to manufacture PVP-based functional nanocarriers, in a single step, with high yields and tunable properties. After irradiation, no expensive or time-consuming purification procedures are required, as no recourse to catalysts, initiators or surfactants is made. Simultaneous sterilization can also be achieved, by a proper selection of the irradiation doses. All the generated NGs are non cytotoxic, non immunogenic and able to stably bind biological molecules. While the final fate of these nanoparticles will be the subject of future investigations through animal in-vivo and ex-vivo test, different strategies to bind anticancer drugs to the nanogels using cleavable linkers are being tested showing very promising results.

References

- [1] R.T. Chacko, J. Ventura, J. Zhuang, S. Thayumanavan, *Advanced Drug Delivery Reviews*, 64 836–851, 2012.
- [2] C. Dispenza, M.A. Sabatino, N. Grimaldi, D. Bulone, M.L. Bondi, M.P. Casaletto, S. Rigogliuso, G. Adamo, G. Ghersi, *Biomacromolecules*, 13(6), 1805–1817, 2012.
- [3] N. Grimaldi, M.A. Sabatino, G. Przybytniak, I. Kaluska, M.L. Bondi, D. Bulone, S. Alessi, G. Spadaro, C. Dispenza, submitted.
- [4] C. Dispenza, M.A. Sabatino, N. Grimaldi, G. Spadaro, D. Bulone, M.L. Bondi, G. Adamo, S. Rigogliuso, *Chemical Engineering Transaction*, 27, 229-232, 2012.
- [5] R.B. Login, J.S. Shih, J.C. Chuang, Patent US005219950A, 1993.
- [6] G. Ghersi, H. Dong, L.A. Goldstein, Y. Yeh, L. Hakkinen, H.S. Larjava, W.T. Chen, *The Journal of Biological Chemistry*, 277, 29231-29241, 2002.
- [7] G.T. Hermanson, “Bioconjugate Techniques”, Elsevier, 2008
- [8] P. Stepanek, “Dynamic Light Scattering: The Method and Some Applications”, Oxford University Press: Oxford, U.K., 1993.
- [9] C. Dispenza, M. Ricca, C. Lopresti, G. Battaglia, M. La Valle, D. Giacomazza, D. Bulone, *Polymer Chemistry*, 2, 192-202, 2011.
- [10] B.J. Lambert, J.M. Hansen, *Radiation Physics and Chemistry* 52, 11-14, 1998.
- [11] C. Dispenza, N. Grimaldi, M.A. Sabatino, S. Todaro, D. Bulone, D. Giacomazza, G. Przybytniak, S. Alessi, G. Spadaro, *Radiation Physics and Chemistry*, 81(9), 1349-1353, 2012.
- [12] M.A. Sabatino, D. Bulone, M. Veres, A. Spinella, G. Spadaro, C. Dispenza, *Polymer*, 54 (1), 54-64, 2013.
- [13] S. Rigogliuso, M.A. Sabatino, G. Adamo, N. Grimaldi, C. Dispenza, G. Ghersi, *Chemical Engineering Transaction* 27 247-252, 2012.
- [14] N. Grimaldi, M.A. Sabatino, D. Bulone, M. Mangione, M.L. Bondi, M.P. Casaletto, G. Spadaro, C. Dispenza, submitted